Modelling and Diagnostic Study of Flow in an Optical Engine with Negative Valve Overlapping for Homogeneous Charge Compression Ignition

By

Marcin Frackowiak

A thesis submitted to
The University of Birmingham
For the degree of
DOCTOR OF PHILOSOPHY

The University of Birmingham
School of Engineering
September 2009

Abstract

The three-dimensional bulk gas motion in an engine cylinder with different flow scales generates a varied range of shear stresses and deformations in the fluid, which leads to the gas turbulence. These flow irregularities combined with periodic engine operation induce gas fluctuations over time and cylinder volume. This affects the thermal in-homogeneity of the in-cylinder gas mixture composition.

A novel approach to the formation of in-cylinder flow that promote Homogeneous Charge Compression Ignition HCCI engine by generating various patterns of the in-cylinder flow has been proposed. Two types of inlet manifold diffusers were experimentally applied to a 4-valve pentroof optical engine and the spatial flow in-homogeneities were carefully analysed. Additional special effects in the in-cylinder flow fields were induced by using the Negative Valve Overlap (NVO) technique. Case studies for internal nonreactive 'COLD' flow structures were investigated using a motored single cylinder optical engine and Particle Image Velocimetry (PIV) technique to validate a 3-D CFD engine model.

The optical diagnostics and CFD modelling of the in-cylinder HCCI 'COLD' flow show that two different porting strategies with fixed Negative Valve Overlap (NVO) significantly affect the in-cylinder flow structures. A comparison of in-cylinder flow effects generated by different intake deflectors indicate that a low-swirl port configuration can potentially improve the fuel and thermal homogeneity by producing higher values of Root Mean Square (RMS) of velocity fluctuation and turbulence intensity. The high-swirl port configuration generates high stratification of gas flow field at Top Dead Centre (TDC). The final part of the study investigates the stratification of gas temperatures. The

studies show that both of the intake shrouds generate differences in the rate of change of the large scale rotating flow affecting the gas transport and mixing process within the engine cylinder.

DEDICATION

Dedicate To My Family

Marek, Miroslawa, Ilona and Mariusz

ACKNOWLEDGMENTS

The author would like to express his deepest gratitude and sincere thanks to my supervisor Prof. Hongming Xu and associate supervisor Prof. Miroslaw Lech Wyszynski, for their support and valuable guidance throughout this project. Dr Athanasios Tsolakis is also greatly appreciated, for his help.

Technical support by Peter Thornton, Carl Hingley and Lee Gauntlett was highly valuable and appreciated.

Special thanks to Jaguar Land Rover for their financial and technical support especially that provided by Dr. Trevor Wilson and Dr. Jun Qiao. Without this it would have been impossible to conduct and complete this thesis.

List of Publications, Related Work and Achievements

1. M. Frackowiak, et al., 'The Effect of Exhaust Throttling on HCCI - Alternative Way to Control EGR and In-Cylinder Flow', University of Birmingham 2008, SAE Technical Paper Series, SAE 2008-01-1739, 2008.
2. M. Frackowiak, 'Analysis of the Spray Development under a Backpressure Conditions-Optical Bomb Case', University of Birmingham 2007
3. M. Frackowiak, 'Optical Measurements of Engine Direct Injection Spray Development', University of Birmingham 2006

CONTENTS

List of Figures

List of Tables

List of Definitions and Abbreviations

Roman Symbols:

C	Constant
cp	Specific Heat at Constant Pressure
E	Specific Internal Energy
f	External body force
F	Flow variable
g	Acceleration due to gravity
G	Production of turbulence kinetic energy due to velocity gradient
H	Specific angular momentum of the in-cylinder flow
h	Specific enthalpy
I	Engine cycle
I	Unit vector in x-direction
J	Diffusion heat flux
J	Unit vector in y-direction
k	Coefficient of thermal conductivity
k	Turbulence kinetic energy
K	Unit vector in z-direction
m	Mass
N	Number of engine cycles
n	Crank shaft rotational speed
No	Number of computational cells
P	Pressure
S	Strain-rate tensor

S	Source term
t	Time
T	Temperature
U	Mean Velocity
v	Fluid velocity vector
x, y, z	Cartesian coordinates
y	Wall distance
Y	Mass fraction

Greek symbols:

δ	Kronecker's delta
ε	Turbulence dissipation rate
θ	Crank angle
κ	von Karman constant
λ	Second coefficient of dynamic viscosity
μ	Coefficient (first) of dynamic viscosity
ρ	Density
σ	Turbulent Prandtl number for k
σ	Turbulent Prandtl number for ε
τ	Shear stress tensor
φ	Scalar quantity of fluid properties
ω	Angular velocity
Ω	Mean ratio tensor
ω	Turbulence specific dissipation rate

Subscripts:

CV	Cyclic variability

E	Energy
E	Ensamble-average
i, j, k	Direction unit vectors
K	Turbulent kinetic energy
l	Laminar
m	Mass
P	State point
r	Species
t	Turbulent
w	Wall
ε	Turbulent dissipation rate

Acronyms and Abbreviations:

1D, 2D, 3D One-, two- and three-dimensional

aTDC	After Top Dead Centre
BDC	Bottom Dead Centre
BMEP	Break Mean Effective Pressure
BSFC	Break Specific Fuel Consumption
bTDC	Before Top Dead Centre
CAD	Crank Angle Degrees
CAD	Computer Aided Design
CAI	Controlled Auto-ignition
CFD	Computational Fluid Dynamics
CI	Compression Ignition
CO	Carbon Monoxide
COV	Coefficient of Variation

CPS	Cam Profile Switching
CR	Compression Ratio
DAQ	Data Acquisition
DES	Detached Eddy Simulation
DFI	Direct Fuel Injection
DM	Dynamic Mesh
DNS	Direct numerical simulation
EGR	Exhaust Gas Residuals
EVC	Exhaust Valve Closing
EVO	Exhaust Valve Opening
EWT	Enhance Wall Treatment
FDM	Finite Difference Method
FEM	Finite Element Method
FFT	Fast Fourier Transform
FVM	Finite Volume Method
GUI	Graphical User Interface
HC	Hydrocarbons
HCCI	Homogeneous Charge Compression Ignition
IC	Internal Combustion
IGES	Initial Graphics Exchange Specification
IMEP	Indicate Mean Effective Pressure
IVC	Intake Valve Closing
IVO	Intake Valve Opening
LDA	Laser Doppler Anemometry
LDV	Laser Doppler Velocimetry
LES	Large Eddy Simulation

LIF	Laser Induced Fluorescence
MFB	Mass Fraction Burned
MIE	MIE Scatter Light
MOP	Maximum Opening Point
Nd:Yag	Neodymium-Doped Yttrium Aluminium Garnet
NOx	Nitrogen Oxides
NVO	Negative Valve Overlapping
PDF	Probability Density Function
PISO	Pressure Implicit Splitting of Operator
PIV	Particle Imaging Velocimetry
PMEP	Pumping Mean Effective Pressure
Pr	Prantl Number
PTU	Programmable Time Unit
PTV	Particle Tracking Velocimetry
PVO	Positive Valve Overlapping
RANS	Reynolds-average Navier-Stokes
Re	Reynolds Number
RNG	Renormalization Group
RSM	Reynolds Stress Model
SI	Spark Ignition
SIMPLE	Semi-Implicit Method for Pressure-Linked Equations
SR	Swirl Ratio
TDC	Top Dead Centre
TLS	Turbulent Length Scale
TR	Tumble Ratio
TTL	Transistor Transistor Logic

UDF	User-defined function
VCT	Variable Cam Timing
VVT	Variable Valve Timing

Chapter 1

INTRODUCTION

1.1 Introduction

The term 'Internal Combustion Engine' usually refers to a reciprocating type of engine in which the combustion of a fuel occurs with an oxidiser (usually air) where the work is done in a combustion chamber. The purpose of an internal combustion engine is to produce the work by the chemical energy contained in the fuel bonds and exchanging it for the potential energy of cylinder gas pressure and heat. The mechanical work is transferred by a medium (working fluid) and by the mechanical components of the engine, e.g. the piston, cylinder and the crankshaft. Moreover, the working fluid within an engine prior to combustion is a mixture of air-exhaust gases and fuel, with a flammability range that is strongly dependent on flow effects such as turbulence, large-scale flows, fuel type and combustion strategy [1].

Internal combustion engines can be divided into three groups of combustion and mixture preparation type. The Spark Ignition (SI or OTTO-cycle) and the Compression Ignition (CI or Diesel engine) are the most widely used combustion systems in the current engine commercial. The third group of internal combustion engines follow the concept of Homogeneous Charge Compression Ignition (HCCI) which is in the experimental stage of development. In terms of its mixture preparation and combustion, the HCCI engine uses a relatively new technique, and it combines the best features of the SI and the CI engines. In an HCCI engine the generally homogeneous fuel-air mixture (as in the SI engine) is compressed by the piston and ignited by that in a hot in-cylinder atmosphere (similar to the diesel engine). It must be noted that it has a higher engine efficiency than the SI engine due to reduced pumping losses, as no throttling body is used to control the engine load and a highly diluted

mixture, therefore the gasoline HCCI engine approaches a level of efficiency similar to a Diesel with a significant reduction in NOx and soot emissions [2].

The Homogeneous Charge Compression Ignition (HCCI) has emerged as a promising future technology for the decrease of exhaust emissions and an improvement in the fuel economy of internal combustion engines [3]. There are generally two proposed methods of realising HCCI operation. The first is through the control of gas temperature in the cylinder and the second is through the control of the chemical reactivity of the fuel and air mixture. For both methods the temperature of the charge must be high enough to reach auto-ignition near the TDC of compression.

In HCCI engine, control of the auto-ignition process is realised partially by retaining a portion of hot residual gases which have a high heat capacity and temperature compared to the fresh charge. Residual gases change the chemical reactivity and thermodynamic properties of the diluted mixture and influence the duration and maximum temperature of combustion. Hence the mixing gas mechanisms along with residuals have an important role in the active control of combustion phasing. The amount of residual gases available with the in cylinder chamber and the method of ensuring the presence of hot gases have a global impact on BSFC (Brake-Specific Fuel Consumption) and BMEP (Brake Mean Effective Pressure) [4]. EGR trapping, i.e., recycling a large quantity of hot burned gases by using special valve-train events (e.g. negative valve overlap), seems to be practical for many engine configurations and can be combined with any of the other HCCI enabling technologies. The NVO and the large amount of trapped residuals within the cylinder reduce exhaust emissions, mainly of NOx, by using lower average temperatures during combustion [5]. While this method has been widely researched, limited information has been published about the concerned in-cylinder flow and thermal in-homogeneities during induction and compression with various intake port configurations and an NVO strategy for a HCCI engine. In addition, it must be denoted that

three dimensional in-cylinder flow and complex aerodynamics significantly influence the mass transport and mixing process throughout the cylinder. In-cylinder turbulent gas flow that has been transferred by large-scale eddies and the high level of RMS, which subsequently affects the fuel-air mixture and ultimately the combustion process due to mixture in-homogeneity.

In theory, a further improvement in engine fuel economy, emissions and engine operating windows can be achieved by linking both the concepts of HCCI combustion and turbo-charging technologies [6]. Moreover, HCCI combustion technology is inherently associated with a high rate of internal EGR management by systems such as variable cam timing (VCT) and cam profile switching (CPS). The HCCI engine load is a function of specific amounts of EGR and inherent in-homogeneity in the cylinder, and therefore EGR is a crucial factor for the control of the auto-ignition and the main combustion phase. Any variation in the EGR rate can cause a disturbance and lead to a misfire or knock combustion with a high value coefficient of variation (COV) [7].

1.2 Objectives

The main objective of the present research is to find the major gas structures and flow mechanisms that affect the in-cylinder gas mixing process and the development of spatial cylinder in-homogeneities. In addition, an extended knowledge about the internal aerodynamic processes is to be acquired to gain a better understanding of the thermal cylinder stratification and the possible regions of auto-ignition in the HCCI engine. A experimental single cylinder optical engine has been fitted with varied intake port geometries and with symmetrical NVO of valve events for the sensitive ‘COLD’ flow study cases. The single cylinder engine is a 4-valve four-stroke direct injection engine with a pentroof head. For the designated work, both experimental and computational methods are utilised, including building an optical laser bench and a CFD full-scale three-dimensional engine model. The in-

cylinder flow induced by three types of intake ports, and the created flow cylinder effects are measured and computed by using the PIV and CFD methods respectively.

The in-cylinder fluid flow is divided into three major flow structures recorded via the PIV system. The Jet-Jet, Jet-Wall and Bulk gas structures, which are filtered from the general flow pattern, show features of the gas transport within the engine cylinder. The obtained group of large flow patterns simplify the analysis of and give suggestions for the major mechanisms of the gas transport and possible regions of higher RMS velocity fluctuations as well as field in-homogeneities. The chosen in-cylinder flow strategy is based on 70 consecutive engine cycles in order to produce results similar to those produced by the CFD Reynolds Averaged Navier-Stokes (RANS) solver. In addition, use of the coupling of large-scale PIV flow patterns with a 1-D numerical analysis has been considered to characterise the pressure fluctuations and temperature history within the cylinder and intake manifolds. The 1-D solver outputs are preferable as the initial and boundary conditions for further CFD analysis.

In this thesis, the commercial finite volume Computational Fluid Dynamics (CFD) package FLUENT 6.3 and the Reynold Average Navier Stokes (RANS) solver have been utilised for the modelling of the in-cylinder turbulent flow. In addition, a 1-D gas dynamics WAVE code has been applied to calculate manifold gas fluctuation effects in order to decrease CFD computational costs.

The study includes the following subjects:

- Effects of port geometry on in-cylinder spatial and temporal large scale flow and turbulence development (during the induction and compression phase) for a symmetric NVO in a HCCI engine.
- Effects of the back flow on the in-cylinder gas mixing process (during early and late induction) for a symmetric NVO in a HCCI engine.

- Effects of port geometry on the in-cylinder spatial and temporal thermal gas pattern development (during the induction and compression phase)
- Effects of Intake jet and separation flow on the large scale in-cylinder flow gas process mixing

1.3 Thesis Outline

The thesis is divided into ten consecutive chapters which extensively covers the physical aspects of in-cylinder turbulent 'COLD' flow within the HCCI motored engine and includes theoretical and computational approaches, and the data is heavily based on a 4-valve pentroof HCCI single cylinder optical engine with a fully transparent cylinder liner and modified intake ports. The in-cylinder 'COLD' flow is examined throughout the experimental laser techniques as well as the CFD computational approaches. Following this introduction, chapter 2 is devoted to a 'Literature Review', which summarise the current and past investigations of the complex in-cylinder flow phenomena, including turbulence of gas, and mixing and flow stratification mechanisms. Moreover, the optical and numerical methods to analyse the in-cylinder flow are reviewed.

The theoretical and computational background of the gas dynamics process and the turbulence phenomena are discussed in Chapter 3. The in-cylinder optical techniques for gas flow measurements as well as a detailed description of the experimental engine system are included in Chapter 4. The foundation for analytical work with the turbulent in-cylinder flow phenomena and the methodology for the analysis of large-scale flow development are the subjects of Chapter 5. Chapter 6 has been designated to in-cylinder 'COLD' flow pattern measurements and the analysis of the development of large-scale turbulent gas structures with different port strategies under the symmetric NVO valve event. Moreover, the in-cylinder 'COLD' flow has been compared between each case and the important aerodynamic features are analysed with regards to the mixing gas effect. Based on the obtained experimental data,

Chapter 7 describes in detail the setting up of the CFD single cylinder engine model 'Mk-MF1' and the validation procedure. The CFD three dimensional simulation and the spatial mixing mechanisms are investigated in Chapter 8. In addition, from the parametric study, important scalar values of the cylinder flow field are obtained with the chosen port strategy. The most important thermal characteristics of in-cylinder flow in terms of the HCCI engine under two different port strategies are the subject of Chapter 9. Chapter 10 covers the main conclusions of the present work and possible areas of further investigation.

Chapter 2

LITERATURE REVIEW

2.1 Introduction

Understanding the in-cylinder gas mixing process that is driven by the large-scale flow structures is important for Internal Combustion Engine technology; and it remains one of the main challenges to the current time. One commonly known difficulty with analysing the auto-ignition phenomena is our limited knowledge about the spatial and temporal thermo-reactive flow cylinder processes. In addition, it must be noted that because the structure of the engine cylinder turbulent flow as well as the thermal fields have never been homogeneous. They randomly influence the beginning of the auto-ignition process, the combustion process, and the emission phenomena. Therefore a lot of effort has been put in by researchers for a better understanding of turbulence-flow effects and consequently the major dynamic mechanisms responsible for gas thermal transport within an engine cylinder. This chapter briefly reviews the past and current experimental and modelling works in field of fluid dynamics researches in cases of the engine cylinder technology.

2.2 Review of Experimental and Computational Research within the area of engine cylinder flows.

An accurate description of the engine turbulence process as regards its unsteady flow still unknown and needs further development. This definition should take into account numerical and analytical models. J.Lumely proposed the description of in-cylinder turbulent flow as, "…. the turbulence is spreading itself, organized momentum, fuel, residual gases, in fact anything that can be transported throughout the cylinder tries to make everything as

uniform as possible. This is what turbulence does the best (fluid transportation), and it does it much better than molecular transport" [8]. The engine design, valve timing, and engine thermodynamic conditions indirectly govern the magnitude and origin of the turbulence. All of these factors, including the mixture properties, are important for both spark ignition and diesel engines. However, a more sensitive subject is the new concept of cleaner combustion: Homogeneous Charge Combustion Ignition (HCCI), which is controlled only by a thermo-reactive in-homogeneous fluid flow field [9]. A commonly applied strategy used to manage the auto ignition of HCCI engines is the Negative Valve Overlap (NVO) technique with a residual gas recompression phase and a dilution fresh charge effect. The in-cylinder gas mixing process of hot and cold gas structures imposes mass transport across the whole cylinder domain and influences the in-homogeneity of the mixture field. The coupled effects of spatial flow and thermal in-homogeneity are controlled by the turbulent structures, and these effects are not well explored. The thermal mixture stratification concept and in-cylinder flow could be controlled more effectively through the use of consciously arranged fields of velocity fluctuations and the convection of large-scale gas structures.

2.3 Early In-Cylinder Gas Dynamics Experimental and Computational Work.

An early experimental investigation of fluid dynamics within the motored SI engine was conducted by Lee [10]. In that study a few different intake port strategies were considered to evaluate general influences on in-cylinder flow. The intake jet was deflected by a series of shroud intake valves and by altering the shape of the internal cylinder flow. The in-cylinder flow pattern was visualised by mixing incoming air with feathers; and the internal aerodynamic structure was recorded by a high speed camera. This research was undertaken in 1939 and was probably the first recorded complex and modern study of in-cylinder flow phenomena. A series of internal engine aerodynamic experiments were extensively set to

evaluate the cylinder gas penetration, distribution and evaporation of fuel sprays. In addition, from these experiments it was found that flow induced during the intake process is partially conserved by the tumbling motion of the gas at the halfway point for the TDC of compression. Also it was found that any valve shroud geometry can maintain a tangential flow around the cylinder axis imposing a form on the swirl flow and persisting after the combustion phase. It was apparent that in-cylinder velocity is a direct function of the engine speed and is inversely proportional to the port flow valve area. Moreover it was revealed that port and intake manifold geometry influence the internal engine flow pattern effectively as well as the overall fuel and gas mixing process.

The early work of Ricardo et al [11] at Cambridge University was focused on the in-cylinder gas turbulence effect related to the combustion and heat transfer in the IC engine. Increasing flame speed as a possible solution to stop the combustion knock phenomena from occurring was another area of research. It was reported that once the in-cylinder flow is highly turbulent it actively supports high flame speed and reduces the knocking effect. This discovery was important for early SI engine development and gave the foundations for extended development of fluid dynamics in terms of internal engine flow. Also, it was experimentally measured that a centrally mounted spark-plug is the most preferable in terms of a short travel distance for the flame front. This results in a short cylinder burn time and possibly increases the engine's thermal efficiency due to the application of a higher compression ratio without the knocking effect. The interaction between knock combustion and the fuel octane number was discovered and described by Ricardo and had a global impact on the improvement of engines.

The aspect of the engine turbulence generation researched D.P.Hoult [12] was the water engine flow analogy. Two distinct ring vortices were created during intake within the cylinder with regards to the (stability and precession of eddies). The optical measurement

showed that the stability of vortices is strongly dependent on the parameters of the valve locations, stroke ratio and engine speed. The experimental results were used for the extended computational model of the cylinder flow with turbulence and combustion interacting. The CFD model has been compared with available hot-wire measurements for the compression and expansion phases, thus providing a well-scaled picture of the rapid distortion of the ring vortex during compression. From computational data, it is evident that the compressed vortex is affecting the strain field, and it is influenced by the expanding flame front. The turbulent intensity ahead of the flame front increases rapidly, then stays at an approximately constant value until the end of the combustion phase. Moreover, the turbulence intensity depends very weakly on the spark time and initial cylinder pressure and is stronger at lean fuel-air ratios.

A.D. Gosman and Johns [13] developed a predictive computational model which simulated the detailed patterns of gas flow, heat transfer, and combustion in reciprocating engine. A code was developed to simulate both types of flow, laminar and turbulent, and both compressing and non-compressing varieties. The core of the code was based on the Reynolds Average Navier-Stokes RANS equations; and for the full turbulent flow, one of the B.E. Launder and D.B Spalding's. [14, 15] early k-ε closures turbulence models was chosen. The first of the single in-cylinder flow case with an available exact analytical solution gave an acceptably accurate prediction for the calculations. The turbulent as well as the laminar cases generally show agreement with the measurements but do not agree with them for all cases overall. There are some uncertainties surrounding inlet conditions and part of the intake flow slope. In addition, it was found that the inlet process produces the highest mean and turbulent in-cylinder motions which is strongly in-homogeneous. Moreover, the shear stress generated by the intake flow is far higher than the normal stress generated by the piston. Other important information was obtained during the compression stroke phase where the mean and turbulent motions are gradually decaying into the dissipated cylinder flow. It has been found that the

energy dissipation turbulence model applied for this work probably overestimated the compression generated turbulence, due to the limitations of the isotropic k-ε model.

The Particle Imaging Velocimetry (PIV) was used for measuring the SI engine flow and has been quantified experimentally by P. Calendini et al. [16]. The PIV method has been applied to the four valve single cylinder optical engine in terms of instantaneous two and three dimensional in-cylinder field measures. From the obtained two-dimensional PIV data at the specified engine geometry set-up, the induced flow has been categorised as stable with large scale flow structures and small cycle to cycle variations (CBC). The featured compression stage altered the flow characteristics; and the in-cylinder flow pattern performed large unstable eddies with high CBC variations. The three-dimensional PIV flow measurement (stereoscopic), the engine compression stage showed that the in-cylinder flow has a fully three dimensional unstable nature and is fully turbulent. Furthermore, the obtained smooth of the mean velocity does not precisely represent stable flow within the cylinder for an ensemble average of 70 consecutive engine cycles.

Y. Li et al. reviewed in detail the tumbling flow structure induced within the four-valve spark ignition engine by utilising Particle Image Velocimetry (PIV) and CFD techniques [17, 18]. The obtained experimental results showed that the early formed tumble vortex was distorted in the late compression stroke stage. Moreover, the tumble centre was formed near the centre of the geometrical cylinder and moved towards the exhaust side as the piston is went up. It was found that the velocity fluctuation field was in-homogenous during the whole compression process and could hardly represent the ensemble average flow characteristics. A CFD in-cylinder flow analysis was performed with the KIVA™ code and the k-ε closures turbulence model. Part of the computational work described in detail the tumble break-up process and the origin of creation. The results showed that during the intake stroke, two counter-rotating vortices were generated on the two sides of the cylinder chamber.

In addition, the tumble motion strength is dependent on the intake flow along the surfaces on the exhaust side. The CFD results indicated that during compression the tumble vortex partially decayed, breaking up into small eddies and enhancing turbulent gas transport throughout the chamber by increasing the root mean square RMS of the velocity fluctuation.

2.4 Effect of Engine Geometry on Turbulence, Thermal Stratification and Large-Scale Engine Cylinder Flows.

M. Christensen et al have experimentally studied the effect of in-cylinder flow and turbulence on HCCI operation [19]. The experiments were carried out on an in-line six cylinder Volvo™ TD100 truck engine, supplied with an optical access; and the flow was measured by the Laser Doppler Velocimetry (LDV) method. They achieved different level of turbulence by altering the swirl ratio through the use of two bowl piston geometries coupled with varied intake port designs. From the obtained results it is apparent that the combustion chamber plays an important role in HCCI combustion. Under the same engine operational conditions they achieved a longer combustion duration for the square bowl in the piston than for a disc-shaped combustion chamber. In addition, for a late combustion timing the disc-shaped combustion chamber improved the engines thermal efficiency and it was independent of the swirl ratio.

Various factors influencing HCCI combustion were investigated by Zhao et al. [20]. Experiments were conducted with a single cylinder optical engine, using the planar laser-induced fluorescence (PLIF) technique. An optical investigation showed large in-cylinder gradients in the fuel mixture distribution around the chamber periphery under a strong swirl flow. For the obtained cylinder mixture distribution, the auto-ignition phenomena always took place in the middle of the cylinder chamber. From this, they concluded that the main effect was the thermal in-homogeneity of the residual gas. Moreover, the established numerical

model in conjunction with the experiments indicate that chemical effects are not involved in the combustion phase by the residual exhaust gas species.

The thermal stratification of the enhanced natural gas cylinder for the smoothing of HCCI heat-release rates was investigated by M. Sjoberg et al. [21]. The experiments were performed with a Cummins B-series diesel engine which was converted for single-cylinder HCCI operation. The proposed thermal stratification was achieved by increasing the cylinder wall heat-transfer throghout lowering the coolant temperature from 100 ˚C to 50 ˚C. It has been found that thermal in-homogeneity may improve knock resistance and substantially decrease heat-release rates. In addition, this strategy induces higher heat loses which are associated with low thermal efficiency. Furthermore, it has been found that an overall retarded combustion leads to unstable engine operation, resulting in higher IMEP cylinder variations and increased emissions.

The nature of fluid motion in a spark ignition engine (SI) cylinder has been extensively analysed by W. Reynolds with a series of experimental and computational works [22]. Particular attention was paid to the in-cylinder turbulence process, including the formed convection and distortion parts of turbulence gas phenomena. He found that the most active region of turbulence production during intake is in the flow through the valve lip and seat. In this region, strong shear layers are dynamically unstable and break down into the form of ring eddies which later on merge to become large-scale vortices [23]. The in-cylinder complex tumble-swirl break down process into the three dimension motions was analysed by C. Chandrsuda and Clark et. al. [24, 25]. The broad range of the turbulent flow scales, which are inherently part of the intake conical jet flow, were characterised by H. Tennekes, et al [26]. In addition, the study consists of information about the mechanisms involved in the break-up of the turbulence from the large eddies of the order of the conical jet dimension to the small-scale eddies that dissipate the turbulent motion.

W. Reynolds [27] analysed the process of purging and heat transfer during successive engine cycles that are associated with turbulence effects in order to predict the charge stratification and turbulence mixing gas intensity. He postulated that to understand partially combustion effects which produce NOx, CO, CO2 and other species, an investigation must be concerned with the spatial charge stratification via the turbulent in-cylinder fuel-gas mixing process. A combustion analysis that includes governed physical effects requires spatial cylinder information regarding gas turbulence structure and turbulence scales. This is important as one of possible reasons for the formation of pollutants in various amounts and in different cylinder regions due to an inappropriate gas mixing strategy. The computational results showed that general circulation in the cylinder and the turbulence scales play the dominant role in the thermal mixing process and its effect on the combustion duration.

2.5 Summary

In the current chapter a wide range of experimental and computational work, conducted for different engine types and flow regimes has been briefly reviewed. The presented publications were focused on dealing with information about complex in-cylinder flow aspects such as turbulence, thermal in-homogeneity, and the development of large-scale flow structures. Complex engine cylinder flow phenomena has been analysed experimentally by [3, 4, 5, 9, 12, 13, 14, 15] using various optical and laser measuring methods. The most common and powerful spatial methods used for the engine cylinder flow analysis are the PIV and LDV respectively. The PIV and LDV studies were mainly applied to the measurement of the large-scale in-cylinder structures, to investigating the formation, distortion and break-up process within the internal combustion engine. From these studies, it is evident that the turbulent spatial cylinder flow formations impose the ratio of the mass transport and the mixture in-homogeneity spread throughout the cylinder domain. The computational work is another important part of the in-cylinder flow investigations and is subject of a good deal of

work [6,7,10,17,18]. The main challenge in CFD simulation lies in numerical and geometrical limitations of built models. The computative model is simplified and can not resolve all the time and length scales of real turbulent flow. Therefore, the structure of the modelled flow is usually based on the RANS concept and two additional transport equations of the Reynolds stress enclosure concept [7, 8]. Additionally the turbulence models and the flow diffusion computed by enclosure equations must simulate similar experimental flow effects. The CFD codes and validated engine flow cases significantly enhance the knowledge about the air-mixing process, combustion, the time of ignition and effects on emission.

From the presented literature, it is evident that an enormous amount of research has been carried out within the internal combustion engine area. The reactive gas flow structure as well as various valve timings and port geometry strategies were examined by the experimental and computational methods. Nevertheless only a few publications e.g. [10, 13] have been carried out with regards to the in-cylinder flow pattern in HCCI engines. For this reason the current work is mainly focused on the development of in-cylinder aerodynamic structures under the low-valve lift; and uses various porting and NVO strategies. In addition, the cylinder flow in-homogeneity will be analysed computationally in terms of the thermal transport coupled with the experimental velocity vectors flow field. The computational study will be validated experimentally against the PIV research method.

Chapter 3

THEORETICAL BACKGROUND AND COMPUTATIONAL MODELING OF TURBULENT FLOW

3.1 Introduction

The objective of this chapter is to establish a basic theoretical and numerical review of turbulence. The dominant turbulent nature of gas flow within an Internal Combustion Engine (ICE) is evident and is the main consideration of this thesis, since turbulence influences the fluid flow transport, the thermal in-homogeneity and finally, the combustion aberration.

The in-cylinder turbulent flow research using a group of experimental optical methods, in conjunction with a numerical modelling approach, involves several advanced flow diagnostics tools. The numerical approach, which uses complex models, coupled with the experimental results, expands the time and spatial flow field information [28]. However, any arbitrary mathematical model will still not precisely simulate the nature of turbulent flow and it is randomised character. The most effective CFD model used to evaluate the effects of the turbulent gas transport is the Eddy Viscosity Concept, which describes the energy balance between the turbulence time and length scales [29]. The modelled turbulence based on the two-transport equations ***(k)*** (turbulence kinetic energy) and ***(ε)*** (turbulence kinetic energy dissipation) is resolved based on the Reynolds Average Navier-Stokes (RANS) concept of the governing equations [30]. Other turbulent solvers are the Large Eddy Simulation (LES) and the Direct Numerical Simulation (DNS) solvers where some range of turbulent scales are resolved directly on the available discretisation. The direct numerical method, DNS, as well as LES, are still too computatively expensive for a complex engine simulation.

3.2 Turbulence Characteristics

A detailed definition of turbulence has been sought for several centuries, and still today no general approach for the exact solution exists. Assumption regarding the turbulence phenomena, in particular the imposed flow effects, have been postulated by scientists, J.L.Lumley, H.Tennekes [19] and are listed below:

Diffusivity- Turbulence with high velocity and pressure fluctuations enhances the transfer of momentum, mass and energy across the cylinder domain compared to the molecular diffusion. The increase in the flow diffusivity increase e.g. the spreading rate of the momentum exchange within the boundary layers, via jets and vortical structures decreases or delay the wake and separation point for bluff bodies such as cylinders, airfoils and cars. The strong diffusivity flow inputs result in large velocity gradients and the wall friction increases as the system pressure decreases. The diffusivity of turbulence is the most important feature in almost all engineering cases [31].

Dissipation- The amount of energy passed from the main flow to the largest eddies and later on to the lowest scales is dissipated by the molecular viscosity into heat. This effect is called the turbulence cascade process and is an energy dissipation process. It is interesting to note that the rate of the turbulence energy dissipation is not dependent on the molecular viscosity, but is determined by the large-scale structures J.Lumely [1].

Transient (unsteady)- Turbulent flow is the irregular and random movement of particles over time. Stochastic methods are therefore used to define such a flow field. A time-average method has been proposed by Reynolds (1895) and this concept is used in the Reynolds decomposition method for RANS equations and CFD solvers. The Reynolds decomposition concept divides flow into two parts, the mean value and the fluctuation RMS of the flow. The

mean values are based on a fully developed turbulent flow that is quasisteady over the time and fluctuation part of the mean value [15].

Rotational- Turbulence flow is characterised by high levels of three-dimensional fluctuating vortices. In addition the turbulent flows with vortex-stretching phases have three-dimensional velocity fluctuation and large velocity gradient where curl of velocity is non zero [32].

Large Reynolds Number- Turbulent flow occurs at high Re numbers where the inertia force is dominant and any up-stream flow disturbances can be amplified along the flow path. The flow disturbances which are not damped by viscous forces tend to produce random eddies, vortices and flow fluctuations.

Continuum- The general large-scale fluid flow field is assumed as a continuous phenomenon and thus the molecular structure is not considered. In turbulent flow, the lowest scales are described by the Kolmogorov's[1] scales which have many orders of magnitude higher than those of the molecular gas dimension. Thus, turbulence can be treated as a continuous phenomenon.

3.3 Turbulent Flow and Length Scales

The in-cylinder experimental flow data and turbulence intensity parameter indicate that the fluid flow within an internal engine is always turbulent and has varying dissipative flow scales [33]. The wide range of the flow length and time scales, is complex and difficult to analyse due to the dynamic changes in the up-stream fluid conditions and engine geometry configurations, e.g. piston acceleration-deceleration, varied valve curtain areas and the geometry of cylinder head as well as the unsteady character of the intake gas flow. The most

[1] A. N. Kolmogorov introduced the idea that the smallest scales of turbulence are universal (similar for every turbulent flow) and that they depend only on ε and ν. Ref in H. Schlichting 'Boundary Layer Theory'

important parameter, which quantifies such turbulent flow, is the dimensionless Reynolds number Equation (1) a ratio of inertial and viscous gas forces described by the expression:

$$R_e = \frac{U \cdot L}{\nu} \tag{1}$$

Where U (m/s) is the flow velocity, L(m) the typical length, and ν (m^2/s) the kinematic viscosity. In addition, for any given flow several Re numbers usually exist and correlate with various turbulent scales.

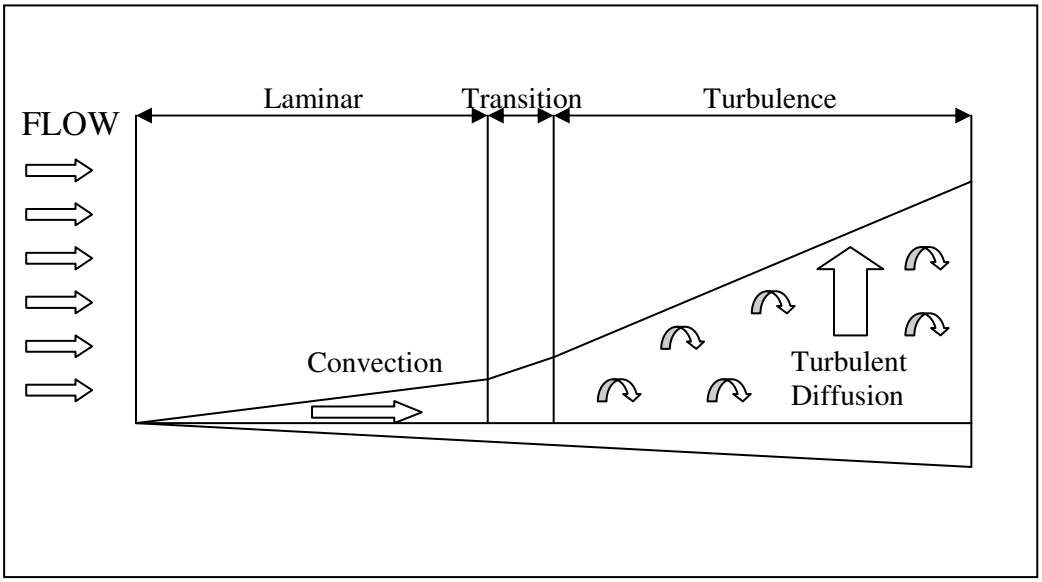

Figure 1: Three Dominant Physical Effects in the Flow (laminar-convection, transition, turbulence-diffusion)

As the Reynolds number increases above a certain number, the laminar flow becomes unstable and any up-stream disturbances that are transported and amplified are not suppressed by viscous forces Figure 1. This instability which generates turbulence is a complex mathematical problem and is related to the viscous and nonlinear inertia terms within the modelled momentum equation. The non-linear partial differential equations formulated by Navier-Stokes (N-S) 1880-1903 have no general analytical solution to the present day. Therefore it is important to understand the physical nature of the turbulent flow and the related effects, since the numerical methods only give approximate results based on the artificial diffusion turbulence models, such as the (k-ε) concept or the resolved computative

cells (LES, DES, DNS) [34, 35]. The computed N-S equations have natural limitations with regards to the applied mathematical schemes and mesh geometry, and must be carefully considered before they are used.

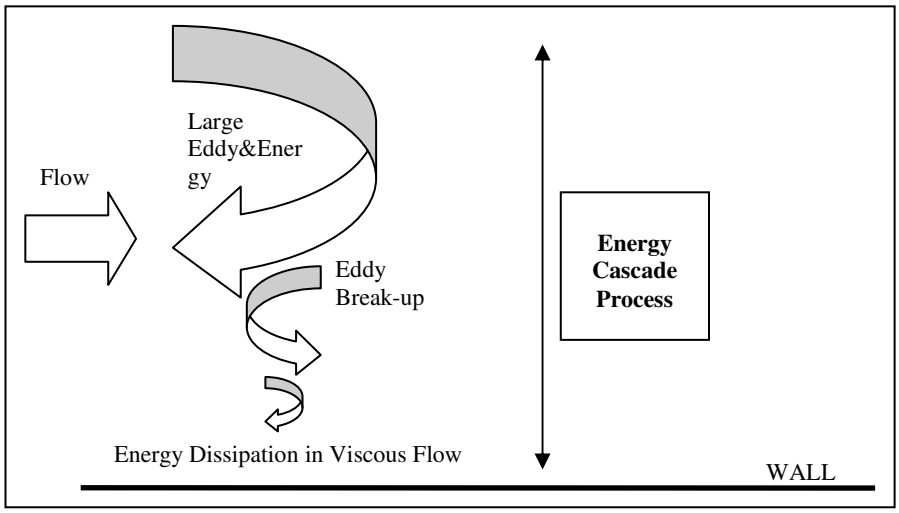

Figure 2: Schematic View of the Turbulent Energy Cascade Process.

The early theory for the dimensional analysis of turbulence was postulated by Osborn Reynolds (1898). It was based on the conceptual model in such a way that the mean flow energy is transferred from the large eddies to the viscous scale by the energy cascading mechanism shown in Figure 2. The lowest turbulent scales contain eddies (Kolmogorov-Scales) which are dynamically dissipated by turbulent kinetic energy into heat increased gas internal energy, especially within the boundary layer region. The source of turbulent kinetic energy, is mainly due to the fluctuated flow field and results in fluid deformation and shear stress in the region of the large velocity gradients [36]. Moreover, the engine geometry and conditions of the flow, which inherently control the intensity of the fluctuated velocity, induce different shear regions. A similar way to produce turbulence includes flow through the complex internal engine geometry; moving valves, pistons and stationary parts are the sources of the fluid shear stresses.

The turbulent process of continual energy transformation from large to small scales is called *dissipation or energy cascade* [37], and is designated by the parameter ***(ε):***

$$\varepsilon = \frac{u'^3}{Li} \qquad (2)$$

$$TLS(k-\varepsilon) = C_\mu \frac{k^{\frac{3}{2}}}{\varepsilon}$$

Where u' is the root mean square (RMS) of the velocity fluctuation and Li is a turbulent integral length scale or TLS (Turbulence Length Scale for the energy contained in the eddies[2]). The turbulent flow contains a wide range of turbulent spatial and time scales which are large enough to fill up the whole engine cylinder as well as eddies that are below a millimetre in size. The largest eddies are theoretically limited by the flow geometry, for example the engine cylinder bore can be the largest turbulence flow scale dimension [1]. Moreover, the TDC piston position, the largest turbulent scales are at the chamber clearance height [1]. The kinetic energy within an in-cylinder flow varies and is dependent on the turbulent scales. The relatively large eddies are weak and susceptible to the break down process which is dependent on the shear mechanism and fluctuation velocity. For instance, any increase in the velocity fluctuation maintain the deformation of work and continues the break-up process of large eddies to lower scales, approaching the kinetic energy peak of the turbulence [1]. The break-up process is non-linear, and for every flow condition the different turbulence scales impose a different kinetic energy peak as shown in Figure 3. The most energetic turbulence scales are roughly of the order of 1/6 of the largest scale and are responsible for the most effective cylinder gas transport process according to Lumely et al. [1].

[2] Li-Turbulence Integral Length scale contained in the most energetic largest eddies

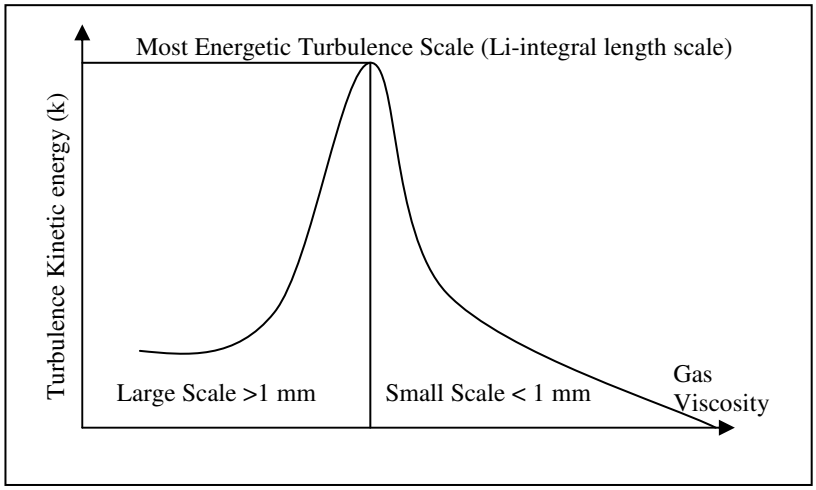

Figure 3: The Peak of the Kinetic Energy of the Turbulence for a Specific Turbulent Length Scale Responsible for Effective Mixing and Fluid Transport [1]

The flow stream energy is converted into the large scale eddies and thus the unstable composition is broken-up into the lower and more energetic turbulent scales. The achieved peak of the turbulent energy for a specific eddy dimension is further broken down to the next lowest scale and turbulent energy level. At these smallest eddy scales, the kinetic energy is transformed into internal energy-'heat' [38].

Kolmogorov Length Scale: $$\eta \equiv \left(\frac{\nu^{3}}{\varepsilon} \right)^{\frac{1}{4}} \quad \textbf{(3)}$$

Kolmogorov Time Scale: $$t \equiv \left(\frac{\nu}{\varepsilon} \right)^{\frac{1}{2}} \quad \textbf{(4)}$$

Kolmogorov Velocity Scale: $$v = (v \cdot \varepsilon)^{\frac{1}{4}} \quad \textbf{(5)}$$

The turbulence process of continuous eddy break down finally approaches the macroscopic scale of turbulent transport defined by the Kolmogorov length and time scales Equations (3, 4 and 5). For the length scale, the parameter η is dependent on the gas viscosity ν, where the turbulent fluid transport mechanism contains homogeneous gas temperature and structure formations. The dynamic behaviour of the small eddies is governed by the energy

provided, ε and the gas viscosity which sets up the rate of mechanical energy to be converted into heat. It is an experimental fact that the ratio of energy dissipation and the size of the molecular viscosity affects the small eddy dimension [19]. It is very interesting that the large-scale energy process is determined only by the fluid flow properties and is not dependent on the molecular viscosity [1]. For a raised viscosity ν, parameter ε does not change, but the scale where kinetic energy is dissipated increases [1].

According to the work of Lumely et. al, [1] turbulent energy dissipation takes place within the engine cylinder for higher piston velocities, and increases by the power of three:

$$\varepsilon \propto \overline{V}_p^3 \tag{6}$$

Where $\overline{V}_p$ is the average piston velocity. The Kolmogorov turbulence length scale for the increased piston velocity decreases slowly by the ratio:

$$\eta \propto \overline{V}_p^{\frac{-3}{4}} \tag{7}$$

Lumely et al. [1] indicate that the turbulent gas dissipation process, which takes place in the lowest scales of η and in the region of a strong friction flow within the cylinder, is able to change the gas temperature in this region to less than 50K. These effects of turbulence change the thermal in-homogeneity distribution and must be accounted for in any HCCI engine combustion analysis where the auto-ignition chemical mechanisms are extremely sensitive to any spatial temperature variations.

3.4 Governing Flow Equations

The mass, momentum and energy equations establish the system of partial differential equations and result from the application of thermodynamics laws on moving fluid. The conservation of fluid mass, momentum and energy within the control volume are all determined by the following equations (written in the general vector notation form):

Continuity

$$\frac{\partial \rho}{\partial t} + \nabla \cdot (\rho \cdot \vec{V}) = 0 \tag{8}$$

Momentum

$$\underbrace{\frac{\partial \vec{V}\rho}{\partial t}}_{\text{Unsteady Acceleration}} + \underbrace{\nabla \cdot (\rho \vec{V}\vec{V})}_{\text{Convective Acceleration}} = \overbrace{\underbrace{-\nabla p}_{\text{Pressure Gradient}} + \underbrace{\nabla \cdot (\bar{\bar{\tau}})}_{\text{Stress Tensor}}}^{\text{Divergence of Stress}} + \underbrace{\rho \vec{g} + \vec{f}}_{\text{Other Forces}} \tag{9}$$

Energy

$$\frac{\partial (\rho E)}{\partial t} + \nabla \cdot (\vec{V}(\rho E + p)) = \nabla \cdot \left(k \nabla T - \sum_j h_j \vec{J}_j + (\tau \cdot \vec{V}) \right) + S_e \tag{10}$$

$$\rho = \frac{p}{RT} \quad \text{Ideal Fluid} \tag{11}$$

Where for the *Continuity* equation, ρ is the fluid density [*kg/m3*], *t* [*s*] represents the time and $\vec{V}$ [*m/s*] is the general velocity vector; and for the Cartesian three dimension coordinates, the velocity vector components are $\vec{V} = [v_x, v_y, v_z]$. The conservation of *Momentum* is derived from the Newton Second Law, and the generic form of the transport equation describes the fluid flow dynamics: where *p* is the static pressure [Pa], $\bar{\bar{\tau}}$ is the stress tensor, and $\rho \vec{g}$ and f are the gravitational and external body forces respectively. The second term on the left-hand side is a convective acceleration term within the momentum equation and the nonlinear core, due to the acceleration of the flow and the change in velocity over position [39]. The second term on the right-hand side of momentum equation is the diffusion flux tensor and is related to the Newtonian fluid shear stress. The viscous stress tensor $\bar{\bar{\tau}}$, has been proposed by Stoke

in the form that assumes the viscous stress field is linearly proportional to the strain rate (Newtonian Fluid):

$$\bar{\tau} = 2\mu S_{ij} - \frac{2}{3}\mu S_{kk}\delta_{ij} \quad \textbf{(12)}$$

Where μ is the dynamic viscosity, δ_{ij} is Cronecker delta; and a unit is a second-order tensor (δ_{ij} =1 if i=j and 0 otherwise). The stress tensor $\bar{\bar{\tau}}_{ij}$ states that the fluid deformation is caused by the velocity gradients $\partial u_i / \partial x_j$, which can be decomposed into a symmetric S_{ij} strain rate tensor and an antisymmetric Ω_{ij} rotational fluid tensor, defined as:

$$\frac{\partial u_i}{\partial x_j} = S_{ij} + \Omega_{ij} \quad \textbf{(13)}$$

$$S_{ij} = \frac{1}{2}\left(\frac{\partial u_i}{\partial xj} + \frac{\partial u_j}{\partial x_i}\right) \quad \textbf{(14)}$$

and

$$\Omega_{ij} = \frac{1}{2}\left(\frac{\partial u_i}{\partial xj} - \frac{\partial u_j}{\partial x_i}\right) \quad \textbf{(15)}$$

To resolve the sequence of N-S equations and the lack of general solutions, a numerical procedure with additional closure models must be applied. The computational fluid dynamics (CFD) codes realise the approximating methods for solving the N-S equations.

3.5 Computational Fluid Dynamics

The essence of the CFD approach is based on the numerically resolved fundamental N-S equations with a wide range of closure models, and it represents a different range of fluid flow problems. In addition, the fundamental concept of CFD is based on the discretised numerical solution for the partial differential equations that describe the conservation of mass, momentum and energy for the fluid flow. The sequences of the conservative partial differential equations (PDEs) are known as the Navier-Stokes (N-S) equations and refer to an

instantaneous three-dimensional transport of mass, momentum and energy processes. The numerical discretisation divides the fluid region into finite volumes where the governed equations are resolved with appropriate boundary conditions. The N-S PDEs, with additional closure models, are resolved by using the following numerical methods; finite element methods (FEM), finite volume methods (FVM) and finite difference methods (FDM). This section provides a brief introduction to the major turbulent closure models used in CFD codes, as well as the program structure.

3.6 Turbulence Modelling and Reynolds Decomposition Models

The aforementioned flow field in an internal combustion engine is fully turbulent and comprises many different spatial and time flow scales. The general conservation equations must therefore be in the turbulent form and invoke additional system models to describe the effects of turbulence on the flow field. It is known that, it is not possible to obtain an analytical solution of Equation (8) to Equation (9) and resolve *all turbulence flow scales* within the near future; appropriate models need to be introduced. The ratio between the integral and the Kolmogorov length scales where turbulent kinetic energy is exchanged due to the energy cascade process is of the order of $\mathrm{Re}^{-3/4}$ and $\mathrm{Re}^{-1/2}$ for the length and time scale respectively [40]. Therefore, for the range of turbulent Re numbers between 10e4 to 10e5 the obtained length and time scales are of the order of 10e-2 and 10e-3, respectively. These small scale eddies require a much smaller resolving time step than the other scales, and denser numerical grids in the region of dissipation inherently increase the numerical cost. To decrease the resolving time, specific models and assumptions for the turbulent governing equations are elaborated. The most important assumption has been introduced by Osborn Reynolds and is known as the Reynolds Decomposition Concept. Here, the instantaneous N-S equations are divided by the sum of the averaged mean and fluctuation values along the time path in the following form [41].

$$\Phi = \overline{\Phi} + \Phi' \tag{16}$$

Where Φ is any instantaneous quantity that appears in Equation (8) to Equation (10) and represents major thermodynamics properties $\Phi \equiv [U, T, P, \rho]$. The mean component of variables over time results in time or ensemble averaging values:

$$\overline{\Phi} = \underset{T-\infty}{Lim} \frac{1}{T} \int_{t0}^{t0+T} \Phi(t)dt \tag{17}$$

$$\overline{\Phi} = \underset{N-\infty}{Lim} \frac{1}{N} \sum_{n=1}^{N} \Phi(t) \tag{18}$$

where N-number of cycles for which data are available

The velocity turbulence effect within the flow is modeled by the quantity u', which is a fluctuation velocity. The fluctuating velocity describes the turbulence intensity parameter and is used for the validation of both experimental and computational approaches. The fluctuation component of the decomposition in Equation (19) is defined by its root mean square value.

$$\Phi' = \underset{T-\infty}{Lim} \left(\frac{1}{T} \int_{t0}^{t0+T} \Phi^2(t)dt\right)^{1/2} \quad \text{where} \quad \overline{\Phi'} = 0 \tag{19}$$

The time-averaged approaches applied by the model of turbulence is statistically derived from the time scales, whereby the time scales decrease at the mean flow and the accounted fluid flow field fluctuations. These assumptions for turbulent engine flow must satisfy a narrow band of energy-containing eddies which are of the same order of magnitude as the time scales of the mean flow and the engine cycle times which decrease with the free turbulence relaxation time.

The above-mentioned ensemble-averaged approaches, with average and fluctuation terms applied to the Navier-Stokes Equation (8) to Equation (10), give the Reynolds Average Navier Stokes (RANS) concept. The following RANS equations are described in Cartesian tensor notation form:

$$\frac{\partial \bar{\rho}}{\partial t} + \frac{\partial}{\partial x_i}(\bar{\rho}\tilde{u}_i) = 0 \tag{20}$$

$$\frac{\partial \bar{\rho}\tilde{u}_i}{\partial t} + \frac{\partial}{\partial x_j}(\bar{\rho}\tilde{u}_i\tilde{u}_j) = -\frac{\partial p}{\partial x_i} + \frac{\partial}{\partial x_j}\cdot(\bar{\bar{\tau}}) + \frac{\partial}{\partial x_j}\left(-\rho\overline{u_i'u_j'}\right) \tag{21}$$

The obtained i.e. Equations (20-21) in averaged Reynolds form are different from the instantaneous N-S form with additional terms that represent the effect of turbulence. The appeared term is called the Reynolds stress, $-\rho\overline{u_i'u_j'}$, and must be modelled by one of several close equations.

- **Algebraic model**. Equations (20-21) are computed based on the *eddy viscosity* model μ_t, which is an algebraic equation of turbulent viscosity. The computed Reynolds stress tensor has employed the Boussinesq hypothesis which relates the appeared stress term to the eddy viscosity and mean velocity gradients [42]. The Boussinesq hypothesis is used for a wide-range of turbulence models, including the Spalart-Allmaras model, the ***k-ε*** models and the ***k-ω*** models.

$$-\rho\overline{u_i'u_j'} = \mu_t\left(\frac{\partial u_i}{\partial xj} + \frac{\partial u_j}{\partial x_i}\right) - \frac{2}{3}\left(\rho k + \mu_t\frac{\partial u_k}{\partial x_k}\right)\delta_{ij} \tag{22}$$

  General Boussinesq Hypothesis equation for eddy viscosity concept (Equation 22)

- **One-equation model**. The Spalart-Allmaras model is a turbulent transport equation model which represents the turbulence eddy *viscosity* ν_t [43].

  Transport equation for the Spalart-Allmaras model:

$$\frac{\partial \bar{\rho}\tilde{\tilde{\nu}}}{\partial t}+\frac{\partial}{\partial x_i}(\bar{\rho}\tilde{\tilde{\nu}}\,\bar{u}_i)=G_\nu+\frac{1}{\sigma_\nu}\left[\frac{\partial}{\partial x_j}\left((\mu+\rho\tilde{\tilde{\nu}})\frac{\partial \tilde{\tilde{\nu}}}{\partial x_j}\right)+C_{b2}\rho\left(\frac{\partial \tilde{\tilde{\nu}}}{\partial x_j}\right)^2\right]-Y_\nu+S_\nu\,, \tag{23}$$

According to Equation (23) where G_ν and Y_ν are terms of the production and destruction of turbulent viscosity respectively. The destruction term is applied to the near-wall region using the viscous damping parameter, σ_ν. The equation parameter C_{b2} is a constant where ν and S_ν are the molecular kinematic viscosity and the user-defined function source term respectively.

$$-\rho\overline{u_i{}'u_j{}'}=\mu_t\left(\frac{\partial u_i}{\partial xj}+\frac{\partial u_j}{\partial x_i}\right) \tag{24}$$

The Boussinesq hypothesis for the Spalart-Allmaras turbulence model excludes the last term of the turbulence kinetic energy from the general assumption.

- **Two-equations model**. The eddy viscosity model, is based on two separate transport equations describing the scalar turbulence kinetic energy (***k)*** and it is dissipation rate **(*ε)***. The ***k-ε*** model is the first complete turbulence model that allows the turbulence length scales and velocity to be computed independently and it was originally proposed by Launder and Spalding [44].

The following closure transport Equations (25-26) for the RANS concept make up are the ***k-ε*** model of turbulence**.** The general form of the transport equations is similar to that of the extended two-equations model: ***RNG*(*k-ε), k-ω*** and ***Realizable(k-ε).***

<u>Standard closure ***k-ε*** model of turbulence:</u>

The Turbulence Kinetic Energy ***(k)*** transport equation.

$$\frac{\partial \overline{\rho}\,\overline{k}}{\partial t}+\frac{\partial}{\partial x_i}(\overline{\rho}\,\overline{k}\,\overline{u_i})=\frac{\partial}{\partial x_j}\left((\mu+\frac{\mu_t}{\sigma_k})\frac{\partial k}{\partial x_j}\right)+G_k+G_b-\rho\varepsilon-Y_m+S_k \quad \textbf{(25)}$$

And the Turbulence Energy Dissipation (***ε)*** transport equation.

$$\frac{\partial \overline{\rho}\,\overline{\varepsilon}}{\partial t}+\frac{\partial}{\partial x_i}(\overline{\rho}\,\overline{\varepsilon}\,\overline{u_i})=\frac{\partial}{\partial x_j}\left((\mu+\frac{\mu_t}{\sigma_\varepsilon})\frac{\partial \varepsilon}{\partial x_j}\right)+C_{1\varepsilon}\frac{\varepsilon}{k}\left(G_k+C_{3\varepsilon}G_b\right)-C_{2\varepsilon}\rho\frac{\varepsilon^2}{k}+S_\varepsilon \quad \textbf{(26)}$$

Where G_k and G_b represent the generation of turbulent kinetic energy due to the flow of the shear stress and buoyancy effects imposed by the mechanisms of velocity and temperature gradients in the mean flow, respectively.

$$G_k=-\rho\overline{u_i'u_j'}\frac{\partial u_j}{\partial x_i} \quad \textbf{(27)}$$

and

$$G_b=\beta g_i\frac{\mu_t}{\mathrm{Pr}_t}\frac{\partial T}{\partial x_i} \quad \textbf{(28)}$$

Where β and g_i are the gas coefficients of the thermal expansion and the gravitation vector field, respectively and Pr_t is the turbulent Prandtl number. In the case of general flow within the gravity field and temperature gradient, the buoyancy effect (G_b>0) for the ***(k)*** equation indicates the production of turbulence due to the unstable gas density stratification [45]. The ***(k)*** turbulence transport equation with Y_m term accounts for the compressibility effect of a high Mach number generated by the "dilatation dissipation" mechanism. The dilatation dissipation effect decreases the spreading rate of the mixing gas within the compressible flow for all increases in the Mach number [33]. The following parameters $C_{\varepsilon 1,2,3}$ are constants which are obtained experimentally for a particular turbulent flow test case. The $\sigma_k,\sigma_\varepsilon$, are Prandtl numbers for turbulent kinetic and dissipation transport equations.

The obtained ***k-ε*** model developed by Launder and Spalding [36] is a semi-experimental model with two transport equations for the turbulence kinetic energy ***(k)*** and its dissipation rate ***(ε)***. The following model is only valid for a fully turbulent flow and ideal for rough and fast simulations in internal engine gas dynamics. The model of the two closure equations ***k-ε*** of the turbulent gas transport process appears with the Reynolds stress tensor and is resolved via the *eddy viscosity* concept μ_t in Equation (29). The eddy viscosity model developed by Boussinesq in 1877 is an analogy for molecular viscosity μ, and represents the turbulent gas momentum exchange performed by eddies [46]. The biggest drawback of the two equations models is the isotropic hypothesis of turbulence.

$$\mu_t = \rho C_\mu \frac{k^2}{\varepsilon} \tag{29}$$

Where $C_{1\varepsilon}, C_{2\varepsilon}, C_\mu$ and σ_ε are the model constants determined from experiments and are widely applied for different types of shear and turbulent flows [36]. The default values for ***k-ε*** model constants are:

$C_{1\varepsilon}$ =1.44	$C_{2\varepsilon}$ =1.92	C_μ =0.09	$\sigma_k = 1$	$\sigma_\varepsilon = 1.3$

Other closure models for N-S equations:

- Reynolds Stress Model (RSM) with an additional five and seven transport equations for the 2-D and 3-D cases has more potential to give accurate predictions of the turbulent complex flow than the one or two turbulence model equations do. The RSM model features an anisotropy turbulence stress model that is applied to cyclone flows, to a highly swirling and rotating flow, and to the stress-induced secondary flows in ducts. This model is computationally expensive and does not always yield results that surpass the simpler turbulence models [47], [48], [49]

- Detached Eddy Simulation (DES) [50].
- Large Eddy Simulation (LES) [51], [52], [53]

3.7 Computational Fluid Dynamics (CFD) Code Structure.

Most commercial CFD codes are of the FVM type using small volumes for spatial discretisation [54], [55], [56], [57]. They hang on the same numerical models and schemes for the flow equations but have minor differences in code optimization and user interface structures. In order to provide a clear and efficient scope at simulating the problem, all commercial codes are equipped with a Graphics User Interface (GUI). This approach is preferable for varying the range of physical cases and it decreases the possibility of user processing set-up errors. In contrast to massive calculations, which are based on optimised models, a non-GUI console was chosen to save computational time and use less computer memory.

The CFD packages have three main stages for solving particular flow problem and are representes by:

- Pre-processing (modelling and discretization)
- Calculations
- Post-processing

For most of the CFD codes, the user has the possibility of setting up the physics of the problem by discretising the flow domain and applying preferable grid types for specific boundary conditions. The stage of grid generation is extremely important for the accuracy of the numerical results due to the dimensional grid constraints and nodes where the conservation equations are applied. Moreover, the discretisation must be suitable for the chosen CFD models and schemes. Therefore, this stage of model preparation, imposed by user skill and experience, include the knowledge of physical complexity and the numerical

aspects of the flow. The main inputs required for pre-processing the CFD problem are as follows: 1) Create the geometry which represents a flow domain, 2) Create the model discretisation, 3) Apply boundary conditions and examine the topology of the grid, 4) Import a discretised model to the CFD solver, 5) Apply appropriate solver models and set-ups to the chosen type of grid topology, 6) Initialise the physical operating conditions, 7) Set-up the control parameters which influence the accuracy and stability of the numerical solution, e.g.: under-relaxation factor, adaptive time step, discretisation schemes

The accuracy of the CFD results is dependent on the grid and numerical models used. For this reason, it is important to generate a series of benchmarked cases which evaluate the flow structure [58]. For general flow cases, a computational mesh must be particularly dense in the region of gradients (e.g., gradient of velocity, temperature, pressure). A dense grid structure is computationally expensive[3], but for a high level of accuracy in simulating the physical effects and decreasing the numerical error, it is essential that the grid structure be dense especially in the region of boundary layer flow, velocity fluctuations and thermal convection.

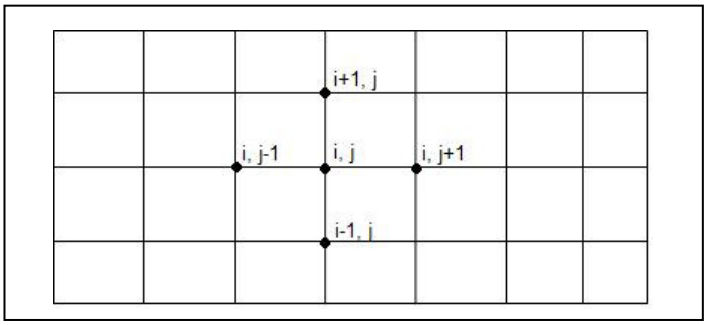

Figure 4: Structural Grid Approach and Spatial Representation of Computational Nodes.

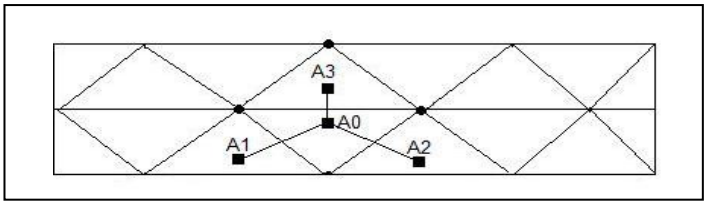

Figure 5: Unstructured Grid Approach and Spatial Representation of Nodes and Volumes. A0 are Scalar Transport Values [p,T,ρ,..] Calculated Into the Centre of the Cell from Neighbouring Nodes.

[3] Computational Time needed to resolve particular problem.

The calculation stage is performed by the CFD code structure via the iterative methods which resolve conservative equations with a given numerical accuracy. The initialised CFD calculations can be performed with different numerical schemes such as finite element methods (FEM), finite volume methods (FVM) and finite difference methods (FDM) [59]. The finite volume methods (FVM) as part of the difference formulation are the most common methods used to solve conservative equations in a CFD problem. The advantage of this formulation is the possibility of using non-structurally coarse grids like Figure 5 which conserve all the transport equations instead of resolving the finite difference scheme on a structured mesh as in Figure 4.

For all the diverse methods, the constitutive equations are integrated over the discretised fluid domain. The terms of the N-S partial differential equations Equations (8-10) i.e., convection, diffusion, and transient are approximated by the Taylor series and are changed into a system of algebraic linear equations. The FVM approach is limited by the second-order spatial discretisation. Although finite volume methods are conserved for all the cell types it is difficult to obtain a higher order of accuracy from them [60]. For the finite difference method, a higher order of accuracy (i.e., above the second order) is obtained and can be applied to the momentum equation.

In order to resolve the problem in the calculated domain, thousands of outputs of the computed flow region must be presented in a comprehensible and usable format. The post-processing results of the CFD model can be presented on a velocity vector field or scalar values can be based on presented numerical grid and graphs. In addition, contours and streamlines can be used for easier analysis of the fluid flow problem. The leading CFD packages are equipped with post-processing visualisation tools featuring: Grid display and domain geometry, Vector field, Contours (line and field), Plane plots, Surface plots, Particle tracking, Streamlines

The leading CFD codes built on the FVM concept are as follows: STAR-CD™, FLUENT™, AVL-FIRE™, FLOW-3D™, KIVA™, CONVERGE™. In addition, CFD outputs can be visualised by using the following postprocessor packages: CEI, ParaView, Tecplot, GMV etc..

3.8 The choice of CFD Platforms for a Simulation of Engine Gas Dynamics

The internal engine flow aerodynamics are calculated through the FLUENT™ CFD package as it is one of the most advanced codes on the market. The reason for using a general-purpose CFD code for a specific engine case lies in the versatility of the FLUENT package and the broad range of technical sources and validation cases available. In addition, the University of Birmingham has an established numerical laboratory with FLUENT as the leading CFD package for calculating flow problems. The general-purpose CFD codes are grouped by a varied range of numerical models and schemes developed by academics throughout the last century which are also available in the FLUENT™ package.

The most important feature of the CFD FLUENT package is the wide physical flow environment and capability to simulate complex laminar flow as well as the turbulent character of the flow. The advantage of FLUENT is that it is a fast and robust numerical solver and carries with it the ability to validate cases against experiments and exact analytical solutions [61]. The disadvantage of the general-purpose codes, such as FLUENT, is their lack of discretisation and other numerical model adjustments for specific types of flows and models. A fully operated model is achieved through extensive test phase execution applied to all models, and this is computationally costly.

The CFD Fluent™ code offers the following physical models: Solver (steady, unsteady), Heat transfer, Compressibility, Viscous, Turbulent or Laminar, Radiation, Acoustics, Combustion (PDF, Chemistry Kinetics EDC), Discrete Liquid Flow Phase, Multiphase, Moving and deforming grid for non stationary flow.

The internal aerodynamic flow which takes place within the engine cylinder is difficult to analyse and validate. This is a result of the highly turbulent and unsteady flow character imposed by valve and piston distortion flow effects. The numerical solution for this type of flow is validated against the averaged large-scale flow pattern according to the PIV experiments [62]. The gas dynamics simulation within an engine's cylinder is utilised by using a group of suitable numerical models in order to obtain the proper physical flow effects. For the single cylinder optical engine, the CFD simulation was based on the following models: the unsteady solver and deforming cylinder mesh, the wall-fluid heat transfer effect and the turbulent flow with non-reactive species modelled by the ideal gas. In addition, other models might be applied for simulating the combustion and liquid-gas phase mixing process.

The computational platform is built on a single processor, Intel Pentium IV 2.4 GHz with 2 GB RAM. The 32 Bit MS Windows system maintains the computer hardware. The lack of a HPC cluster imposes the use of a simplified engine grid model of [400-900k] elements for the CFD simulation. Moreover, the lack of computational power was addressed by simulating the intake gas dynamics process with a 1-D Ricardo™ WAVE code.

3.9 CFD Solver Set-up for In-Cylinder Turbulent Flow

The FLUENT CFD package offers a wide range of turbulent closure models: the Spalart-Allmaras ***k-ε*** models, the ***k-ω*** models, the $v^2 - f$ model, the Reynolds Stress Model (RSM), the Detached Eddy Simulation (DES) model and finally, the Large Eddy Simulation (LES) model. It must be noted that all of the above-mentioned models can be used in general

to simulate the turbulent flow process which takes place within an engine cylinder. The major determinant for a proper choice of turbulence model is based on the CFD user experience and knowledge of code limitations. In addition, models are naturally limited by the available computational power.

Due to the computational cost and lack of a HPC (High Performance Computing) cluster, a coarse mesh and two equations from the ***k-ε*** turbulence model have been applied. The CFD test cases for the fully operated optical engine model (i.e. 400-900k cells and the ***k-ε*** turbulence model) show that a computational time for one engine cycle takes approximately three weeks. Other tests were conducted regarding the numerical stability as well as the numerical errors obtained by following the concept of turbulence. The general ***k-ε*** model is the most suitable one with regards to balancing the mesh demands and computational costs. The isotropic assumption for the two-equations in the turbulence model is a source of error in the region of 3D free shear flow [63].

3.10 Summary

The presented chapter briefly gives information about the nature of turbulence and the mathematical models used for the gas flow analysis. In addition, the gas turbulence theory concerning the length scales and the cascade energy process has been presented and described in detail. The turbulent nature of flow is a very complex phenomenon and only approximate solutions are made via the specific closure models for the N-S equations. All modern CFD packages offer similar turbulence closure models, which must be carefully chosen for the appropriate type of flow. Therefore, any turbulence models like: Spalart-Allmaras, ***k-ε*** models, ***k-ω*** models, $v^2 - f$ model, Reynolds Stress Model (RSM), Detached Eddy Simulation (DES) model, Large Eddy Simulation (LES) can be used to simulate an in-cylinder turbulent flow pattern despite their common limitations. The general-purpose finite

volume CFD FLUENT™ package available at the University of Birmingham has been used to create a dimensional model of the single cylinder engine and to simulate the internal turbulent flow pattern.

Chapter 4

EXPERIMENTAL FACILITIES AND DATA ANALYSIS

4.1 Introduction

This chapter describes the optical engine facilities and the data analysis methodology used for the internal 'Cold Flow' study within singe cylinder optical engine. Additionally, the PIV (Particle Image Velocimetry) data acquisition system used for the HCCI single-cylinder engine flow diagnostics research is presented. In the current work, the following groups of experimental systems and devices have been utilised: the optical engine facility, the Nd:Yag Double Pulse LASER and the Particle Image Velocimetry (PIV) acquisition computer. The engine facility is based on the FORD/JAGUAR experimental optical engine in conjunction with the eddy current dynamometer and the driven AC electric motor. The four-valve, pentroof cylinder head engine features an optical access with a constant compression ratio, low valve lift profiles, negative valve overlap (NVO) and an intake air and cylinder head heater. In addition to this, the bottom part of the crankcase block has hydraulic actuator clamps with an optical liner on the head surface.

The experimental investigation of the internal flow within the 4-valve pentroof optical engine is performed using two different intake port shroud geometries coupled with the aforementioned equipment groups. Additionally, part of the optical engine experimental measuring facility includes intake manifold thermocouples and an in-cylinder pressure transducer.

4.2 Experimental Set-up and Test Facility

4.2.1 General Description

The research engine was a 0.6L FORD/JAGUAR single-cylinder optical engine Figure 6 shows the extended piston and cylinder block designed for the optical purpose, which was used to obtain the in-cylinder flow patterns at different intake port configurations. With four valves (twin d=36mm intake, twin d=30mm exhaust) pentroof 13º cylinder head has a centrally mounted spark plug, the engine has a bore of 89 mm and a stroke of 90 mm respectively. The engine compression ratio is set-up via the piston crown to reach 11:3 and can be varied from 8:1 to 12:1. For the current work, a constant engine speed of 1000 RPM is used from an operating range of 1000-3000 RPM; and a low valve lift of 2.6 mm is chosen for both the intake and exhaust valves. The engine crankshaft is not counter-balanced by any additional shafts and the crankcase is mounted to the cast-iron sub-frame.

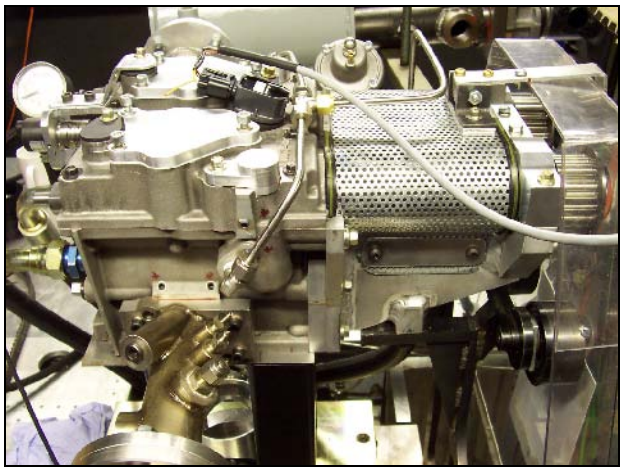

Figure 6: The Optical Engine (exhaust side view)

The engine lubricant system is of the dry sump type with a three-stage oil pump driven mechanically by the crankshaft belt drive. The oil is delivered separately to the crankcase and crankshaft by the first and second stage of the oil pump respectively due to the lack of a cylinder block and oil drain. The third stage is for sucking of oil residuals from the pan, which are returned to a surge tank through a relief valve and a system of oil filters. The oil system,

with an external pump, has a 3 kW electrical heater element within the surge tank and preheated oil is cooled down by the coolant-oil heat exchanger to maintain a stable temperature. The coolant for the cylinder head is circulated by gravity within a closed system and is heated up in the tank by a 2 kW electrical heater. Temperature controllers and four magnetic valve gates control the water and oil temperatures.

4.2.2 Test Procedure

For every optical test, the engine was fully preheated to minimise the steam condensation on the transparent linear and cylinder head-window. Following this procedure, in order to reach stable optical conditions, the coolant and cylinder head oil were warmed up to 90˚C. The temperature was also taken on the cylinder head to simulate partial firing conditions due to its similarity to intake manifold fluid heat transfer. The intake air temperature during all the tests was kept ambient, while the warm-up engine procedure imposing initially air preheated to 100˚C to remove intake manifold humidity. The throttle body for all the tests was in the position of WOT (Wide Open Throttle) and no fuel injection and spark were used due to safety reasons and the quartz linear pressure limitation. These optical limitations and a usually very sharp HCCI combustion pressure rise exclude extended combustion research at full transparent liner variant.

4.2.3 Engine Facility

4.2.3.1 Dynamometer and Electric Motor

The current eddy Dynamometer (TRANS-DRIVE®) coupled with an electrical engine are mounted to a cast-iron frame and are connected to the engine crankshaft by an elastic clutch. The eddy current dynamometer can operate for motoring and firing conditions maintained at a constant engine speed or engine load. It is supplied by a three phase, 340 volt

main power supply. The manually adjustable regulator controls the optical engine's crankshaft speed and is indicated by a digital clock outputted from the crankshaft encoder.

4.2.3.2 Intake Port Modification

Two major enhancements of the standard intake port geometries were executed. The use of two types of inlet manifold deflectors is proposed for the in-cylinder flow field diagnostics and sensitive studies. Both cases are based on the aerodynamic body located within the intake ports that directs the intake jet toward the cylinder chamber. The details of the intake port geometries are presented in Figure 7 where the two types of deflectors introduce more pronounced in-cylinder swirl or tumble flow pattern respectively. It is believed that the convergent vertical aerodynamic plate body deflects the major portion of the gas stream into the right section of the intake canal and generates a tangential flow structure within the cylinder. In this thesis, this case is named the 'Swirl Port'. The horizontal plate body affects the in-flow at the lower intake port section and deflects the core of the gas stream towards the upper section of the intake ports, which in turn generates a tumble structure in the cylinder.

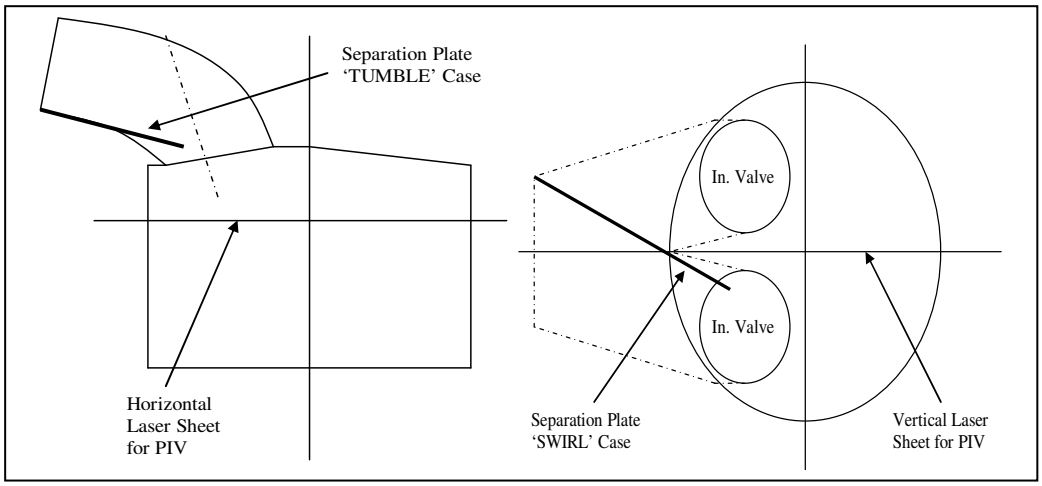

Figure 7: Schematic View of the Intake System, Measurement Planes and Combustion Chamber For the Two Types of Deflector

In a similar fashion to the previous definition, is named 'Tumble' case. The horizontal flat plate deflector is mounted close to the inlet valve seat across the channel and is perpendicular

to the main gas stream. For the 'Swirl' case, the left channel of intake ports is locked and no mass flows through it.

4.2.3.3 Air intake heater system

The optical engine is supplied with two types of air heating systems. One is an electrical induction heater and the other is a thermal convection heat. The forced convection heater is mounted inside the intake manifold and the heat is transferred from the hot coil to the flowing medium. The second heater transfers thermal energy throughout the manifold wall to the medium within the intake manifold. The air temperature is adjustable from a closed-loop system of a thermocouple and PDI (Proportional and Integral and Differential) electronic control. The thermocouple used to measure the intake temperature with controlled feedback is mounted close to the engine port. The maximum operational temperature for the heating systems is 150 ˚C at 1000 RPM in ambient conditions. During the optical engine tests, the intake air is preheated to a point where no steam or fog is present within the cylinder at the early induction stage and the engine head coolant and oil reach 90 ˚C.

4.2.3.4 Valve Lift and Engine Timing

The experimental Ford/Jaguar single cylinder engine is run at a low 2.6mm valve lift profile for both intake and exhaust valves with the sprockets driven by the engine's camshaft. In this thesis, for the internal 'COLD FLOW' analysis, the symmetrical 110 NVO (Negative Valve Overlap) is chosen, as shown in Figure 8. Table 1 also shows these valve events and the engine parameters.

Where Intake Valve Open (IVO) at 55° aTDC, IVC at 205° aTDC, EVC at 55° bTDC and EVO at 205° bTDC. The maximum intake and exhaust valve lifts and the maximum opening points (MOP) are at 2.6 mm/130° aTDC and 2.6 mm/130° bTDC respectively.

Engine type	4 valves per cylinder, cyl.
RPM	1000
Bore	89.0 mm
Stroke	90 mm
C.Rod	150 mm
Compression Ratio	11.3
Intake Valve Open	IVO415CAD
Exhaust valve Close	EVC305CAD
Intake Temperature	300 K
NVO	110 CAD
Valve IN, EX Lift	2.5 mm

Table 1: Engine Motored Conditions Data

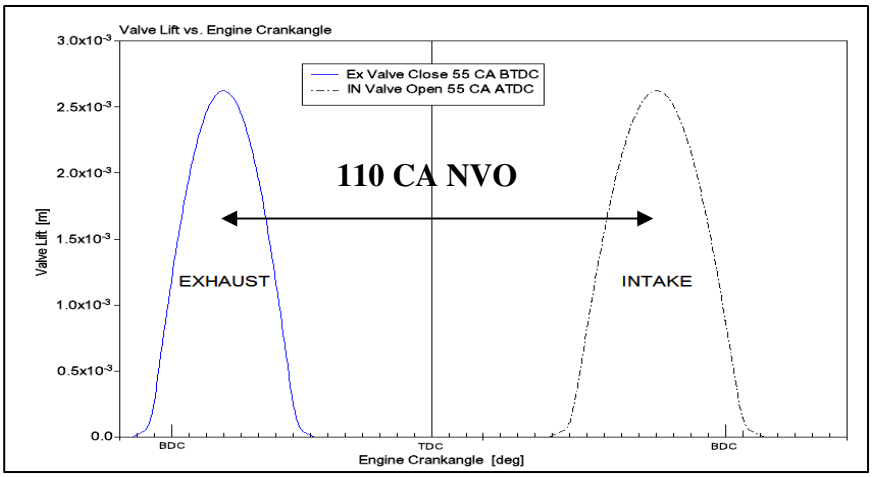

Figure 8: Optical Engine Valve Events: IVO, EVC and 110 CAD NVO

4.2.3.5 High Pressure Direct Injection System

The integral part of the pentroof cylinder head is the direct fuel injector placed close to the spark plug. For the Jaguar HCCI research project, a high-pressure direct injection system HDI was developed as shown in Figure 9. The system has been designed to operate with a maximum pressure of 13 MPa and works with different types of fuels. In addition, the minimum operating fuel pressure, limited by the fuel injector's design for the current DI BOSCH injector, is 5 MPa. The maximum amount of fuel allowed in the fuel-accumulator Figure 10 and pipe network is limited to 2L for safety reasons. The built FSCB (Fuel System

Control Box) has an ergonomic design to minimise the maintenance time and the possibility of accidents. For fire safety reasons, the system is pressurised by nitrogen. In addition, the system is designed to operate on different facilities (e.g. engines DI, DIESEL or Optical Vessels) and is easy to reassemble. In Apendix A the present design is shown including the details of the high-pressure direct injection system with a list of the certified parts and a schematic view of the fuel accumulator.

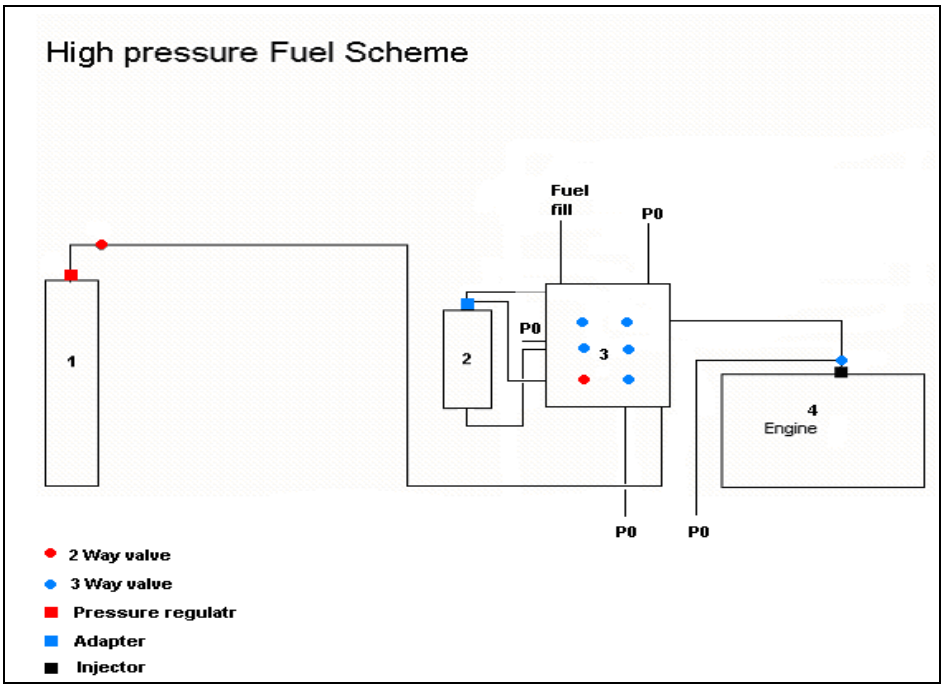

Figure 9: High Pressure Fuel DI System Scheme

Legend:
1-N2 Bottle
2-Accumulator
3-Control Box
4-Engine

The Bosch injector pulse-width and injection timing are controlled via an 'Jaguar Oxford-Birmingham Control System'[4] reading the triggering signals from the shaft encoders mounted on the crankshaft and camshaft, respectively. The control unit takes two signals: the one from the cam which is triggered once per camshaft revolution. The second signal triggers 360 pulses per crankshaft revolution. This is essential for setting the ignition timing, the

[4] Control engine TTL signals system developed at the Oxford and Birmingham University base on Lab-View software and the Jaguar Cars DAQ system.

trigger computer DAQ system of the in-cylinder pressure measurement and the fuel injection point. The injector pulse width, which determines the fuel rate, can be set-up in the range of 1ms to 50ms. The start injection point per cycle can be set-up for a wide range of crank angles. For the HCCI technology, there are usually three different strategies for starting the injection point to optimise the engine load and emission conditions. The first strategy is related to the early injection during the recompression phase at a wide NVO with a reforming process [64]. The second is for preparing a homogeneous mixture, whereby the injection starting point is set-up with the intake valve open. The last one is for the late injection phase with a stratified mixture. All of these strategies can be realised on the Optical Engine via the control injection system.

Figure 10: High Pressure Fuel Accumulator

4.2.3.6 Ignition System and Shaft Encoder

The shaft encoder is made by KISTLER and is rated at 360 TTL pulses per crankshaft revolution. The optical engine coil ignition system, previously described, is an integral part of the Jaguar-Oxford control system. The variable spark timing can be altered for any spark-combustion strategy.

4.2.4 Laser and Engine Optical Facility

4.2.4.1 Optical Engine Parts

Optical Piston and Silica Quartz

Figure 11: A) Optical Piston and B) Silica Quartz

The flattop optical pistons with Torlon® rings have a diameter of 87mm Figure 11 and were used for the in-cylinder flow diagnostics. The pistons feature a removable crown insert made of either fused silica quartz or aluminium. The geometrical difference between the pistons lies in the ring belt and land configurations imposed by the cylinder liner design.

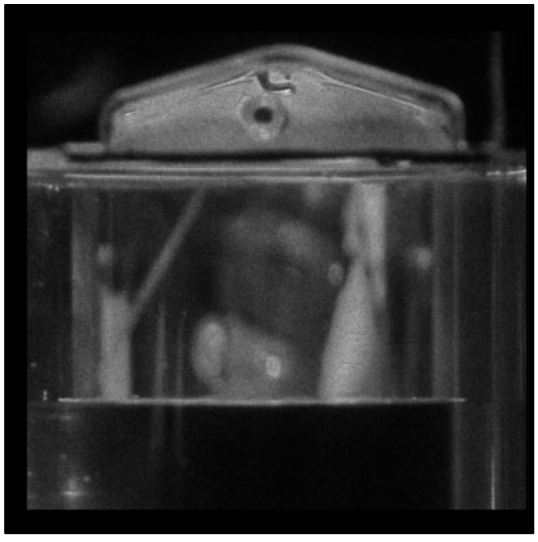

Figure 12: Optical Cylinder Liner

Cylinder Liner

The fused silica optical cylinder liner is fully transparent Figure 12. The thickness of the cylinder wall and diameter are 25mm and 90mm, respectively. The gaskets seal the bottom and the top of the cylinder surfaces.

Seed Generator

An oil seed generator (fluid flow laser tracer), with an adjustable oil atomisation and mass flow rate, has been used.

4.2.4.2 Nd:Yag Laser System Optical Set-up

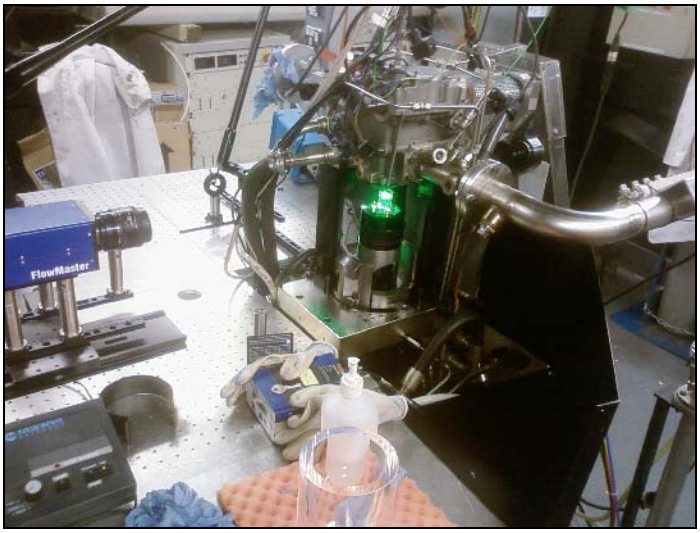

Figure 13: PIV Test Setup with the Optical Engine Piston Access

The visualisation process for the gas velocity distribution within the optical engine cylinder is performed by the LaVision™ PIV system and the Matlab™ package. The Particle Image Velocimetry (PIV) is commonly used for the quantitative and non-intrusive flow measurement method. For calculating the velocity distribution within the flow field, an additional seed material must be injected which is called a 'tracer', e.g. water or an oil aerosol. It has been assumed that the small diameter and light tracer particles follow the flow cylinder pattern truthfully. The Davis solver calculates the displacement of the tracers within

the pair of pictures obtained from the double pulse laser, which is formed by a light sheet in a short time interval.

Two Nd:YAG (Neodynium-Doped Yttrium Aluminium Garnet) lasers developed by NEW WAVE RESEARCH CORP [65], were used to illuminate the cylinder chamber and were rated with a second wave harmonic output of 532nm. The single pulse energy for each of the lasers was 120 mJ per pulse at a wavelength of 532 nm and a pulse width of 3-5 ns. Each laser beam was formed into a planar laser sheet with a thickness of 0.1 mm; its waist was formed from a spherical lens (f=1500mm) and a plane-concave lens (f=-100mm), before entering the engine chamber (see Figure 13). The sections of UV (ultraviolet) mirrors were placed at an angle of 45° between the laser head and the first lens. The laser sheet configuration is shown schematically in Figure 14.

The Kodak Charge Couple Device (CCD)[5] Flowmaster double-frame camera, with a resolution of 1024x1280 pixels, is controlled by the LaVision software package (v6.2) to acquire the sets of pictures [67]. A double exposure mode was applied to record two planar laser pulses with an exposure time of 10μs for the first window and 150μs for the second. The obtained pair of pictures was set in such a way that the first laser pulse was realised at the last part of the first image exposure term and the second laser pulse at the beginning phase of the second exposure. The current timing and laser shot mode has been presented in a signal diagram in Figure 15. A crank pulse generator was used as the external trigger to control the laser timing shot mode according to the PTU Programmable Time Unit (hardware) and the LaVision software. The acquired pair of pictures from the MIE[6] scattered light from the PIV experiments are computed by the cross-correlation method [66] using the Davis™ code and

[5] CCD-Charge Couple Device invented by 1969 by Willard Boyle and George E. Smith at AT&T Bell Labs. Ref.in LaVision™.

[6] MIE – 'Mie theory, also called Lorenz-Mie Gustav theory is an analytical solution to Maxwell's equations for the scattering of electromagnetic radiation by spherical particles (also called Mie scattering effects)'. The MIE effect is generated by the elastic scattered light of particles that have a diameter similar to or larger than the wavelength of the incident light. Ref. in [LaVision™].

post processing with Matlab™ code. The post data processing are performed on-line and then display of velocity vectors are presented in Figure 30 - Figure 40 in chapter 6.

The PIV-Laser beam configurations, presented in the schematic view, of Figure 14 are chosen as follows: one vertical plane is projected onto the cylinder axis of symmetry, as well as on two horizontal planes arranged at 10mm and 65mm beneath the cylinder head surface. The horizontal and vertical planar laser sheets were introduced into the cylinder chamber through the bottom quartz piston window and into the cylinder liner. The bottom quartz window (*d*=65mm) was flat creating a low squish cylinder head area.

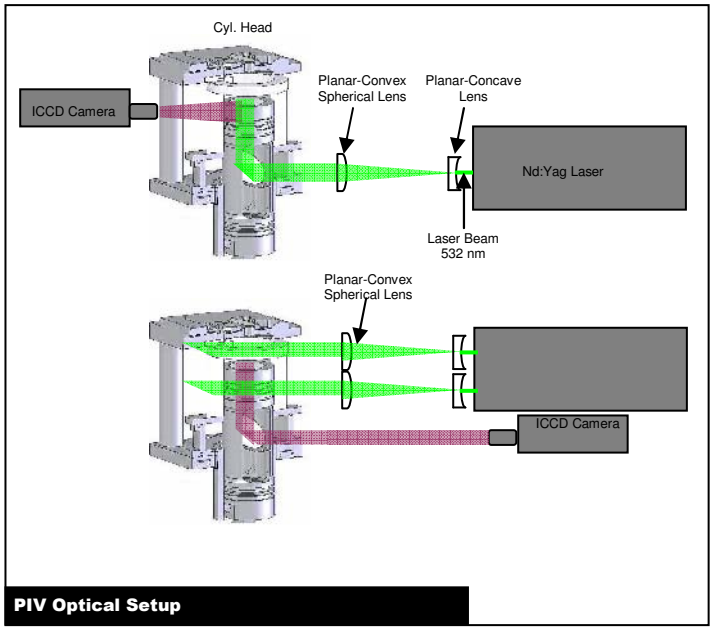

Figure 14: PIV-Vertical and Horizontal Laser Optical Arrangement, A) Side, B) Bottom

4.3 Experimental Measurement and Data Analysis

4.3.1 In-Cylinder Gas Pressure Measurement

The in-cylinder pressure measurement is one of the most important experimental parameters which quantify the combustion and flow phenomenon. The importance of the in-cylinder pressure data is crucial for heat release analysis, mass fraction burn rate and engine performance evaluation. The biggest drawback of using this method lies in the averaging of spatial physical effects to the non-spatial form of the cylinder pressure. From this point of

view, it is impossible to recognise important gas stratification field effects and only simple assumptions can be correlated with initial gas conditions. For a more complete in-cylinder analysis, optical methods must be added to the pressure measurements.

A non-cooled piezoelectric pressure transducer (Kistler type 7040A) is installed in the cylinder head on the opposite side of the pentroof optical access region. The high impedance 1.5m shield cable connects the pressure transducer head with a charge amplifier (Kistler) which is mounted to the optical bench. The electric charges, which are induced by compressed piezoelectric material, are amplified by the Kistler charge amplifier and outputted as a modulated voltage. The calibration of the pressure transducer was performed on a oil weight bench machine in the range of 1MPa/1V to 10MPa/10V. The obtained characteristics of the pressure transducer were applied to the charge amplifier as a tuned coefficient. The Kistler piezoelectric system has a range of absolute pressure measurements between 0.08-10MPa.

4.3.2 Temperature Measurement

K-type thermocouples were used to measure the temperature of the intake air within the cylinder head port and the intake plenum. The k-type thermocouple is capable of measuring the gas temperature between -80 ˚C and 800 ˚C, and has been calibrated to measure boiling temperature points under ambient conditions. The thermocouple type (K) and induce charges are amplified, and the outcomes voltage is read by a digital temperature indicator.

4.3.3 Data Acquisition System

The data acquisition system is an integral part of the PIV LaVision system. The system hardware is based on a PCI bus card type installed into the PC as a programmable time unit (PTU). The PTU is grouped into the ensemble cards developed for the creation of

the complex patterns of pulses. The pulse width and time intervals are synchronised automatically in accordance with the computer hardware demands. The laser, camera and computer hardware are managed by the PTU synchronised signals. The data acquisition board ports have two I/O TTL ports as well as two signal inputs with PTU ports A and B. The PTU has 16 pulse outputs, an arming input and a trigger input. All signals are divided into the PTU port channels with appropriate sequences programmed at the beginning and end of the acquisition routine.

The PTU external trigger mode for 'Cold-Nonreactive' flow is imposed by signals (TTL 5V/50Ω/1μs) from the Oxford control system. The PIV CCD Camera is connected via the double BNC cable to the camera interface board. The serial data transfer between the camera and the PCI-Interface is developed by a double coaxial cable with an impedance of 50Ω. The signal synchronisation for the Laser flash and camera shutter is programmed by the PTU and is presented in Figure 15.

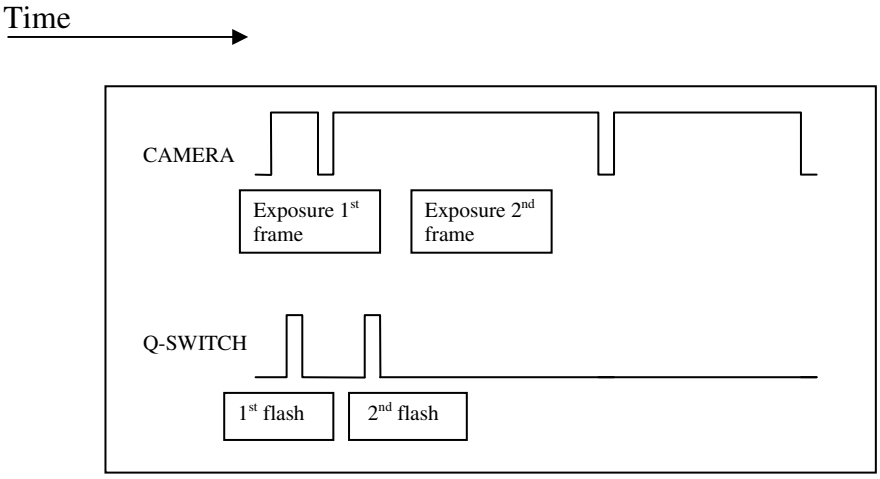

Figure 15: PTU synchronisation signal for Laser and Camera triggering.

4.4 Data Processing and Analysis

4.4.1 DaVis Solver and Cross-Correlated Methods Set-up and Uncertainness of Measurements

The PIV solver offers two methods of particle displacement analysis based on the Cross-Correlated and Auto-correlated algorithms performed by Fast-Fourier-Transform FFT [67]. The particle image Cross-Correlated evaluation algorithm is based on the camera recording double frame and double laser exposure mode Figure 16 B. The digital PIV solver divides the acquired main frame into subareas called 'interrogation windows'; the first interrogated frame is compared to the recorded scatter light from the second frame. Another type is the Auto-Correlation picture evaluation method based on the recording camera sequence where only one frame is produced onto a double laser exposure Figure 16 A. For the 'COLD' flow engine analysis, only the double frame, double exposure method has been used.

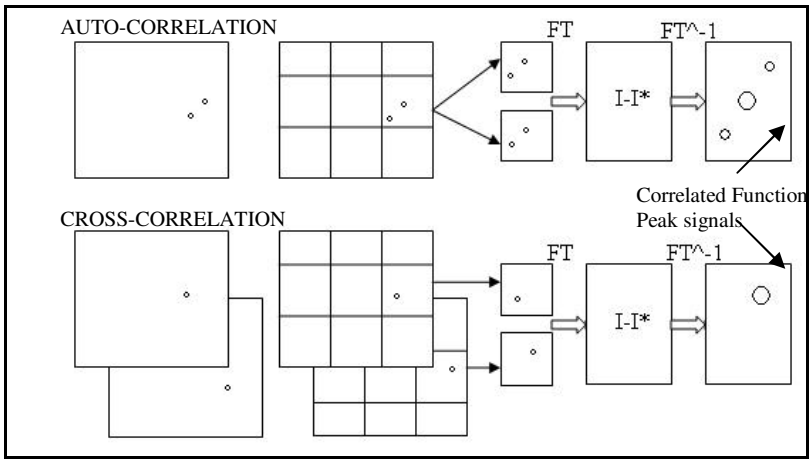

Figure 16: Diagrams of Auto and Cross-Correlation Methods for Vector Displacement Evaluation Recordings. A) Single Frame/Double Exposure; B) Double Frame/ Double Exposure

The 'standard' correlated function, used to evaluate two discrete sampled pictures from CCD fast shutter cameras, is defined as:

$$\Phi(dx,dy)=\sum_{x=0}^{x<n}\sum_{y=0}^{y<n} I_1(x,y)*I_2(x+dx,y+dy) \text{ where } (-\frac{n}{2}<dx<\frac{n}{2}),(-\frac{n}{2}<dy<\frac{n}{2}) \quad \textbf{(30)}$$

Where $I_1(x,y)$ and $I_2(x+dx,y+dy)$ are the intensity distribution of the interrogated images with (dx,dy) being the pixel offset between both pictures and $\Phi(dx,dy)$ the cross-correlation function. From the $\Phi(dx,dy)$ function, it is apparent that the statistical maximum of the correlated function can be found. The tracking particles are grouped by a defined interrogation size and are numerically computed for the maximum signal intensity found at the displacement (dx,dy). For known particle displacements (dx,dy) and picture acquisition times (dt), the velocity vectors are calculated according to the following definition:

$$V_{x,y}=\frac{(dx,dy)}{dt} \quad \textbf{(31)}$$

The interrogation dimension for the acquired data has been chosen in the range of 16x16 and 32x32 pixels, depending on the quality of the seeding field and the computational time of the velocity vectors.

Methodology and Solver Set-up

The seeding machine and the PIV Davis™ solver have been set up throughout the series of optical tests. The experimental trial and error analysis method was chosen for particle tracer evaluation in order to preserve the quality of the velocity vector flow field representation. The series of tests were conducted during steady and unsteady fluid flow conditions.

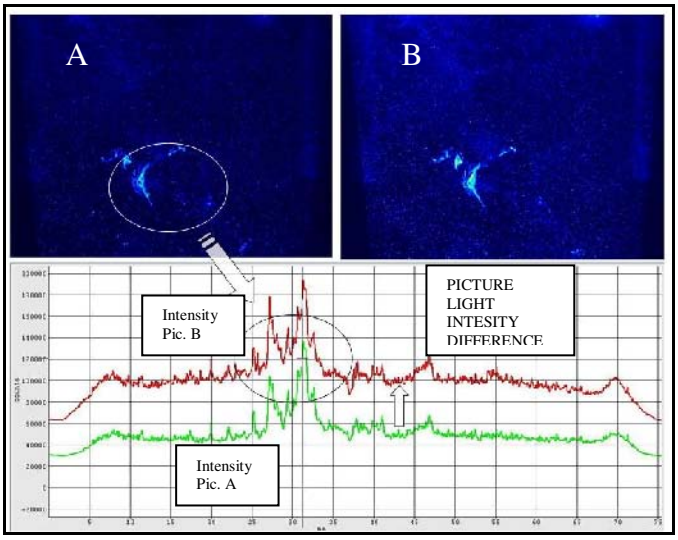

Figure 17: Laser Light Intensity-Difference for both Cross-Correlated Pictures.

The Figure 17 and Figure 18 present the sequences of test pictures, which include the laser beam configuration, the acquisition time, and the solver equations parameters for the region of unsteady flow in the cylinder. It is clear that the light intensity profile obtained from both pictures (Figure 17) does not have an appropriate MIE scatter light intensity and a high level of background light noise. The thick 0.2-0.5 mm laser plane, which illuminates the oil seed field, creates an extremely fuzzy image (Figure 18) with a strong halo effect on the piston crown edge which prevents the use of the Cross-Correlated method to solve the velocity vectors. It must be noted that the optical piston was slightly damaged; part of the broken crown generates an additional halo effect, shown by the inappropriate light scatter balance.

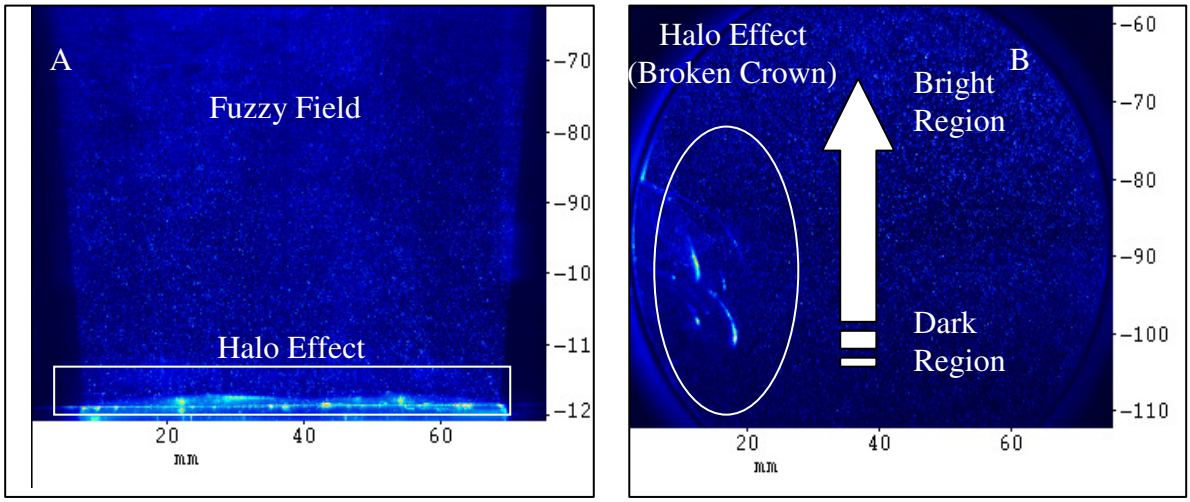

Figure 18: The Non-uniform Laser light Intensity Across: A) Vertical; B) Horizontal Cylinder Position

Based on the obtained data and the calculated test velocity vectors field, the following enhancements for the acquisition procedure are proposed:

- Decreasing the mass flow rate of the oil seed
- Reducing background noise (mainly reflected light not from the laser source)
- Subtracting the test background (no seeds) picture from the picture sequences
- Balance the power of the laser flashes to a uniform level of light intensity balance with a medium

Both A and B in Figure 19 show the effects of the lens and light-background optimisation in the case of the scattered light distribution within the cylinder at two different positions. Both pictures indicate a more uniform light intensity balance and an improved quality of the seeding region.

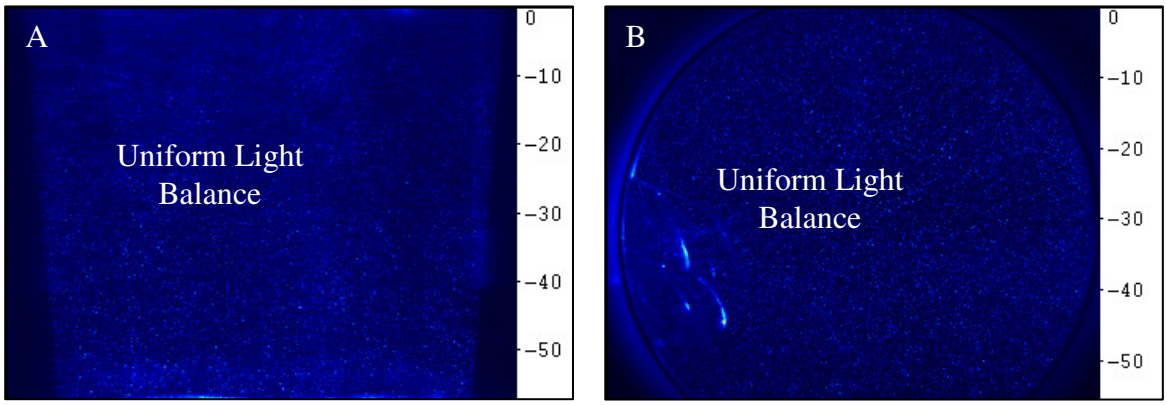

Figure 19: The Uniform Laser Light Intensity Across A) Vertical and B) Horizontal Cylinder Position

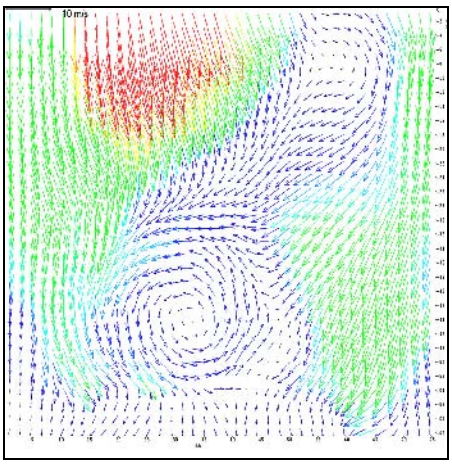

Figure 20: Average Velocity Vectors (70 engine cycles) on Vertical Laser Plane Position.

The example of the velocity vector fields calculated via the Cross-Correlated method is shown by A in Figure 19. For an appropriate quality of seeds in the field and a uniform intensity of background light following the set-up of the PIV solver, the following postprocessing techniques have been chosen:

- Standard Correlation function DaVis™ via FFT.
- Average Velocity Vectors from (60-70) engine cycles
- Multi-pass interrogation cells approach for large flow field fluctuations.
- Final interrogation of each cell, from 16x16 pixels.
- Filter (median removed and replacement if 1.3 RMS of neighbours)
- Smooth vectors field .

4.5 Summary

Experimental facility arrangements for the Ford/Jaguar optical engine have been presented in this chapter, including the following experimental systems: Nd:YAG Laser, ICC Camera, DAQ and PIV computer. All of the referred to systems are used to investigate the in-cylinder 'COLD' flow structure induced by the negative valve overlap (NVO) technique and two types of deflectors within the intake port. The optical engine is motored by an AC motor connected to an eddy current dynamometer and can operate at different temperatures which are controlled by an applied heating system. In addition, two systems of DFI (direct fuel injection) and the optical facilities using the Nd:Yag Laser operation are made by the author in accordance with the HCCI project research. The PIV system is provided by LaVision and has been used for data acquisition and partial postprocessing, parallel to the Matlab™ code.

Chapter 5

METHODOLOGY OF IN-CYLINDER GAS FLOW ANALYSIS

5.1 Introduction

This chapter will describe major assumptions for the complex analysis of the cylinder flow phenomena. The in-cylinder fluid flow is divided into three major flow structures recorded via the PIV system. The Jet-Jet, Jet-Wall and Bulk gas structures, which are filtered from the general flow pattern, show the features of the gas transport within the engine cylinder. The obtained group of large flow patterns simplify the analysis of and give insights into the major mechanisms of the gas transport and the possible regions of higher RMS velocity fluctuations as well as field in-homogeneities. The chosen in-cylinder flow strategy is based on 70 consecutive engine cycles to produce results similar to the CFD Reynolds Averaged Navier-Stokes (RANS) solver. In addition, it is proposed that the coupling of large-scale PIV flow patterns with a 1-D numerical analysis be made to characterise the pressure fluctuations and temperature history within the intake manifolds. The 1-D solver outputs are preferable as the initial and boundary conditions for further CFD analysis.

5.2 Methodology of In-Cylinder Gas Flow Analysis

HCCI is also known as Controlled Auto Ignition (CAI) [68]. The sensitivity of the auto-ignition phenomena is strongly dependent on the in-cylinder gas flow structure which is determined by the temperature and charge homogeneity. From a fluid dynamics point of view, the Homogeneous Charge Compression Ignition (HCCI) method can be described by the definition of the mixture properties and the state of the in-cylinder flow structure. In addition the internal cylinder gas flow is strongly affected by the intake and exhaust gas dynamic

process. Moreover, the flow process imposes a thermal gas convection and a spatial temperature distribution, which influences the beginning of auto-ignition and the chemical kinetic reaction rate. Therefore, the velocity vector fields obtained from the PIV experiments are important and give some indirect information about possible in-cylinder thermal in-homogeneities. Four possible states of the in-cylinder gas structure are proposed, which are argued by researchers to be fundamental to the HCCI concept:

- Homogeneous thermal and mixed structure (ideal for HCCI conditions)
- Thermal in-homogeneity (stratification-real conditions)
- Fuel-gas mixture in-homogeneity (stratification-real conditions)
- The thermal and mixture in-homogeneity (usual case)

The thermal bulk gas structure is the most effective auto-ignition control factor, controlled by the careful selection of Negative Valve Overlap (NVO) events. The selected valve timing has a strong influence upon the global in-cylinder gas exchange process and is an inherent part of the HCCI engine concept. Therefore, experimental PIV velocity vectors and CFD models support and help to build up a cylinder thermodynamics flow history by thermal gas convection, composition and heat transfer evaluations.

For the optical flow diagnostics, the author attempts to organise the in-cylinder PIV data analysis to all the various categories discussed in this chapter and to establish an indication and block interpretation diagram. General PIV experiments result in an interpretation diagram of the complex in-cylinder velocity vectors field, which is presented in Figure 21. The two different types of coherent flow structures are marked as follows: the dashed arrow indicates flow under the top of the exhaust valves; the solid line points to the tumble flow region close to the piston surface. The second type of coherent structure analysis

in this thesis is the flow over and under the intake valves close to the cylinder wall, which are indicated by doted-lines.

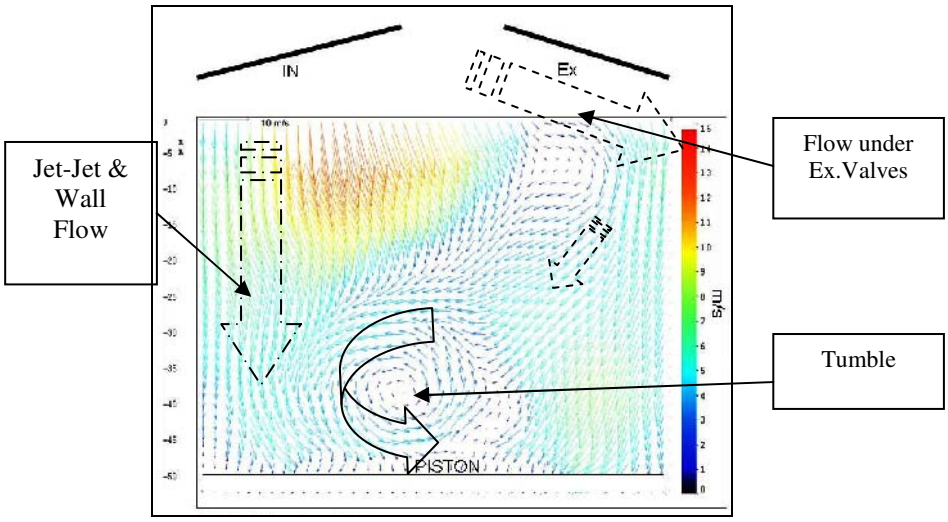

Figure 21: Interpretation of Velocity Vector Flows Obtained from the PIV Experiment.

The 'Road Map' for the in-cylinder PIV experiment has been established in Figure 22 for flow clarification and a better understanding of the analysed data. The presented division of the specific flow structures within the 'Large Scale Motion' group classifies the in-cylinder coherent structures such as vortices, recirculation zones, and air jets. This clarifies the large-scale mechanisms that affect the in-cylinder mixing process.

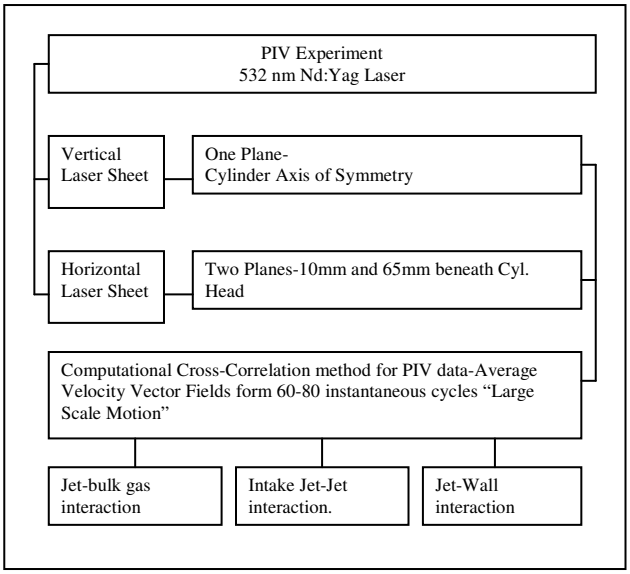

Figure 22: Road Map for the Tumble and Swirl Experiment, using PIV Measuring Method for Estimating Velocity Vectors.

In the current experimental PIV study, three main mechanisms of in-cylinder flow development are visualised and analysed. The interpretation of in-cylinder large-scale structures are as follows:

- Interaction of intake gas streams (Jet-Jet).
- (Jet-Wall) gas interaction.
- Jet with cylinder bulk gases (Jet-Bulk) interaction.

The (Jet-Jet) flow structure interaction, with its narrow horizontal cross-section jet area, is created by the strong axial convection flow generated from the contain upwind domain of the valves; and it splits the cylinder into two independent flow regions, as shown in Figure 21 (PIV data of vertical vectors plane) and Figure 23 (3D CFD visualization of jet-jet interaction). The high velocity intake vertical jet prevented two recirculation cylinder regions from mixing with each other. The vertical jet is the most significant large-scale cylinder structure, which drives the turbulent energy production [69]. Apart from the importance of different scales of flow production, the (Jet-Jet) interaction carries a vast amount of the fresh charge. In this narrow region, it is expected that there will be higher in-homogeneities in relation to the global in-cylinder balance of scalar values e.g. temperature, density, chemistry and mixture.

The strong part of the (Jet-Jet) flow close to the cylinder wall evolves and produces another high shear structure called the (Jet-Wall) interaction. This large structure acts in a similar fashion to the (Jet-Jet) case, where one of the flow components is less important and the flow can by threaded as a quasi two dimensional flow with a high shear stress rate [70].

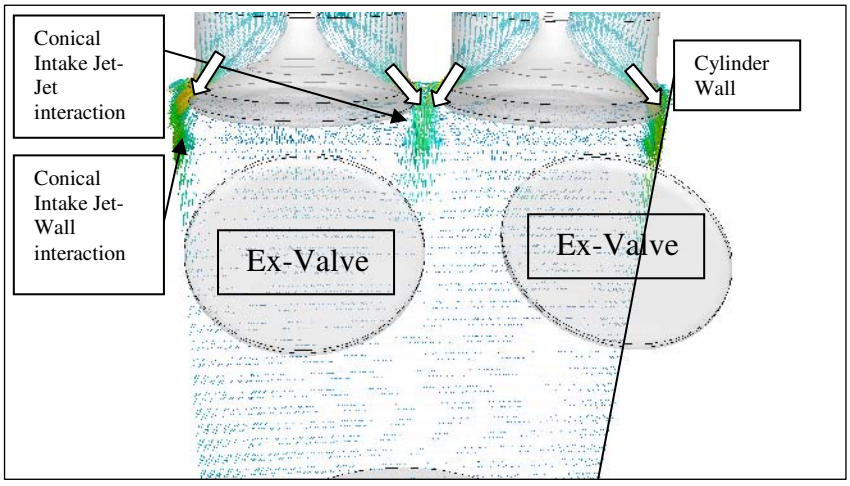

Figure 23: CFD Velocity Vectors Visualization of the Intake Conical Gas Jet-Jet and Jet-Wall Interaction for a 2-D Middle Intake Valve Plane.

The interaction between these two major gas structures (Wall-Jet) and (Jet-Jet) appears in the velocity vectors PIV data within the rear region of the inlet valve seats and the cylinder wall. Additionally the (Wall-Jet) deflected by the piston surface creates a recirculation structure on the piston crown which leads to a large vortex creation during the induction phase. Later in the intake stroke (180 CAD aTDC) the jet-bulk gas structure became more important with its pronounced, complex three dimensional flow due to the intake mass-flow rate decreasing, as well as less production of the kinetic energy at this stage. Moreover, the large tumble structure becomes less visible and decayed into the dissipative and 'eddy' flow currents [69]. Also, part of the swirling (z-axis of rotation) flow within the cylinder could survive until the late TDC phase. This effect is dependent on the rate at which the cylinder volume is changed and controlled by the conservation of the tumble angular momentum and flow distortion during the compression phase. It can be seen that the velocity-z (Vz) component in the Cartesian reference-frame, is changed periodically according to the engine stroke function. The reciprocating effect is one of the main factors destroying and creating the in-cylinder 'tumbling' flow structures, in according with the energy supply in the compression phase and the swirl pattern via the shear forces [1].

Another important issue for further PIV analysis and further clarification of the results is coupling the measurement of in-cylinder pressure with the analysis of the velocity vector

field. In-cylinder pressure results for both conditions are presented in Figure 24 A. A complex internal flow process with hollow length scale is both intake and in-cylinder pressure dependent. Any additional analysis of the in-cylinder pressure is important. Also for this reason, a 1-D Ricardo Wave™ Code has been used as a helpful tool for detailed studies of intake gas dynamics. The dimensions and boundary conditions of the modelled engine have been presented in chapter 7. The length and dimensions of the intake and exhaust manifolds have been matched to get similar experimental in-cylinder pressure. In Table 2 the intake port gas events are presented with the emphasis on the cylinder pressure, mass flow rate and Mach numbers.

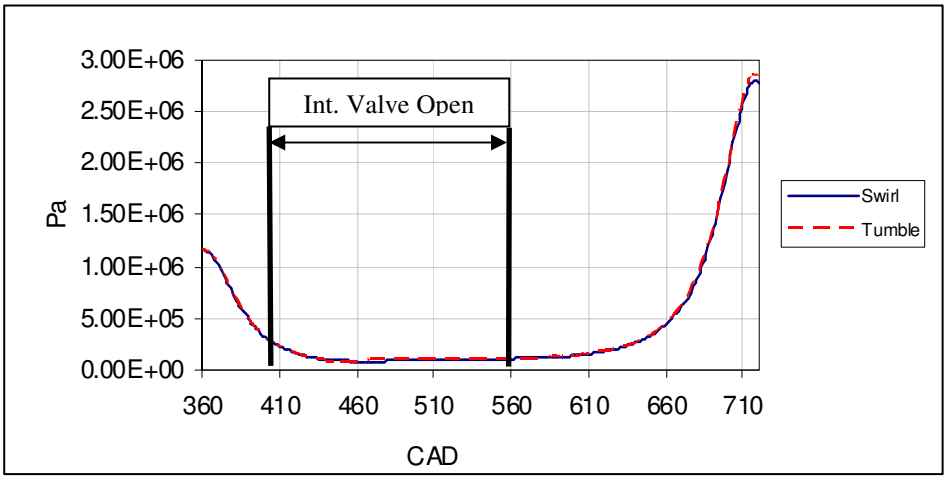

Figure 24 A: Experimental Cylinder Pressure for 'Tumble' and 'Swirl' cases. Two Inlet Deflectors Generating 'Swirl' and 'Tumble' In-Cylinder Flow Structures

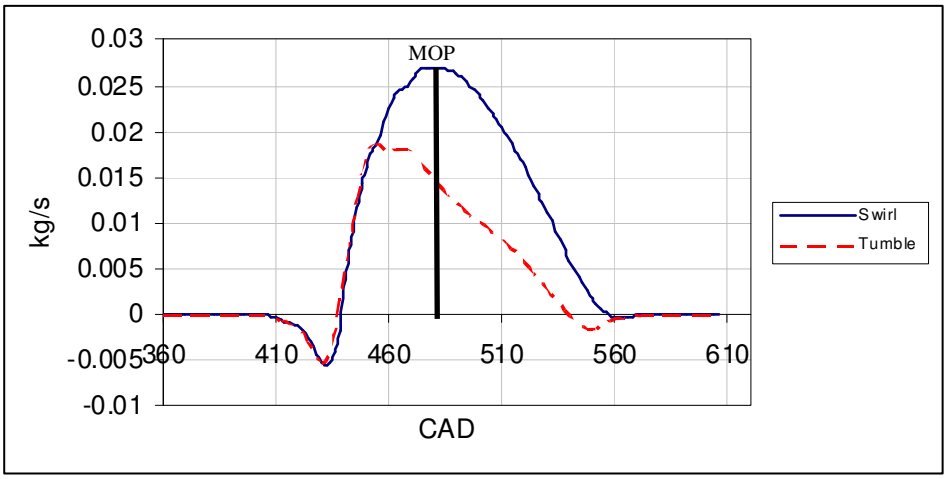

Figure 24 B: Time History of the Mass Flow Rate per one Inlet Valve for Motoring Case WAVE™. Two Inlet Deflectors Generating 'Swirl' and 'Tumble' In-Cylinder Flow Structures.

The final two results are obtained from the 1-D engine simulation according to a selected experimental crank angle position. The time histories of the Mach numbers and mass flow rates as well as the average in-cylinder temperatures are presented in Figure 24 B to Figure 26, respectively.

INDUCTION PHASE							
CAD aTDC	0	55	110	130 **MOP**	180	190	230
CAD	360	415	470	490 **MOP**	540	550	590
Cyl. Pressure							
TUMBLE [Pa]	1.15e6	1.5e5	0.98e5	0.99e5	1e5	1.1e5	1.1e5
SWIRL [Pa]	1.15e6	1.5e5	0.91e5	0.90e5	0.98e5	1e5	1.1e5
Mass Flow Rate [kg/s]							
TUMBLE							
+ inward	-		0.032	0.025	0		0
- outward	-	-0.016				-0.001	
SWIRL							
+ inward	-		0.027	0.026	0.006	0.001	0
- outward	-	-0.008					
Mach Number							
TUMBLE	0	1	0.3	0.18	0	0.18	0
SWIRL	0	1	0.58	0.5	0.23	0.18	0

Table 2: Cylinder Pressure, Inlet Valve Mach Number and Mass Flow Rate for Specific CA's in Relation to PIV Experiments.

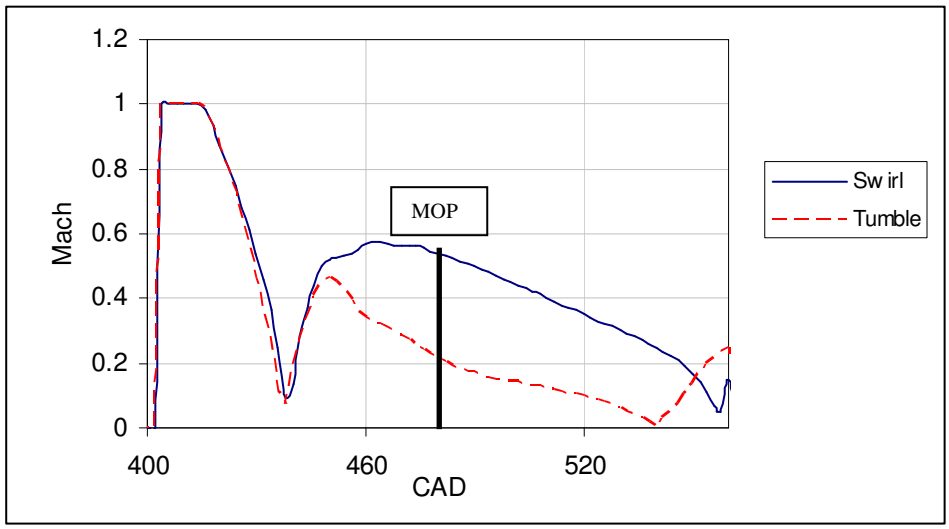

Figure 25: Time History of Mach Number on Inlet Valve Curtain for Motoring Case WAVE™. Two Inlet Deflectors Generating 'Swirl' and 'Tumble' In-Cylinder Flow Structures

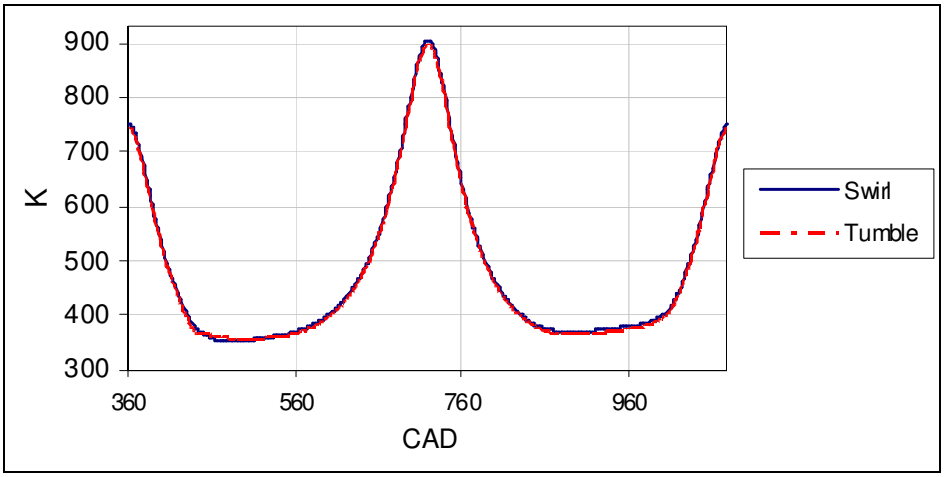

Figure 26: Time history of In-cylinder Temperature Predicted by Motoring Cases 1-D Code WAVE™. Two Inlet Deflectors Generating 'Swirl' and 'Tumble' In-cylinder Flow Structures

5.3 Uncertainty of In-Cylinder Flow Field Optical Measurements: Foundations for the PIV Experiments and Engine Intake Port Geometry.

Fluid flow processes occurring inside an engine manifest themselves in a hollow range of turbulent aerodynamic gas structures represented by different length-scales and flow complexity. Despite of an enormous amount of analysis in this area, designing any internal combustion engine still draws more from previous experience than from a scientific approach,

especially in terms of internal fluid flow [71]. Major problems exist with the different scales of turbulence and the complexity of flow interactions between these structures, which are difficult to predict and describe by even the most sophisticated numerical models, like the Large Eddy Simulation (LES) and the Direct Numerical simulation (DNS).

The Optical-laser techniques together with the CFD models provide a possibility for improvement in our knowledge about the key factors governing these flow structures. Therefore, it is important to group in-cylinder large flow structures obtained from the optical PIV experiments, in order of their global gas mixing process and influence on thermal stratification. Besides this, chapter 5 clarifies the PIV experimental approach as well as a foundation for the 'Road Map' for an analysis of gas flow results.

PROBLEMS ENCOUNTERED: OPTICAL ACCESS, OIL AND WATER MIST AND THE DEFORMATION OF PICTURES FOR EARLY FLOW AT 110 CAD ATDC

In Figure 30, in-cylinder 'Tumble-port' data at 110 CAD is indicated; the deflected intake jet on the exhaust side is not fully developed in reference to the 'high-swirl' port case. The highest gradient and the narrowed structure are achieved near the wall beneath the inlet valves. An additional analysis suggests that a substantial fraction of the flow moves upwards to the cylinder head, and is dispersed and non-uniform. This is due to the shape of the combustion chamber space. Unfortunately, the 2D PIV method does not deal with all the complex global 3D information regarding the flow, especially within the pent-roof area where achieving optical access is difficult. Therefore, additional measurements for the horizontal planes will be applied for a better analysis and approximation of the in-cylinder flow process. Additionally, it must be mentioned that significant measurement problems were encountered for the early engine intake phase. One of them is the effect of in-cylinder water vapour and oil mist and another is the deformation of the image due to the oil film on the cylinder-wall. This

is due to the top part of the cylinder liner which could not be removed as piston rings leave the oil residuals. The transparent region of the cylinder wall generates a high image deformation. The poor output of MIE scatter signal is also affected by intense background noise caused by clouds of mist within the cylinder. With ambient conditions close to 30% humidity and 25°C, taking a proper signal for a specific engine CAD is excluded; this disables the cross-correlating method of calculating estimated velocity vectors. Therefore, the engine room must be air-conditioned to decrease the level of humidity. Figure 27 and Figure 28 show in-cylinder mist and image deformation effects for 110 CAD degrees.

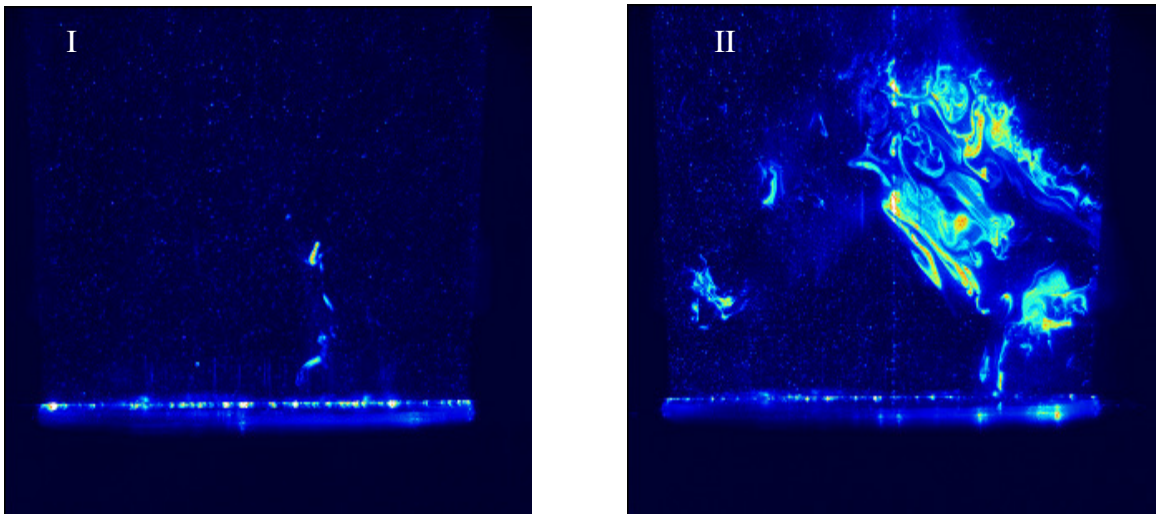

Figure 27: The Oil Mist Effect at 110 CAD aTDC (I-Tumble Case, II-Swirl Case)

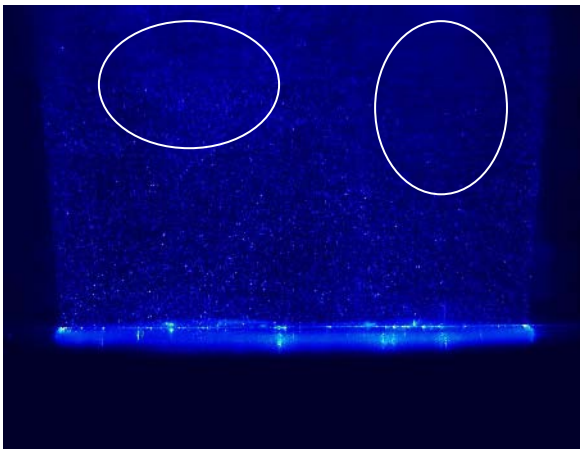

Figure 28: Oil Wall Film and Deformation Image Effect (18μs between pulses).

The mist phenomena is in-cylinder pressure dependent. For the 'high-swirl' port configuration the mist effect is more apparent and is controlled by the in-cylinder underpressure. Low in-cylinder pressure and high port velocity induces mass flow losses as well as higher blow-by losses. Two major mechanisms are proposed as being responsible for these mist effects:

- The water saturation pressure attained for this CAD condition
- The oil-air mixture and atomisation effect due to a strong backflow crevice jet

It could be stated that based on the raw pictures and the frequency of mist generation for successive CAD cases it is possible to diagnose flow loss effects. The flow for the swirl-port case during the induction phase is caused by chocking; and the effect of frictional gas can be estimated according to the Re and with an indication of the average velocity. The in-cylinder experimental pressure diagram in Figure 65 clearly shows this underpressure region as well as the lower TDC compression pressure of the swirl-port case and demonstrates the effect of mass flow

5.4 Summary

From an experimental approach, three large and dependent in-cylinder flow structures are proposed as the phenomenological 'Flow Analysis Tools'; and they will be used to describe the large scale structures: the intake valve gas (Jet-Jet) interaction, the (Jet-Wall) interaction and the jet with bulk gases (Jet-Bulk) interaction. The proposed combination of 'flow' tools allows an examination of the most important in-cylinder fluid flow effects including mixing, gas convection, and some approximation of the development of fluid thermal in-homogeneity. Moreover, the phenomenological experimental approach is the key to CFD validation and gas dynamics optimisation which is a subject of the next chapter.

Chapter 6

EFFECTS OF INTAKE DEFLECTORS GEOMETRY ON THE IN-CYLINDER 'COLD' FLOW STRUCTURE FOR SYMMETRICAL NVO

6.1 Introduction

The novel HCCI combustion technology of lean mixtures is strongly dependent on the control of the mixing process for the recycled burnt gasses. For this reason, a special valve-train with a specific symmetrical Negative Valve Overlap (NVO) was utilised. The analyses show [72] that the generally in-cylinder in-homogeneities play the dominant role in an active control of auto-ignition phenomena. The present chapter has been designated for a quality study of the influence of the experimental inlet manifold deflectors to generate more pronounced 'Swirling' or 'Tumbling' flow within the engine cylinder. The effects on the 'COLD' (without combustion) flow gas structure and the development of the fields of flow in-homogeneity for the symmetrical 110 CAD Negative Valve Overlap (NVO) timing at 1000RPM are experimentally measured. The obtained experimental and computational in-cylinder data are useful to recognise that regions of higher cylinder shear flow produce turbulence and maintain different gas mixing regions. In addition, it is believed that temporal and spatial turbulence development strongly affects the gas thermal convection process and in consequence affects the HCCI auto-ignition time and combustion.

The in-cylinder flow analysis is based on the parametric 1-D computational study as well as an in-cylinder optical-laser diagnostic method. The optical method involved in this project is the Particle Image Velocimetry (PIV), an imaging technique utilising a high energy

source of coherent laser light built up by a 120mJ Neodymium doped Yttrium Aluminum Garnet (Nd:Yag) double pulse Laser. The numerical approach includes a detailed 1-D engine gas dynamics model matched to experimental results, e.g. in-cylinder pressure, mass flow and intake temperature.

6.2 The Intake Deflectors Effects-Measurement

A comparison study of in-cylinder compressible gas flow measurements with different aerodynamic large-scale structures is presented in this section. The objective of the PIV experiments was to investigate the effect of changing engine intake port architecture on the in-cylinder flow structure, mean velocities and velocity fluctuations. Besides this, the effect of changing the geometry of intake port is used as a sensitive flow case study to evaluate the level of in-cylinder flow field homogeneity as well as to create reliable input data for a further computational CFD model.

The series of Figure 30 to Figure 41 represent the time-history of the in-cylinder flow fields for two types of port deflectors obtained by the PIV optical-laser measurement. The shape of the inlet deflectors as well as the valve timing impose the 'Tumbling' and 'Swirling' flows within the engine cylinder. The PIV experiment has been performed on the vertical and horizontal laser sheet planes generated by a double-puls Nd:Yag laser with a group of lenses and mirrors. Additional technical details about the optical-laser methods and engine setups have been presented in Chapter 4.

6.3 Case 1. Early Open Intake Valve (55 to 110) CAD aTDC

The PIV technique provides the details of the velocity vector fields generated by the 'Tumble' and 'Swirl' port types; and the difference for the initial stage of in-cylinder flows at 110 CAD aTDC is presented in Figure 30 I, II. The aforementioned data has been obtained at the middle section of the cylinder which is intersected by the Nd:Yag double pulse planar

laser sheet. The vertical planar laser sheet was introduced into the engine through the piston optical access with a beam thickness of approximately 0.1 to 0.5 mm. To maintain the experimental conditions the Nd:Yag double pulse time laser separation was established at the same value of 12 μs for both cases and constant 10ns for the laser duration. Generally, for both cases the internal flow pattern is built up from the intake valve curtain and valve seat areas. It is worth noting that for the gas induction phase at 58 CAD aTDC with a 110 CAD NVO a critical back-flow to the inlet ports with M=1 as well as the chocking effect for both inlet port configurations are expected [5]. The back-flow effect predicted by the 1-D Wave model during this early open intake valve is presented in Figure 29. Moreover, any hot cylinder residuals fill-up and are mixed into the intake runner, thereby increasing the temperature of the fresh charge and influencing the later in-cylinder mixing process.

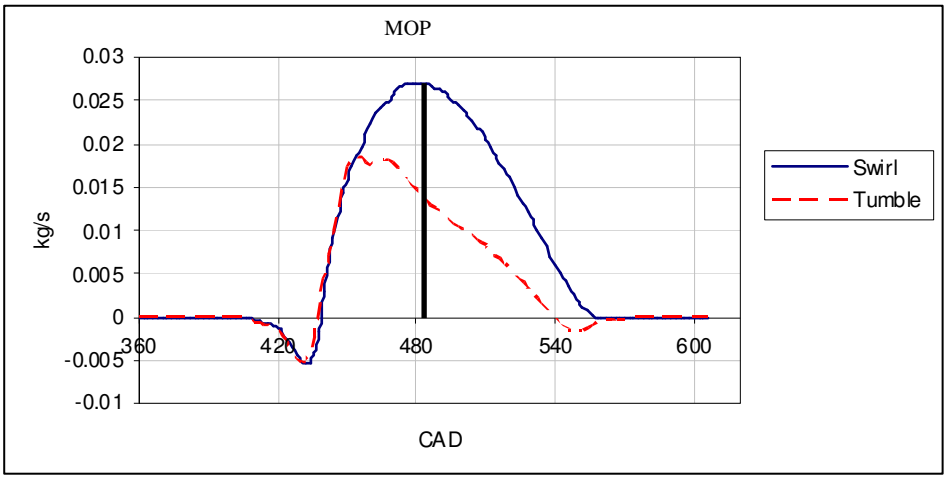

Figure 29: The 1-D Prediction of the Mass Flow Rate Per One Inlet Valve For the Motoring Case (1000RPM) WAVE™. Two Cases of Inlet Deflector Type: 'Swirl' and 'Tumble' for Generating Other In-Cylinder Flow Structures.

The back-flow to the intake manifold occurs because a higher cylinder recompression pressure is encountered during the early opening of the inlet valve and is approximately equal to the cylinder pressure for the exhaust valve closure phase. Moreover, based on the experimental data and Mach number for the early intake phase a strong positive pressure to wave travel throughout the intake system towards the open end of the system we expected. In addition, during motored tests the strong inlet pulsations are perceptible and visible as a

deformation effect due to the elasticity of the intake-air box connector pipe and are characterised by the pulsation 'rumbling' sound.

The obtained data at 110 CAD aTDC shows the inward flow into the cylinder chamber for both types of intake geometries. For the low-swirl port 'Tumble' arrangement case, where only the right part of the poppet valve in the 'Swirling' high-swirl port case is active, a characteristically higher velocity magnitude is developed over the upper half of the cylinder chamber during inward flow. The (Jet-Jet) flow with a highly downward axial velocity component for the low-swirl 'Tumble' ports, peaking at 20 m/s in Figure 30, case I. For this case also, the (Jet-Wall) structure is recognised on the rear part (dotted line) of the cylinder wall beneath the inlet valve seats, due to converging flow from the two intake valves in accordance with the (Jet-Jet) structure. Also an interesting observation is that this data is recorded at 110 CAD, after the piston reaches the maximum downward velocity and the intake valves are on their opening ramp and therefore at a relatively low lift with a low valve curtain area. The above mentioned effect agrees with the conservation of engine mass balance due to periodical changes during the induction phase and the reciprocating character of the system.

The in-cylinder 'negative[7]' tumble visible in Figure 30 is created by part of the gas jet flowing through the inlet valve curtain area on the exhaust side. A substantial fraction of the high velocity intake stream flow upwards to the exhaust site of the cylinder head, where it is deflected with a velocity peak of 10 m/s in the recirculation zone. This region with its high velocity shows that the top of the cylinder gas stream (which is not apparent in Figure 30 due to a lack of optical access for the cylinder head) is oriented by to the valve poppet and is highly dependent upon inlet manifold geometry, i.e. the pent-roof angle and valve curtain area. This is one of the reasons why CFD computational three dimensional engine models

[7] Negative sign for the vortex rotation is chosen according to the right hand side thumb law.

must be applied for better understanding of in-cylinder flow phenomena in this particular region.

A different flow pattern without a visible strong (Jet-Jet) and (Jet-Wall) interaction obtained for the 'Swirl' port configuration is presented in Figure 30 II. The flow close to the exhaust part of the cylinder head is similar for both events, but the major tumble structure at the front of the cylinder is more developed for the 'swirling' case at this CAD. Thus suggests that flow over the top part of the cylinder head obtained for the given CAD on the vertical plane characterises a higher gas velocity stream in a horizontal direction and a more complex structure compared to the measured 'Tumble' base. The tip of the core of the tumble structure is near the top of the cylinder head for the current CAD.

The PIV 2-D evaluation of complex in-cylinder spatial flow using only two components of velocity vectors cannot describe tangential velocity components related to the cylinder axis of rotation and flow over the cylinder head. This is because the 'Swirling' case manifested highly asymmetric and tangential flows. Any additional interaction with a strong axial jet leads to the creation of a strong in-cylinder helicity pattern, which inherently is 'strongly 3D[8]' and is described by [73].

For both intake port arrangements, the (Jet-wall) and (Gas-Bulk) flow structures deflected by the piston surface create the counter-rotating vortices visible in Figure 30 I, II. For the high-swirl port configuration, the 'Jet-Wall' interaction is not visible but the recirculation region close to the surface of the engine piston suggests that for this condition a high downward 'wall-flow' is accomplished. The aforementioned example shows the difficulty of making a three dimensional in-cylinder flow analysis based on two dimensional vertical PIV measurement.

[8] Name 'highly 3-D flow' is related to the structure of the fluid flow without any symmetric features, especially when rotating the flow around an axis parallel to the direction of motion.

IN-CYLINDER SHEAR FLOW AND ADVERSE PRESSURE AT 110 CAD aTDC

For the engine 'Swirl' condition, the centre of the positive vortices is close to the cylinder wall and the flow structure is dispersed with a substantial fraction flowing upwards towards the cylinder head. This effect of spreading vortices controlled by the shear flow effect takes place on the broadside of two visible structures; and the interaction between the large-scale tumble structure (dashed arrow and continuous line), and an adverse pressure gradient under the inlet valves lead to a separation of the flow [74].

A POSSIBLE IN-CYLINDER THERMAL-FLOW STRATIFICATION EFFECT AT 110 CAD aTDC

The 'Tumble' case I at 110 CAD aTDC shows the highest value for the velocity vectors at the inlet region. This value is obtained for all sets of the in-cylinder data and gradually decreases toward the (Maximum Open Point) MOP of the intake valves. The front of the intake jet, presented by the 'doted-line', propagates from the inlet valve to the piston surface at several times the mean piston speed (3 m/s). The (Jet-Jet) core flow developed under the inlet valves is characterised by a compact and narrow stream structure with approximately 3-5 mm cross-section thickness. The flow over the cylinder head originates from the valve curtain area and spreads throughout the hollow chamber domain.

The second major gas stream forming within the cylinder at 110 CAD aTDC is visible at the front part of the cylinder head (dashed arrows), close to the exhaust valves where a major portion of induced jet is deflected downwards to the piston. These flow regions, especially these near to the inlet valve gap and the upper part of the cylinder head, indicate the intake flow structure as a region of vast thermal stratification and finally, of gas temperature gradients. For all fluid flow regions, its expected that for gas with the least flow, the gas core temperature and the nearest near intake valve domain will not exceed 350 K during the later

induction phase in accordance with [75,76]. The upper cylinder gas temperature is approximately a third of that of the fluid under TDC recompression. However, the early engine induction phase indicates a higher inlet gas temperature due to backflow and the mixing process within the inlet manifold. According to the obtained sets of the experimental PIV data, an in-cylinder flow pattern with a region of colder gas is expected close to the piston surface, the upper cylinder head and the cylinder walls due to the mass transport by the large-scale 'COLD' tumble motion as well as (Jet-Wall) and (Jet-Jet) interaction.

For further discussion and clarification of the results, it should be stressed thus the subject of this work, is to find the characterisation of engine in-cylinder internal flow as a possible way to predict the thermal gas field evolution based on the large-scale flow structures. Ultimately, information from the PIV experiments and the CFD modelling is helpful for evaluating the combustion process as well as for a better understanding of the auto-ignition phenomena. An effective in-cylinder gas mixing process is crucial for both thermal and chemical analysis and leads to a concept for auto-ignition combustion control (CAI) and inherently to (HCCI) technology.

IN-CYLINDER TURBULENT FLOW: REYNOLDS NUMBER, MEAN AND RMS OF FLOW AT 110 CAD aTDC.

The in-cylinder turbulence (low scale) and the large-scale convection motion are the two most effective forms of in-cylinder mass transport and mixing processes [73]. Both dimensionless numbers Re and Pr are usually used to describe turbulent mixing and the potential of gas heat exchange within the fluid.

A timeline of the in-cylinder average Re number for combining three planes of measurement is presented in Figure 42 as complementary trend of the fluid turbulence process. Combining the three measurement planes, two horizontal and one vertical in order to

obtain average in-cylinder Re number prediction is more effective and accurate than conducting a one-plane evaluation. The average kinematic viscosity for the in-cylinder gas is obtained from the 1-D gas dynamics simulation where the diameter of the cylinder is chosen as a characteristic length scale for the Reynolds Equation (32). From the available data, it is apparent that for the tumble-port, almost up to the BDC, the in-cylinder flow has a higher Re number and is built-up by, coherent large-flow structures compared to the swirl-port case. The flow (Jet-Jet) and (Jet-wall) structures presented in Figure 30 for tumble-port reach the piston wall carrying a major portion of bulk gas within a high Re number. This turbulent region of the engine cylinder flow features a high gradient and RMS of velocity fluctuation in Figure 44, which inherently shows a higher spatial turbulence intensity and the gas turbulence kinetic energy TKE.

$$\mathrm{Re} = \frac{|V| \cdot D_{cyl}}{\nu} \tag{32}$$

$$k^{'} = \frac{2 \cdot v^{'2}}{3} \tag{33}$$

The average in-cylinder turbulent kinetic energy is calculated from Equation (33) for both types of deflectors and is presented in Figure 43. Any increase in the rate of gas diffusion and convection with a strong RMS of velocity fluctuation inherently builds up a strong effect of turbulence.

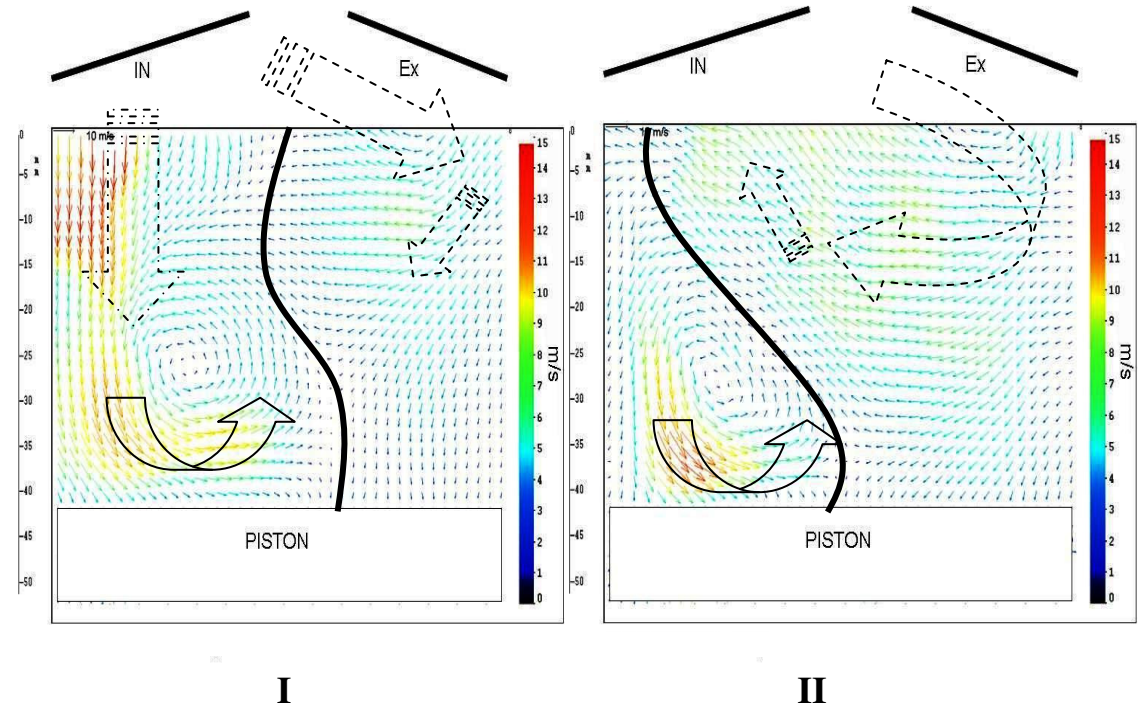

Figure 30: In-cylinder Velocity Vectors Obtained from the Vertical PIV Plane at 110 CAD. I-Tumble Port; II-Swirl Port

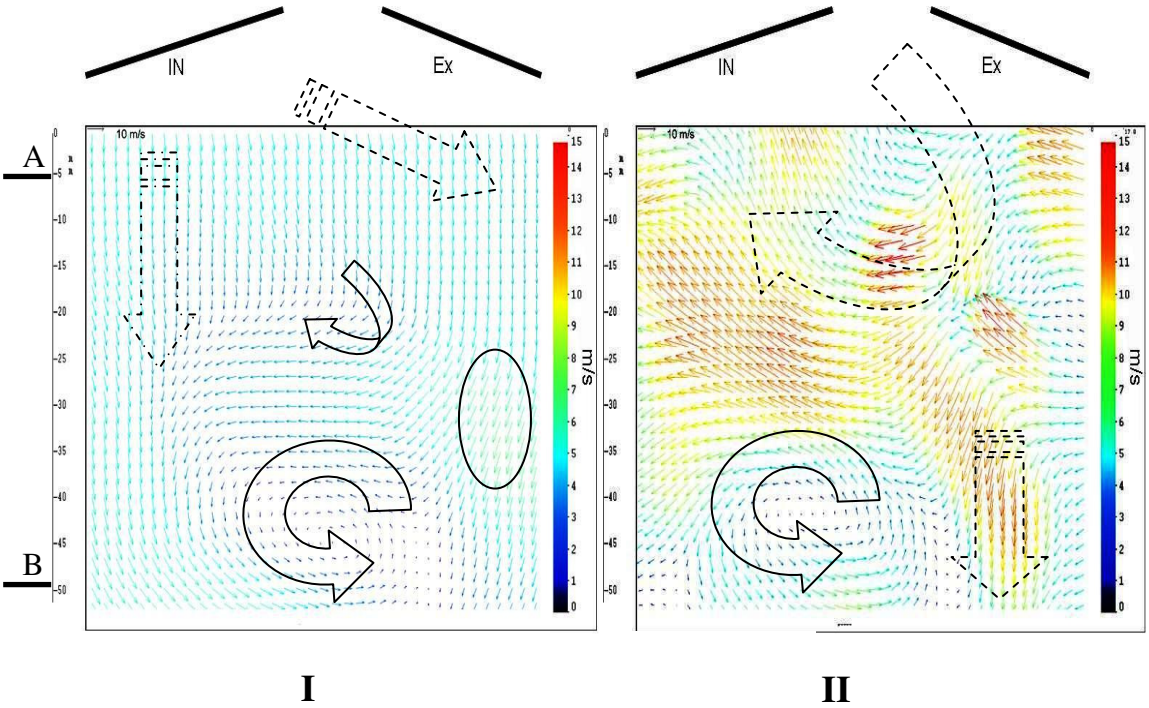

Figure 31: In-cylinder Velocity Vectors Obtained from the Vertical PIV Plane at 130 CAD. I-Tumble Port; II-Swirl Port

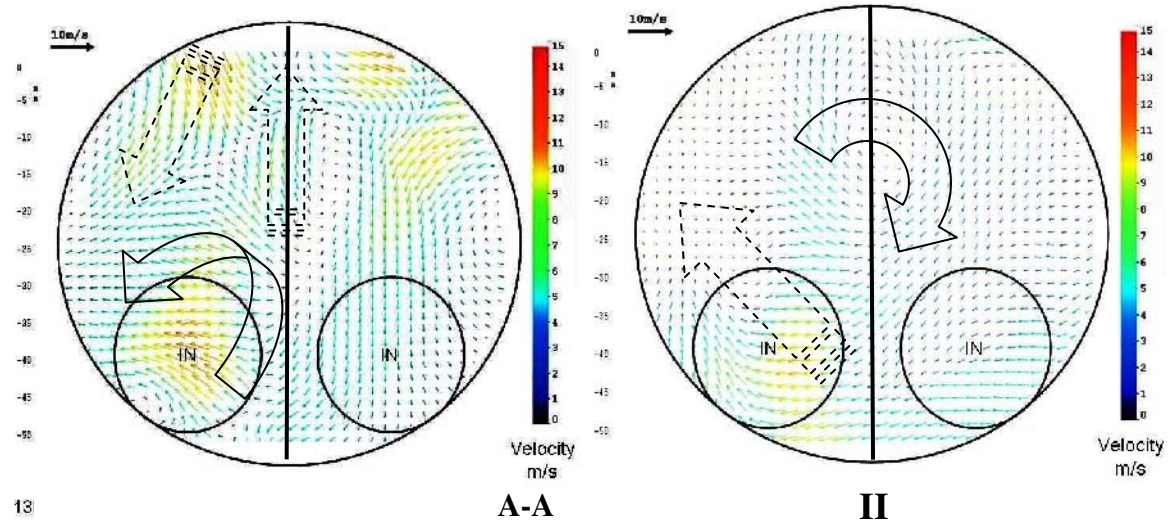

Figure 32: In-cylinder Velocity Vectors Obtained on the TOP Horizontal A-A PIV Plane at 130 CAD. I-Tumble Port; II-Swirl Port

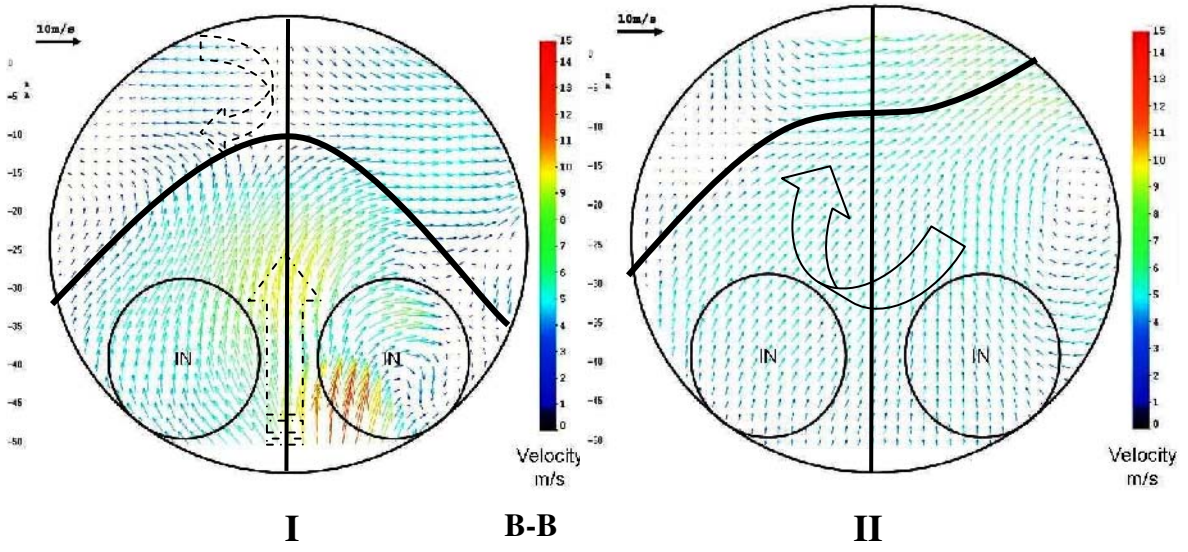

Figure 33: In-cylinder Velocity Vectors Obtained at the BOTTOM Horizontal B-B PIV Plane at 130 CAD. I-Tumble Port; II-Swirl Port

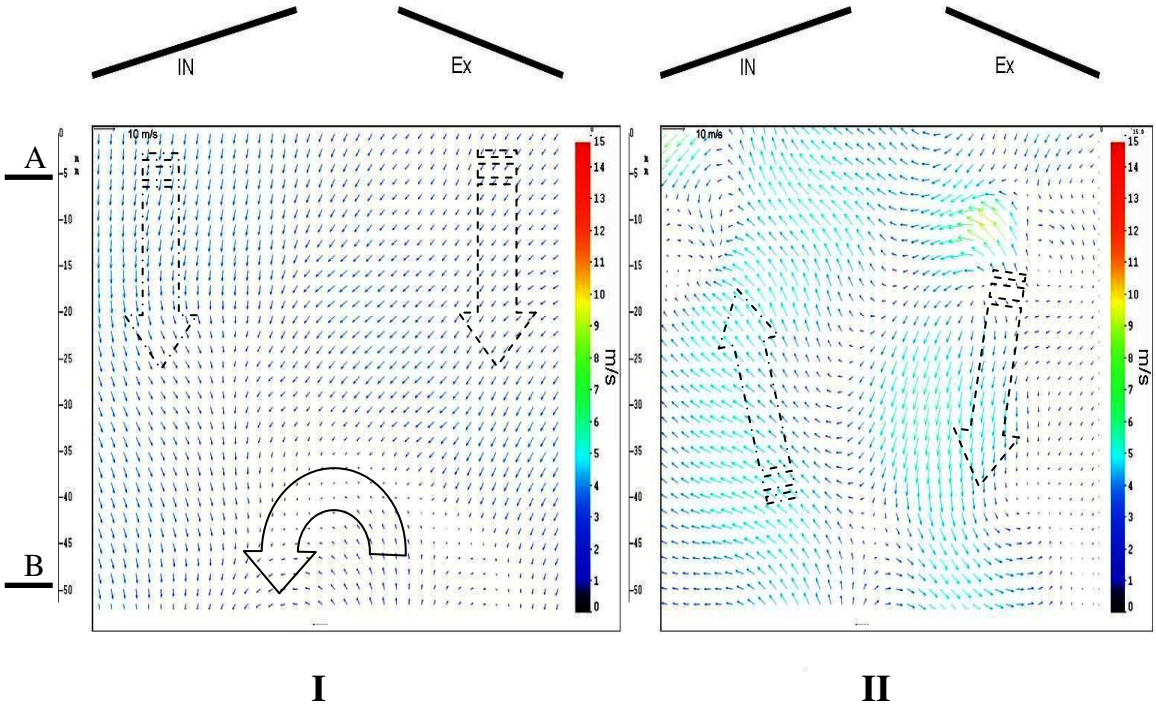

Figure 34: In-cylinder Velocity Vectors Obtained from Vertical PIV Plane at 180 CAD (BDC). I-Tumble Port; II-Swirl Port

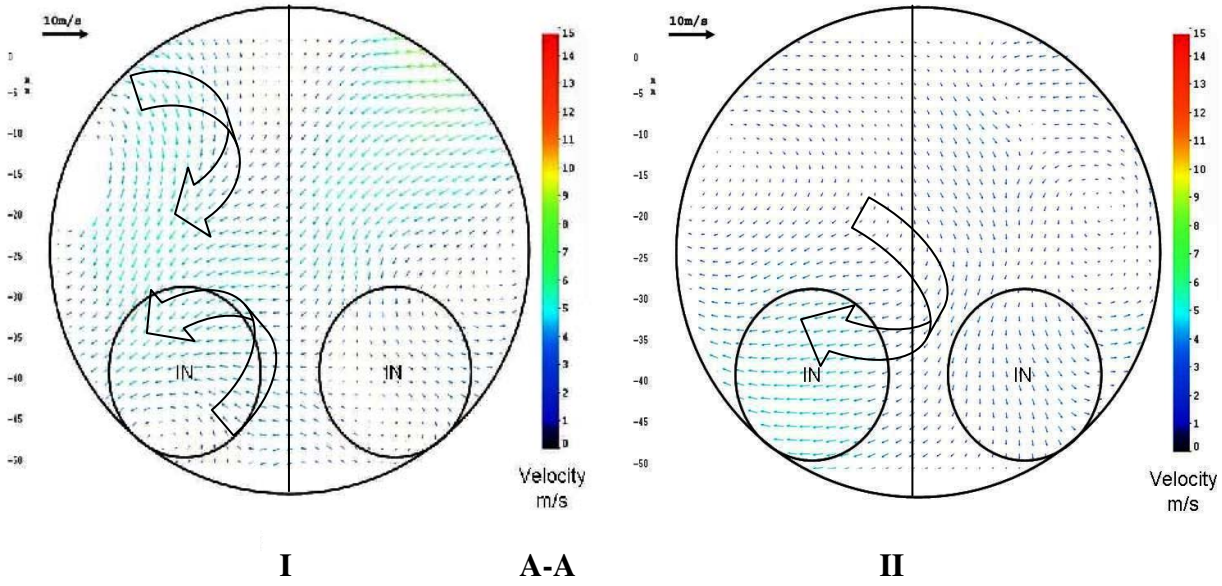

Figure 35: In-cylinder Velocity Vectors Obtained at the TOP Horizontal A-A PIV Plane at 180 CAD (BDC). I-Tumble Port; II-Swirl Port

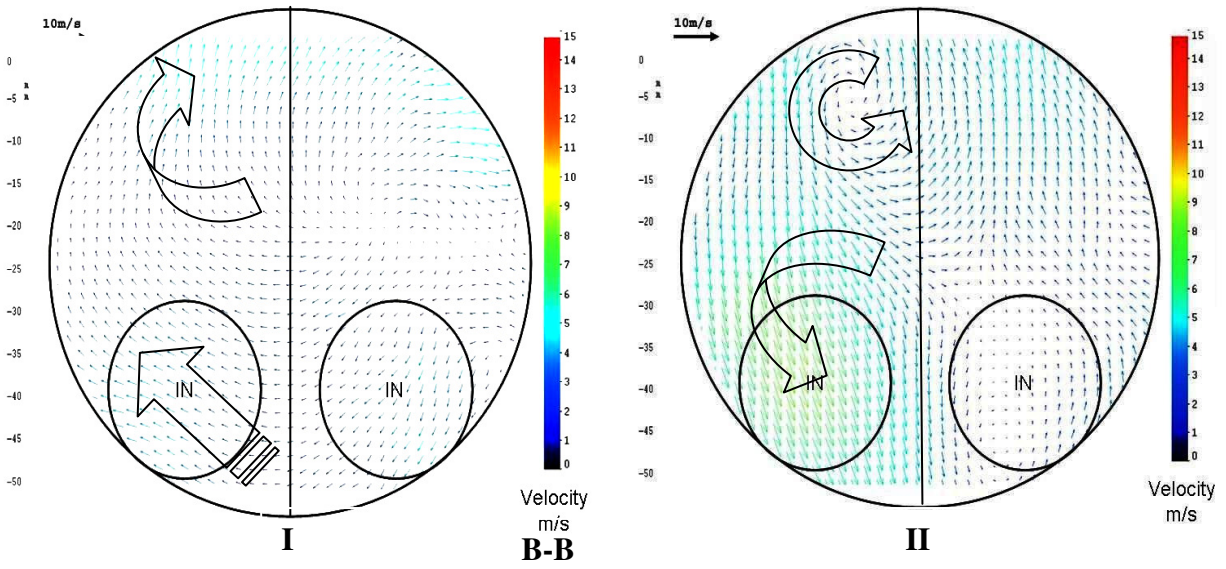

Figure 36: In-cylinder Velocity Vectors Obtained at the BOTTOM Horizontal B-B PIV Plane at 180 CAD (BDC). I-Tumble Port; II-Swirl Port

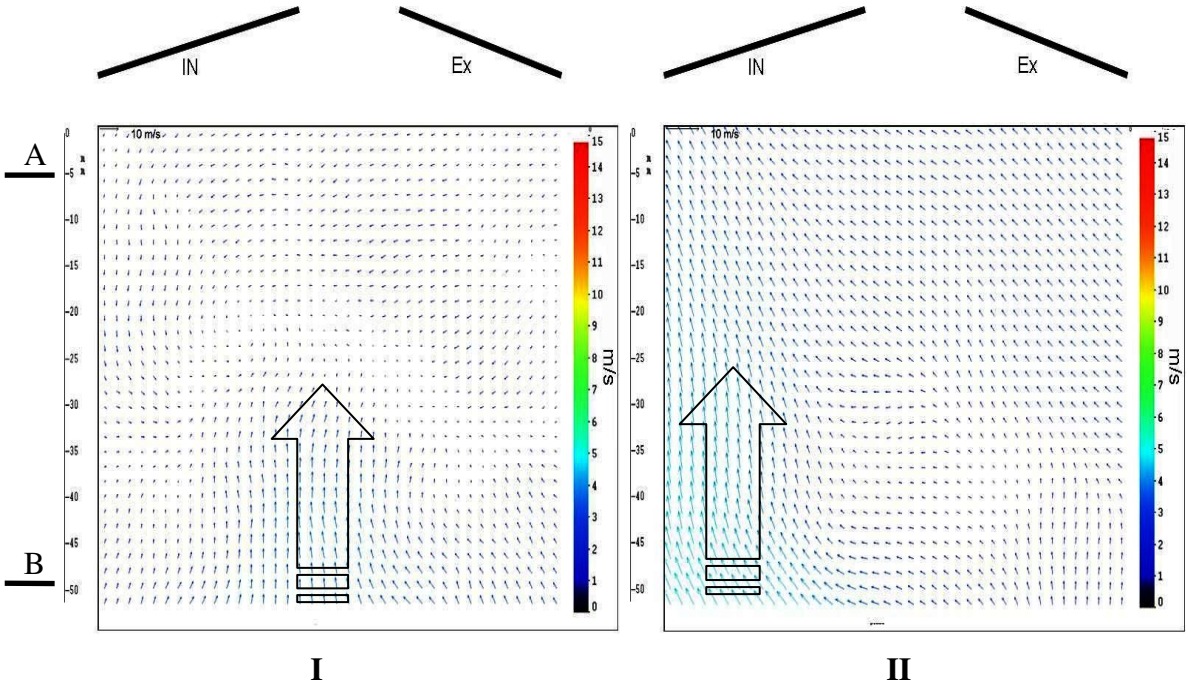

Figure 37: In-cylinder Velocity Vectors Obtained from the Vertical PIV Plane at 230 CAD. I-Tumble Port; II-Swirl Port

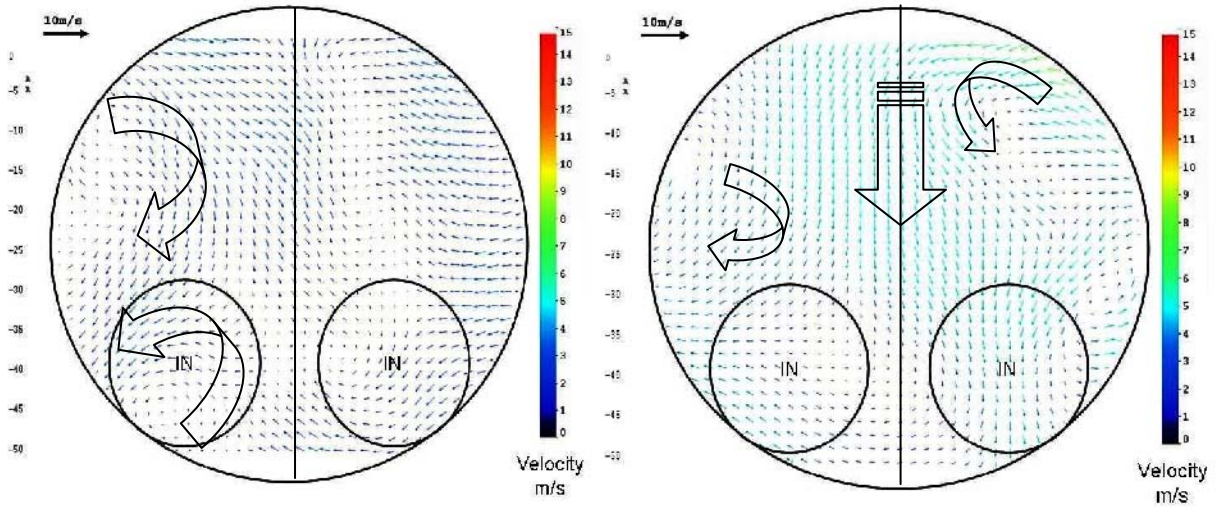

I A-A II

Figure 38: In-cylinder Velocity Vectors Obtained at the TOP Horizontal A-A PIV Plane at 230 CAD. I-Tumble Port; II-Swirl Port

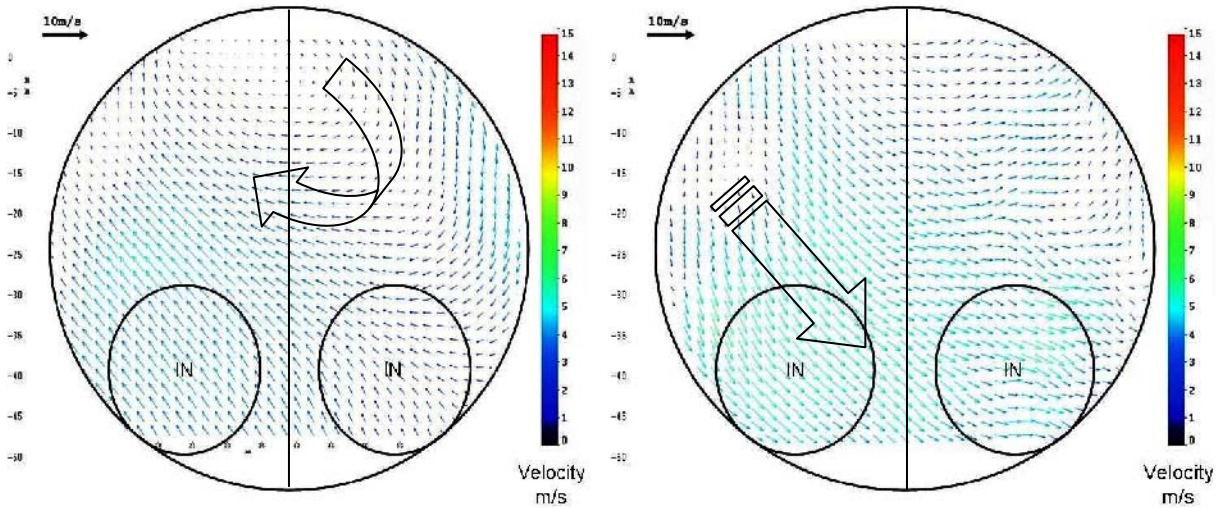

I B-B II

Figure 39: In-cylinder Velocity Vectors Obtained at the BOTTOM Horizontal B-B PIV Plane at 230 CAD. I-Tumble Port; II-Swirl Port

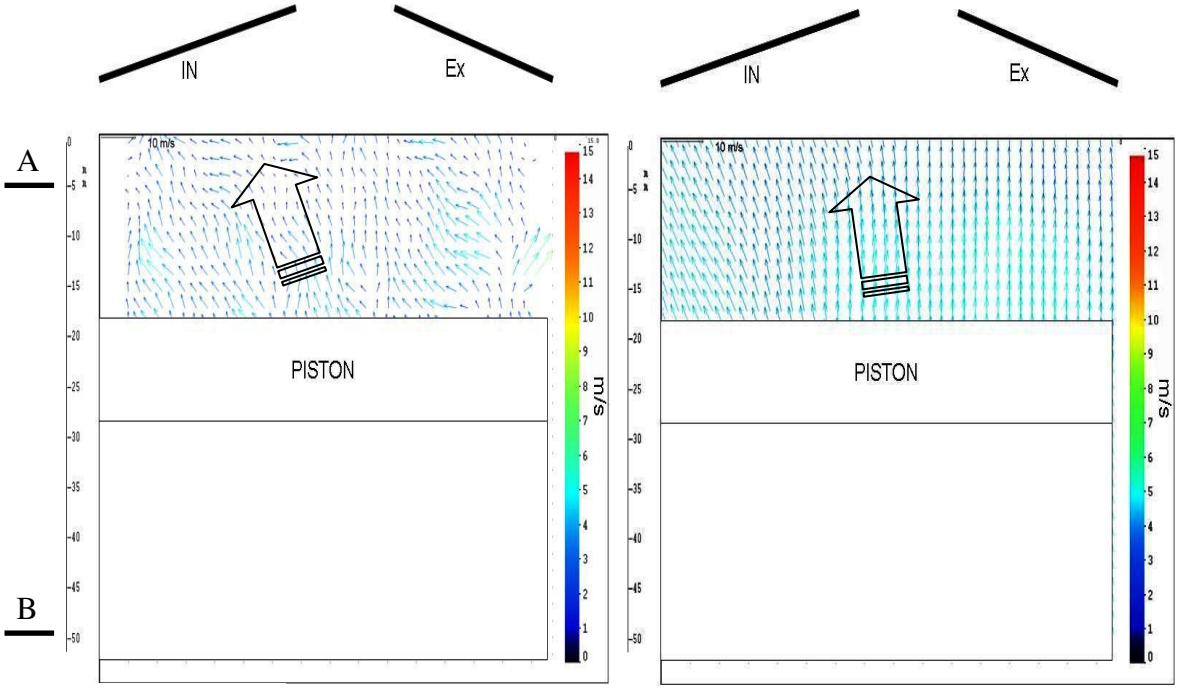

I II

Figure 40: In-cylinder Velocity Vectors Obtained from the Vertical PIV Plane at 300 CAD. I-Tumble Port; II-Swirl Port

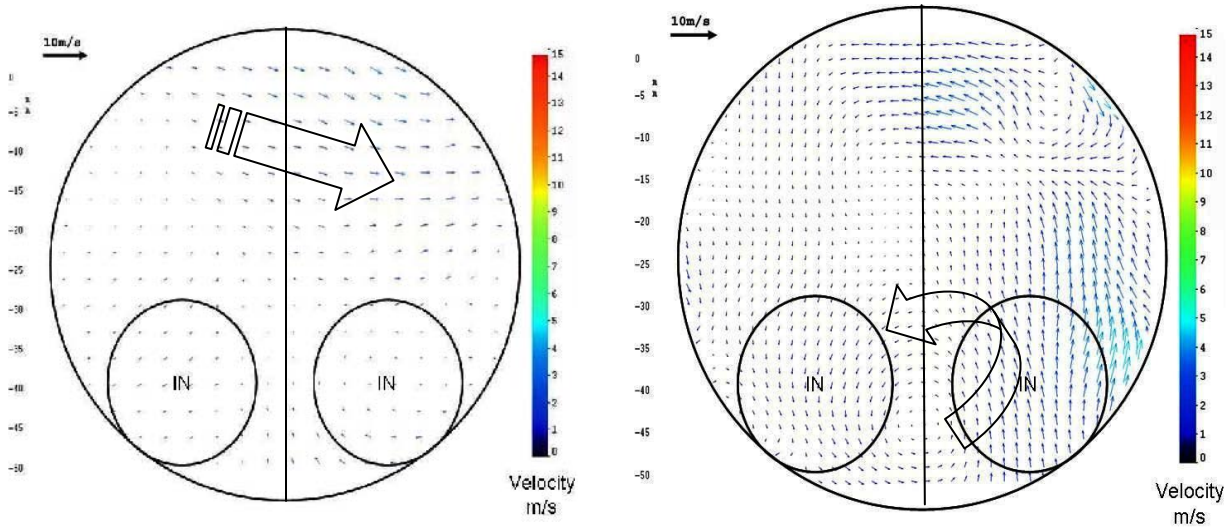

I A-A II

Figure 41: In-cylinder Velocity Vectors Obtained at the TOP Horizontal A-A PIV Plane at 300 CAD. I-Tumble Port; II-Swirl Port

THERMAL IN-HOMOGENITIES AND MIXING PROCESS PREDICTION AT 130 CAD.

The 'Tumble' case provides the maximum in-cylinder average Re number. It suggests that visible fluid flow such as the 'Jet-Wall', 'Jet-Jet' and 'Tumble-Jet' structures carry cold gas in the range 290° to 440° K in the initial induction stage [74]. For this temperature range, the intake gas has a lower kinematic viscosity compared to the hot (500-700K) air remaining in the cylinder from the previous cycle. Differences in the molecular viscosity between gases affect the transport process within the region of wall boundary layer as well as the rate of change of heat transfer through the cylinder wall. The molecular viscosity plays an important role, especially in the micro-scale region of the dissipation flow (Kolmogorov length-scale). Two different concepts, turbulent[9] and molecular viscosity govern the gas transport process and affect the in-cylinder thermal stratification as well as the general mixing process. In Figure 31 the regions of gas recirculation with the higher fluctuation velocity components are presented , which affected the better gas thermal mixing.

IN-CYLINDER HORIZONTAL VELOCITY VECTOR FIELD STRUCTURES AT 130 CAD

The Figure 32 I, II show the major features of the intake flow generated within the cylinder. The region of the high axial velocity beneath the inlet valves, presented on the vertical plane for 'Tumble' case I, is multiplied by the horizontal vector field pattern in the middle section, with the field divergence indicated by the dashed arrow in Figure 32 section I. Moreover, the suggestion that a substantial fraction of the flow travels towards the exhaust site in the cylinder head has been confirmed by two strong deflected jets on the engine's exhaust side, which are indicated by the contrary dashed arrow. When the planar laser sheet is located 10 mm beneath the surface of the cylinder head surface, a fraction of the in-cylinder bulk gases exhibit counter-clockwise flow compared to the pent-roof bulk mass. Partially, this

[9] Eddy Viscosity is not a function of fluid properties.

is due to the effect of separation flow under the valve head controlled by the adverse gradient of pressure.

The high-swirl inlet deflector case II demonstrated an upper in-cylinder flow pattern which exhibits a clockwise swirling flow with a central point near the cylinder's axis of rotation. The bottom cylinder plane of measurement indicates in Figure 33 the core of the cylinder swirl, displaced near the exhaust wall site. This effect is caused by the strong helical flow pattern generated by the intake (high-swirl) port deflector [73] as well as the geometry of the piston surface and combustion chamber. It is noteworthy that the results for the lower cross-section cylinder planes obtained at 65 mm below the cylinder-head surface and presented in Figure 33 I and II show deflected (Wall-Jet) fluid when the diverging jet is near the surface of the piston. This region of 'spreading' demonstrates a comparatively high velocity peak of 15m/s for the 'Tumble' case and appears extraordinary symmetrical, which is marked by a parabolic curve. Moreover, an earlier theory about the gas (Wall-Jet) stream for the 'Swirl' case has been confirmed by the convected jet structure near the surface of the piston directly attached to the exhaust side. Furthermore, for the 'Tumble' case there is a visible interaction and boundary between 'Wall-Jet' and 'Jet-Jet' streams and the large-scale tumble motion stretched across the surface of the piston. The new structure is deflected toward the cylinder wall perpendicular to the main flow streams and is indicated by a dashed arrow in Figure 33 I.

SHEAR FLOW AND ADVERSE PRESSURE AT 130 CAD aTDC: (HORIZONTAL PLANES OF PIV)

The engine inlet site beneath the intake valves is manifested for both events when there is a higher gas convection and a diffusion region represented by the swirling structures caused by shear stress and wall-cylinder interaction. In addition, the vast effect on the in-

cylinder flow pattern is due to the separation flow under the intake valves, which is driven by the effect of adverse pressure. The majority of the convected gas is visible as the jet stream affects the in-cylinder tumble structure, controlling the counter-clockwise swirl, and the dimension of the eddy. This is presented on the vertical plane for 130 CAD aTDC. Important questions about the development of in-cylinder thermal structures and the range of temperatures are open and will be further explored by using a CFD 3-D numerical approach.

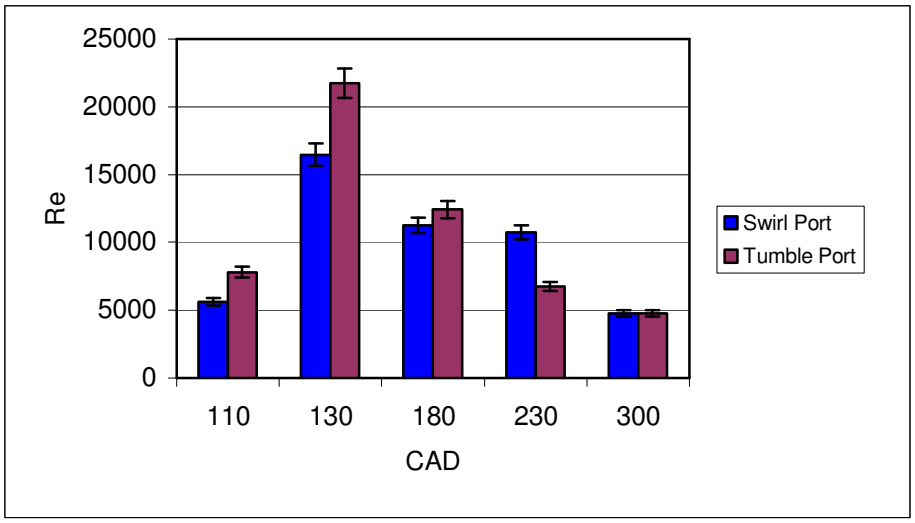

Figure 42: Cases 'Tumble' and 'Swirl' Ports-Average In-cylinder Re Numbers vs CAD.

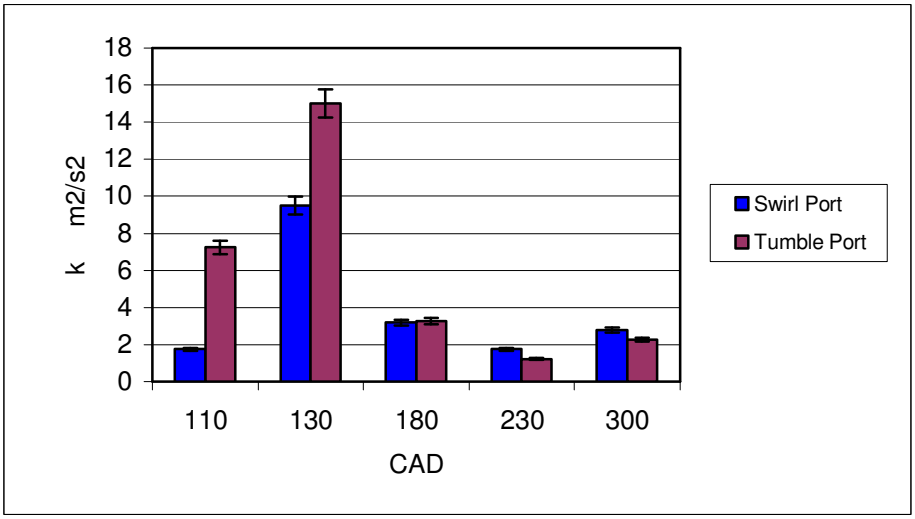

Figure 43: Cases 'Tumble' and 'Swirl' Ports-Average In-cylinder Turbulence Kinetics Energy Numbers vs CAD.

6.4 Case 3. In-Cylinder Flow Structure at BDC.

The above mentioned analyses with the two cross-section horizontal planes assess more detailed cylinder flow structures and are useful for the reconstruction of complex in-cylinder flow processes. The major drawback for the PIV technique is the lack of quantified information about the distribution of pressure and temperature fields in the cylinder. Therefore, the PIV experiments were coupled later on with a CFD computational study. For instance, the interaction of a free flow-wall boundary layer leads to an adverse axial pressure gradient during stroke commencement and might be manifested as a small vortex appearing on the corner of the cylinder head-wall. This can change the transport properties of a gas [16]. These phenomena show the importance of cylinder pressure distribution as the driving force for convection and diffusion gas processes.

An impression of the later evolution of the flow structure at BDC is presented, projecting on three laser sheet planes presented in Figure 34 to Figure 35 respectively. All the planes demonstrate a uniform structure for the velocity vector field for 'Tumble' case I, without the regions of the high gradient fluctuations. The low middle section of the engine cylinder reveals the remains of the counter-clockwise vortex (circulation arrow) structure. Regrettably, for reasons of inadequate optical access, these measurements did not include the region of the surface of the piston. Unlike the 'Tumble' case the 'Swirl' case is represented by the different sharper flow patterns Figure 34 case II with two opposite convected jets and the visible degradation of the tumble structure.

IN-CYLINDER GAS VELOCITY AND RMS OF VELOCITY FLUCTUATION AT 180 CAD aTDC

The series of Figure 44 to Figure 47 show charts of the ensemble-average and RMS in-cylinder gas velocity differences for the 'Tumble' and 'Swirl' port cases with three PIV

measure planes. The uniform BDC velocity vector field and the ensemble-average velocity quantification suggest that the kinetic energy carried by the tumble flow formation is intake mass flow rate dependent and decreases during this engine phase. A similar flow performance is predicted by the 1-D model for the 'Tumble' case in Figure 29 with no mass flow rate at BDC.

The decayed large-scale flow Figure 34 is discharged and dissipated into the lower length scales of turbulence [1] and leads to the eddy break-up of the middle section of the cylinder flow for both the 'Tumble' and 'Swirl' cases. The horizontal and bottom vector planes associated with the current CAD in the 'Tumble' case I show a similar flow pattern to that observed at 130 CAD aTDC but with a lower magnitude of velocity fluctuation shown in Figure **45**. Also noteworthy is the fact that both of the vortices presented under the inlet valves in Figure 35 persist until the BDC and the flow is driven by gas inertia.

Probably the most visible changes can be found in the flow field near the wall area beneath the inlet valves on the bottom measurement plane, where the strong inlet jet has vanished, due partially to the fact that the flow is less intense, when the piston is at the BDC position and the deflected flow is out of the scope.

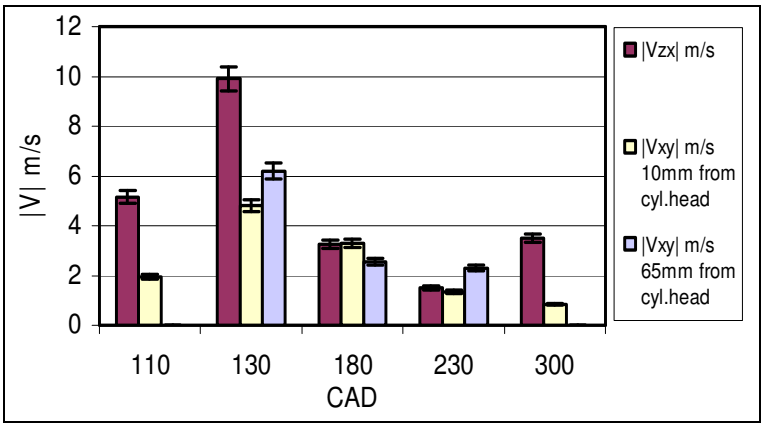

Figure 44: 'Tumble' case. Details of In-Cylinder ENSEMBLE-AVERAGE Velocity on PIV Vertical Vzx and Horizontal Vxy,z measurement planes.

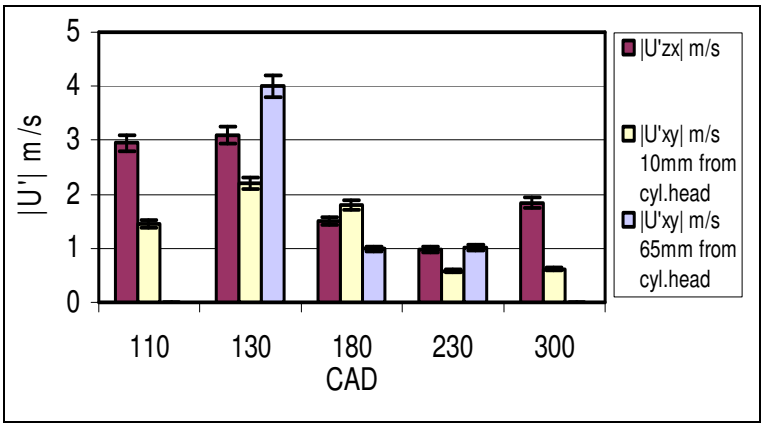

Figure 45: 'Tumble' case. Details of in-cylinder RMS of fluctuation velocity on the PIV Vertical Vzx and Horizontal Vxy,z measurement planes.

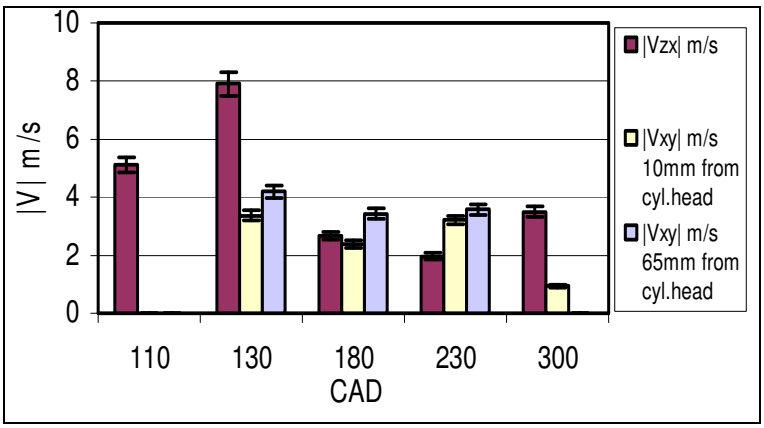

Figure 46:'SWIRL' case. Details of in-cylinder ENSEMBLE-AVERAGE Velocity on the PIV Vertical Vzx and Horizontal Vxy,z measurement planes.

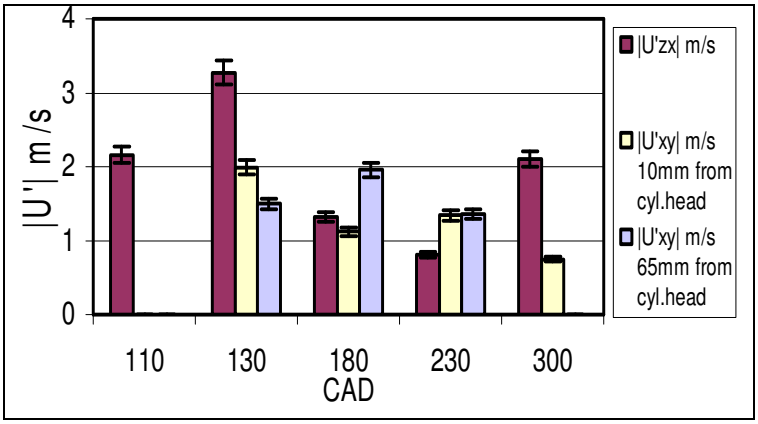

Figure 47: 'SWIRL' case. Details of in-cylinder RMS of fluctuation velocity on the PIV Vertical Vzx and Horizontal Vxy,z measurement planes.

The ‘Swirl’ case suggests that the intake mass flow rate decreases but the in-cylinder velocity field has an inherent moment of inertia due to the earlier strong induction flow through one of the intake ports. Additionally, information from the 1-D numerical simulation in Figure 29 suggests that for the ‘Swirl’ case, no back-flow occurred during the inlet valve closing phase and the flow was continuously moving inwards after BDC. The asymmetric flow coupled with the effects of piston movement produces a more in-homogeneous velocity vector field and is maintained during the later compression phase. Moreover, for the ‘Swirl’ event at the bottom vectors plane, the opposite rotation direction is encountered for the major structure in contrast to the 130 CAD case; this probably is the effect of the eddy break-up at the centre flow within the cylinder.

In Figure 34 as well as Figure 46 to Figure 47 sets of the in-cylinder average velocity measurements show the ‘Swirl’ case has a higher average velocity level and RMS than the ‘Tumble’ case does for the lower horizontal measurement plane. In addition, the higher RMS of velocity fluctuations enhances the mixing process for the bottom cylinder region. For the other PIV planes the ‘Swirl’ case demonstrates lower ensemble-average and velocity fluctuations. This suggests that the intake process is less ‘dynamic’ as was expected for this CAD, and that the flow is highly non-symmetrical.

6.5 Case 4. In-Cylinder Flow Structure at 230 CAD aTDC

At 230 CAD aTDC for both intake port configurations the cylinder ensemble-average velocity vector fields are strongly influenced by the piston movement and there is no additional inducted mass into the cylinder since the inlet valves are fully closed. The vertical planes of the flow field Figure 37 I, II indicate the absence of the characteristic large-scale structures of fluid motion. The engine compression phase degenerates the middle section of the in-cylinder flow along with the remains of the eddy structure and it convects the bulk of the mass towards the cylinder head for both analysed cases. The earlier in-cylinder tumbling

flow structure and the large-scale flow at this regime vanished and decayed into incoherent flow. The velocity fluctuation parameter in Figure 45 and Figure 47 show higher values for the 'Swirl' case, which suggests a greater potential for gas mixing.

The horizontal PIV bulk gas motion measurement obtained for both cases at the 230 CAD aTDC shows differences between patterns of the top and bottom in-cylinder velocity vectors, Figure 39. The direction and the shape of the velocity vector fields, with two characteristic vortices on the top plane for the 'Tumble' case, are conserved and similar to earlier measurements. The bottom measurement plane for 'Tumble' reveals the presence of a large asymmetric swirl (black arrow) that produces a similar average velocity magnitude to the previous CAD. For the current investigation, the gas stream flows into the exhaust site. The effect of the continually conserved in-cylinder gas movement is dependent on piston compression and angular momentum. The movement of the conserved gas within the tumble structure controls the form of the in-cylinder swirl pattern and supplies energy to maintain other gas movements.

The progression of the 'Tumble' flow field obtained at the lower horizontal cross-section plane reveals a piston shield effect as well as a homogeneous gas swirling structure within a single centre of rotation. The progression and the structure of flow development for both the horizontal planes of measurement, reveal that the ensemble-average velocity vector is uniform from 180 CAD to 230 CAD aTDC at the lower plane closer to the piston surface with a limited third axial velocity component (z-direction). The reason for the swirling movement after the inlet valves close is the conservation of angular momentum and piston action on the tumble structure that partially increases the angular velocity and acts through a gas shear stress on the swirling structures. Ultimately, it can be stated that the visible swirl structure in Figure 39 case I is driven by shear forces and the deflected effect of tumble from the front part of the combustion chamber hemisphere.

The ensemble-average velocity and the RMS of the 'Tumble' case shown in Figure 44 to Figure 45 reached the functional minimum of values; different the 'Swirl' case where the average-velocity is similar to the BDC event. Besides this, for case II it is apparent that 230 CAD aTDC has a higher fluctuation RMS and average velocity as well as a different in-cylinder fluid flow structure Figure 39. A large difference is encountered at the bottom plane where the flow is directed on the inlet side and some of the structure is convected near to the cylinder wall towards the cylinder head. From obtained flow details it is evident that the tumble and swirl intake ports an effective in control of in-cylinder flow pattern on the RMS of velocity fluctuation level. As was stated earlier, and base on the RMS of velocity factors the swirl case at these cylinder flow conditions shows better gas mixing potential.

6.6 Case 5. In-Cylinder Flow Structure at 300 CAD aTDC

The internal flow at 300 CAD aTDC exhibits uniform bulk cylinder motion on the vertical measurement plane; and no large-scale flow structures are visible for cases I and II, Figure 40. For both mentioned cases, most of the in-cylinder bulk gas movement is sloped towards the inlet valve area. The region of the intake cylinder head chamber acts on the major flow field by deflecting it, by reorganising into the tumble flow, and by redirecting it towards the exhaust site. Unfortunately, the cylinder head has limited optical access due to the problem of MIE scattering light, and therefore, this interesting region is out of visible scope.

At Figure 41 for the 'Tumble' case, it is apparent that only a limited region of the exhaust engine site displays clockwise gas movement which is similar to the rotated swirl structure obtained for 230 CAD aTDC at this PIV plane. One of the effects responsible for this exhaust gas circulation structure is the deflected cylinder chamber geometry which imposes tumble flow on the exhaust site which was mentioned earlier. An inspection of the

other cylinder regions suggests that the flow in the inlet part of the cylinder chamber is uniform and quasi one dimensional with a major Z velocity component. This is confirmed by the vertical plane of measurement. Similar flow features are recognised for the 'Swirl' case.

IN-CYLINDER ENSEMBLE-AVERAGE AND RMS OF FLOW AT 300 CAD aTDC.

Both port intake configurations affect the late in-cylinder gas compression phase as indicated by the RMS of velocity fluctuation and the average velocity for bulk gas at 300 CAD aTDC. However, different outcomes are obtained for the horizontal planes of measurement where the RMS and average velocities for the 'SWIRL' case decrease, gradually reaching minimum values Figure 47. The 'Tumble' case displays a similar level for the RMS to the previous CAD.

The velocity vector data for the current CAD presents the effect of piston compression on the tumble gas structure i.e.: that it increases the angular velocity. The same effect is believed to keep the swirl velocity fluctuation at a comparable level to that obtained for 230 CAD aTDC. Also, the obtained data suggests that the swirling movement and the RMS of velocity fluctuation are damped by increases in gas viscosity and by friction losses; hence the fluid within the cylinder has a high temperature and a high kinematic viscosity.

The PIV flow data at this engine phase shows an amplified in-cylinder tumble structure by the piston and cylinder head geometry for both engine cases, which inherently enhances the gas mixing process. Surprisingly, higher RMS of fluctuation and ensemble-average velocity at the vertical plane is obtained for the 'Swirl' case. This can be explained by the late mass induction process during the inlet valve closure. The situation for the swirl flow structure is altered for both cases where the average velocity and RMS of fluctuation are not actively inducted by the geometry of the piston and the cylinder chamber volume. However, for the high squish area at the end of the compression stroke it is possible to amplify the

tangential in-cylinder velocity and generate an additional swirl flow structure [73]. Unfortunately, 300 CAD aTDC is the last appropriate optical measuring position without a large amount of MIE scattering noise (due to light reflections and the oil wall deformation effect).

6.7 In-cylinder Gas Turbulence Intensity and The Mixing Process for Symmetric NVO at 1000 RPM

The in-cylinder mixing process is mainly controlled by the large convection flow structures such as the high velocity gradients and turbulence length-scales [73]. Therefore, the turbulence gas intensity parameter is appropriate to describe the mixing effect due to the convection and the RMS of fluid. For the turbulence intensity analysis, the mean piston speed has been related as the average velocity component in the Equation (34).

$$Ti = \frac{u'}{|V|} \tag{34}$$

The exchange gas momentum maintains the in-cylinder large-scale flow structures through the eddy-viscosity mechanism which is induced by the shear flow and turbulence. Moreover, the reciprocating character of the in-cylinder volume changes the internal flow pattern and imposes an additional turbulence gas effect. The swirl and tumble flow structures are developed at the early intake phase and persist to the end of the compression stage, whereas the tumble flow is affected a lot more by the piston and by cylinder volume changes as well as by the conservation of gas angular momentum phenomena [77]. In Figure 48 the in-cylinder average turbulence intensity parameter is calculated from Equation (34) based on the velocity vectors field and is used to evaluate the gas mixing process within the cylinder. As was stated earlier, the ‘Swirl’ port case extends the mass induction stage after the BDC and imposes a stronger in-cylinder turbulence intensity at the end of the compression phase.

Besides this, the high swirl port indicates higher flow losses and a higher Mach index due to utilisation of the single intake port.

The various effects of gas dynamics occur at the BDC of the 'Tumble' port case, where the back flow process to the inlet manifold has been generated. This process inherently decreases the gas kinetic energy of the internal flow at the late induction phase (during the intake valves closure). During engine compression, large flow patterns like swirls are continuously decaying, however the tumble structure is maintained by the conservation of angular momentum and the effect of the central cylinder vortex distortion.

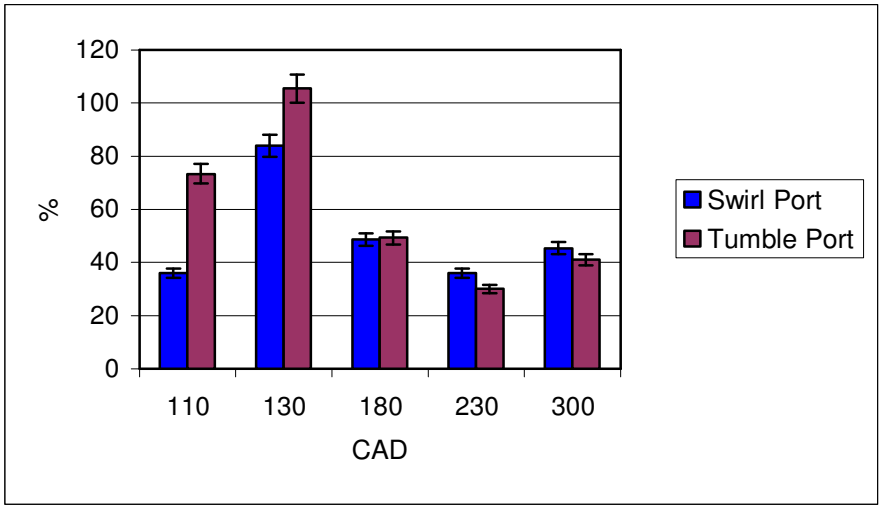

Figure 48: In-cylinder Turbulence Intensity for Tumble and Swirl Intake Ports

When considering the timeline of the in-cylinder turbulence intensity shown in Figure 48 with both intake port configurations it is clear that a stronger turbulence intensity has been achieved for the low swirl port configuration at (55-180) CAD aTDC. Moreover, the analysed turbulence intensity for the 'Tumble' when compared with the 'Swirl' case suggests that the general in-cylinder gas mixing process at the early induction phase is more complete for the low-swirl port configuration which inherently enhances the fuel-gas mixing process, residual-fresh gas mixing process and the thermal homogeneity. Another conclusion has been obtained

from the engine compression phase where the in-cylinder mixing process is more intense for the high swirl port configuration.

6.8 In-cylinder Swirl and Tumble Gas Effects for Different Intake Port Configurations for a Symmetric NVO

In-cylinder bulk fluid motion is often characterised as the ensemble-averaged Tumble and Swirl cylinder ratios calculated from Equation (35), which are utilised as common engineering parameters for an engine gas combustion-flow analysis [78]. These parameters, together with the in-cylinder mean kinetic energy and the turbulence intensity, could be used to evaluate the temporal gas mixing process [73]. Figure 49 to Figure 50 show the temporal development of the tumble and swirl ratio for the motion of the in-cylinder bulk gas. For simplification, the complex in-cylinder flow analysis is divided into three main stages in order to identify the certain features of the bulk gas motion according to the PIV spatial in-cylinder flow investigation.

$$SR, TRx, TRy = \frac{\sum_{i=1}^{n} (m\vec{r} x \vec{v})}{\omega \sum_{i=1}^{n} (m\vec{r} \cdot \vec{r})} \quad \textbf{(35)}$$

Stage 1: The Decayed Phase of the In-Cylinder Flow-Vortex

The decayed phase of the cylinder vortex is maintained during the IVO to the BDC crank angle piston position. Both of the intake ports at 110 CAD aTDC produce the highest tumble ratio, especially for the tumble port deflector. As was stated before, the beginning of the in-cylinder inward flow is visible with apparent high velocity gradients and strong wall-jets, particularly for the tumble-port case. Besides, the tumble-port generates a higher in-cylinder tumble ratio which is then maintained by the formation at two opposing vortices,

Figure 31 I, which vary substantially during the change, of in-cylinder volume and lead to the altered sign of the tumble ratio close to the BDC. The tumble port is more effective for this phase for the sake of late engine compression and the conservation of gas angular momentum. This means that the axial valve flow is driving this structure more effectively than the large tumble-jet in the exhaust site. There are different results for the swirl-port case where the intake gas stream is directed into the exhaust site and gradually supplies a clockwise vortex, becoming more pronounced after the 130 CAD aTDC and changing the sign of the tumble ratio in Figure 49. For both port geometries the induction gas stage within the cylinder is characterised as two tumble ratio sub-phases with the sign change.

The swirl ratio in Figure 50 indicates that the swirl-port case has a larger magnitude of in-cylinder tangential flow at the beginning of the gas induction and changes sign close to the IVC. The tumble-port case has a much lower magnitude of swirl ratio, however, it has an effect on the swirl ratio at 160 CAD aTDC similar to the Tumble case. In addition, the swirl ratio calculated for both port configurations is dependent on the intake gas dynamics and back-flow process, which was earlier calculated by the 1-D simulation.

Stage 2: In-Cylinder Flow Stabilization Phase

The vortex stabilisation phase as shown in Figure 49 exists between the BDC and the intake valve closure. The tumble ratio for both ports has a characteristic point of suppression at 180 CAD which is the maximum value of the negative tumble ratio. For the swirl port case, it is apparent that the in-cylinder gas tumble structure is driven more effectively by the extended intake jet and the valve curtain area. After BDC the tumble motion developed by the intake valve jet on the exhaust site decays and the negative tumble ratio is restricted by the upward movement of the piston. At 230 CAD for the tumble port, the piston affects the internal flow structure; and the centre of the positive intake site vortex which is trans-located

onto the middle of the cylinder interacts with the tumble-jet. Due to the lack of inlet mass flow, the large structure of the tumble-jet becomes unstable and is dissipated, Figure 37 I.

The swirl ratio for both port geometries varies significantly, where the tumble port configuration as well as the back-flow effect changes the sign of the swirl ratio after BDC. The gas mixing process encountered during the tumbling flow is more complex rather than the swirling movement which generally is used for mixture stratification [74]. However, both generated swirling and tumbling structures which can significantly improve mass transport across the cylinder. Moreover, it is interesting that for the swirl-port the negative swirl ratio decreases, gradually reaching 0 at IVC event and a positive sign for the further development of in-cylinder flow. Also, the swirl ratio in Figure 50 seems to be well maintained by the continuous flow from the intake port after BDC. For both port configurations, the valve timing and gas dynamics process control the in-cylinder large-scale structures at this stage.

Stage 3: Flow-Vortex Compression (spin up) Phase

After the intake valve closure the in-cylinder flow pattern is controlled by motion of the piston-bulk gas motion. The tumble-port configuration in Figure 49 indicates that the piston movement and the gas angular momentum amplify the tumble ratio. A different situation for the in-cylinder flow is visible for the swirl-port, where a strong negative tumble-ratio previously driven by the late inlet induction phase is now decaying with a retained negative sign. In Figure 50, the late swirl-ratio for both cases achieve similar magnitudes however, with opposite signs. The obtained results for both port arrangements show the influence on the in-cylinder large-scale gas structure and the difference in the effect of the gas mixing process near the TDC.

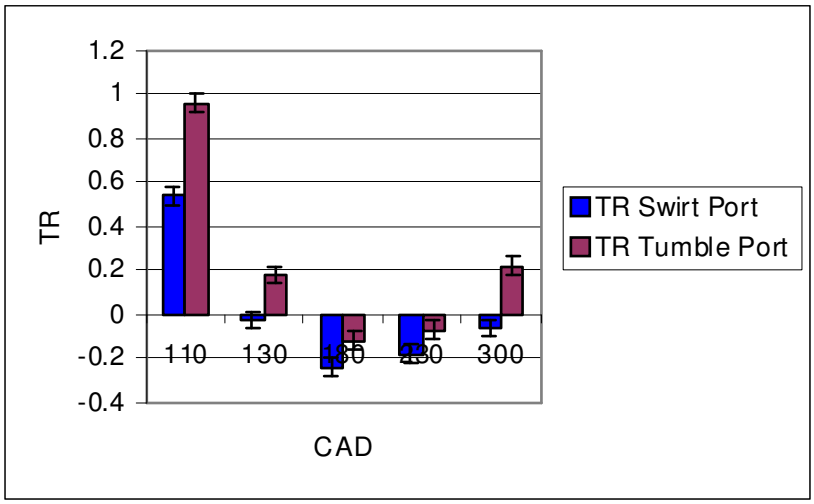

Figure 49: In-Cylinder Tumble Ratio (TR) at Both Intake Port Configurations

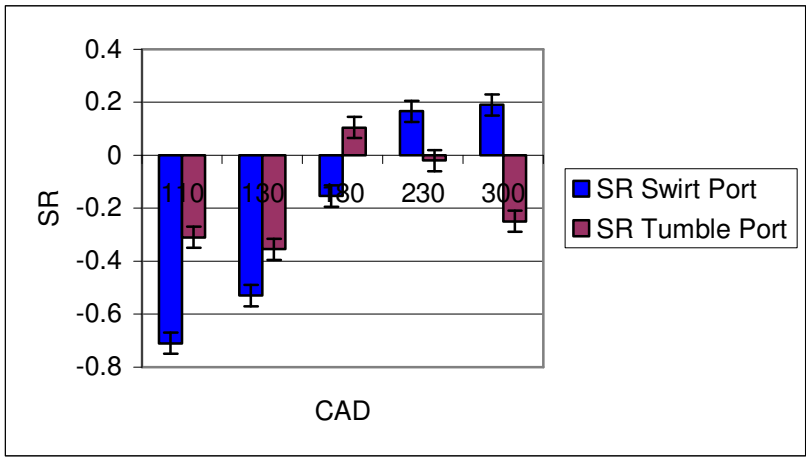

Figure 50: In-Cylinder Swirl Ratio (SR) at Both Intake Port Configurations

6.9 Discussion and Summary

DISCUSSION

One of the biggest drawbacks of the HCCI combustion technology is insufficient control of the spatial and temporal beginning of the auto-ignition process, driven by non-uniform thermo-reactive flow as well as the gas turbulence-mixing effect. Unfortunately, the Ford/Jaguar single cylinder optical engine was not designed to run in the combustion-PIV mode; therefore, the complex-flow analysis is done based on the development of the in-cylinder 'COLD' flow structure. As far as major large-flow structures exist at both engine

conditions it seems that the 'COLD' flow and sensitive case studies can be crudely evaluated due to valve pressure differences and similar manifold gas dynamics processes. Besides, varied flow structures e.g.vortices, and gas jets show major mechanisms of the in-cylinder mass transport and mixing process due to gas convection and turbulence effects. These are the most important mechanisms in order to estimate the in-cylinder gas structures and the field of in-homogeneities. Additional information obtained from the internal 'COLD' flow analysis is useful for development of a fuel injection strategy and injection timing the particular engine conditions, e.g. stratification or homogeneous charge mode.

The modified geometry of the intake ports strongly modulates the pattern of the cylinder flow and the turbulence intensity during the induction and compression phase; and it is believed that it inherently affects thermal gas mixing. The major in-cylinder gas mixing parameters are represented by the time average in-cylinder turbulence intensity and the RMS of velocity fluctuation, which was obtained from the series of the PIV results. Moreover, RMS could be used in parallel with the CFD investigations to give a crude approximation of higher gas cylinder temperature regions. Hence, two-gas structures (hot and cold gases) under a well-defined region of high RMS are better mixed and colder. Therefore, the cylinder region of the highest in-cylinder turbulence intensity as well as of the highest spatial velocity could be used to evaluate general in-cylinder gas thermal stratification. Surprisingly, for the HCCI combustion concept higher thermal in-homogeneities should give for possibility to some level of control over and prediction of the in-cylinder spatial and temporal beginning of auto-ignition within the reactive case. This is the reason why the cylinder history of the gas turbulence prior to the HCCI auto-ignition and combustion phenomena cylinder history is important.

SUMMARY

Two different port geometries have been applied to the HCCI single cylinder optical engine at a symmetrical 110 CAD Negative Valve Overlap (NVO) in order to measure their effects on complex internal flow structures, and to evaluate the level of the in-cylinder mass transport process. The in-cylinder mass distribution and gas convection have been characterised by the temporal and spatial sequences of the PIV cross-correlated velocity vectors obtained at the vertical and horizontal in-cylinder laser planes. The 2-D velocity vectors of the horizontal and vertical planes are characterised by the following crank angle sequences: (130, 180, 220, 300) CAD aTDC.

The examined in-cylinder velocity field shows that the intake jet for both types of intake port deflectors strongly affects the structure of the in-cylinder bulk gas during the intake and compression phase and imposes a great impact on the global gas mixing process. The PIV results with the visible large-scale flow patterns clarify the statement that for auto-ignition control, the region of a poor cylinder gas mixing process is probably the most interesting for the case of the development of the auto-ignition process, due to the larger temperature gradient. In other words, the region of the cylinder with a low gas temporal RMS of velocity fluctuation 'higher temperature of residual gases' should be considered preferable for beginning of auto-ignition. Some evaluations can by deduced based on the PIV data and the in-cylinder turbulence intensity parameter. The swirl-port case promotes lower in-cylinder average turbulence intensity as well as an in-cylinder ensemble-average RMS of velocity fluctuation during the induction process. For this phase, it seems that the port-swirl delivers the worst in-cylinder mixing process in order to achieve thermal homogeneity, especially for mass transport in the bottom of the cylinder. Additionally, the lower mass flow rate obtained for this case induces less of a mass of cold gas at this phase.

An open question is ‘How can 2-D PIV velocity vectors be used to evaluate real 3-D spatial in-cylinder flow and the global thermal gas mixing process ?’. Therefore, an additional CFD modelling has been further applied. Additionally, for the optical diagnostics study the phenomenological ‘Flow Analysis Tools’ have been developed to characterise the large in-cylinder flow structures, i.e. (Jet-Jet) interaction, (Jet-Wall) interaction, (Jet-Bulk) interaction. In the case of the ‘Flow Analysis Tools’, other important parameters were used, i.e. the average turbulence intensity, the RMS of the gas velocity fluctuation, the Tumble Ratio (TR) and the Swirl Ratio (SR). The data for the ensemble-averaged velocity vectors was analysed in order to examine the bulk flow behaviours and reduce the effect of cycle-to-cycle variation in flow. Therefore, the experimental data is suitable but for the further validation of the CFD RANS (Reynolds Average Navier-Stokes) model and can not be compared with the LES solver form results.

Chapter 7

SINGLE CYLINDER CFD MODEL: VALIDATION AND TEST CASES

7.1 Introduction

Optical experimental methods are crucial for the analysis of complex in-cylinder flow patterns and for the examination of turbulence phenomena. The measured velocity vector field shows the future of cylinder engine design and effectively indicates the internal gas mixing process. The significant drawback of optical methods like the Particle Image Velocimetry (PIV) method lies in the lack of scalar cylinder flow information i.e. pressure, temperature, and gas composition. As was stated previously, in a HCCI engine thermal and mixture fields actively influence the combustion process and emissions. For this reason, scalar fields must be evaluated by using a validated CFD model coupled with the experimental velocity vector fields. The current chapter presents the consecutive steps for building a computative engine and for the validation and solver set-up. The CFD numerical engine model has shown good velocity vector field agreement with the obtained experimental PIV results. In addition, similar large-scale flow patterns for spatial and temporal cylinder positions have been obtained.

7.2 CAD geometry and Computational Domain

The design of the single cylinder optical engine CFD model is divided into three main building phases. The created CAD engine model shown in Figure 51, is exported as the Standard for the Exchange of Product Model Data (STEP) format to the GAMBIT postprocessor; and volume discretisation is applied. The next step is to import the engine

mesh file into the CFD FLUENT™ code and set-up the initial boundary conditions for the chosen appropriate physical models.

The engine geometry used for the CFD work was developed by the author and is based on the measured Ford/Jaguar single cylinder engine dimensions. Moreover, the created geometry includes four valve ports with the valves and the groups of intake and exhaust manifolds. The cylinder head geometry is a pentroof type with a 14˚ roof slope, 33mm and 29mm diameters for intake and exhaust valve heads respectively. In addition, the poppet valve geometries are created in the early open position so that the TDC piston enrol into the best procedure for further grid creation. The created mesh is hanged at the TDC piston position for a better spatial distribution and quality of applied finite volumes.

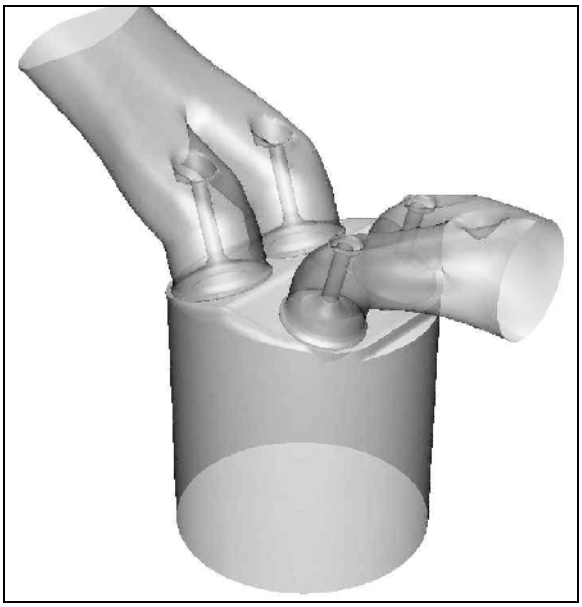

Figure 51: The CAD Model of the Single Cylinder Ford/Jaguar Optical Engine.

The small engine geometry modifications are made in the valve seat regions and the top cylinder head in order to lessen the grid complexity of the model. The main limitation of the engine geometry-mesh is in the engine regions between the volume of the valve seat and the cylinder chamber. Detailed information about the grid limitations will be presented in section 7.4.

Both the experimental and the modelled engine piston were flat type. The engine CAD geometry also includes the following features: a centrally mounted direct injector geometry and the spark plug.

7.3 Dynamic Mesh Functions

The single cylinder optical engine model consists of a couple specific zones where the applied mesh structure is featured as the deformable and fully removable. The Fluent code offers embedded mesh functions during the in-cylinder moving and deforming of boundaries and updating of every computational step. The cylinder regions associated with the moving and deforming of meshes include the following functions: *local remeshing, dynamic layering* and *spring smoothing* [79]:

- The Local Re-meshing (Figure 52) function offers a series of the criteria, which must satisfy the size and the cell skewness of every computational time step. If one of the following criteria is not met, the code activates the remeshing function which locally changes the grid structure to the one that is valid for that particular time [80]. This function is only executed for triangular and tetrahedral cell types.
- The Dynamic Layering (Figure 52) function is used to add and remove layers of cells adjacent to a moving boundary. It utilises as criterion the height (h) of the layer adjacent to the moving surface. With Fluent, the code user can choose to split or merge the height parameters. This function is only executed for the hexahedral or wedge cell types.
- The Spring Smoothing (Figure 52) function offers limited displacement of nodes without removing them, and it remeshes them into the domain. This function is based on the equilibrium state of the mesh at the initial spacing before any boundary motion is generated. Any movement of nodes is proportional to the force acting on the edges between any two-mesh nodes which are idealised as a network of interconnected spring. The displacement of the nodes is calculated from Hook's law Equation (36).

$$\vec{F}_i = \sum_j^{ni} k_{ij}\left(\Delta\vec{x}_j - \Delta\vec{x}_i\right) \quad \textbf{(36)}$$

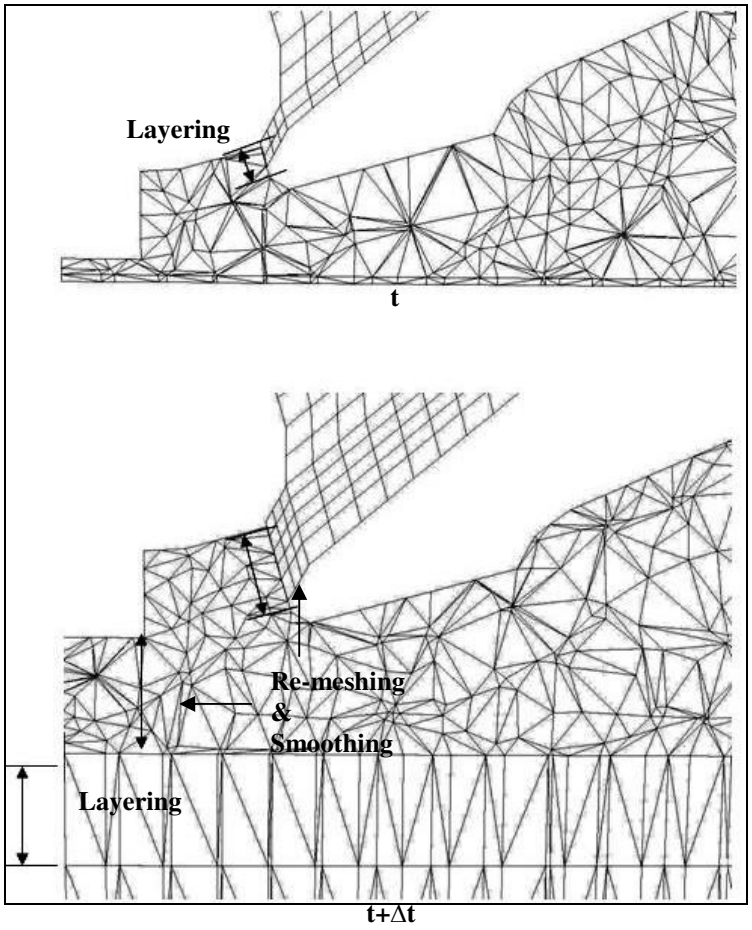

Figure 52: Three Grid Functions used for the Moving Boundaries at t and t+Δt

7.4 Single Cylinder Engine: Grid Generation and Dynamics Mesh Regions

The modelled single cylinder engine mesh is presented in Figure 53 I, II at both the BDC and TDC piston positions respectively. For the chosen mesh types, a special attention was paid to the valve ports and the cylinder head areas. This particular cylinder head and valve port region is presented in Figure 52 for the computational time (t). Both mesh structures are built on two different grid elements which are hexahedron and tetrahedron, respectively for a dynamic mesh strategy. Both engine volumes are coupled with a standard Fluent interface function which performs flow within the mentioned engine region. It must be noted that the interface function and the CFD output generated by it are highly sensitive to the

grid quality, e.g. cell skew-ness, and cell ratio [79]. Moreover, the most error prone case is encountered during the IVO phase and with an early transonic flow condition as shown in Figure 25. In general, the low mesh quality for this flow condition produces the over-predicted effect of turbulence gas viscosity due to the increase in numerical diffusion and the function of analytical boundary layer wall [80]. Therefore the geometry of the valve seats and the grid structure must hang on a detailed and computational hexahedral element of better quality [80].

During the engine mesh design process, all physical aspects of the flow must be considered in case potential numerical errors develop, e.g. Mach number vs Turbulence Models, TKE vs Turbulence Models. From this point of view because of this the grid is tested via 2D and 3D cases for less complex geometric structures with the varied flow conditions. All the validated CFD test cases were developed by Fluent™ and supplied as CFD models representing various physical flow effects. The most important information obtained from the Fluent validated test cases was used during the creation stage of the single cylinder optical engine mesh. More information about discretisation effects on the CFD out-comings resolution can be found in [79, 81].

The optical engine mesh is built on two types of elements in order to obtain the best computational quality for the mesh dynamics of less complexity, e.g. a faster convergence with a lower numerical diffusion. The dynamic mesh requirements mentioned in section 7.3 are presented as the expanded view of the decomposed geometry of the engine model in Figure 54. Moreover, the composition of the engine regions and the type of elements used to create the mesh volume as well as the quality index are described below.

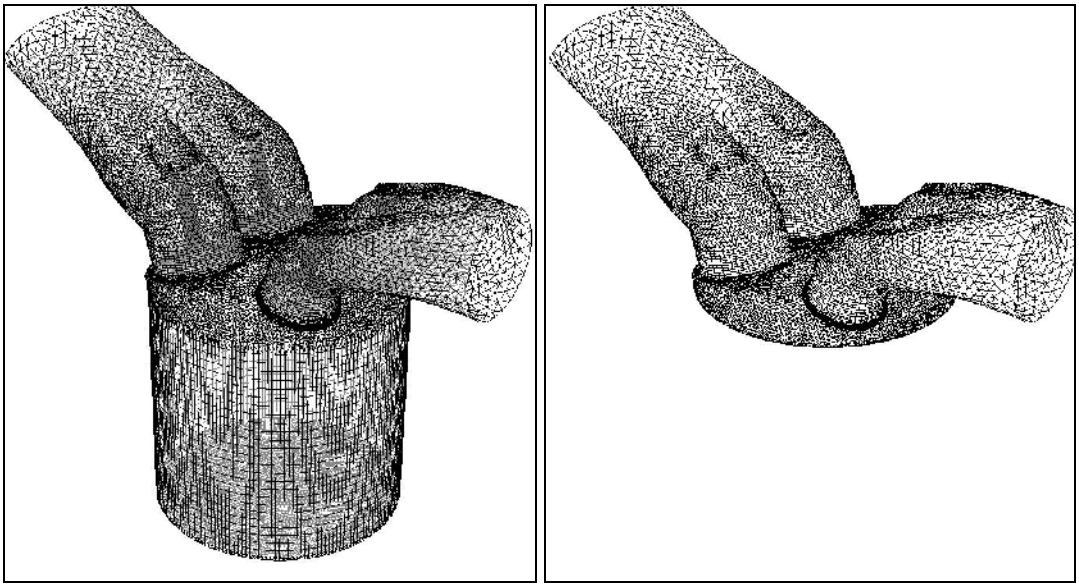

I II

Figure 53: The Single Cylinder Mesh Model and Geometry Composition: I) BDC , II) TDC

- The cylinder head volume features the deformable and removable fluid regions which are influenced by the valves moving towards the piston surface. In accordance with the definitions of the dynamic mesh functions, the tetrahedron element type has been used for the creation of the top of the cylinder head volume. The calculated average of the cell index quality for this geometry is 0.65.
- The four valve ports are built on a wedge element type; and a dynamic layering mesh function is applied. The calculated average of the cell index quality for this geometry is 0.45.
- The cylinder volume hangs on the wedge/prisms element type; and a layering mesh function is applied to the moving boundaries. The calculated average of the cell index quality for this geometry is 0.43.
- The tetrahedron element type has been used for the static engine manifolds for the complexity of the geometric structure. The average of the cell index quality for this geometry is 0.78.

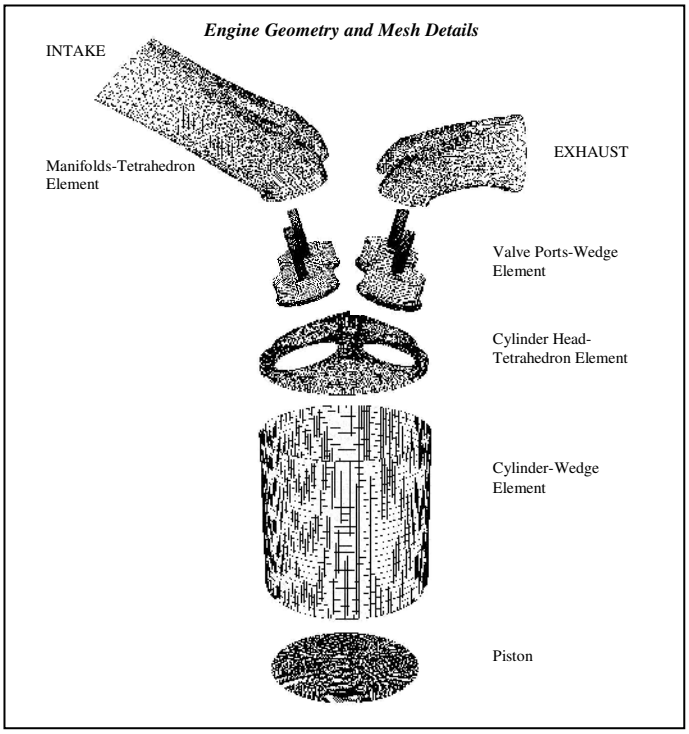

Figure 54: Exploded Mesh Geometry and View of the In-Cylinder Different Zones

7.5 Cfd Solver Settings

The CFD solver set-up is preceded by a reading of the engine mesh file from GAMBIT in the FLUENT code structure as shown in Table 3. The mesh structure is automatically examined throughout the input process by the CFD code and any errors are reported. The next stage is the engine model-scaling process which has been arranged in SI units. The valve and intake pressure profiles obtained from the 1-D simulation are imported as tabularised data. The boundary conditions for all the engine zones have been applied, including the cylinder head and the wall temperature as well as the pressure in the inlet and outlet engine regions. The intake pressure boundary condition is applied throughout the User-Define-Function (UDF), which tracks the pressure profile. This approach provides the possibility of simulating more realistically the effects of intake gas dynamics and it has influence on the engine mass flow rate. The 3-D engine base model has been built with shorter intake canals in order to avoid extensive computational effort. The boundary conditions assigned to the current CFD model are listed in Table 4 A.

ENGINE MESH	GRID	MODELS		SUB-MODELS	SOLVER CONTR.	
Read-Model.msh	SCALE	SOLVER	UNSTEADY		EQUATIONS	MASS
			ENERGY			MOMENTUM
			VISCOUS	k-e Realizable		ENERGY
			Wall-Function	SWF	INITIALIZE	RUN SOLVER
		MATERIAL	AIR	IDEAl GAS		
		GRID	DYNAMICS	MOVING		
		B. COND	WALL			
			TEMP.			
			PRESS.			

Table 3: General CFD Code Set-up Model Structure.

The general moving and deforming mesh functions are managed by the dynamic grid panel. Then the deforming mesh quality is examined for all engine events by the special mesh kinematic function executed for a series of engine cycles. The parameters of the in-cylinder engine simulation are presented in Table 4 section A, B.

SECTION A	
Intake/Exhaust pressure	profile/1e5 Pa
Intake/Exhaust temperature	300K
Inlet turbulence intensity	5% of mean flow
valve events	profile
walls&piston	345K
SECTION B	
Crank Engine Speed	1000RPM
Crank Angle Step Size	0.5 CA
Piston Stroke	0.09 m

Table 4: The Boundary Conditions and In-cylinder Simulation Parameters Section A, B respectively

The internal cylinder flow is assumed to be fully turbulent; and for this type of flow one of the turbulence CFD models is chosen. The most common and widely used for any turbulent flow analysis is the k-ε '*Realizable*' model with the additional wall functions [79]. Therefore, the CFD simulation of the current engine model is based on the k-ε '*Realizable*' model of turbulence with a chosen Standard Wall Function (SWF) for boundary layer prediction. Additionally, it must be noted that an engine mesh with a calculation of $y^{+} \geq 30$ [10]

[10] Based on log-law of the wall. A wall-function simulation normally requires that y plus of the first cell outside the walls is in the log-layer, which starts at about y plus 20 and, depending on the Re number, extends up to say y plus 200. In the log layer, there is equilibrium between production and dissipation of the turbulent kinetic energy, therefore decreasing turbulent instability in near-wall simulations in Ref. to 'CFD-Online'

for the first cell of the log law is not appropriate for a more sophisticated two layer Enhancement Wall Treatment (EWT) function [79].

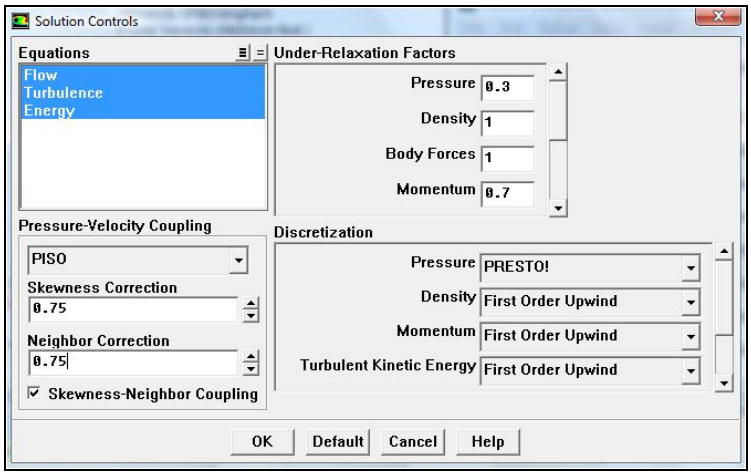

Table 5: Solution Control Panel

The last step prior to running the code is the define the solver control limitations. In Table 5 the 'Solution Control' panel is shown with the discretisation and under-relaxation parameters for the ensemble conservation equations. The discetrisation panel includes settings which control the convective and diffusive terms of the N-S equations. The recommended solutions in order to achieve numerical stability for the first run is to use the first order of upwind discretisation as well as the PRESTO (PREssure Staggering Option) scheme for pressure interpolation. Moreover, the PRESTO scheme is favourable for a highly swirling flow with strong pressure gradient effects [79]. In addition, for both velocity-pressure coupling fields the PISO (Pressure-Implicit with Splitting of Operator) algorithm is applied [80]. For a fully developed case of flow, all the lower differential discretisations are shifted towards higher discretisation algorithms applied to the density, the momentum, the turbulence kinetic energy, the turbulence dissipation rate, and energy equations.

The last steps prior to the running the solution are to initialise the engine flow field and to evaluate the numerical time step for which for 1000RPM and 0.5 CAD is 8.333e-5 [s]. The numerical residuals for the continuity and momentum equations and the sub-interations per one time step are 1e-3 and 90 respectively.

7.6 The Distribution of In-Cylinder 'Cold Flow' Velocity Vectors: CFD MK-MF1 Model Validation with PIV Results.

The results of experimental PIV flow cases show the effects of the gas transport and spatial mixing driven by the large-scale fluid structures which are induced by different intake port types. Moreover, the performed 2-D PIV experiments and obtained products do not reveal important information about the time and spatial history of the in-cylinder scalar fields, e.g. temperature, density and pressure. Nevertheless, the in-cylinder flow field does indicate the level of turbulence intensity; and it favours a region of the gas mixing process with a possible level of homogeneity formation and the bulk temperature distributions.

To complete the information about the in-cylinder gas transport process which has influence on the evolution of spatial gas mixing, a 3-D computational CFD method is required. Hence, a non-ideal HCCI combustion technique is mainly controlled by in-cylinder thermo-reactive fluid properties and the spatial gas composition is managed by the varied flow structures with different levels of in-homogeneity. Moreover, the auto-ignition process is dependent on the development of in-cylinder extremities. The coupling of both CFD and the PIV technique has been proposed as an appropriate approach for the characterization of HCCI engine gas flow in order to develop scalars in-homogeneity. The CFD-PIV coupling study has been divided into three subjects: the optical PIV experiment at motored conditions, the CFD numerical model built for an analysis of the 'COLD' flow structures and the simulation of the in-cylinder thermal gas transport process, closely related to engine firing conditions.

To simplify the CFD model as well to make accurate predictions of the in-cylinder large flow formations the single cylinder engine has been modelled without shroud port parts compared with similar sets of PIV experimental data carried out at different crank angles. The base geometry of the single cylinder engine is chosen for the sake of CAD file preciseness,

and includes major cylinder head dimensions instead of the inaccurately defined geometry found in modified port cases. It is believed that any intake port design differences greatly influence the in-cylinder flow pattern; therefore only simple engine geometry is chosen for further flow comparisons. Moreover, modifying the intake port geometry makes a computational grid far too complex; and any change in geometry has an impact on the grid quality and may cause higher numerical diffusion.

The CFD modelling work was divided into two important parts: the realisable spatial discretisation of the engines geometry and appropriate numerical models familiar to the higher-order discretisation schemes, boundary conditions and the 'Realizable' k-ε model of turbulence. Ultimately, for the CFD single cylinder engine, the short inlet manifold was built in order to increase the quality of the cylinder-chamber grid representation as well as to keep computational time at a suitable length. The effect of the intake manifold gas dynamic was predicted by a 1-D gas dynamic model coupled with a 3-D simulation and applied as a boundary inlet pressure profile. This approach is less accurate, in terms of the effect of intake manifold gas mixing but is computationally preferable due to the lack of a High Performance Computing (HPC) cluster. The CFD single cylinder engine base model is mounted on an unstructured grid with a maximum of 900,000 elements for the BDC position of the engine piston. The computation work has been realised with a single 2.4GHz Pentium IV processor with L1 L2 2Mb cache.

Figure 55 to Figure 60 show a comparison of the results for the experimental PIV and the computational CFD predictions for the distribution of the in-cylinder 'Cold Flow' velocity vectors. The computational 3-D HCCI model of the single cylinder engine has been related entirely to motored engine operation with a constant speed of 1000 RPM. Both sets of data are represented by the velocity vectors project on a cylinder plane of symmetry. The displayed results are at 90°, 110°, 130°, 180° and 230°, 300° CAD aTDC with a NVO of 110° CAD.

The intake and exhaust valve timing are chosen as follows: Intake Valve Open (IVO) at 55° aTDC, IVC at 205° aTDC, EVC at 55° bTDC and EVO at 205° bTDC. The maximum intake and exhaust valve lifts and maximum opening points (MOP) are at 2.6 mm/130° aTDC and 2.6 mm/130° bTDC respectively. The PIV equipment set-up is in line with the experiments presented in chapter 7.

OBTAINED IN-CYLINDER VELOCITY VECTORS MAP COMPARISION

EXPERIMENT **CFD**

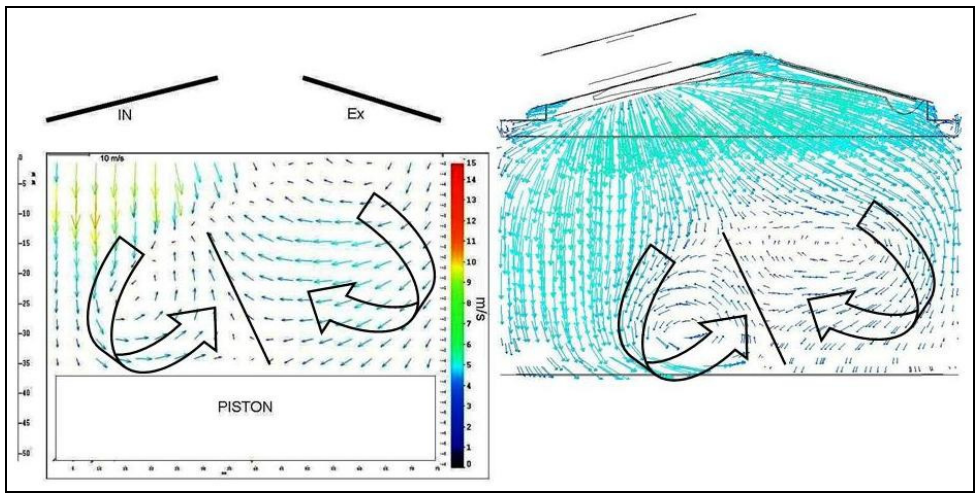

Figure 55: Distribution of the In-cylinder Velocity Vectors 90 CAD Middle Cylinder Plane: Left PIV Experiment, Right CFD Prediction

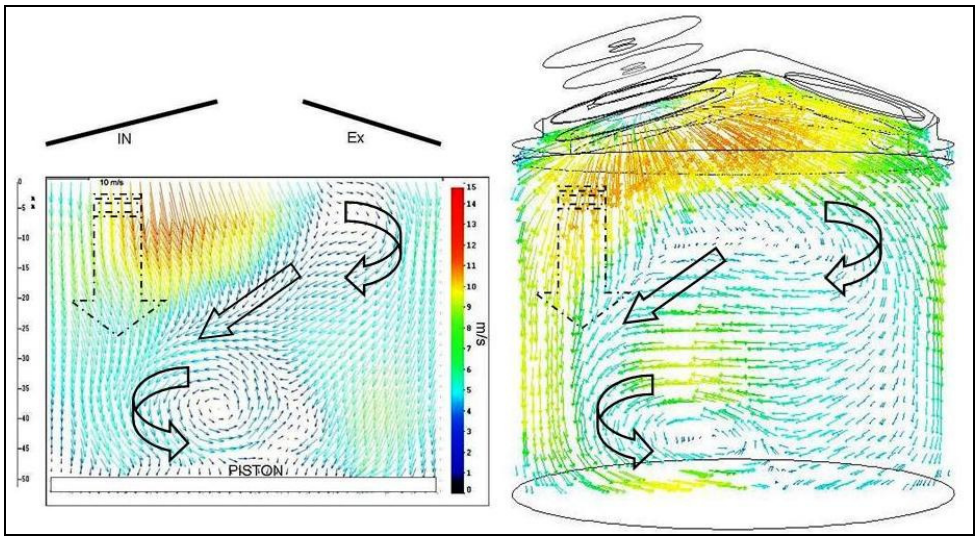

Figure 56: Distribution of In-cylinder Velocity Vectors 110 CAD Middle Cylinder Plane: Left PIV Experiment, Right CFD Prediction

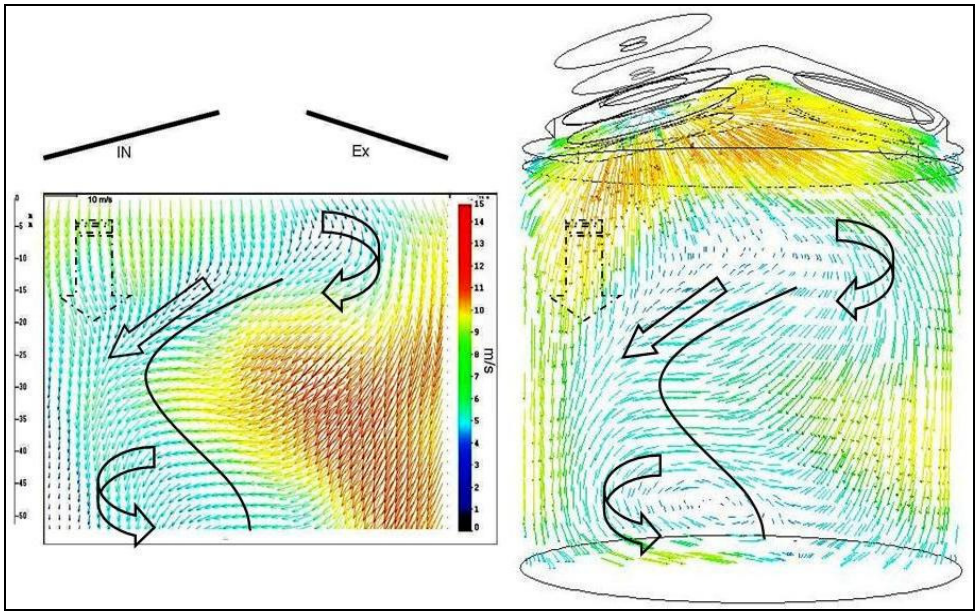

Figure 57: Distribution of In-cylinder Velocity Vectors 130 CAD (MOP) Middle Cylinder Plane: Left PIV Experiment, Right CFD Prediction

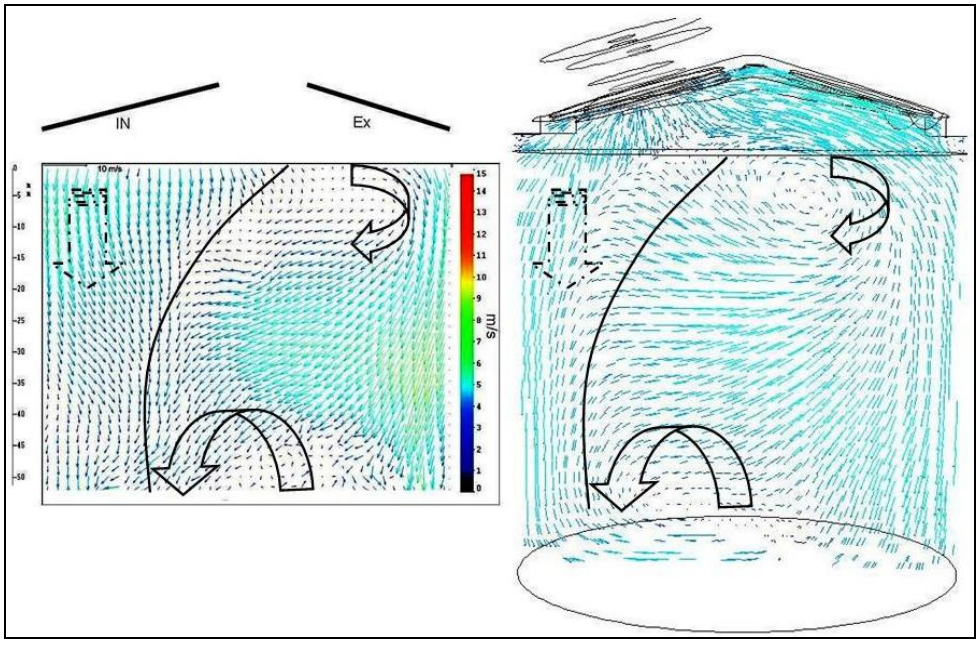

Figure 58: Distribution of In-cylinder Velocity Vectors 180 CAD Middle Cylinder Plane: Left PIV Experiment, Right CFD Prediction

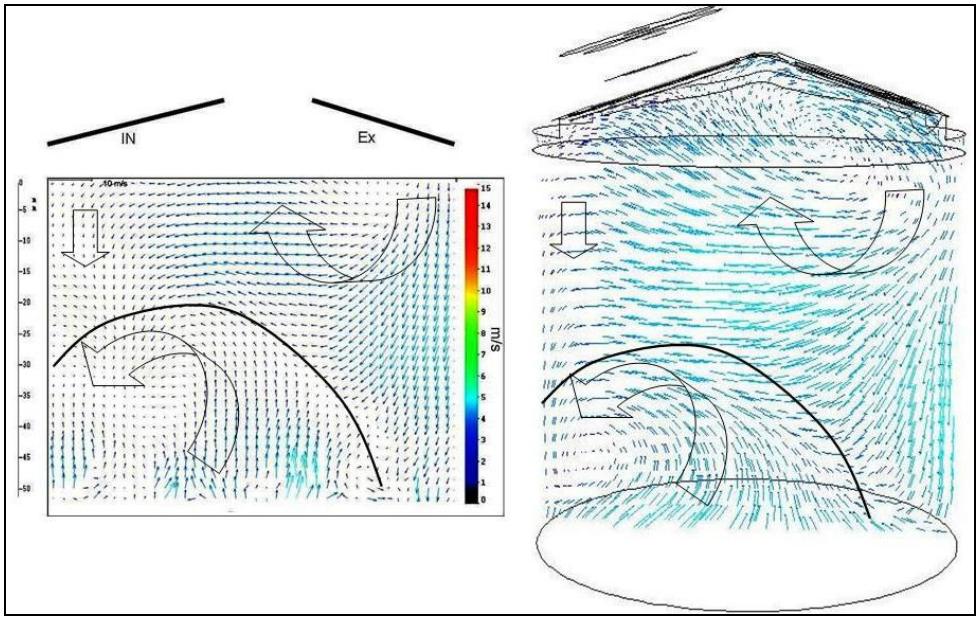

Figure 59: Distribution of In-cylinder Velocity Vectors 230 CAD Middle Cylinder Plane: Left PIV Experiment, Right CFD Prediction

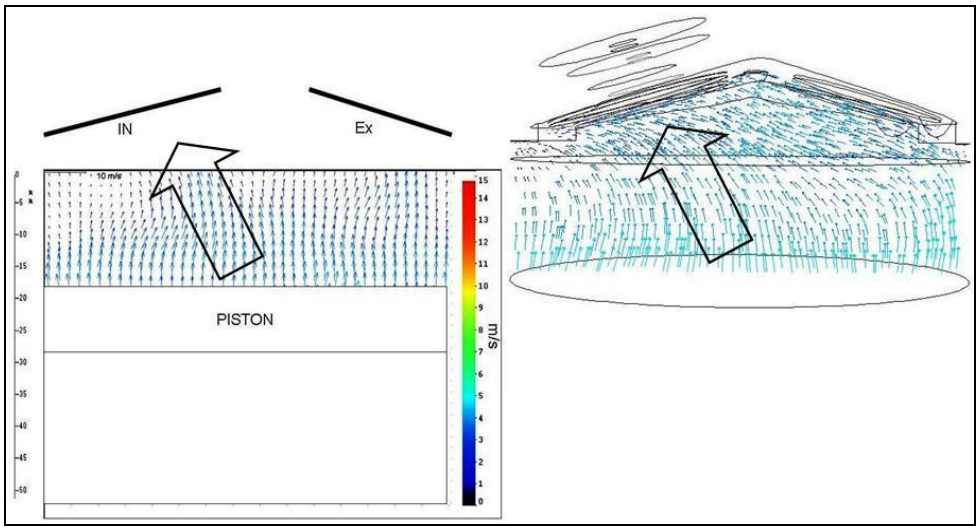

Figure 60: Distribution of In-cylinder Velocity Vectors 300 CAD Middle Cylinder Plane: Left PIV Experiment, Right CFD Prediction

The qualitative study of the in-cylinder 'COLD' Flow is illustrated by the series maps of the experimental and computational ensemble average of velocity vectors at varied CAD in Figure 55 to Figure 60. The sequence of the computational results is generated by the 3-D RANS 'MK-MF1' model and is compared with the average PIV data obtained at the seventy consecutive engine cycles for the middle cylinder plane.

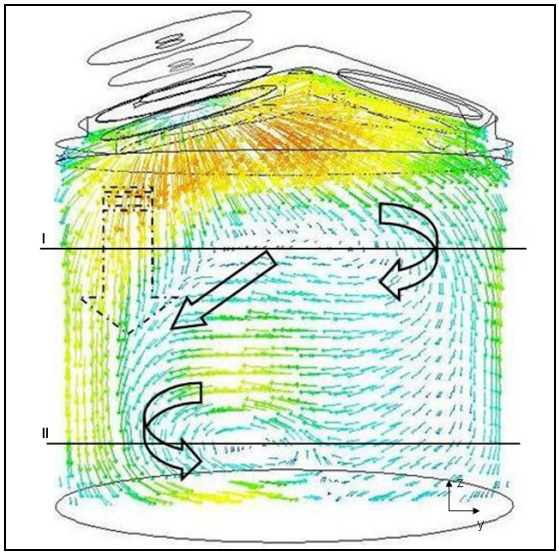

Figure 61: Details of the Velocity Vectors Obtained for the Middle Cylinder Plane at 110 CAD ATDC.

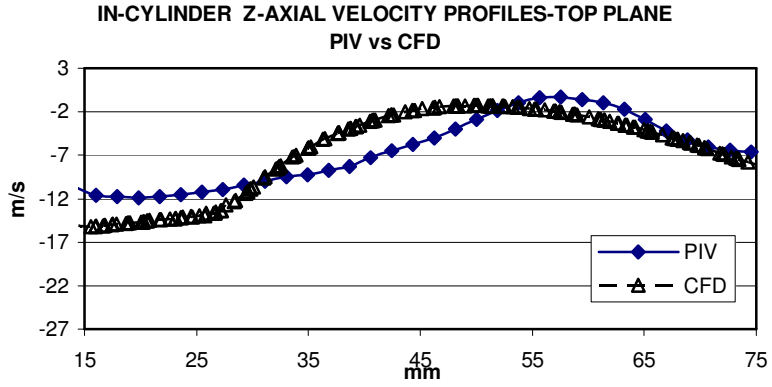

Figure 62: Top Plane I (15mm below cylinder head surface) -Experimental and Numerical Comparison of the Cylinder Axial-Velocity Components.

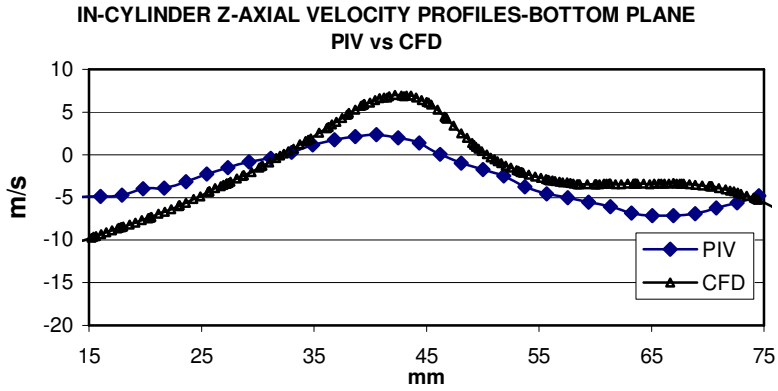

Figure 63: Bottom Plane II (55mm below cylinder head surface) -Experimental and Numerical Comparison of Cylinder Axial-Velocity Components.

The structure of the in-cylinder CFD velocity vectors field performed by the 'MK-MF1' model reveals that the major large-scale structures are well scaled to the cylinder and maintain a similar shape and strength of the flow as obtained from experimental data. Additionally, for all the compared maps it is visible that the extremities of the whole cylinder flow including the direction of the flow and the highest velocity magnitudes are fairly well predicted for a similar spatial cylinder position.

Special focus was placed on the development phase of the computational grid in order to obtain the in-cylinder velocity profile agreement as well as a low numerical diffusion. In the quantity study, the computational flow data is compared with the experimental data at two chosen spatial cylinder positions, represented by the regions which have a strong divergence of flow and a vortex generation. These regions are the most suitable for exposing the numerical prediction difficulties and extremities which appear within the flow. Figure 61 shows strong axial jet forms from the upper part of the middle cylinder head as well as the complex shape of the flow at the middle and lower cylinder position due to the hemispheric valve separation flow at 110 CAD aTDC. The simulation matches the experimental upper fraction of negative vortex as well as the region of the gas jet deceleration region, pointed out by the sloping arrow in the picture.

The computational and experimental axial velocity profiles, shown horizontally, which measure a plane of 15mm below the surface of the cylinder head surface are compared in Figure 62 for the aforementioned engine conditions. It is important to note that the computational shape of the axial velocity profile is similar to the experimental out-comings, but with a slightly different magnitude of velocity. The most visible axial velocity difference is reported in the middle cylinder section. The 3-D RANS computational model has over-predicted the region of the wall flow and the middle cylinder velocity has been reduced slightly. These discrepancies between the CFD and the PIV data are because of geometry and

manifold gas dynamic effects due to the of use of the 1-D Code WAVE coupling to simulate transient manifold flow effects and due to the lack of experimental instantaneous manifold pressure records. Another reason lies in the cylinder discretisation domain and **y+** parameter related to the analytical function of the logarithmic boundary layer thickness, which over-predicts shear stress and friction velocity.

In Figure 63 velocity profiles are presented which have been obtained from the bottom of the horizontal plane located at 55 mm below the surface of the cylinder head. The position of the profile is marked as the horizontal line in Figure 61 and is chosen to quantify the bottom velocity magnitude within the vortex as well as both of the opposite in-cylinder large-scale jet structures. The velocity comparison between the experimental and simulation profiles reveals a similar shape and magnitude for the velocity with a small discrepancy that increases towards the cylinder wall flow. A fairly good bottom velocity profile agreement between the simulations and the experimental cases is obtained in terms of the large-scale structures and the strength of the in-cylinder flow built up during the engine intake phase.

The structure of the in-cylinder complex velocity vectors presented in Figure 61 at 110CAD and it is in agreement with the experimental data which validates the in-cylinder CFD field prediction for the measurement of the vertical plane. The quantitative study suggests that the wall-jet created at the back of the cylinder-wall below the inlet valve seats, as well as the positive vortex near the piston, have a similar velocity magnitude and general jet strength to the experimental one. An similar situation occurs for the fractional clockwise vortex formation close to the exhaust region of the upper engine, which is well predicted by the numerical simulation and presented in Figure 56.

A difficulty was encountered during the engine compression phase, where the spatial and temporal flow discrepancies accumulated and gradually over-predicted the cylinder flow

pattern. Moreover during engine compression stage the in-cylinder flow pattern is maintained by the residuals of the large flow structures from the induction phase. It is also maintained by the gas dissipation process controlled by the micro-scale of the turbulence transport process. From the obtained computational and experimental data it is clear that the created CFD model shares the major features of in-cylinder flow structure with a good agreement for all CAD positions.

7.6.1 Numerical 1-D Single Cylinder Engine Model

A 1-D gas dynamics simulation (Wave, Version 7.2) has been applied as a supporting computational tool to enhance the analysis of the PIV motoring results. For the aforementioned PIV experiments, a 1-D single cylinder engine model has been created with one or two active inlet valves able to simulate the in-cylinder pressure losses and temperatures at successive crank angles. Figure 64 shows a schematic view of the 1-D model built in the Wave™ package.

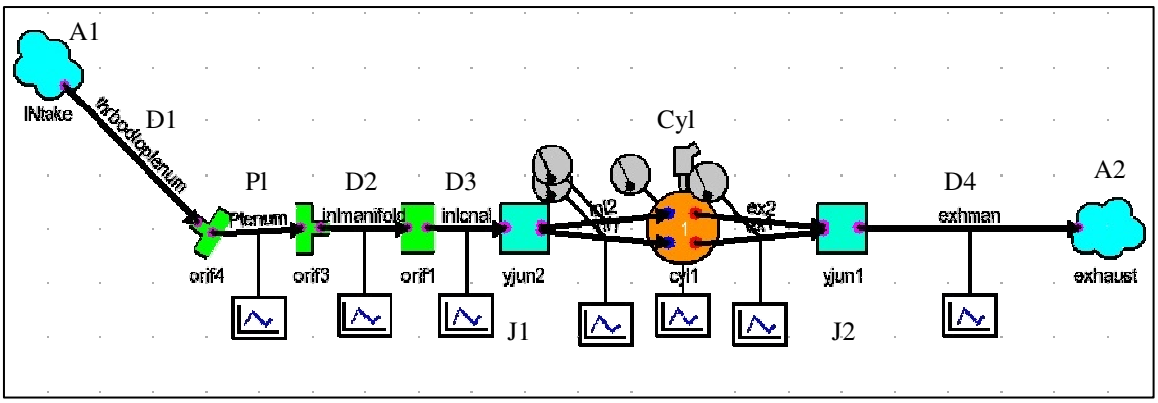

Figure 64: Ricardo™ WAVE 7.2 Model for the Single Cylinder Optical Engine (A-Ambient, D-Duct, Pl-Plenum, J-Junction, Cyl-Cylinder)

7.6.2 1-D Model Validation

$$\delta = \frac{\left|P_{approx} - P_{\exp}\right|}{\left|P_{\exp}\right|} \times 100 \qquad (37)$$

The experimental motor cylinder pressure has been chosen as a convenient validation parameter to compute the 1-D engine model. Figure 65 shows measured and calculated in-cylinder pressure results at 'Tumble-port' motoring engine conditions. From the presented pressure chart, it is evident that the computational results are burdened by a 4% margin of error calculated by Equation (37). And they have a maximum pressure divergence of 10% for 86 CAD aTDC. The in-cylinder pressure discrepancy indicated by the 1-D model during the gas exchange process is caused by the simplification of the geometry and the flow discharge coefficient. The discharge coefficient for the intake port has been measured at a steady state of the port bench and the results were applied to the 1-D code. A small modification to the intake runner geometry was applied in order to account for the cylinder blow-by-losses due to the lack of a Wave™ license for an advanced cylinder 'LISA' model.

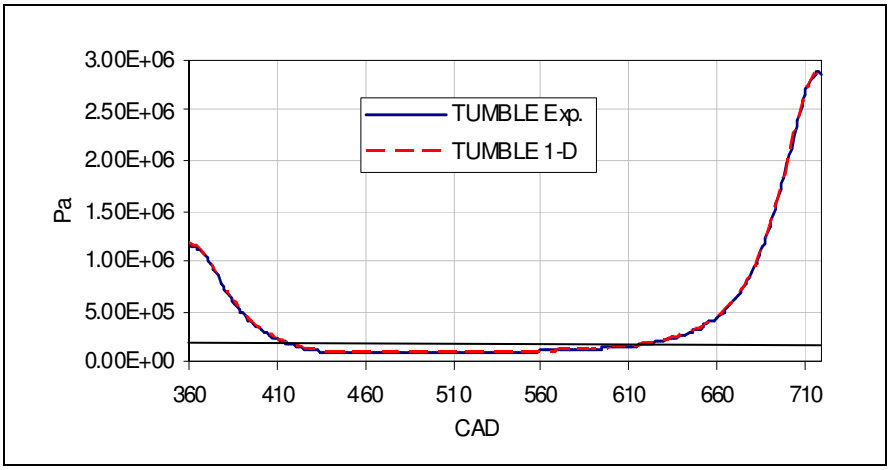

Figure 65: In-cylinder Experiment and 1D Modelling Pressure Comparisons

7.7 Summary

The sets of modelled and experimental velocity vector fields indicate that the range and the spread of the velocity jets which appeared between the intake valves, the cylinder wall and the top of the cylinder chamber, are simulated reasonably well for the induction and compression engine phase. The numerical simulation indicates similar features for the structures the dissipation of the flow based on the 'Realizable' k-ε model of turbulence with regards to the measurement of the experimental planes. It is important to mention that the

created computational model has many simplifications, e.g. the model of the flow (turbulence time, the average k-ε 'RANS' solver), the boundary conditions, the initial conditions, the numerical schemes, the geometry of the engine, and the crevice. It seems that the general Large Eddy Simulation (LES) 'not time average' flow solver approach is more suitable for large turbulent in-cylinder structures; however it needs more powerful high performance computing (HPC) resources than for a common RANS solver. All these simplifications affect general in-cylinder flow prediction and cause discrepancies between the simulation and experiment.

Chapter 8

THE THREE DIMENSIONAL CFD STUDY OF IN-CYLINDER 'COLD' FLOW FOR A BASE ENGINE GEOMETRIC CONFIGURATION.

8.1 Introduction

The present chapter has been designated for a parametric PIV and CFD 'Cold Flow' study which looks at the distribution of the in-cylinder average velocity vectors characterised by the large-scale flows and at the gas turbulence effects obtained for the symmetric NVO event. Moreover, for the HCCI four-stroke engine project, a three and one dimensional CFD models were developed in order to filter the important spatial and temporal mechanisms that maintain the stratification of in-cylinder flow. The large-scale flow structures were found and utilised as tracing factors of the in-cylinder gas transport process, mixing effect and level of in-cylinder gas in-homogeneity during successive crank angles. The large-scale flow appeared within the cylinder as different geometric structures, e.g. intake jets, vortices, shear and wake flows, as well as a strong convection flow dividing cylinder regions, were analysed during the development of the cylinder flow.

The 3-D CFD engine motored simulation, including the complete gas exchange process, was carried out over several cycles in order to obtain stable velocity vectors field for analysis. The CFD model of the three-dimensional single cylinder engine is validated against the experimental data and becomes an advanced flow analysis tool, built for HCCI sensitive

study cases to extended necessity of spatial and temporal gas in-homogeneity information. The global in-cylinder mass transport and mixing process has been characterised by the spatial and temporal formation of in-cylinder gas streams and by the level of turbulence intensity for particular cylinder regions.

Coupling both analysis methods (experimental and computational) for the in-cylinder flow field and evaluating other flow effects e.g. thermal transport, pressure differences, wake flow and other throughout a series of CFD data leads to a better prediction of spatial in-cylinder scalars gas homogeneity. Moreover, a validated computational model of the HCCI engine is crucial for an advanced analysis of the in-cylinder turbulent thermal transport where the complex 3-D flow is too expensive to measure and is out of the scope of the experimental work. The effect of thermal stratification with regards to in cylinder flow structures will be presented alone in the next chapter.

For the current research, a symmetrical (110CAD) negative valve over-lap (NVO) of valve events, has been utilised in reason of experimental results similarity. A detailed 3-D CFD unstructured grid model of the single cylinder engine was built in conjunction with the k-ε turbulence model and the RANS solver to characterise the in-cylinder flow process for particular NVO and to characterise the experimental velocity vectors. Moreover, for the chosen NVO additional important flow parameters have been utilised: Turbulence Viscosity, Velocity Gradient and the Gas Turbulence Kinetic Energy.

8.2 Effect of the Symmetrical NVO valve timing on a 'Cold Flow' Intake Gas Exchange Process. A CFD Case Study

The NVO valve timing is utilised for the HCCI engine concept as thermal-flow management to control the range of the engine load due to the cylinder gas exchange process [82] and amount of fresh 'COLD' air trapped under the cylinder. During the early engine

induction phase at the chosen symmetric IVO, the differences between the in-cylinder and the manifold pressure generate a strong backflow and a positive pressure wave towards ambient. The pressure difference at IVO for the symmetric NVO is a function of the in-cylinder pressure obtained during the exhaust valve closure phase. It is also dependent on other factors, e.g. cylinder blow by losses and injection timing. Typically, if the opening of the intake valve is advanced the pressure difference is higher and a stronger back-flow occurs towards the intake manifold.

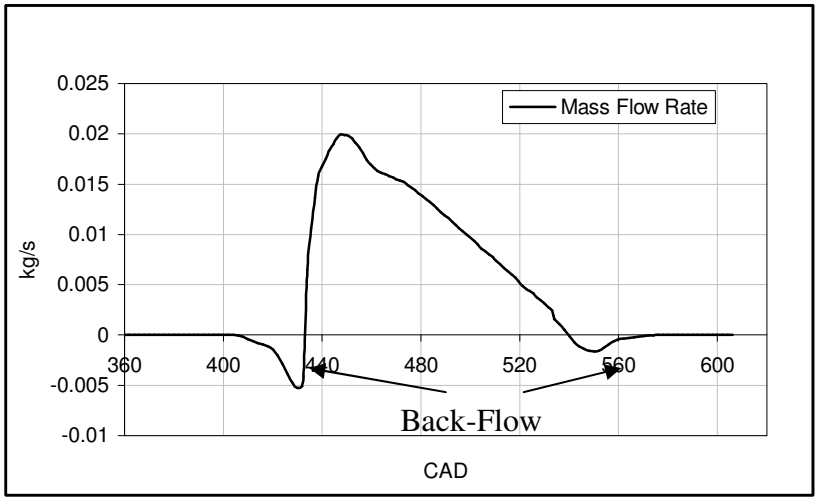

Figure 66: The Profile of the Mass Flow Rate per One Intake-Valve as well as the Back-Flow Effect Predicted by the Three Dimension CFD Model.

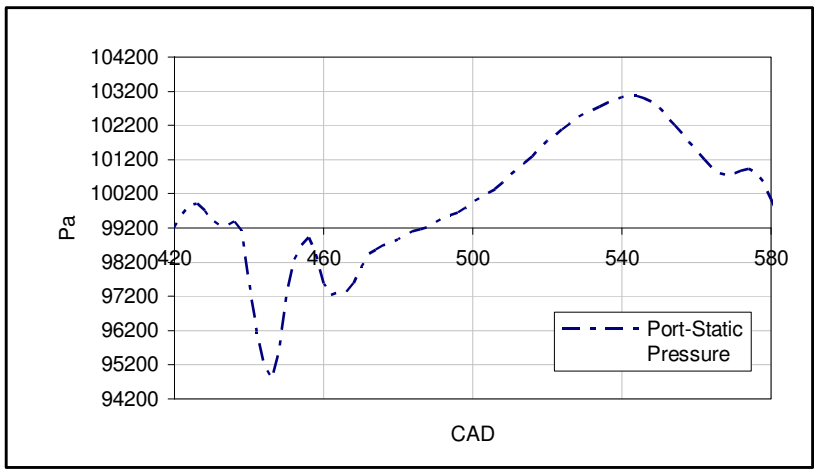

Figure 67: The CFD Profile of Intake Port Static Pressure

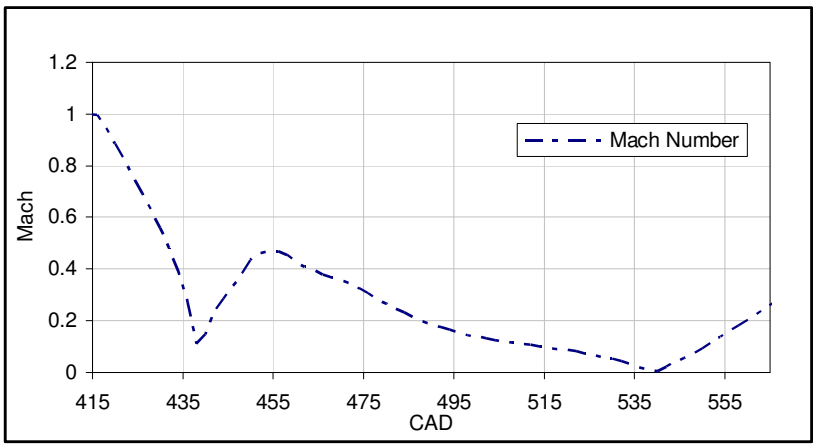

Figure 68: CFD prediction of the Intake Valve Curtain-Mach Number

As can be seen in Figure 66 for the chosen symmetric NVO valve timing at an IVO of 55 CAD and 200 CAD aTDC respectively, a strong back flow of hot in-cylinder gas occurs. The CFD simulation indicates in Figure 67 that this process of gradually expanding in-cylinder gas to the manifold takes 15 CAD and is associated with strong pressure fluctuations within the intake manifold (wave pressure and velocity propagation). Furthermore, at the beginning of back-flow process the critical pressure is reached and the flow becomes chocked when it reaches M=1 at the minimum cross section of the valve curtain area, which is presented in Figure 68. As the piston moves downward the in-cylinder pressure drops suddenly due to the flow of outward gas momentum and the increasing ratio of cylinder volume. The decrease of an in-cylinder pressure caused by the gas momentum amplifies the pressure difference on the valve port; and in the next step it creates a stronger inward flow to the cylinder which is visible as a steep sloped line of mass flow rate in Figure 66 and an increasing Mach number.

The sudden inward flow with the high Mach number and increase in the valve flow area creates a depression of pressure within the intake port and generates a rare fraction wave which approaches the open pipe end. Near to the BDC of the piston position, the low intake port pressure is affected by the strong positive pressure wave travelling from the open pipe

end by the inward flow to the manifold. The late induction phase presented in Figure 67 shows the dynamics effect of coupling pressure wave propagation and decreases is the cylinder volume. The produced effect is contrary to the back-flow and is dependent on the rare-faction pressure wave. After the BDC inward flow decays the under-pressure 'negative' wave arrives from the open end and accelerates the back-flow to the inlet manifold as presented in Figure 66.

Engine type	**4 valves per cylinder, 1cyl.**
RPM	1000
Bore	89.0 mm
Stroke	90 mm
C.Rod	150 mm
Compression Ratio	11.3
Intake Valve Open	IVO415CA
Exhaust valve Close	EVC305CA
Intake Temperature	300 K
Vol. Eff	88%
BackFlow/Total	6.1%
PMEP	-0.026 MPa
Tivo-cylinder	461K

Table 6: Engine Data

In Figure 69 and Figure 70 CFD velocity vector maps are presented with the intake back flow process at 70 CAD and 190 CAD aTDC respectively for the middle valve plane. It is interesting to note that the late back flow process leads to an inlet manifold that is filled up with a mixture which stays there until it is sucked back into the next cycle. In addition, the early back-flow process fills-up intake manifold with the cylinder gas products and it decreases the volume of fresh charge sucked back at the induction period, thus affecting the engines volumetric efficiency (η_v). For the current symmetric NVO valve timing, the calculated percentage of the back flow over the total in-cylinder mass is 6.1% with a volumetric efficiency of 88%; and the pumping mean effect pressure (pmep) is -0.026 MPa as indicated in Table 6.

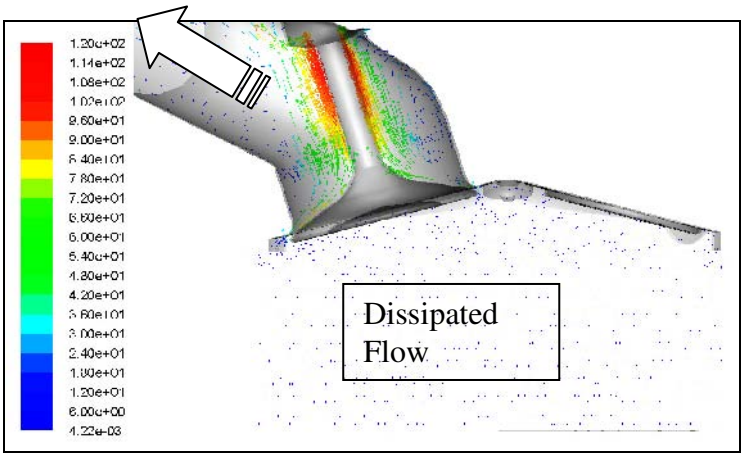

Figure 69: Map of the Velocity Vectors on the Valve Plane of Early Back-Flow 70 CAD aTDC. 'MKIMF' CFD model prediction

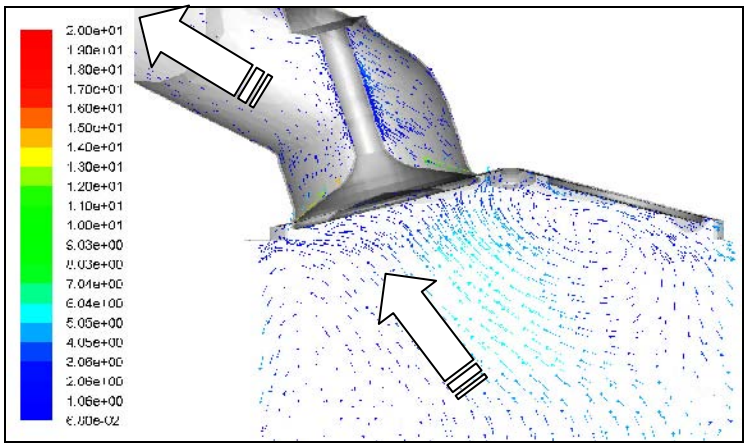

Figure 70: Map of the Velocity Vectors on Valve Plane of Late Back-Flow 190 CAD aTDC. 'MKIMF' CFD model prediction

8.3 Effects of Intake Valve Separation on In-Cylinder Flow Character

The validated three-dimensional CFD model of the single cylinder HCCI engine has been used to extend the spatial and temporal information about the internal engine flow structures raised during the early gas induction phase. The validated computational results shown in Figure 55-Figure 60 show the large-scale cylinder flow mechanisms created by the valve separation and the effects of cylinder wall deflection. It has been found that the in-cylinder gas flow pattern, in the favourable range of 90-130 CAD for the high mass flow rate, potentially induce a strong shear flow and turbulence production. Furthermore, the development of the turbulence and coherent structures at the beginning of induction have an impact on the later gas mixing process and the spatial character of the large-scale flow. Part of

the flow creates swirling structures, which dissipate energy very late in the compression phase and influence gas stratification and the mixing process.

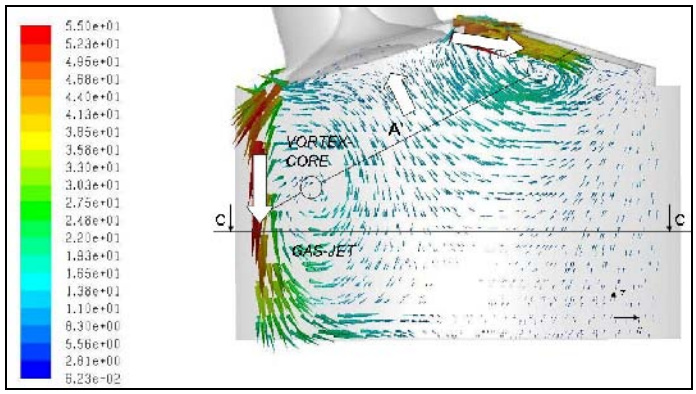

A) Middle Valve Plane A-A

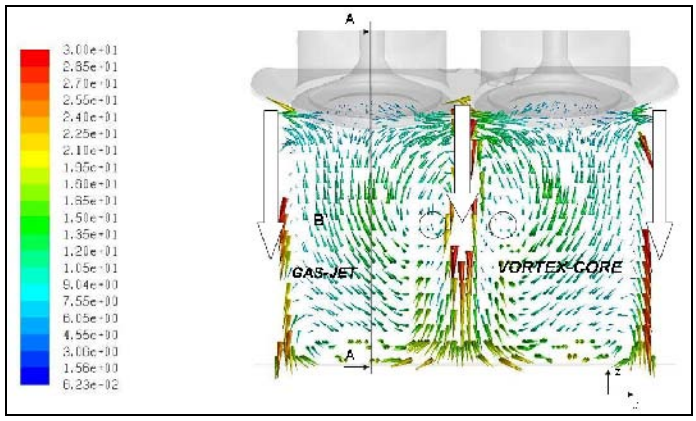

B) Across Valve Plane B-B

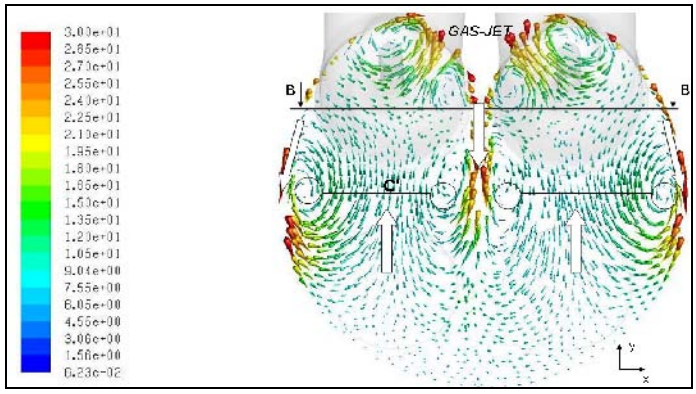

C) Middle Cylinder Plane C-C

Figure 71: In-cylinder Velocity Vectors Obtained at Three Measurement Planes for 90 CAD ATDC: A) 90 CAD Side Valve Plane A-A and Velocity Profile Axis A'; B) 90 CAD Across Valve Plane B-B and Velocity Profile Axis B'; C) 90 CAD Middle Cylinder Plane C-C and Velocity Profile Axis C'

In Figure 71 A, B, C average velocity vector maps are presented, having been computed by the CFD 'MK-MF1' model which encompasses the three different cylinder planes for a case of a maximum mass flow rate. The computational results indicate various coherent structures such as the swirling and jet fluid patterns spread across the cylinder. The vertical plane of the middle valve in Figure 71 section A displays two large coherent contrasting vortices due to the intake valve separation flow and the adverse pressure effect. For structures apparent at 90 CAD, the range of the stretched flow is characterised by the wall jet-vortex concurrence operating in the cylinder domain. The expansion of the front valve gas jet induces the development of a small vortex situated in the middle cylinder section. In comparison, the rear part of the valve flow and part of the wall-jet approach the pistons surface and create an early transverse vortex. From the computational data it is clearly visible that the upper flow is not able to approach and mix with the bottom cylinder bulk gas and strongly influence the exhaust cylinder head gas structure.

For both swirling structures visible on the side of the picture, the shape of the flow is governed by the varied static pressure balanced on the fluid element under centrifugal force and this affects the gas transport and mixing process within the cylinder [83]. It is important to note that the core of each vortex attains the lowest velocity magnitude and the maximum of vorticity as well as a low static pressure compared to the rest of the flow field, which is pointed out by the circles in Figure 72, Figure 73 A, B, C respectively. For the centres of both of the side vortices, the precession velocity is approximately 7 m/s towards the piston compared to 40 m/s and 4.7 m/s of the jet-wall peak and piston velocity respectively. Additionally, a decelerated wall-jet gas structure is affected by a strong cylinder wall shear stress mechanism induced near to both of the wall-sides due to the velocity gradient and driven form the forced vortex. Moreover, the centres of the vortices and the flow region beneath the intake valve are away from the main wall-flow characterised by the velocity

profile in Figure 72 A. The superposition of both types of vortex within the cylinder and under the intake valves establishes the velocity and pressure profile, similar to those of the 'Rankine Vortex' [83] which is usually part of the cyclone flow pattern.

The varied scales of the velocity magnitude in Figure 71 rise in the cylinder domain as a mutual process of the jet-walls and vortices action, organised by complex aerodynamic effects. The velocity magnitude extremities encountered in a narrow flow region manifests, a separation flow under the intake valves and they are the origin of the large-scale vortices and the mechanisms of the gas stratification structures. The apparent intake jets impose a cylinder flow which experiences a strong turbulent advection process towards the piston surface and carries intake gas that is fresh compared to the rest of the flow field.

In Figure 74 A, B and C the calculated turbulence intensity is presented across the coherent flow structures, and the effect of turbulence is visible within the free jet of the middle chamber region as well as near the cylinder walls, with low values at the core of the vortices. The above mentioned phenomena of the turbulence advection process and the mean flow are the major factors responsible for the gas transport and the quality of the cold gas mixing at early intake. Moreover, the rear cylinder regions of the strong wall-jet are limited to the length of 45mm of the cylinder wall and are not sufficient to develop an effective mixing-time with the surrounding gas structures or to influence the rest of the cylinder fluid.

In addition, Figure 71 shows intake conical jets and the screening effect of the cylinder wall as important factors generating a strong shear flow and a strong turbulence intensity production at this CAD position. Moreover, it must be noted that the induced turbulence controls the gas transport and mixing between the hot and cold gas structures. The core of the early conical gas jet exhibits nearly homogeneous composition, based on the obtained velocity

profile, and has a strong influence on the thermal gas cylinder stratification as well as on the later development of the in-cylinder flow structure.

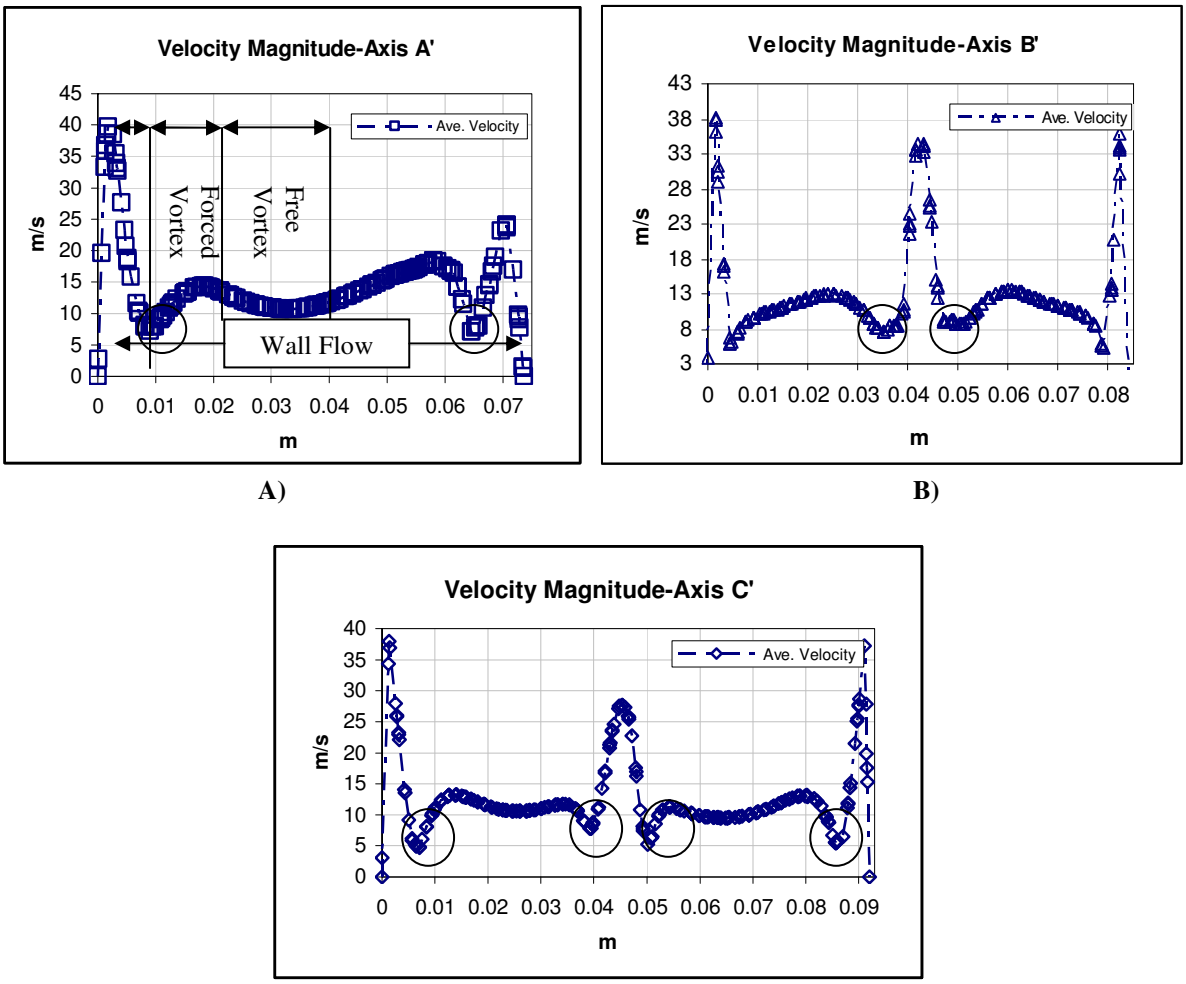

Figure 72: In-cylinder Velocity Magnitude Obtained at the Three Measurement AXIS at 90 CAD ATDC: A) Velocity Profile Axis A', B) Velocity Profile Axis B', C) Velocity Profile Axis C'

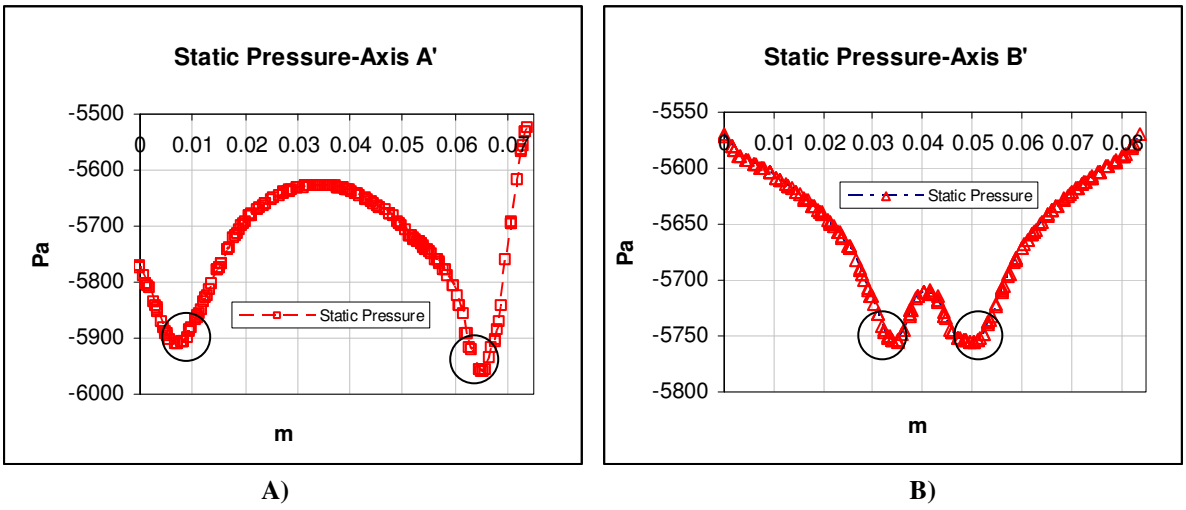

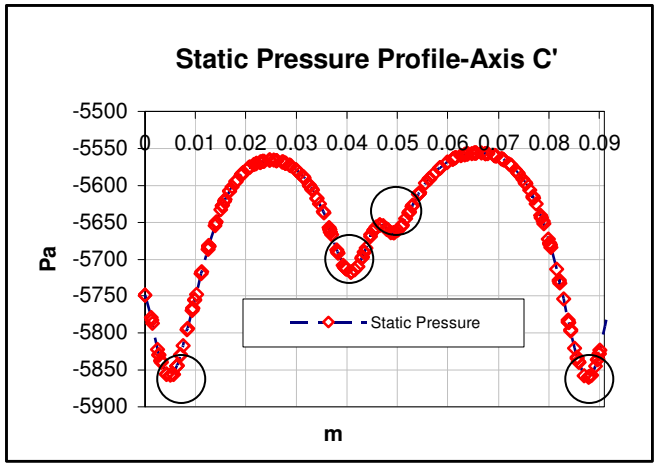

C)

Figure 73: In-cylinder Static Pressure Obtained at the Three Measurement Axis at 90 CAD ATDC: A) Static Pressure Axis A', B) Static Pressure Axis B', C) Static Pressure Axis C'

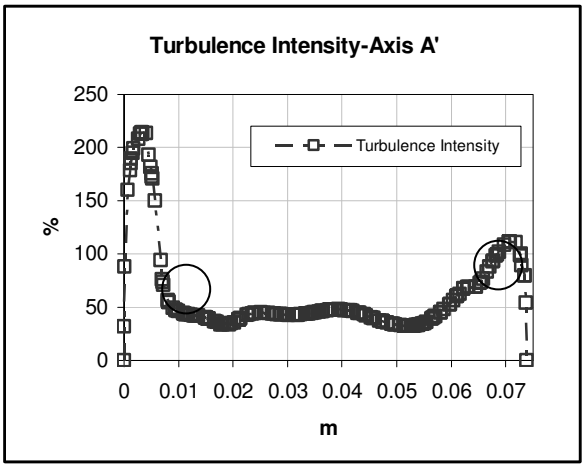

A)

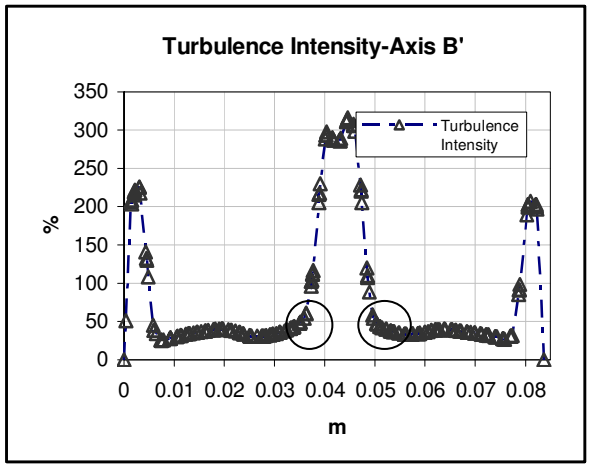

B)

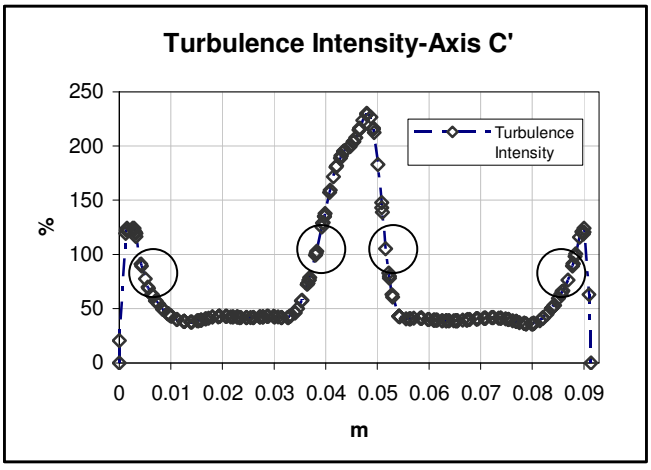

C)

Figure 74: In-cylinder Turbulence Intensity Obtained at the Three Measurement Axis at 90 CAD ATDC: A) Turbulence Intensity Axis A', B) Turbulence Intensity Axis B', C) Turbulence Intensity Axis C'

The velocity fluctuations within the middle cylinder jet enhance the turbulent mass transport of the fluid and the heat transfer for the whole cylinder domain in comparison to the core of the large-scale vortices. In Figure 75, the valve-body shroud effect on the gas turbulence viscosity parameter ***vt*** is presented, which characterises the mixing progress beneath the intake valve. The centre of both vortices in Figure 71 A, seem to dissipate the in-cylinder flow more effectively in relation to a low RMS of gas velocity fluctuations and a constant angular velocity profile in the middle part of flow under the intake valve, based on Equation 29. The part of the wall flow can be characterised by the forced vortex and is induced by the wall-jet flow causing a high strain rate. It also differs from the outside part of the swirling structure. The outer flow path has a similar profile to the free vortex region and indicates a lower energy dissipation of the flow. This effect influences the turbulent gas momentum exchange under the intake valve region; and it shows that the parameter of TKE is the exponential function of mixing in accordance with the Equation (29).

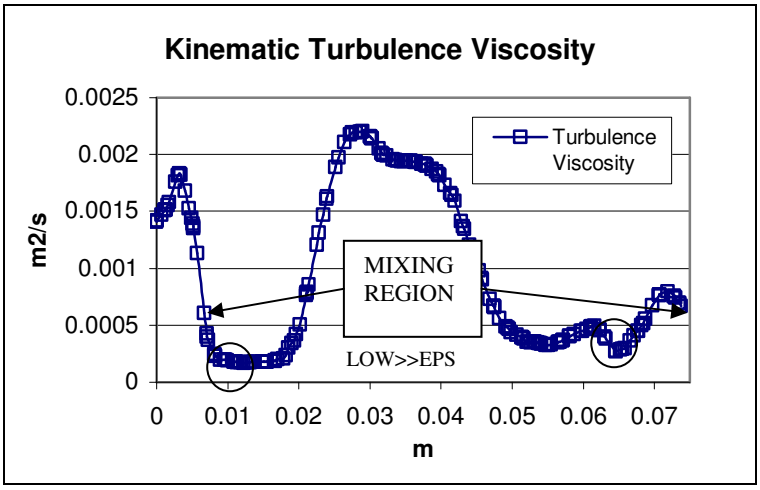

Figure 75: In-cylinder Turbulence Viscosity Parameter and the Effect of Lower Dissipation Energy Calculated at the Region of the Middle Valve Flow. The Measurement obtained at AXIS A' for 90 CAD ATDC.

Furthermore, the free vortex profile confirms a long-term swirling life and lower energy dissipation. In addition, the core of the vortex prevents a coherent gas structure from mixing with the cold intake gas due to the angular inertia force and higher gas density [1]. This effect

is also known as the vortex density stratification process and can dampen turbulence production, especially in a gravity field [85].

All the swirling gas structures visible in the experimental PIV and CFD computational data in Figure 55 to Figure 60 contain lower levels of the energy dissipation compared to the shear jet and can conserve longer the gas kinetic energy that is realised near the TDC because of the gas turbulence resulted from vortex structure breakdown. The in-cylinder PIV velocity profiles and validated CFD results confirm the existence of swirling flow structures near the end of TDC which inherently manifest a lower energy gas dissipation process. This effect has strong implications for the thermal gas analysis within the cylinder, where the core of the horizontal vortex can be much hotter with a lower gas density than the outside part of the rotating fluid.

The effect of rapid distortion of the vortex near the TDC is experimentally difficult to measure but must be accounted for the analysis and it can possibly be visible as TKE increases within the CFD analysis [76]. Another factor which has an impact on the vortex structure is the density ratio between two mixed gases and the diffusion process. These effects will be presented in the next chapter which is focusing on thermal aspect of in-cylinder gas structure. The general low pressure encountered beneath the intake valve-heads due to the presence of the separation flow is essential and influences the general in-cylinder transport process. In Figure 76, I and II are maps of the static pressure diagrams calculated across the cylinder domain and indicate the range of the pressure drop within the cylinder. From the obtained pressure maps, the dimension of the depression and the influence of valve geometry on the inward flow process and the possible direction of the major in-cylinder free flow which affects gas mixing are apparent

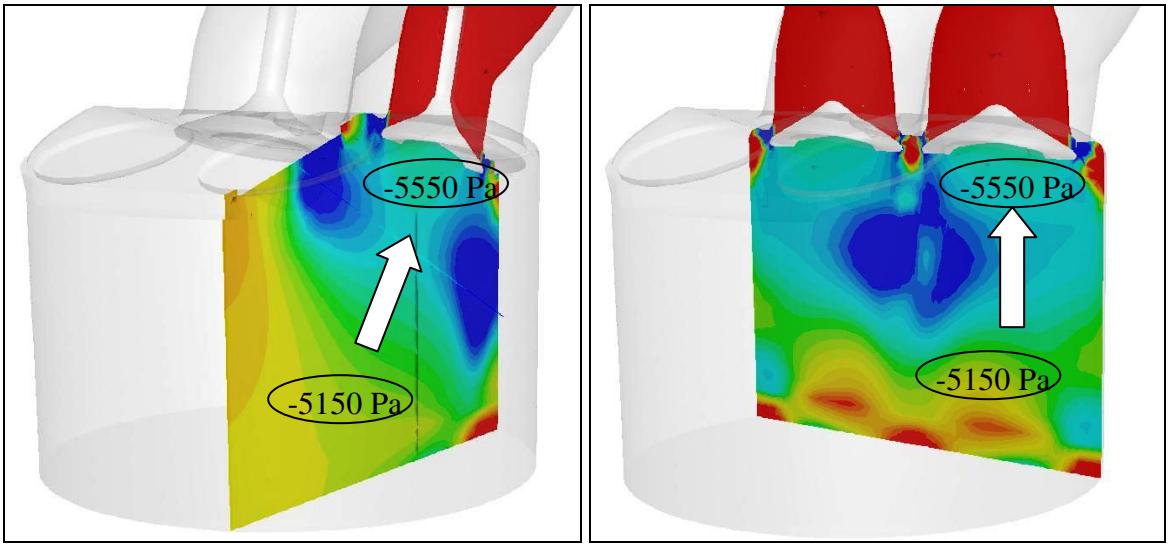

I) II)

Figure 76: Iso-View of the Side and Front Visualisation of Static Pressure Distribution under the Intake Valve at 90CAD. I) Middle Valve Plane (-5550, -5150)Pa; II) Cross-Section Valve Plane (-5550, -5150)Pa

. The intake valve is an inherently obstructive body for the intake gas stream and it is shrouded beneath the cylinder zone from the direct action of the cold intake jet. This effect strongly affects the character of the cylinder flow, where the gas is flowing from the higher-pressure cylinder region -5150 Pa to a lower -5550 Pa situated under the intake valves.

In the HCCI cylinder engine, the composition of a mixed gas structure controls the level of reactivity of the field. The gas stratification mechanism driven by the valve-shrouding effect produces all the scales of swirling flow structures, where the large-scale flow proceeds towards the intake valve head. Figure 77 presents the calculating mechanism of the hot gas transport phenomena which occurs at the exhaust bottom side towards the bottom of the intake valve, due to the lower pressure action under the intake valve. In addition, the schematic diagram reveals that the internal hot gas continually supplies the intake valve chamber region and counteracts the cold intake gas, holding the core of the vortices as a homogeneous structure.

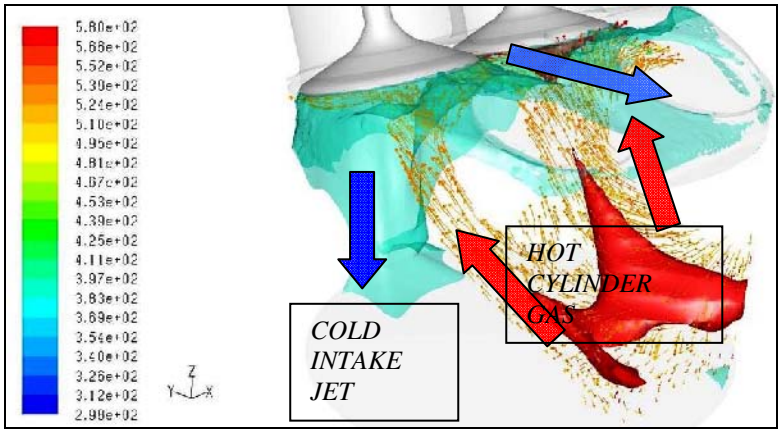

Figure 77: The 3-D details of the spatial gas transport within the HCCI single cylinder engine at 90 CAD for 110 CAD NVO.

In the HCCI cylinder engine, the composition of mixed gas structure controls the level of in-homogeneity. From this point of view, the role of large scale vortex structures in the active transport of the gas properties through the cylinder chamber is crucial because of the long life-time of coherent swirling structures and the dissipation process. For 90 CAD aTDC, only a fraction of the cylinder volume is affected by the above-mentioned flow structures. This process is manifested by the general low average cylinder pressure as well as the maximum mass flow rate obtained at this condition. In order to extend the knowledge about the evolution of the in-cylinder flow generated by symmetrical NVO, the condition of 130 CAD aTDC has been chosen for a comparison.

In Figure 78, A and B present differences in the flow structure between two successive flows at (90,130) CAD aTDC. The velocity path-lines are chosen to visualise chamber penetration by the jets and vortices. It is clear that at 90 CAD for the case of the maximum mass flow rate, the strong coherent jets formed from the valve mouth regions are at the early stage of development; and part of the cylinder volume is not affected by the cold gas streams (a detailed structure of the flow under the valves will be analysed later into this text). At 130 CAD aTDC, the in-cylinder flow is fully developed and has become more complex.

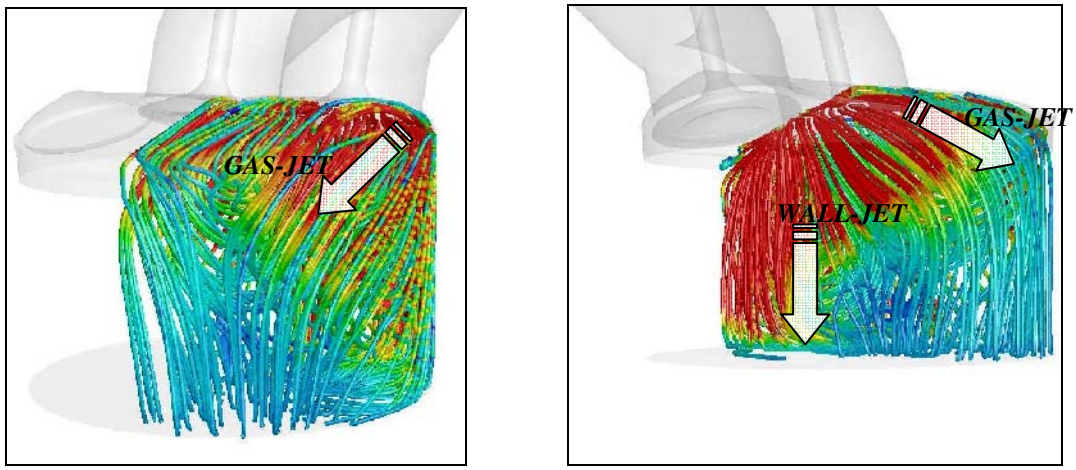

A) 90CAD

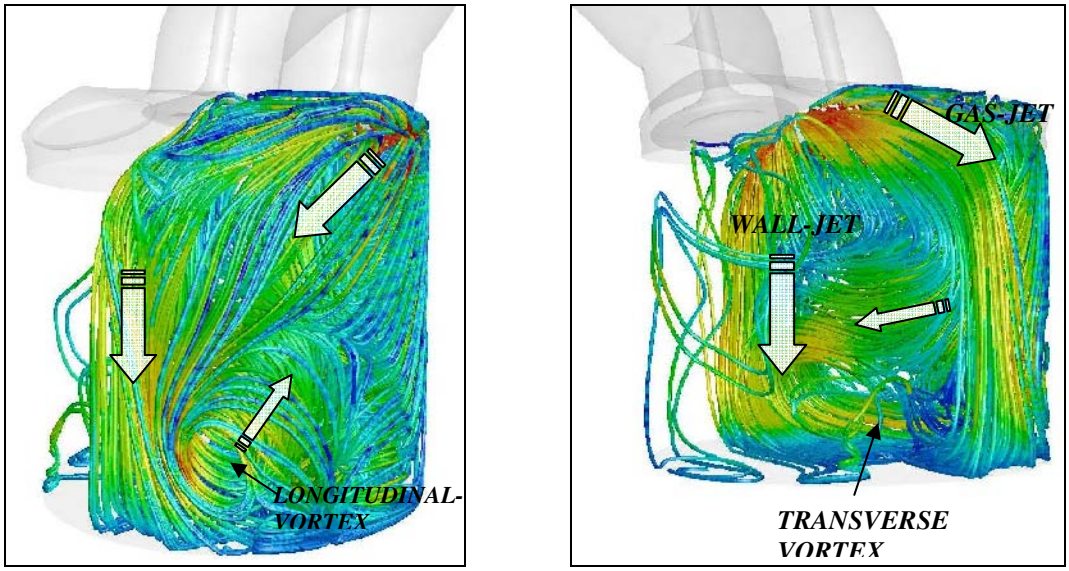

B) 130 CAD

Figure 78: In-Cylinder Spatial Flow Pattern Obtained for Two Engine Conditions Indicated the Creation of Vortex and Coherent Structures: A) PATHLINE-VELOCITY(0-20 m/s) 90CAD aTDC; B) PATHLINE-VELOCITY(0-20 m/s) 130CAD aTDC

Moreover, it is interesting to note that within the highly dissipated and disorganised flow structure at 130 CAD there appear 'long-life' coherent structures which partially exist at the TDC compression stroke. It can be assumed that the long-life flow structures are crucial for control of HCCI auto-ignition because of the thermal and spatial mixture in-homogeneity and the amount of thermal energy conserved in the vortices.

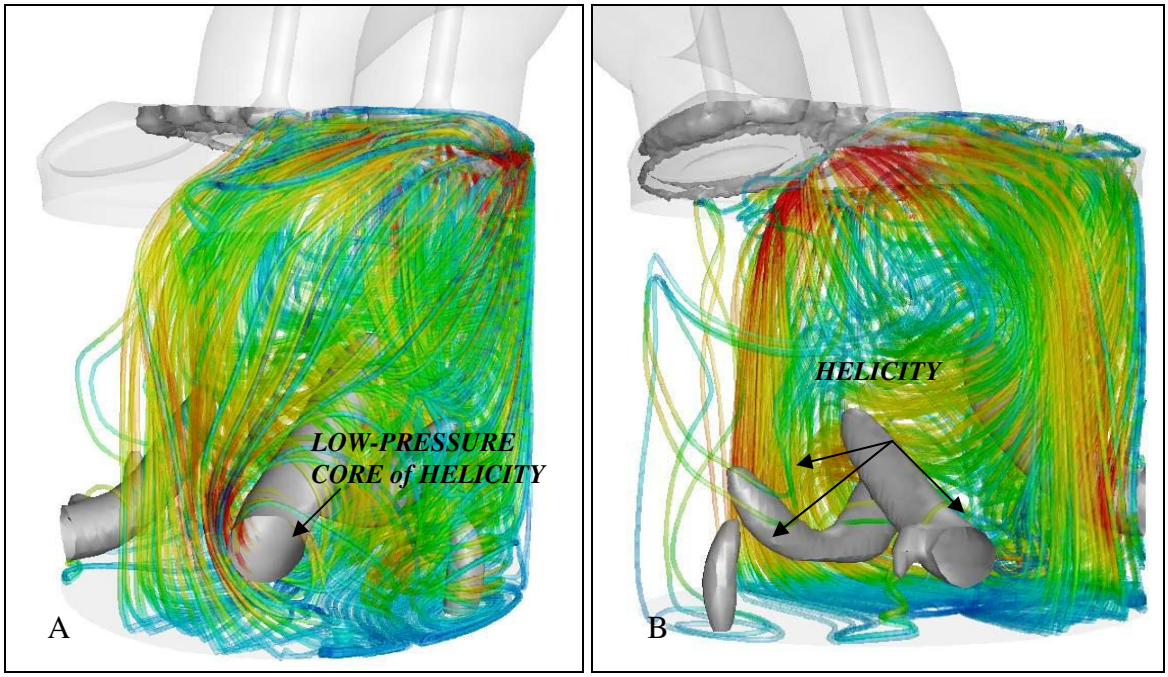

Figure 79: Quality View of the In-Cylinder Helicity Induction at 130 CAD: A) and B) Velocity 0-20m/s Iso-Value of Pressure -540 Pa

In Figure 79 at 130 CAD, the large-scale helicities become apparent and affect the gas pressure and density distribution across the domain and inherently set-up the cylinder gas transport process. The turbulent gas transport process for the internal combustion engine is three-dimensional and thus the vortex can be treated like a two-dimensional representation of a complex helicity structure. The helicities are the key factors for controlling the in-cylinder large-scale flow structures; they govern the different rates of the gas transport and they stratify the flow regions, affecting the gas formation during the compression phase.

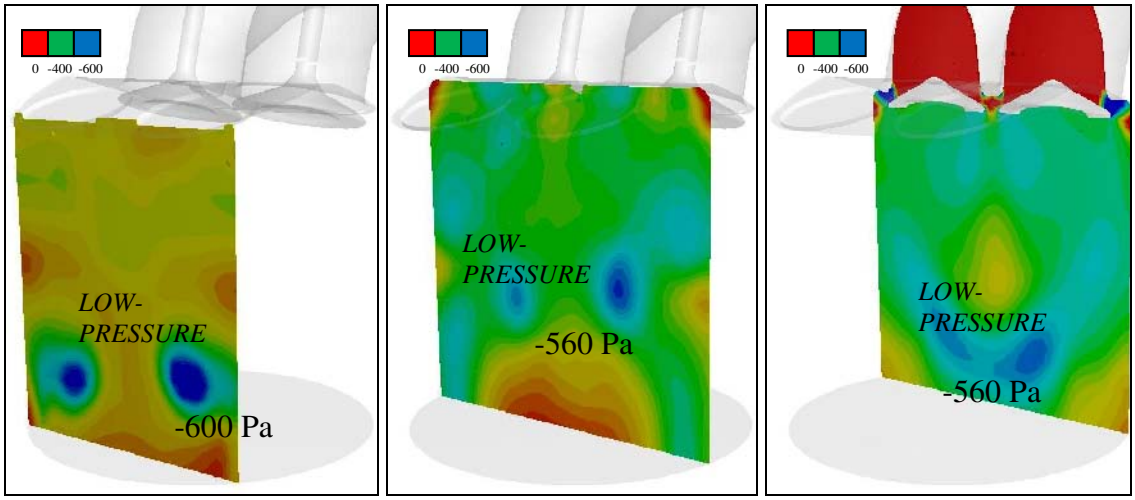

A) B) C)

Figure 80: Map of the Static Pressure at 130 CAD: -600 to 0 Pa for Three Measurement Planes (A, B, C)

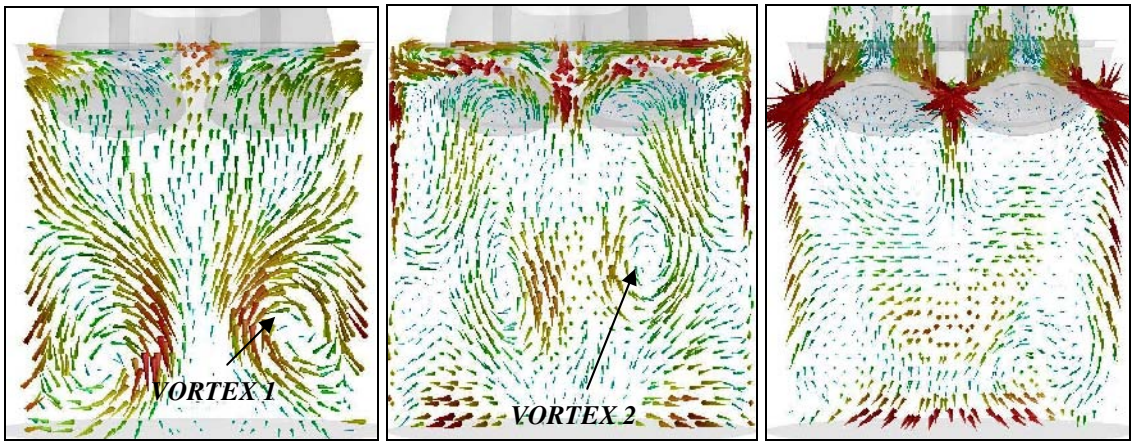

A) B) C)

Figure 81: Velocity Vector Structure at 130 CAD: 0-20m/s for Three Measurement Planes (A, B, C)

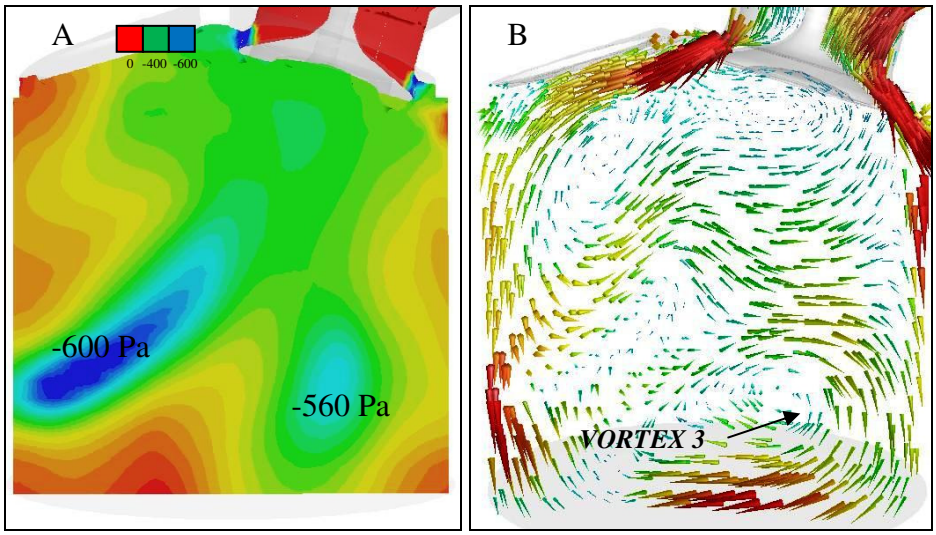

Figure 82: Cross-Symmetry Intake Valve Plane at 130 CAD: A) Static Pressure Contours (-650 to 0 Pa), B) The Distribution of Velocity Vectors (0-20m/s)

One of the most visible stratification effects due to the action of helicites is a decrease in pressure within the core of a vortex [84]. Figure 79 presents an iso-view of the static pressure distribution within the large-rotating coherent structure at 130 CAD aTDC. Additionally, the details of the low-pressure distribution as well as the velocity vector structures in the cores are presented for three vertical cross cylinder planes in Figure 80 A, B, C and Figure 81 A, B, C. From these three projected planes, the results indicate that at the exhaust site both of the counter-rotating helicities recording the lowest static pressure drop into the core reaches -680 Pa. The gradual increases in static pressure towards the intake valve head are presented in Figure 82 A. Moreover, the bottom transverse helicity structure (Vortex-3) is maintained by the jet-wall flow; and the jet-jet flow attains -560 Pa of the static pressure within the core.

Figure 83 shows a quantitative static pressure distribution within the vortices and the low-pressure levels maintained in the cores of the rotating bulk gas, driven by centrifugal force. The depression in pressure is recorded in the core of all the vortices and the flow is treated as rotational where fluid rotates rigidly and it is velocity increases proportionally to the radius [83]. The second part of the vortex is maintained by the conservation of angular momentum similar to irrotational[11] flow characteristics. Figure 84 shows the velocity distribution and visible rotational and irrotational boundary regions for the aforementioned vortices, where the tangential velocity profile obtained a maximum value for Vortex-3.

A pressure comparison for Vortex-1 and Vortex-2 indicates $\Delta p =$ 140 Pa of pressure difference and an increased maximum tangential velocity of $\Delta V =$9 m/s for a low-pressure Vortex-1 case. Moreover, the Vortex-1 indicates a higher pressure recovery in free flow at a similar spatial dimension to Vortex-2.

[11] An irrotational flow structure is a low level of shear force or the tangential velocity v varies inversely as the distance r from the center of rotation, so the angular momentum, rv, is constant.

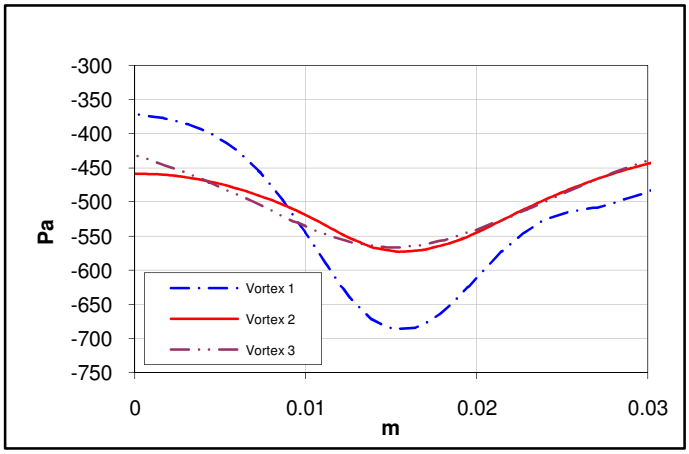

Figure 83: Profiles of Static Pressure within the Helicities at 130CAD: Vortex1, Vortex2, Vortex3

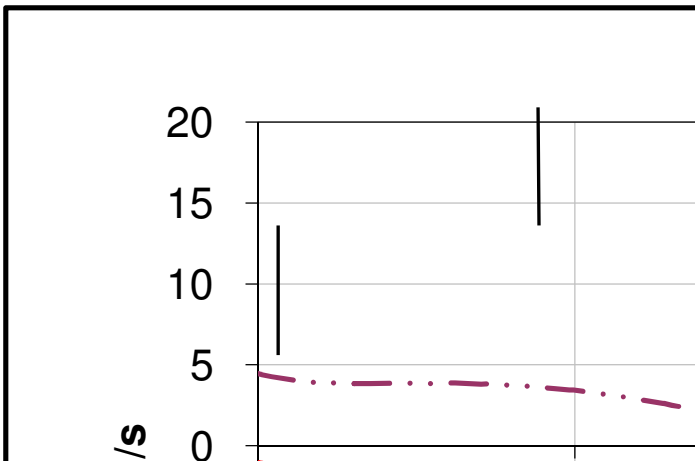

Figure 84: Profiles of Axial-Velocity Vz within the Helicities at 130 CAD: Cross-section plane Vortex1, Vortex2, Vortex3

Figure 85 shows the relations between vortices dimensions and the dynamics of the turbulence diffusivity effect (mixing). From the obtained data it is apparent that for all cases the centre of the vortex produces the lowest value of the dynamics eddy viscosity. The eddy viscosity parameter strongly influences the scalars transport and gas momentum exchange, e.g. the gas density and temperature concentration. Additionally, both of the created helicities are aligned within the valve axis of symmetry, carrying the old gas structure across the cylinder as shown in Figure 77.

The analysed vortices induced two important regions of the flow with respect to the mixing process and a favourable turbulence diffusivity level for this process. A low value of

the RMS of velocity fluctuation is found within the core of the vortex in Figure 85 and organises the flow as homogeneous and separated from major gas streams.

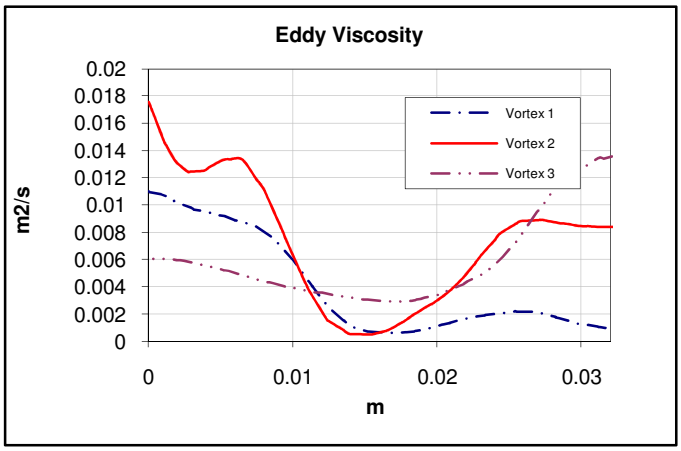

Figure 85: Profiles of Turbulence Diffusivity within the Helicities at 130 CAD: Cross-section plane Vortex1, Vortex2, Vortex3

The space enhanced mixing process is reminiscent of the amplification of the eddy diffusivity process because of the high mean and fluctuation velocity between the boundary of two vortex regions. The flow profile of Vortex-1 in Figure 81 and the second, counter-rotating symmetrical vortex exhibits irregularity and the higher eddy diffusivity parameter, near to the main discharged inlet jet, forms from the intake seats. As was previously mentioned, the strong intake jet separated the cylinder into two-formed large-scale rotating structures and split the middle cylinder section, intensifying the turbulence on the broad jet-vortex as shown in Figure 71.

The turbulence diffusivity structure characterised by Vortex-1 shows an asymmetrical pattern of dynamics eddy viscosity νt and visible deviations from the other analysed vortices. The concept of conserving a large-amount of kinetic energy and less dissipated flow within the vortex structure is very important for the HCCI engine where thermal in-homogeneities are the major factor controlling the beginning of auto-ignition.

8.3.1 Origin of the Long Time Vortices of the In-Cylinder Flow Characteristics

The CFD 'MK-MF1' model of the HCCI single cylinder engine is suitable for the study of the ensemble average long-term flow structures which appear within the cylinder for the induction and compression conditions. The sets of Figure 86 to Figure 91 present calculated velocity vector fields at the middle horizontal cross-cylinder plane for successive crank angles. It has been identified that two large-scale counterrotary coherent structures exist in the in-cylinder flow and persist until the TDC of the compression. The origin of both of the swirl structures is visible at 90 CAD aTDC in Figure 86, where a strong interaction between intake jet flows that were formed from the valve mouths and cylinder walls has taken place. The cylinder head shape directs the upper part of the gas streams towards the exhaust engine site; these gas streams are widespread near the cylinder head surface. The other part of the intake jet is transferred when the structure is deflected to the piston and changes momentum because of the surrounding cylinder gas. This structure manifests itself as a swirling gas region and appears when the horizontal component of vector field is close to the cylinder wall as in Figure 86.

From the earlier 3-D CFD analysis, it is known that the region of the upper cylinder head flow has a longer development-time[12] than the gas jet-wall flow over the rear part of the intake valves. Additionally, from the PIV data it is evident that the rear part of the vertical gas wall-jet approaches the piston's surface at 90 CAD aTDC. Figure 87 shows both symmetrical intake gas jet structures obtained at 110 CAD aTDC, while the centre of each vortices proceeds towards exhaust site. The noticeable recirculated gas streams are due to the effects of the separation flow under the intake valves as well as the helicity pattern visible in Figure 81 and Vortex-1 for the vertical plane of measurement. Additionally, it must be noted that the

[12] This is the time needed for gas to fill up the whole cylinder volume and approach the surface of the piston.

symmetrical pattern of the flow is maintained by the strong mid-cylinder jet covected from the valve bridge region; at this phase of the flow the valve bridge region has almost divided the cylinder volume into two independent flow regions. The presentation of the flow pattern at this plane reveals that the gas composition is strongly affected by the cylinder convection driven by the early large-scale cylinder structures. A similar flow pattern is observed at 130 CAD aTDC with a visibly intense flow within the middle cylinder region as well as under the intake valves.

In Figure 89 the BDC flow is maintained by the dynamics of the cylinder bulk gas inertia and is not affected by the piston movement. The most intense flow structure is encountered at the plane of cylinder symmetry and is managed by the large-scale rotating flows, at the intake side conserved within the 3-D lateral and longitude helicities presented earlier in Figure 79. Figure 90 presents the in-cylinder swirling flow affected by the piston movement in the later compression phase at 270 CAD. For both of the symmetrical swirling structures, the piston movement induces the swirling flow pattern near the exhaust combustion chamber.

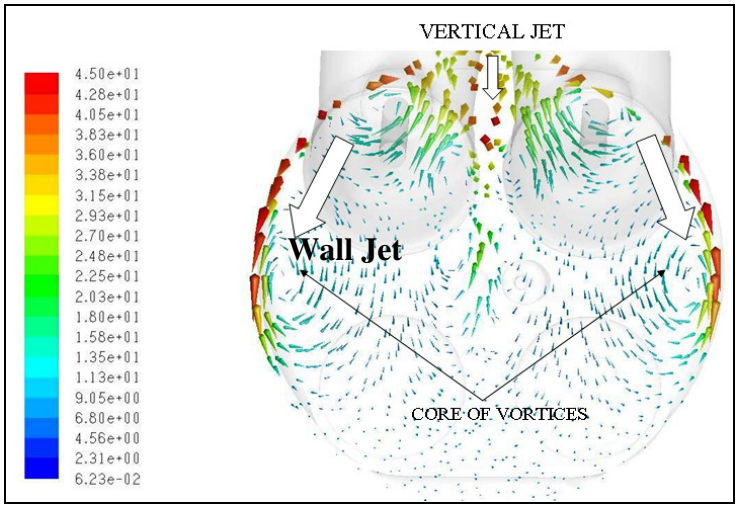

Figure 86: Middle Cross-Section of the Cylinder Plane-Early Swirl Development at 90 CAD aTDC.

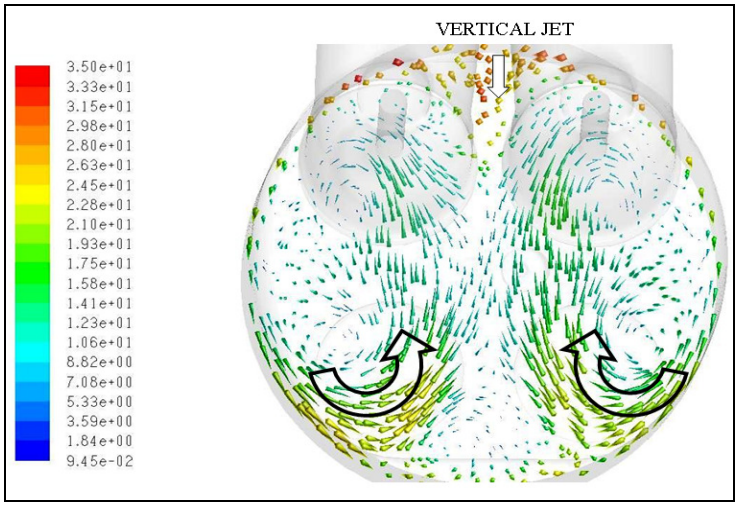

Figure 87: Middle Cross-Section of the Cylinder Plane-Early Swirl Development at 110 CAD aTDC.

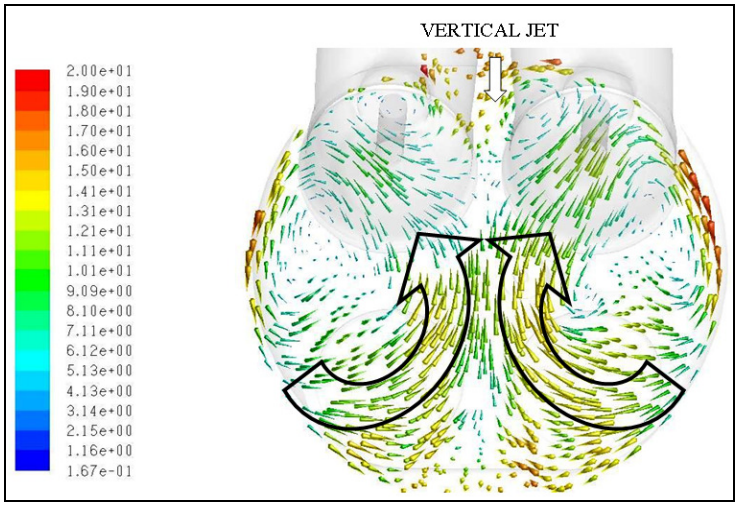

Figure 88: Middle Cross-Section of the Cylinder Plane-Early Swirl Development at 130 CAD aTDC.

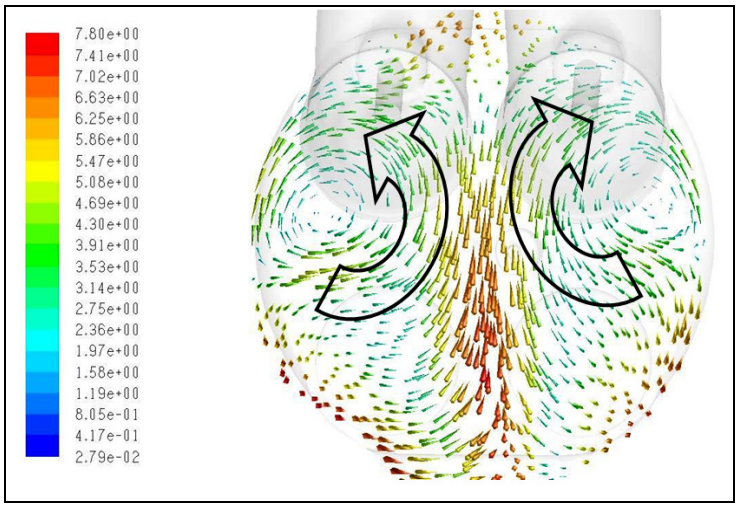

Figure 89: Middle Cross-Section of the Cylinder Plane- Swirl Development at 180 CAD aTDC.

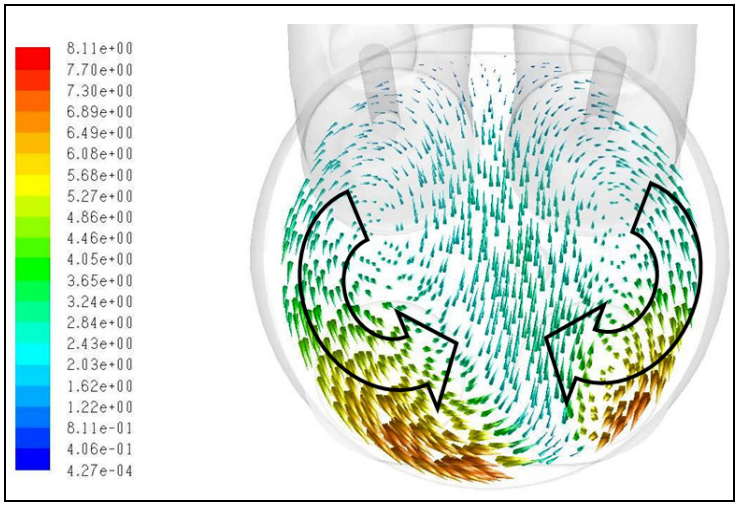

Figure 90: Middle Cross-Section of the Cylinder Plane- Swirl Development at 270 CAD aTDC.

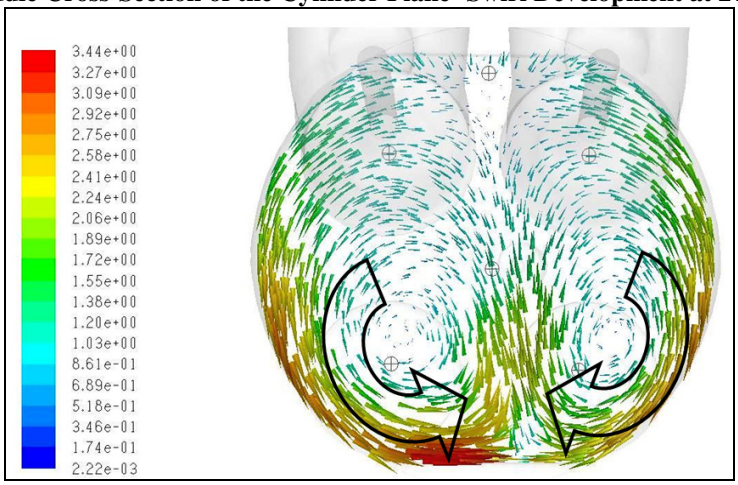

Figure 91: Middle Cross-Section of the Cylinder Plane- Swirl Development at 360 CAD aTDC.

This effect of intensifying the flow and slow preceding of both of the dominated swirl vortices at the exhaust side is controlled by the in-cylinder tumble flow distortion due to the gradual change in cylinder volume and the effect of tumble angular momentum conservation. It is interesting to note that the flow over the exhaust cylinder region during this amplification induced a similar magnitude of velocity to that obtained at 180 CAD (BDC). The effect of tumble compression and distortion is compounded effect of the spin up of the swirling flow, since in-cylinder flow is complex and 3-D.

The TDC velocity vector field presented in Figure 91 at the cross-cylinder plane shows that the general structures of the gas flow as well as the two major vortices have not vanished and continually transport the cylinder properties. The magnitude of the in-cylinder

velocity is roughly two times less than that at 270 CAD aTDC and still these structures intensely maintain the flow over the exhaust region. Moreover, both vortices exhibit dislocation in the direction of the exhaust cylinder wall. Figure 93 presents a timeline for the vortex's precession in the Y-axis, superimposed from the horizontal middle cylinder plane.

From the generated data, it is visible that after the BDC the middle section of the vortex is dislocated towards the exhaust engine part; this process is closely related to the intake valve closure phase and the extinct mass flow rate. For this stage, the pressure difference between the average cylinder pressure and the core of the vortex decreases as presented in Figure 94.

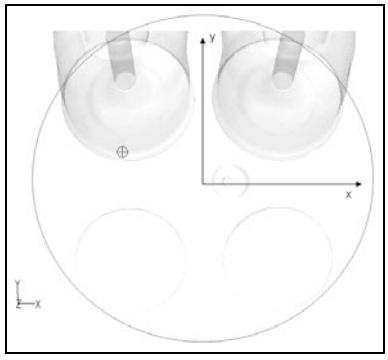

Figure 92: Cross-Section Plane of the Cylinder.

Moreover, the time history of the vorticity presented in Figure 95 indicates that the flow within the average middle cylinder region is continually maintained by the conservation of the angular momentum.

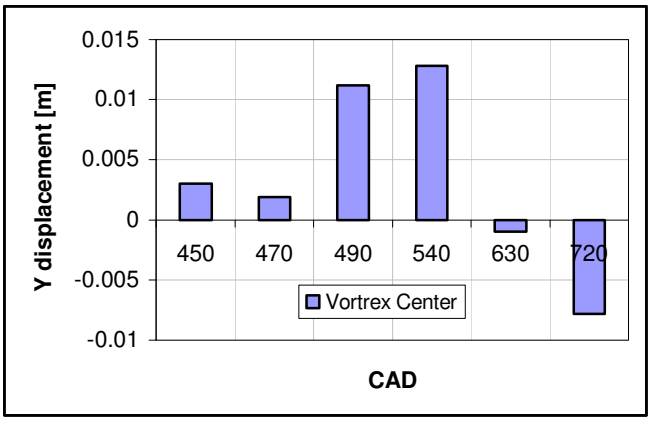

Figure 93: Vortex Precession Measured within the Left Side of the Engine Chamber in the Y Axis

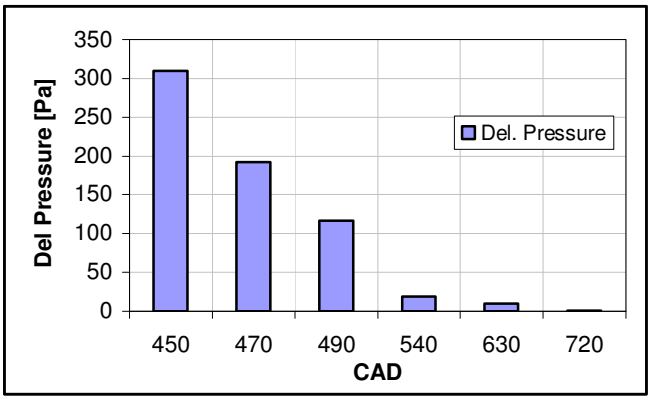

Figure 94: Pressure Difference (Del. Pressure) Obtained in the Core of Vortices Related to the Average in-cylinder Pressure

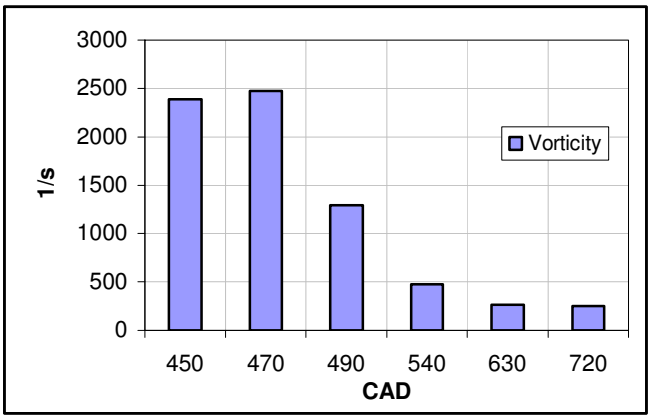

Figure 95: Average In-Cylinder Vorticity at the Cross-Section Plane

8.4 The Effect of NVO on the Development of Global In-Cylinder Turbulence, Vortex and Mixing Development.

The novel part of this work is based on the spatial characterisation of the coherent flow structures that appear within the HCCI single cylinder engine for the symmetric NVO valve timing at a constant engine speed of 1000 RPM. The role of the turbulent gas convection effect on the stratification of the in-cylinder scalars is crucial and has been analysed numerically for the induction and compression phase. It is believed that the analysed data can be useful for the improvement of the HCCI combustion control. For this reason, the mechanisms responsible for turbulence enhancement throughout the large-scale flow have been synthesised and related to distinct engine stages. In addition, the turbulence formations

are considered in detail with regards to the maintained role of the large-scale turbulent transport process established with the cylinder.

Figures 96 A and B present the time history of the in-cylinder ensemble-average turbulence intensity as well as the ratio of the angular momentum and the moment of gas inertia predicted by the computational model accordance with Equation (35). The averaged turbulence intensity parameter indicates the global trend of an in-cylinder mixing process without any specific spatial region distinction. In order to study about the bulk turbulence intensity process which has taken place within the cylinder, the main engine capacity is divided into two distinct volumes: the cylinder head and the swap-cylinder respectively. In Figures 96 A, it is pointed out that the first half of the intake stroke produces a strong turbulence intensity within the cylinder head domain which is dominant at these flow conditions. This is the result of the shear stress generated by the streams of the coinciding intake jets which are directed by the intake ports as well as the pentroof surface geometry.

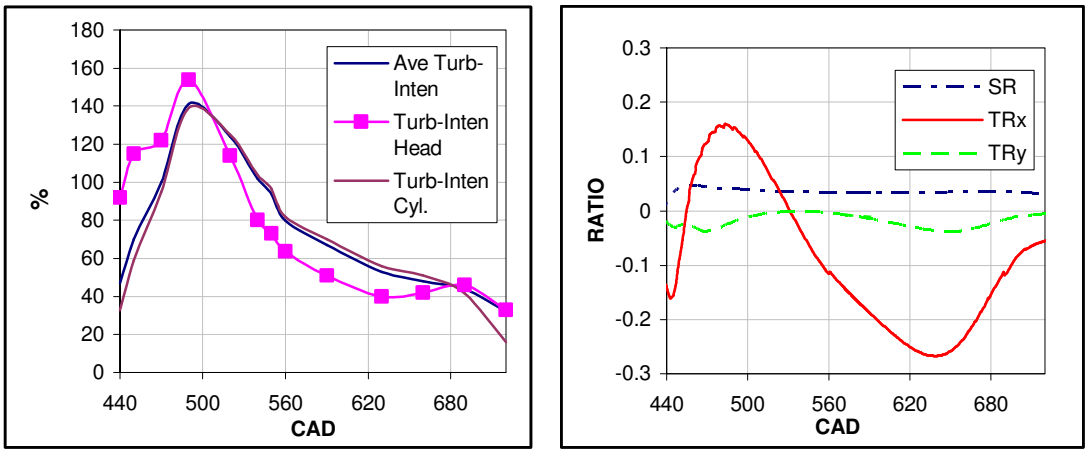

A) B)

Figures 96: A) The Time History of Average Turbulence Intensity within the HCCI Single Cylinder Engine (1000RPM) as well as in the Cylinder Head Chamber and Cylinder; B) Total In-Cylinder Tumble and Swirl Ratio (Gas Ang. Momentum/Moment of Inertia).

When the intake process gradually decays within the cylinder head domain the turbulence intensity becomes less pronounced, and the major mechanism of turbulence production switches to the large-scale flow structures. This effect is clearly visible in Figures

96 A). Within the cylinder head during the late compression phase the large scale rotating structures are compressed and their angular velocity are increased in accordance with a conservation of angular momentum to the point that there is not enough space within the cylinder and thus a breakup process ensures which enhancing turbulence. This effect is also visible in Figures 96 B; the tumble ratio is increased to its peak at 285 CAD aTDC and later on is gradually decreased, enhancing the global turbulence within the cylinder head region. Additionally, from the obtained characteristics of the cylinder tumble and swirl ratio profiles its apparent that the dominant asymmetric flow in the x-axis of the rotation is affected significantly by compression. On the other hand, the swirling structure in the z-axis conserves it is ratio and persists to the end of the TDC stroke, manifesting as two opposite vortices which were presented earlier in this thesis. The structure of this gas flow has strong implications in stratification and in the global mixing process due to weak radial transport.

The cylinder energy balance between the Turbulence Kinetic Energy (TKE) production and its Dissipation Energy (EPS) is performed with the k-ε 'Realizable' turbulence model [79]. The RANS solver and k-ε model are widely used as conceptualisations of turbulence to deal with the transient gas problem and to calculate energy balance, and to evaluate the mixing process and gas transport within the engine cylinder. The symmetric valve events for the HCCI engine and the low valve lift with the maximum mass flow rate are associated with high-energy dissipation. As a result, at 90 CAD in Figures 96 A, the turbulence intensity is increased within the cylinder head region due to the induced strong shear flow by the directed gas jet from the intake seat on the combustion chamber and cylinder walls. The minimum flow area at the intake valve curtain initialises a high average and RMS of velocity fluctuations, which is limited by the strong gas dissipation process (EPS). This expends the kinetic energy of the intake jet. In particular, the cylinder head region is responsible for the highest TKE and EPS with peak values of 27 m2/s2 and 300000 m2/s3

respectively as shown in Figure 97 A and B at 90 CAD. The deficiency of the kinetic jet energy within the cylinder is due to the partial transference of kinetic energy into heat. Inherently, this process increases the Entropy of the flow and decreases the Exergy and the possible amount of mechanical work which can be used to develop large-scale flow and gas transport.

All the aforementioned values indicate that for the early phase of the flow, the fluid at the top of the cylinder head yields a strong deformation and inherently produces a strong shear stress. For the sake of proper engine design and gas flow efficiency, spatial regions of high dissipation should be recognised. In Figure 98, an iso-view of the single cylinder engine is presented with marked regions of high shear stress at 90 CAD which reach 50 Pa. As was stated before, the source of the gas RMS fluctuation and enhanced shear stress lies in the cylinder head and the valve mouth geometric design as well as in the flow properties within the regions of the coinciding intake jets. Moreover with regards to the problem of the two fluid jets mixing, a cylinder flow region with a high shear stress is most effective for transporting and mixing liquid and gas e.g. fuel spray and free gas jet. In addition, the entrainment and droplets break up process is strongly dependent on the shear stress due to the high gas velocity fluctuation within the jet structure.

The HCCI engine combustion concept with various valve events for EGR trapping and recompression strategy in essence is affected by the internal flow field and temperature distribution. Unfortunately, with regards to volumetric efficiency, a gas state under strong deformation is not satisfactory as the optimal solution but it can influence the combustion efficiency due to the quality of the gas mixing process. For this reason, the gas dynamic process is visualized within the engine cylinder; and the energy balance between the dissipation and production of TKE is represented by the turbulent length scale (TLS) of Equation (2).

In Figure 99 A, the Turbulence Length Scale (TLS) reaches a minimum value of 9e-5 m at 80 CAD for both engine regions, e.g. the cylinder and head volumes. Figure 99 B, shows a high dissipation term for the EPS ***(ε)***, which appears in the Equation (2) and the eddy size is offset by the Klomogorov length-scale[13] calculated from the Equation (3). The lowest value of the TLS expends in-cylinder turbulence and decreases transport across the cylinder domain which for this phase is almost dissipated by the gas friction close to the poppet valve. The TLS and Turbulence Time Scale (TTS) dissipates its flow energy EPS ***(ε)*** in the coefficient of power to three compared to the TKE which is the function of the power to two.

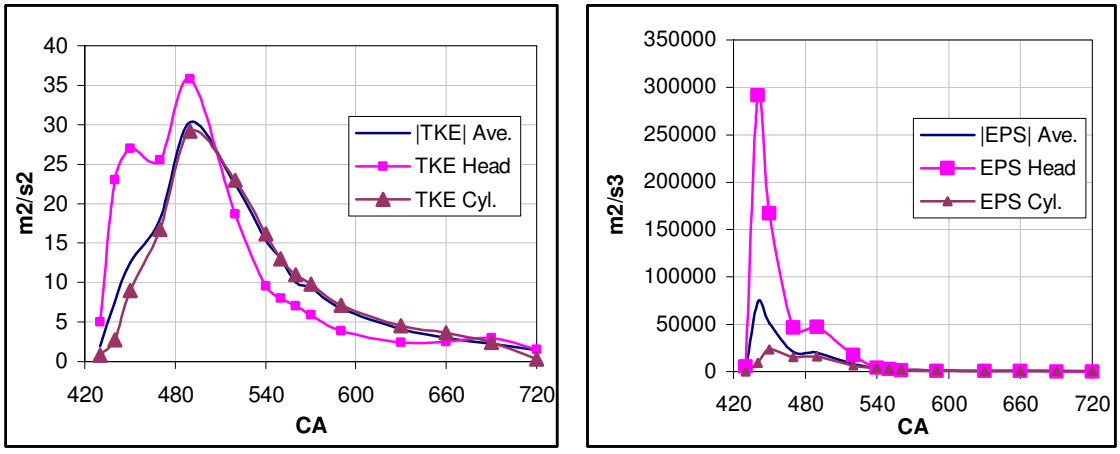

A) B)

Figure 97: A) TKE of the Cylinder Timeline; B) EPS of the cylinder Timeline

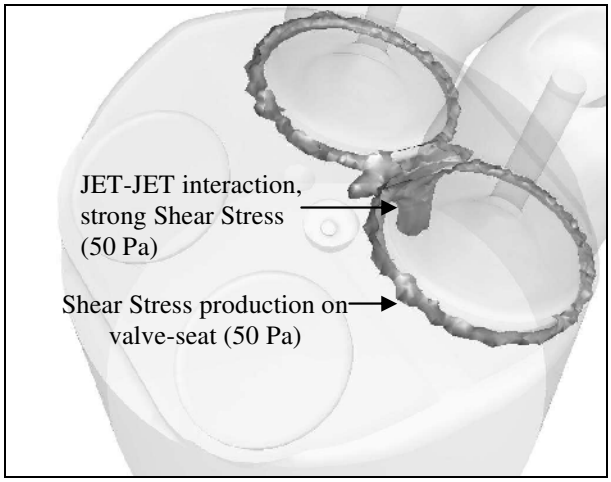

Figure 98: Engine Iso-View at 90 CAD: Mechanisms and Regions of Engine Shear Stress Production A) Intake Valve Seat; B) JET-JET Interaction

[13] The Kolmogorov LENGTH-SCALE theoretically provider the finest turbulence structure, close to the molecular scale of gas transport [1]

A simple comparison between TKE and EPS shows that the turbulent flow is always dissipative; the most efficient mixing flow contains the optimum value of TLS in the eddy structure. J. Lumley, proposed that 1/6 of the largest turbulent eddies are the main energetic turbulent eddies responsible for the most effective gas transport (mixing) within the engine cylinder. From the current numerical simulation, the calculated cylinder average-TLS has the maximum TKE of approximately 0.00125 m and is shown in Figure 99 B. The optimal average of the TLS has been extracted for the whole cylinder domain, but it must be noted that there are spatial differences within the cylinder volume. Based on the turbulence length scales definition, the most energetic structures are described as the ***(Li)*** Integral Length Scales.

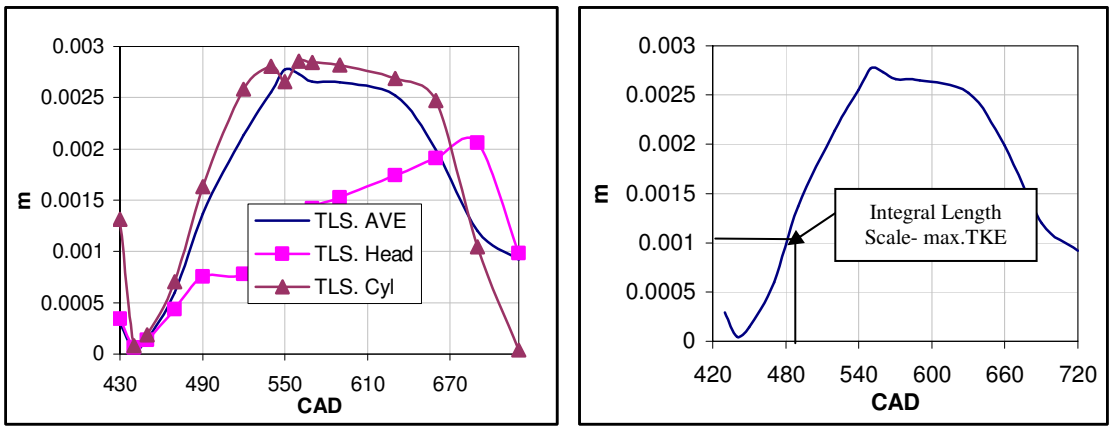

A B

Figure 99: A) The Time History of the Average In-Cylinder Turbulence Length Scale Extracted from the Cylinder Head Volume, The Cylinder and Total Engine Capacity. B) The Numerical value of the most energetic turbulence length scale TLS within singe cylinder engine.

It is remarkable that the maximum average in-cylinder turbulence intensity presented in Figures 96 is obtained near to the MOP of the intake valve rather than for the case of the maximum mass flow rate. One of the reasons for this is due to the optimal energetic TLS of the intake jet dimension, which for 130 CAD is of the maximum valve lift order. A generally less dissipated flow for the 130 CAD is obtained mainly near the valve seat and the bottom cylinder head parts. The free shear intake jet, which fills up the whole cylinder domain with

optimal velocity, is another reason for the higher averaged in-cylinder TKE. In Figure 100 and Figure 101 A and B the spatial cylinder PDF functions of the TKE and TLS across the cylinder domain are based on the Equation 2 for two cases, 90 and 130 CAD aTDC respectively. It has been found that for both of the cases, 90 and 130 CAD aTDC, apart from the average value of the cylinder TLS, the most energetic spatial representation of the eddy structures with a low turbulence energy dissipation is obtained for the turbulence length scales in the range of 0.003-0.004 m. The most energetic TLS for both conditions is represented in Figure 102 by the gas structures situated beneath the intake valves and the bottom cylinder region respectively. The higher turbulence energy dissipation EPS process within the valve port and the upper cylinder head region at the MOP imposes a higher volumetric-fraction of the TKE which is represented in Figure 97 A and B and characterised by the charged jets and vortices.

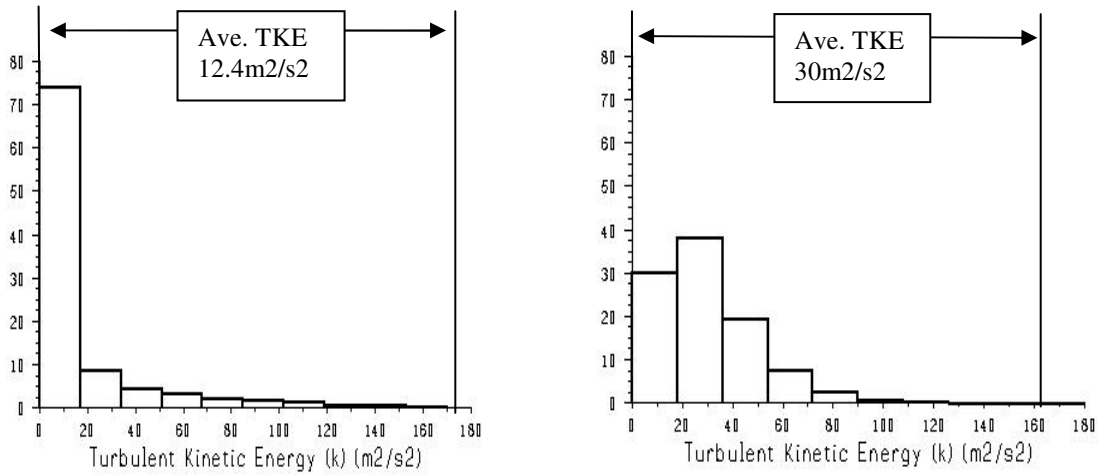

A) PDF function of TKE at 90 CAD aTDC B) PDF function of TKE at 130 CAD aTDC

Figure 100: PDF Function of the Spatial Flow Representation of the In-Cylinder Flow: A) TKE at 90 CAD aTDC; B) TKE at 130 CAD aTDC

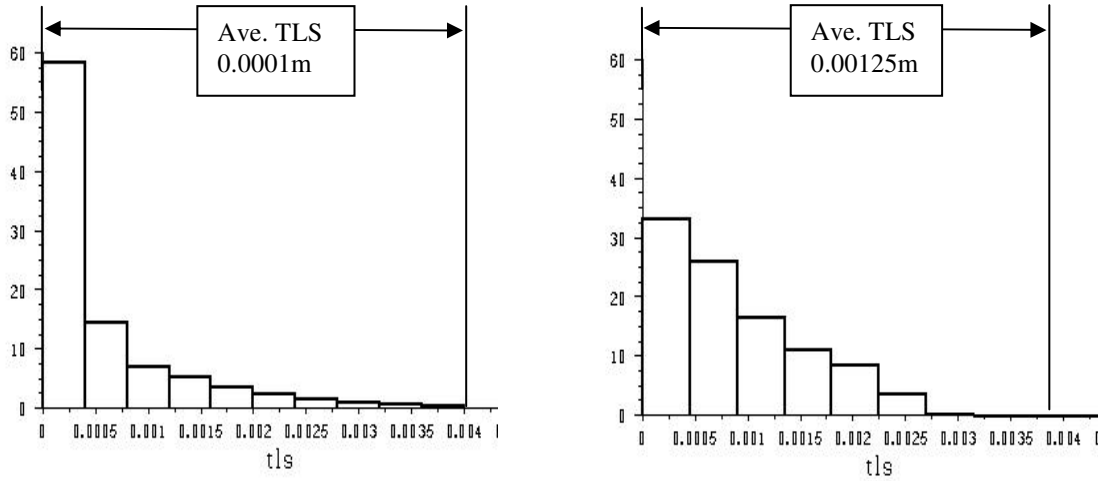

A) PDF function of TLS at 90 CAD aTDC B) PDF function of TLS at 130 CAD aTDC

Figure 101: PDF Function of the Spatial In-Cylinder Turbulent Flow Representation A) TLS-Turbulence Length Scale at 90 CAD aTDC; B) TLS-Turbulence Length Scale at 130 CAD aTDC

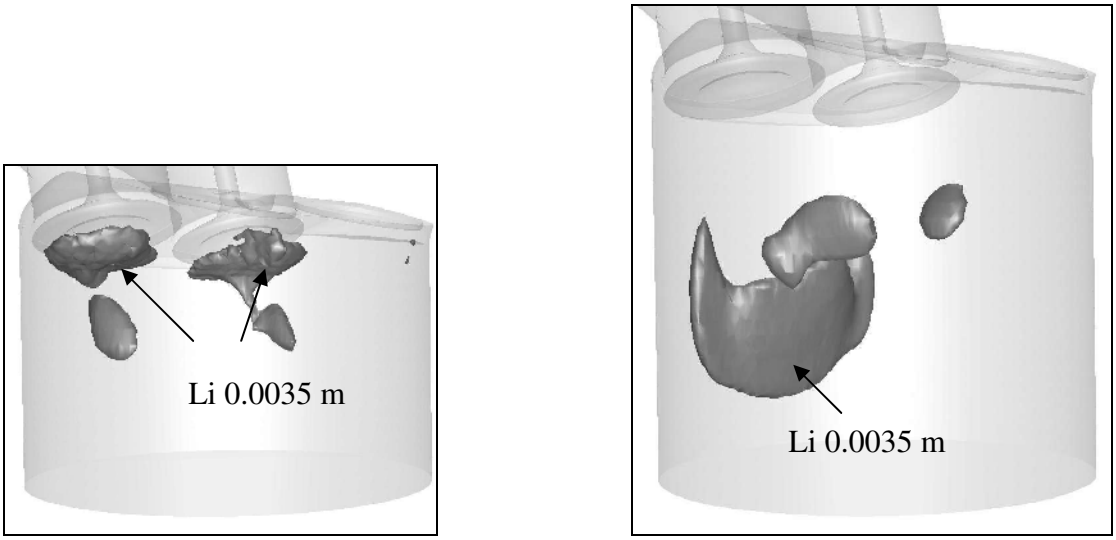

A) ISO-View TLS at 90 CAD aTDC B) ISO-View TLS at 130 CAD aTDC

Figure 102: ISO-View of the Spatial Turbulent Integral Length Li Scale A) TLS at 90 CAD aTDC; B) TLS at 130 CAD aTDC

The in-cylinder volume is filled-up at the BDC by the organised structures, e.g. the vortex and the jet action across the cylinder domain and it transports the gas properties. As was presented before the flow cylinder structures with a low EPS and a high TKE are favourable to enhance the in-cylinder gas mixing process. These structures are crucial in the later compression stroke where the contained energy is realised as turbulence due to the shear flow and vortex break-up process [85]. The vortex break-up process enhances gas transport

and influences thermal stratification. The mentioned organised structures are induced within the engine cylinder through the piston movement in relation to the engines geometry and the mass flow rate. During the decrease of the volume near the BDC position, the major intake jets become more unstable since not enough energy being supplied from the inlet flow. Moreover, the large vortex structures become cylinder dominant. This effect generates large-scale flow with a generally low TKE and a larger TLS. It features a lower dissipation process and persists to the end of the compression stroke.

For the late compression phase in Figures 96 B and Figure 97 A it is apparent that part of the tumbling flow is spun-up and discharged into smaller turbulence length scales and that the TKE is enhanced within the cylinder head due to the cascading process [1]. Moreover, the dynamic process of the tumble break-up near the TDC maintains the decayed flow. Figure 103 presents a 2-D spatial TLS representation of the in-cylinder gas flow affected by the two opposite swirls and the region of higher gas velocity. It is apparent that the most energetic flow structures are performed by the largest TLS eddies within the middle part of cylinder head volume and are coupled with the large-scale swirl flow effect. The most energetic TLS at this region is within the range of 0.002-0.0025 m which is coupled with the two high TKE cylinder zones of 2.38 m2/s2 presented in the iso-view Figure 103. The two cores of the TKE divide the cylinder chamber into two regions and lie along the intake valve-axes. Both of the visible spatial cores of the TKE are coupled with the energy distortion of the two longitudinal large-scale helicities, which were set during the intake process. At the engine compression phase, the TKE energy contained within vortices is dissipated more intensively near the walls and the piston, due to the shear force. The most intense in-cylinder flow at the TDC generates shear stress itself and the cylinder properties tend to become uniform [1, 75]. In addition, the higher TKE at TDC is conserved within the middle part of the cylinder head's geometry and is presented in Figure 103

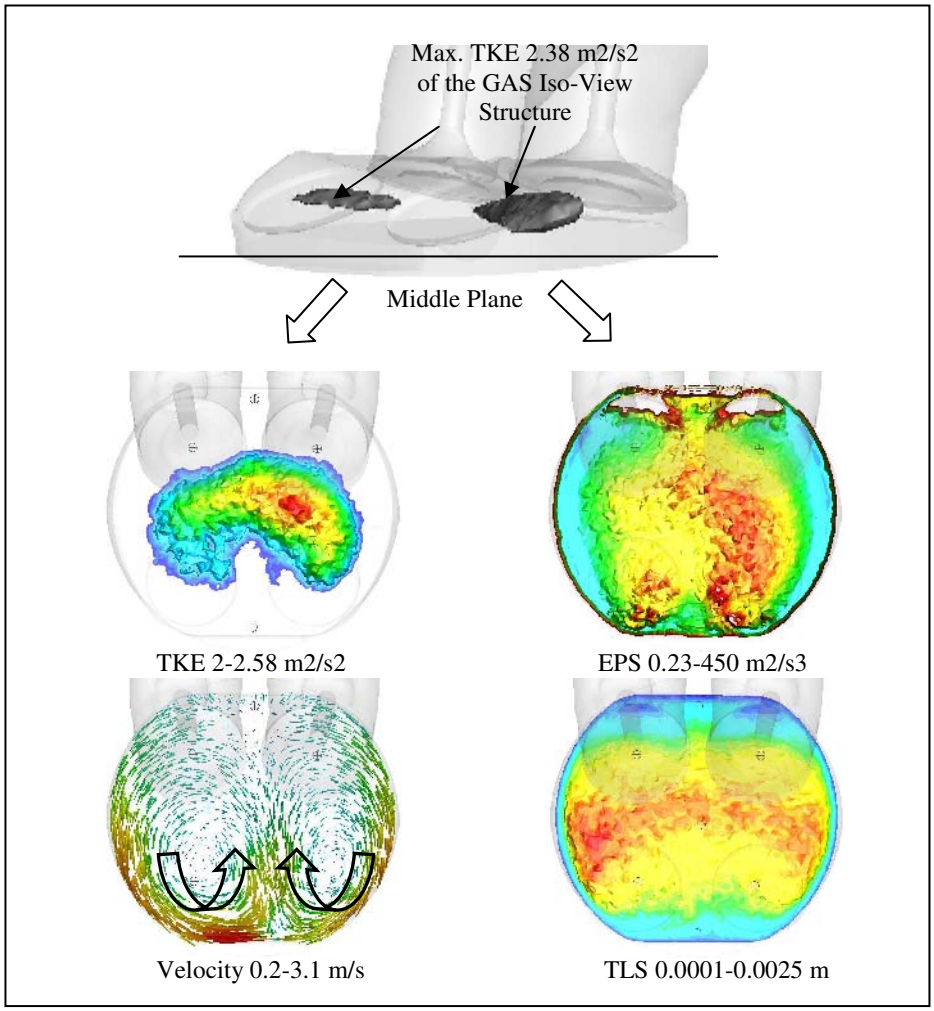

Figure 103: The Complex Characteristics of the In-Cylinder flow at TDC base on the TKE, |V|, EPS, TLS parameters.

8.5 The Qualitative Representation of the Engine Cylinder Mixing Phenomena

The numerical 'RANS' solver, with a Reynolds decomposition form for the major equations, and an additional k-ε model for the closure Reynolds Stress term are used to predict the energy balance between the largest and the lowest scales of flow via turbulence kinetic energy and the dissipation effect that takes place in the Kolmorgorov micro-scale. Two important mechanisms influence the effectiveness of the gas mixing process: the set up of the large-scale gas advection process by the boundary conditions, e.g. the geometry of the engine and the valves, the piston velocity and the Mach Number; and turbulence transportation which is indispensable part of the flow [86].

The large-scale cylinder flow is characterised by the convection effect of macro structures visible as coherent products such as gas jets, vortices and regions of the wall flow. These structures are mainly responsible for the transport of gas properties and they affect the balance of the global in-cylinder scalars as well as turbulence production. Figure 104 illustrates the spatial and temporal iso-maps of the averaged turbulence kinetic energy (TKE) obtained within the modelled single cylinder engine for the following crank angles: 90, 130, 180, 230, 270 and 360 CAD respectively. The aforementioned quality data are chosen to illustrate the higher spatial in-cylinder velocity fluctuations, set to level of 20-35% above the average values of the cylinder TKE. The range of the high level of the TKE is reminiscent of the wide cylinder volumetric representation of the velocity fluctuation within bulk gas vortices and jet structures.

The quality pictures A and B during the early gas induction process in Figure 104 indicate the spatial and temporal variations of the in-cylinder turbulence development. The qualitative analysis shows that at 90 CAD the presented average gas structure of TKE for the chosen 35 m2/s2 is characterised by the most energetic gas formation in the middle and upper cylinder regions. These gas formations are maintained by the intake gas jets. The highest values of the TKE manifested by the high-fluctuating velocity components exceed 150 m2/s2 of the TKE in the core of the middle cylinder flow region. Additionally, it must be noted that within the remaining cylinder volume the gas turbulent structure is uniform. Figure 105 presents the statistical PDF of TKE formation within the cylinder. From the statistical data, it is apparent that almost 75% of the cylinder volume has a TKE in the range of 0-18 m2/s2 at 90 CAD aTDC. A comparison of 130 and 360 CAD aTDC has been presented.

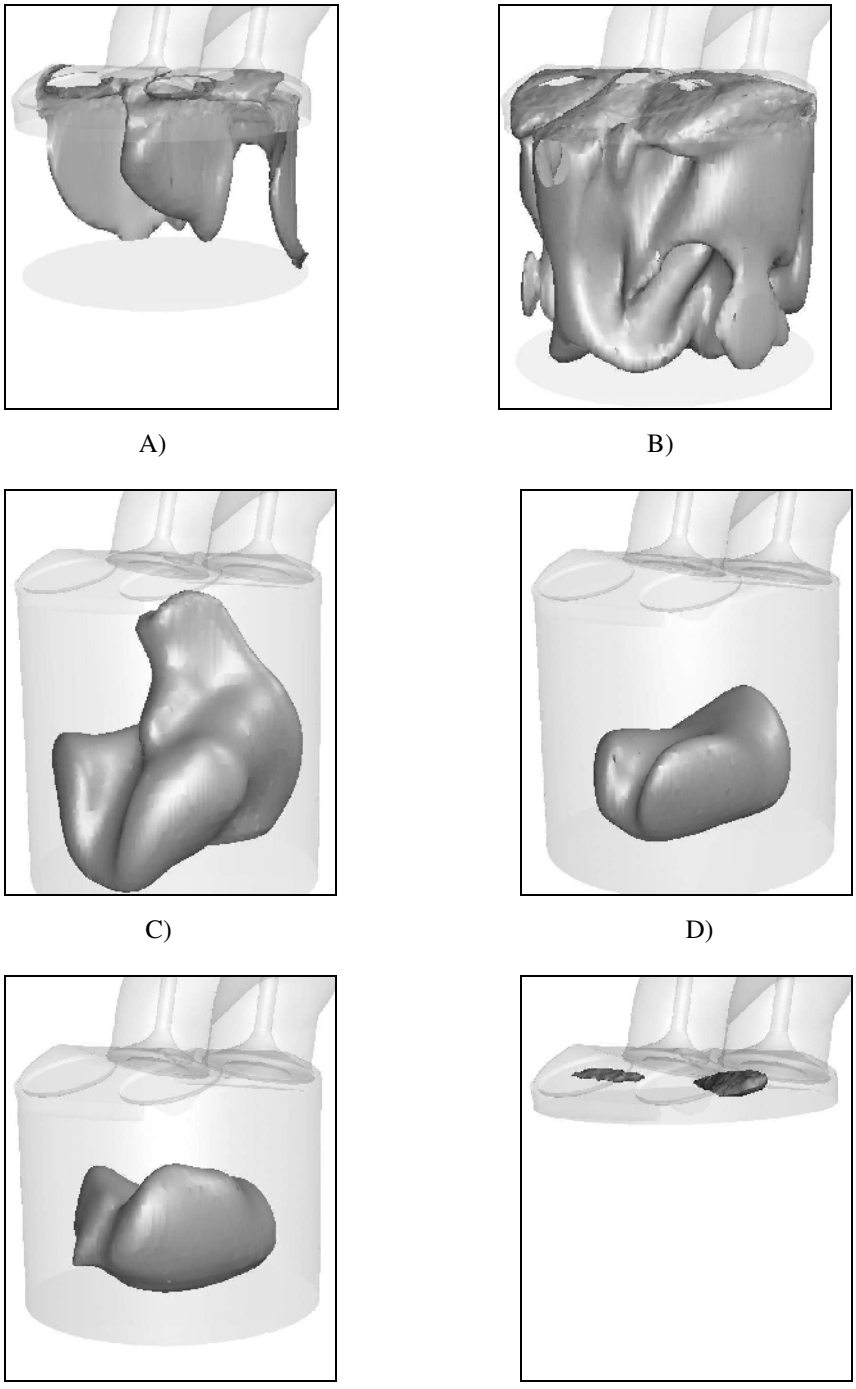

Figure 104: Temporal Development and Spatial Representation of Turbulence Kinetic Energy within the Engine Cylinder-Offset above 35% of average Turbulence Kinetic Energy (iso-surface): A) 90 CAD iso-TKE 32 [m2/s2]; B) 130 CAD iso-TKE 32 [m2/s2]; C) 180 CAD iso-TKE 20 [m2/s2]; D) 230 CAD iso-TKE 10 [m2/s2]; E) 270 CAD iso-TKE 6 [m2/s2]; F) 360 CAD iso-TKE 2.3 [m2/s2]

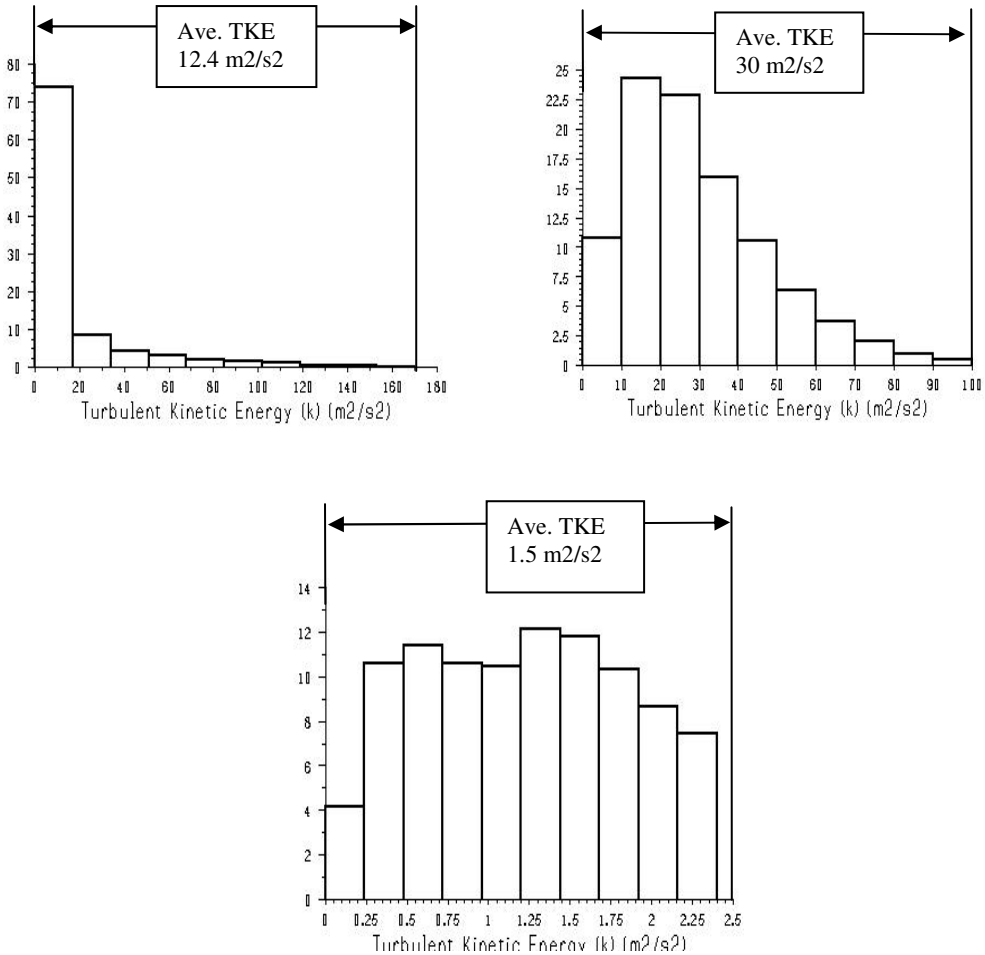

Figure 105: PDF Function of TKE for Consecutive (90, 130, 360) CAD aTDC

8.6 Discussion and Summary

The in-cylinder CFD three-dimensional 'COLD' flow data has been combined with the 2-D PIV results in order to extend the spatial and temporal scalar information about the internal engine flow at 1000 RPM. Moreover, at a chosen symmetric NVO valve timing, the gas exchange process and the gas mixing quality in the four-stroke DI HCCI engine have been examined. Another important achievement is obtained by building the numerical model of the single cylinder engine which is able to predict the major large-scale flow structures along the engine induction and compression phases. In addition, a built Mk-MF1 CFD model supplies a

fairly good prediction of the cylinder TKE and Turbulence Intensity as well as raising the possibility of using various flow strategies and physical models for the future work.

For the current study, a 3-D numerical multi-cycle single cylinder engine was built and the CFD k-ε RANS solver was used to calculate the spatial in-cylinder turbulence intensity, Eddy Viscosity, TKE, EPS and TLS. The computational results were compared and validated against the experimental PIV velocity vector fields and the in-cylinder pressure data. The series of results were analysed for specific CAD and over several cycles to gain stable flow conditions. The single cylinder HCCI numerical model has achieved good accuracy in terms of in-cylinder flow structure accuracy as well as the similarity in velocity magnitude for the chosen plane of measurement. The large-scale in-cylinder flow is predicted correctly with a whole type of structures, e.g. vortex motion, gas jet interaction and the near surface effects on eddy induction.

It has been found that the in-cylinder gas formations, in the favourable range of 90-130 CAD aTDC as regard the high mass flow rate, potentially induced a strong shear flow and produced turbulence. Moreover, the development of the turbulence and the development of coherent structures at the beginning of induction have an impact on the later gas mixing process and the spatial character of the large-scale flow. Part of the flow creates swirling structures, which dissipate energy in a very late compression phase and influences the on gas stratification and the mixing process. From the computational data, it is clearly visible that the upper cylinder flow is not able to approaches and mix with the bottom cylinder bulk gas. This influences strongly the structure of the exhaust cylinder head gas. It is important to note that the core of each vortices attains the lowest velocity magnitude and maximum level of vorticity as well as low static pressure compared to the rest of the flow field.

The varied scales of the velocity magnitude rise in the cylinder domain as a mutual process of the jet-wall and vortex action, organised by complex aerodynamic effects. The velocity magnitude extremities encountered in the narrow flow region manifest as a separation flow under the intake valves and are the origin of the large-scale vortices and the gas stratification structural mechanisms. The visible intake jets produce a cylinder flow which experiences a strong turbulent advection process toward the piston's surface and carries the intake gas that is fresh compared to the rest of field. The above mentioned phenomena of the turbulence advection process by the mean flow is one of the major factors responsible for the gas transport and the quality of the cold gas mixing at the early intake stage.

The existing RMS of the velocity fluctuations within the middle cylinder jet enhances the turbulent mass transport (mixing) of the fluid and enhances the heat transfer for the whole cylinder domain in comparison to the core of the large-scale vortices. Figure 65 presents the valve-body obstacle effect on the gas turbulence viscosity parameter. This is characterised by the progress of the mixing beneath the intake valves. The centre of both vortices seems to more effectively dissipate the in-cylinder flow in relation to the lower RMS of gas velocity fluctuations and constant angular velocity profile.

Chapter 9

NUMERICAL INVESTIGATION OF THE IN-CYLINDER GAS THERMAL CONVECTION EFFECT ON SPATIAL THERMAL STRATIFICATION

9.1 Introduction

The previous chapter with the CFD-PIV coupled analysis shows the complex nature of the development of the in-cylinder scalar, vector and tensor fields. Furthermore, the thermo-flow field analysis for HCCI technology is important because auto-ignition combustion control needs a good understanding of difficulties is preferable in order to spatial mixing and gas convection. These two most important scalar fields, e.g. temperature and mixture composition under fluid convection and diffusion mechanisms, are maintained by the in-cylinder gas flow and they can be simulated by the CFD model. However, in this thesis only the non-reactive cases are considered.

The present chapter has been designated for the parametric CFD study in order to gain information about the level of the in-cylinder gas thermal stratification induced by the intake port deflectors. A three-dimensional CFD model of the single cylinder engine is used to calculate the spatial and temporal gas temperature distribution convected throughout the large-scale flow structure mechanisms. For the current research, a symmetrical (110CAD) negative valve overlap NVO strategy has been chosen as the most common way to keep a desirable amount of the gas thermal energy within the cylinder; and it is utilised for the active autoignition control in HCCI engines. Moreover, for the thermal simulation all the engine

walls have a temperature set to 350 K and are in line with the experimental 'COLD' flow data.

9.2 Distribution of the In-Cylinder Gas Thermal Coupled with Early and Late Gas Induction Phase.

The valve timing and intake gas dynamics process control the level of internal residual gases trapped within the cylinder and transport them along the large-scale flow structures. The coupling of both thermal and flow gas effects gives the possibility of a better analysis of in-cylinder thermal in-homogeneity mechanisms since the current experimental PIV method captures only the velocity vector flow pattern. The initial and boundary conditions for thermal engine gas simulation are present in Table 7.

CFD Engine	**4 valves per cylinder, 1cyl.**
RPM	1000
Bore	89.0 mm
Stroke	90 mm
C.Rod	150 mm
Compression Ratio	11.3
Intake Valve Open	IVO415CAD
Exhaust valve Close	EVC305CAD
Intake Temperature	300 K
Initial Cyl. Gas Temp (TDC recompression)	750 K
Intake Pressure (table)	Wave 1-D code
Initial Cyl. Wall and Piston Temp.	350 K

Table 7: Initial and Boundary Conditions for CFD Thermal Simulation

In previous chapter, the validated CFD model calculated the major in-cylinder flow structures and presented the main mechanisms responsible for them. Based on the CFD 'RANS' single cylinder engine model, the thermal stratification effect can be captured spatially and temporally within the cylinder. The CFD simulation is less expensive than the experiment and it could also be fully three-dimensional. An indirect method of coupling the experimental flow velocity vectors and the temperature field is a potential way forward in the field of HCCI research. In addition, hot cylinder gas transport is evaluated, including the

mixing process in the region of the high eddy viscosity flow. The different rates of gas mixing process, which occur across the cylinder domain, control the thermal gas stratification. In this work, the following engine phases are presented as the most significant for the HCCI thermal field development: engine gas induction with apparent early and late back flow effects, as well as large-scale mixing structures which transport gas across the cylinder domain.

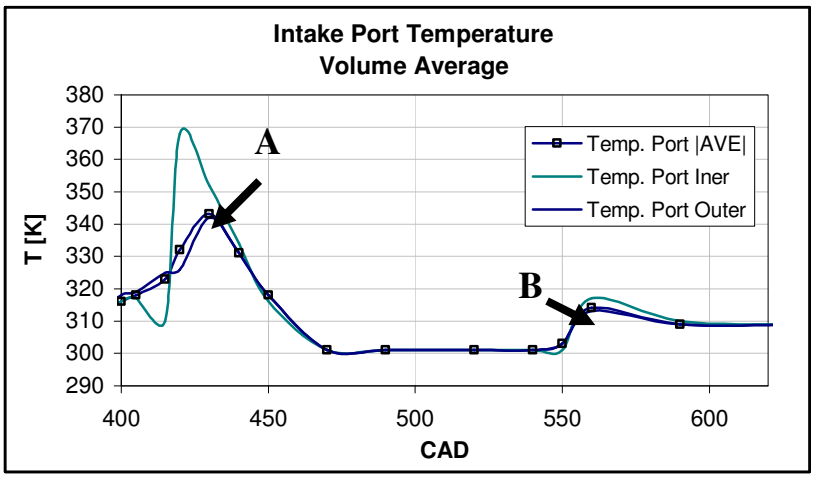

Figure 106: The Average Gas Temperature within the Middle Valve Port Region (Back-Flow)

At the early and late intake phase for the chosen symmetric NVO of 110 CAD, the cylinder pressure difference induces a strong back flow towards the open-end of the channel. The early and late engine stage costs in-cylinder thermal energy and affects the thermal stratification of the bulk mass. In addition, part of the hot internal recompressed fluid expands into the intake port and mixes with remaining gas from the previous cycle as well as with fresh intake air. After the back-flow stage, all the dumped gases within the port pocket are sucked back with the fresh air and influence the development of the cylinder mixture and the quality of the transport process in terms of intake.

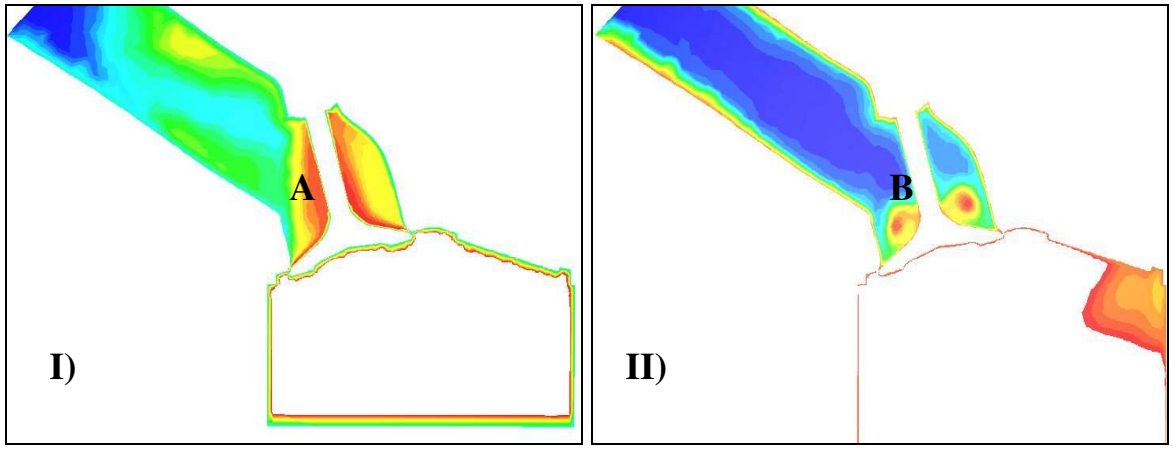

Figure 107: The CFD Representation of The Gas Thermal Flow Compositon(Red colour 380K, Blue 310K). I) Back-Flow at 70 CAD aTDC, II) Back-Flow at 190 CAD aTDC

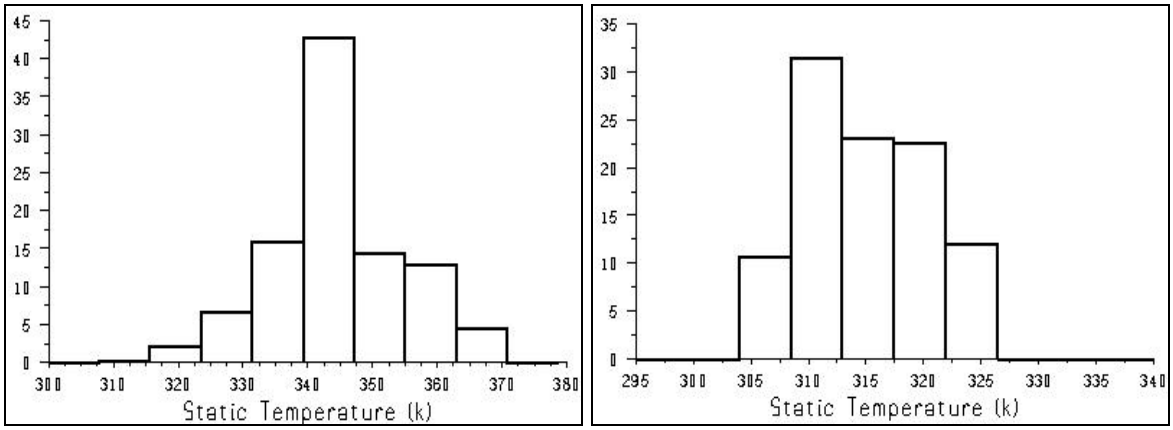

Figure 108: The PDF of Gas Temperature differences within The Valve Port for 70, 190 CAD aTDC

In Figure 106 and Figure 108 the computational results are presented for the average volume and the spatial port gas temperatures at 90 CAD and 190 CAD aTDC respectively. From the CFD data it can be seen that the hot expanded gas attains a temperature peak of 370 K at 70 CAD aTDC near the intake valve stem and 340 K in the upper part of the canal. Moreover, the outward cylinder gas flow fills-up almost 80% of the intake manifold volume, with an average temperature of 320 K at this phase. In Figure 108 B, the presented PDF graph indicates a much lower temperature peak of 325 K with the average gas port temperature of 306 K for the 190 CAD aTDC back-flow phase.

The back flow to the intake manifold modifies the in-cylinder gas temperature distribution in the later inward gas flow process. The velocity vectors and the thermal scalar field interaction at 90 CAD aTDC in Figure 109 A shows the velocity vectors coloured by the

temperature scalar field on the middle cylinder plane. The in-cylinder large-scale flow varies thermally across the cylinder volume. The lowest gas temperature of (298-305) K is apparent within the core of the real intake jet deflected by the cylinder wall towards the pistons surface.

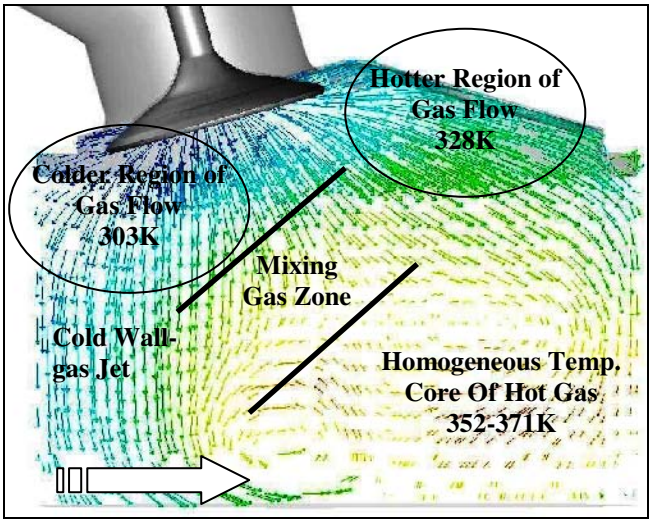

A) The Middle Cylinder Plane of the Gas Thermal-Flow Structure at 90 CAD aTDC

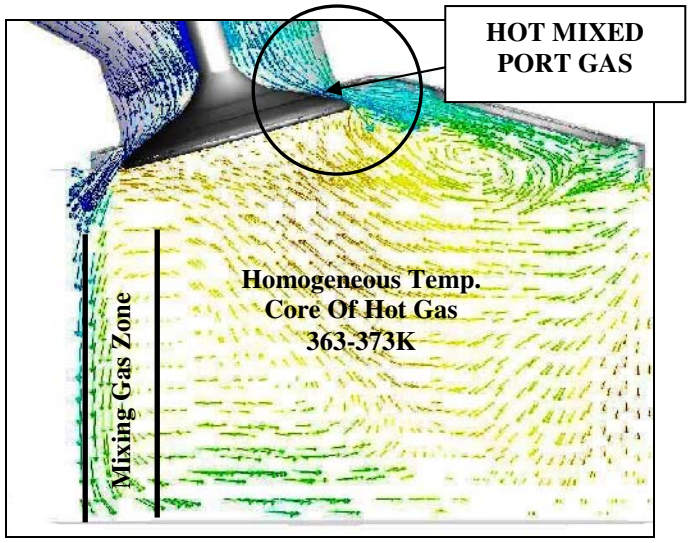

B) The Intake Valve Cylinder Plane of the Gas Thermal-Flow Structure at 90 CAD aTDC

Figure 109: The Thermal Gas Structure within The Engine Cylinder; A) Temperatures on the Middle Cylinder Plane of Flow; B) Temperatures on the Middle Cylinder Plane of Flow

In addition, the middle cylinder flow indicates the explicit effect of the thermal gas mixing process between cold and hot cylinder fluid structures. The main mechanism responsible for the deep in-cylinder penetration and the complex gas mixing process is the turbulent structure of the jet-jet gas interaction origin from the upper part of the cylinder head bridge. As was stated in chapters 5, 6 and 7 the jet-jet highly turbulent aerodynamic structure carries the main

intake jet charge across the cylinder domain with a large RMS of velocity. The cylinder region with a wide turbulent gas mixing zone and the jet-jet structure is indicated by two lines in Figure 109 A. On the other hand, the homogeneous hot gas core of (352-371) K and the two counter-rotating vortices point out significant differences within the thermal flow field at the bottom middle cylinder region. In addition, the gas jet flow from the top cylinder head is directed at the exhaust side and characterises the higher temperature of the gas structure, thus the rear cold wall-jet. This is the effect of the later discharging of the hot gases from the front part of the intake port. The manifold flow is not yet fully developed at this CAD.

Unlike at the middle cylinder plane of symmetry the thermal gas flow structure at the intake valve plane indicates a cylinder temperature field that is more homogeneous and hotter i.e. (362-373) K. The intake valve acts as an aerodynamic body which shrouds this cylinder region and prevents both cold intake and hot cylinder gases by direct mixing. The separation gas effect of the intake valve increases the average field temperature from 340K to 361K at the middle valve plane due to a poor mixing with fresh gases. However, the strong separation flow which takes place beneath the intake valves generates a complex flow pattern that is characterised by a low turbulence intensity. The turbulence intensity peak calculated at both planes are 140.2% and 65% of the mean piston speed for the middle and valve region respectively. It must be noted that the hot cylinder gas core is convected toward the intake valve head according to Figure 77. The mixing gas structure visible at the valve plane imposes a strong temperature gradient near the cylinder wall-jet flow region as well as at the bottom of the pistons surface.

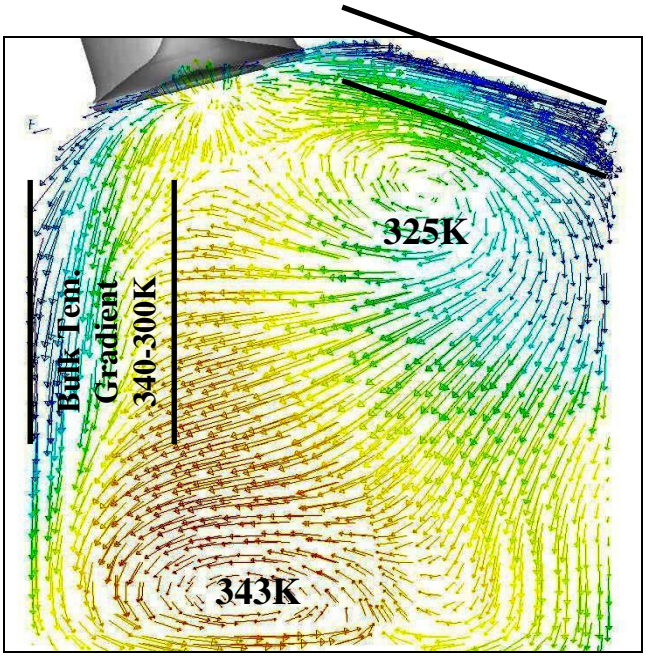

A) The Middle Cylinder Plane of the Gas Thermal-Flow Structure at 190 CAD aTDC

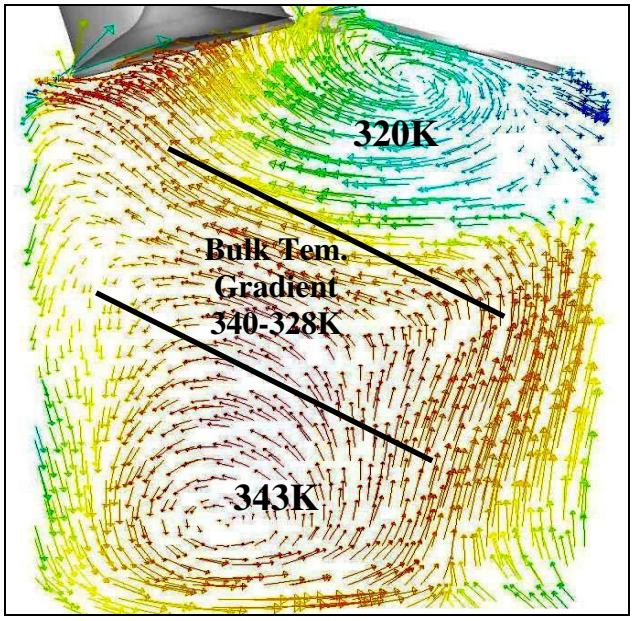

B) The Intake Valve Cylinder Plane of the Gas Thermal-Flow Structure at 190 CAD aTDC

Figure 110: The Thermal Gas Structure within The Engine Cylinder A) Temperatures at the Middle Cylinder Plane; B) Temperatures at the Valve Cylinder Plane of Flow

A stronger in-cylinder thermal in-homogeneity appears in the spatial gas distribution occurring at the late back-flow of 190 CAD aTDC in Figure 110 A and B. The large-scale vortices change the cylinder flow pattern significantly on both the middle and the intake valve measurement planes, especially in the cylinder region under the intake valve head as shown in Figure 110 B, where the hot gas is mixed with the cold gas structure convected from the upper

part of cylinder. This is partially the dynamic effect of the remaining adverse pressure forces and the balance of the gas density in this cylinder region. The upper fresh gas mainly is structure enclosed by the vortex with a visible density stratification as shown in Figure 110 A. A similar gas effect of bottom density stratification is produced at the vortex near the piston's surface with the hottest fluid core for all the domains.

Both of the cylinder thermal regions indicate the lower average temperature difference which at this stage is $\Delta T=14$ K. However, large thermal gradients for the convected gas still are visible, even at the end of the induction phase. This suggests that the large-scale flow structures characterised in the previous chapter, especially the vortices and wall-jet, actively control not only the flow but also the thermal gas mixing process. It must be noted that natural convection occurs at the cylinder wall and the large temperature gradient also strongly influences the thermal gas mixing process, especially at the TDC of compression.

9.3 In-Cylinder Thermal Gas Distribution at Engine Compression TDC

Two different intake port strategies have been applied in order to evaluate the development of gas cylinder in-homogeneity. The 'SWIRL' type of intake port deflector as well as the standard port geometry was taken to make the thermo-flow cylinder comparisons. The initial cylinder thermodynamic parameters at 5 CAD before IVO for both of the intake port types were chosen as follows: 88000 Pa, 440 K; these were approximated to one dimension and to the experimental values discussed in chapter 7 and 8. The gas velocity and temperature are set-up as uniform fields across the cylinder domain for a comprehensible indication of the effects of intake ports on the progress of thermo-flow. The temperature of the computational engine walls, including the piston, is set to 350K throughout for both simulations.

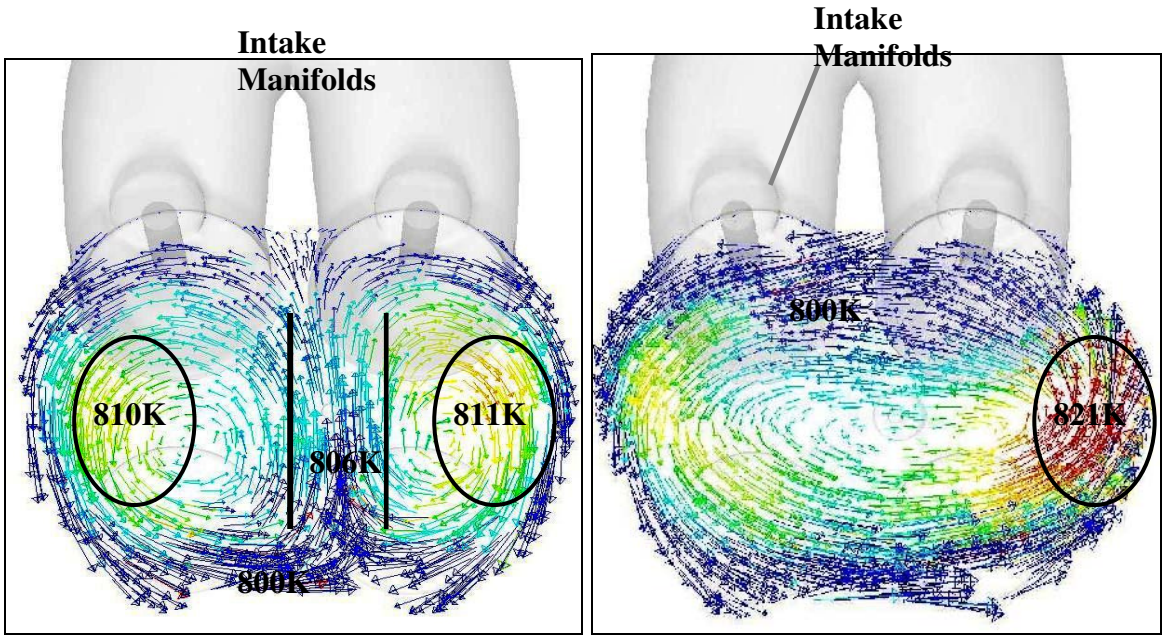

Figure 111: The Comparison of the CFD In-Cylinder Gas Temperature Predicted at TDC for the Middle Cylinder Plane: A) Base Intake Port Case.; B) Swirl Intake Port Case

The strong in-cylinder gas thermal in-homogeneity is indicated at the TDC for the 'Swirl' case in Figure 111 B. The highest spatial gas temperature is visible within the right hemisphere of the cylinder head region for this model. This is partially due to the effect of the gas squish and the convection of the hottest structures during piston compression.

Also, it must be noted that the swirling structures are very complex in a 3-D engine environment and the flow history sets-up the thermal in-homogeneities at the TDC. It seems that in general an asymmetric in-cylinder flow generated by the swirl port tends to be almost circular close to the piston's surface. Moreover, the highest gas temperature and a weaker mixing process are achieved in the vertical cylinder direction (tumble). This is due to the piston distortion mechanism during the compression which influences the swirl pattern leading to a high gas angular momentum in part of the bottom cylinder part. Such a homogeneous swirling flow becomes dominant in the cylinder and actively affects the thermal in-homogeneity and mixing process until the TDC.

The features of the upper part of in-cylinder thermal structure for the 'Swirl' port case at the BDC are shown in Figure 112 I and II. As was stated before, the highest average temperature of the gas is achieved in the lower part of the cylinder swirling gas structure. For this engine condition it is 341 K, compared to 329K for the upper cylinder part. Moreover, the top cylinder thermal pattern indicates the adverse pressure effect on the fluid which keeps the hottest gas structure under the intake valves in a separation bubble. The dominant anticlockwise swirling flow pattern presented at the engine TDC is in a form similar to the bottom swirl structure at the BDC. It is suggested that the aerodynamic structures withstand piston compression time and are driven by the gas mixing at the TDC via shear mechanism.

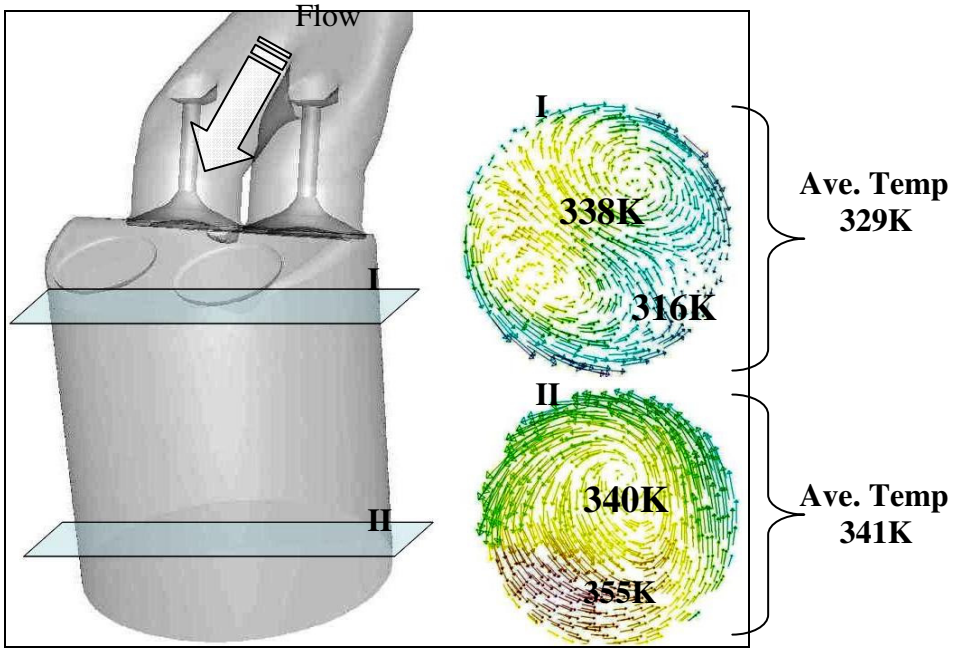

Figure 112: The CFD 'Swirl' case prediction of the gas thermal structure at BDC for: A) Top cylinder plane with average Temp. 329K; B) Bottom cylinder plane with Ave. Temp. 341K

As the opposite to the swirl case, the base intake port configuration generates much more symmetrical and uniform flow across the cylinder domain at all CAD as shown previously in chapter 7 and 8. The thermal gas mixing structure is inherently covected by the large-scale flow, such as tumble and swirl mechanisms supplied by the cold intake jets. Figure 111 A indicates that the middle cylinder region between the two counter-rotated vortices has a slightly lower gas temperature. Two mechanisms are responsible for this thermal effect: the

first is controlled by the thermal stratification the vortex and the second is generated by the cold jet flow during the engine's induction phase.

From the analysed data, it is apparent that the history of the in-cylinder mixing and the intake port geometry strongly affect the TDC cylinder thermal gas composition. Figure 113 A and B present the function of the in-cylinder PDF temperature calculated for both of the engine port configurations at the TDC crank position. Both of the port configurations indicate a comparable average cylinder temperature and a higher spatial thermal in-homogeneity for the 'SWIRL' case. In addition, it can be clearly seen that the 'Swirl' case has a higher gas temperature which inherently can affect the auto-ignition time characteristic in any HCCI engine. The higher gas temperature at the cylinder TDC gives evidence that for the swirl port configuration the mixing process between two gases is less intense, especially on the bottom cylinder region. In comparison, for the base port geometry the wall-cold jets are achieved via the piston during the induction time and mix much more intensely with the bottom hot fluid structure to create a large tumble vortex and a more uniform thermal gas structure.

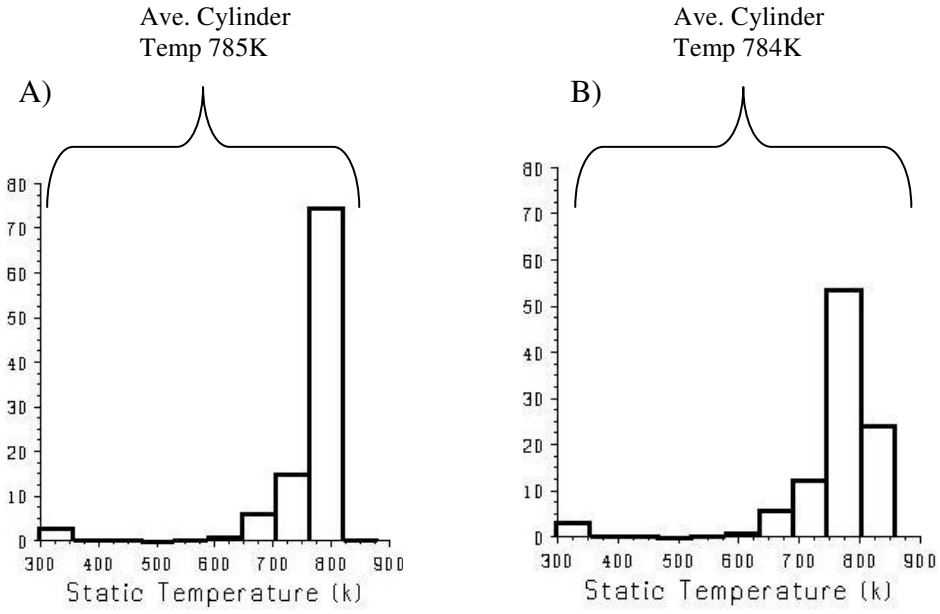

Figure 113: The In-Cylinder PDF Temperature Function for the TDC Piston Position: A) 'Base' Port Case, B) 'Swirl' Port Case.

9.4 Summary

The chosen intake port strategy has a significant impact on in-cylinder thermal field development during the engine induction and compression until the TDC. From both of the presented cases it is apparent that the directed cold gas conical jet divides the cylinder thermal structure into hot and cold regions. The upper middle cylinder head and wall flow transport the cold gas structures from the top to the bottom cylinder region. However, the base engine port configuration seem to be much more effective in mixing gas, especially within the lower part of the cylinder. As was stated earlier the base port configuration generates a large symmetric bottom tumble which actively mixes hot and cold gas structures. A different situation is encountered for the swirl port case where the incoming cold jet is less vertically convected and swirl structures dominate the in-cylinder volume. The weaker cylinder large-scale tumble motion inherently affects the gas transport process across the cylinder and thermally stratifies the bottom part of the cylinder. During the compression and near the TDC the partially mixed gas forms the swirling structure and proceeds towards the large in-cylinder thermal in-homogeneity. A second important phenomenon is apparent under the intake valves where the large-scale separation flow generates an aerodynamic bubble with much higher gas temperatures. This effect is visible for both of the intake port cases and is due to the adverse pressure force and the effect of the intake valve cold gas shroud.

For the symmetric NVO strategy, the additional back-flow gas effect must be considered in the thermo-flow analysis. The base engine port geometry and the intake valve opening and closing vastly influence the intake thermal gas structure as well as the further development of the cylinder's thermal gas. It must be noted that for HCCI engine technology, the spatial field of the in-cylinder gas temperature is crucial for any analysis of auto-ignition phenomena. Therefore, the created computational model 'MK_MF1' is useful tool for

thermo-flow evaluations, especially with the lack of experimental techniques for the direct measurement of spatial temperature fields.

Chapter 10

CONCLUSIONS AND FUTURE WORK

10.1 Overview

As has been presented in preceding chapters, two different experimental intake port strategies along with the symmetrical 110 CAD Negative Valves Overlap (NVO) have been applied for the Homogeneous Charge Compression Ignition (HCCI) engine in order to extend the analysis of the spatial cylinder flow gas in-homogeneity. Case studies for internal 'COLD' flow structures have been investigated using a motored single cylinder optical engine and the Particle Image Velocimetry (PIV) technique, as well as a 3-D CFD engine model which has been extensively validated by experiments.

The objectives of the experimental and computational study were focused on the spatial and temporal turbulence gas flow structures that develop within the HCCI engine cylinder. The following effects have been investigated using both experimental and computational methods: the temporal effect of changing the engine's architecture on the organisation of turbulent in-cylinder flow and the development of mean and RMS velocities during the induction and compression engine phases. The characterisation of the in-cylinder gas flow mechanisms responsible for the development of large-scale tumble and swirl structures obtained for the consecutive CAD was also attempted. Also presented was a qualitative spatial study of the aerodynamic characteristics of turbulent large-scale 'COLD' flow structures i.e. (velocity vector maps and vortices) and of the gas mixing phenomena affected by two different intake port geometries and a symmetric NVO.

10.2 Summary of Presented Work

The 'COLD' Flow Gas Mixing Process within the HCCI Single Cylinder Optical Engine (optical PIV measurements)-Two different port geometry strategies have been applied to the HCCI single cylinder optical engine at a symmetrical 110 CAD Negative Valve Overlap (NVO) in order to measure their effects on complex spatial gas mixing and the in-cylinder mass transport process. The temporal and spatial in-cylinder mass distribution and gas convection over the engine cylinder are characterised by the PIV cross-correlated velocity vector sequences obtained at the vertical and horizontal laser planes. The 2-D velocity vectors are determined by the following sequences of crank angles: (130, 180, 220, 300) CAD aTDC.

The in-cylinder ensemble-average velocity vectors based on the 60-75 instantaneous vector fields are assumed for the inlet manifold deflectors (SWIRL-port and TUMBLE-port) respectively. The engine flow structures for both cases are compared at similar vertical and horizontal planes created by the double pulse Nd:Yag laser, with a uniform 1-10um diameter of the MIE light scattering.

The examined in-cylinder velocity field indicate that the intake jet for both types of intake port deflectors strongly affects the in-cylinder bulk gas structure during the intake and compression phase and has a large impact on the global gas mixing process. For the low-swirl 'Tumble' case port arrangement a characteristically higher velocity magnitude over the upper half of the cylinder chamber develops during the inward flow and is maintained almost to the BDC. The velocity components for low-swirl 'Tumble' ports peak at 20 m/s when the middle cylinder's (Jet-Jet) flow appears a highly downward facing axial flow. For this case the (Jet-Wall) structure is also visible on the rear part (dotted line) of the cylinder wall beneath the inlet valve seats, due to converging flow from the two intake valves in accordance with the (Jet-Jet) structure. Also worthy of observation is that this data is recorded at 110 CAD after

the piston reaches the maximum downward velocity and the intake valves are on their opening ramp and therefore at a relatively low lift with a low valve curtain area. From the available data, it is also apparent that for the tumble-port, the in-cylinder flow has a higher Re number almost up to BDC and is built-up by large-flow coherent structures compared to the swirl-port case

The swirl-port case promotes a lower in-cylinder turbulence intensity as well as an in-cylinder ensemble-average RMS of velocity fluctuation during the induction process. For this phase, it seems that the port-swirl delivers the weakest in-cylinder global mixing process, especially at the bottom cylinder region and it influences the mass transport and inherently the thermal stratification. Additionally, the longer induction process obtained for this case maintains a longer large-scale tumble flow that is visible in the presented results.

The PIV results with visible large-scale flow patterns and a wide range of turbulence intensities clarify that the region of the weak cylinder gas mixing process is probably the most interesting for the auto-ignition development process. This is due to the larger temperature gradient between mixing structures where the intake (jet-jet) has a large Re and cold gas structure which mix with a low Re and gas cylinder residuals. In other words, the region of the cylinder with the low gas temporal RMS of velocity fluctuation should be considered as preferable for auto-ignition to occur.

The open question is ‘How can 2-D PIV velocity vectors be used to evaluate the real 3-D spatial in-cylinder flow and the global thermal gas mixing process?’ Therefore, additional CFD modelling has been applied. Additionally, for the optical diagnostics study phenomenological ‘Flow Analysis Tools’ have been developed to characterise the large in-cylinder flow structures i.e (Jet-Jet) interaction, (Jet-Wall) interaction, and (Jet-Bulk) interaction. In the case of the ‘Flow Analysis Tools’, other important parameters are in use

i.e., average turbulence intensity, RMS of the gas velocity fluctuation, Tumble Ratio (TR) and Swirl Ratio (SR). The ensemble-averaged velocity vector data are analysed in order to examine the bulk flow behaviours and reduce the effect of cycle-to-cycle variation in flow. Therefore, the experimental data is suitable for further CFD RANS (Reynold Average Navier-Stokes) model validation and cannot be compared with the LES instantaneous velocity field solver results.

The Three Dimensional CFD Study of the In-Cylinder 'COLD' Flow for a Base Engine Geometric Configuration and Symmetry 110 NVO- The in-cylinder CFD three-dimensional engine model and 'COLD' flow data have been combined with the 2-D PIV results in order to extend the spatial and temporal information about the scalar flow fields of internal engine flow at 1000 RPM. Moreover, at the chosen symmetric NVO valve timing strategy, the gas exchange process and mixing quality in the four-stroke DI HCCI engine have been examined. An important achievement is obtained in the construction of a numerical model of the single cylinder engine, which is able to predict the major large-scale flow structures along the engine induction and compression phases. In addition, the built Mk-MF1 CFD single cylinder model supplies a fairly good prediction of the cylinder TKE and Turbulence Intensity as well as the possibility to use various flow strategies and physical models for future work, including fuel injection and combustion.

The three dimensional computational results are compared and validated against the experimental PIV velocity vector fields and in-cylinder pressure data. The series of results are analysed for specific CAD and over several cycles to gain stable flow conditions. The single cylinder HCCI numerical model features in-cylinder flow structure accuracy as well as similarity in velocity magnitude for the chosen planes of measurement. The large-scale in-cylinder flow is predicted correctly with whole types of structures, e.g. vortex motion, gas jet interaction and near surface effects on eddy induction. For the current study, the 3-D

numerical multi-cycle single cylinder engine was built and the CFD k-ε RANS solver was used to calculate the spatial in-cylinder turbulence intensity, Eddy Viscosity, TKE, EPS and TLS.

It has been found that the general low pressure encountered during the induction process beneath the intake valve-heads due to the presence of the separation flow influences the later general in-cylinder transport process. As the Mk-MF1 CFD single cylinder model and the obtained static pressure maps shown, the intake valve inherently obstructs the intake gas stream and is shrouded beneath the cylinder zone from the direct action of the cold intake jet. This effect strongly imposes the cylinder flow character, where the gas is flowing from the higher-pressure cylinder region -5150 Pa to the lower -5550 Pa situated under the intake valves at these conditions.

It should be stated that the dimension of the intake valve head can significantly affect the pressure depression and global cylinder gas mixing process. In the HCCI engine cylinder the composition of the mixed gas structure controls the level of field reactivity. The gas stratification mechanism driven by the valve-shrouded effect produces all the scales of swirling flow structures, where the large-scale flow proceeds towards the intake valve head.

In addition, the mechanism of the hot gas transport phenomena has been presented, which occurs on the exhaust engine side towards the intake valve bottom due to lower pressure action under the intake valve. In addition, the schematic diagram reveals that the internal hot gas continually supplies the region of the intake valve and it is counteracted by cold intake gas holding the core of the vortices as a homogeneous structure.

Numerical Investigation of the In-Cylinder Gas Thermal Convection Effect on Spatial Cylinder Thermal Stratification- For the chosen intake port strategy, the engine port base and swirl significantly impact the in-cylinder thermal field development during the

engine induction and compression. From the two presented cases, it is apparent that the directed cold gas conical jet divides the cylinder thermal structure between hot and cold regions. Flow from the upper middle cylinder head associated with the cylinder wall-jet transports the cold gas structures from the top to the bottom cylinder region. However, the base engine port configuration seems much more effective in aiding the gas mixing process, especially within the bottom cylinder. As was stated earlier, the base port configuration generates large symmetric bottom tumble which actively mixes hot and cold gas structures. A different situation is encountered for the swirl port case where the incoming cold jet is less vertically convected and the swirl structures dominate the in-cylinder volume. The weaker cylinder large-scale tumble motion inherently affects the gas transport process across the cylinder and thermally stratifies the bottom part of the cylinder. During compression and near the piston's TDC, the partially mixed gas forms a swirling structure and proceeds towards the large in-cylinder thermal in-homogeneity. A second important phenomenon is apparent under the intake valves where the large-scale separation flow generates an aerodynamic bubble with much higher gas temperatures. This predicted effect is visible for both intake port cases and is due to the force of adverse pressure and the effect of the intake valve cold gas shroud.

For the symmetric NVO strategy, the additional back-flow gas effect must be considered in any thermo-flow analysis. The base engine port geometry and the opening and closing of the intake valve influence vastly the intake thermal gas structure as well as the development of further thermal cylinder gas. It is noteworthy that for HCCI engine technology, the spatial field of in-cylinder gas temperature is crucial for any analysis of auto-ignition phenomena. Therefore, the created computational model 'MK_MF1' can act as a proper tool for analysing the thermo-flow while there is no cheap experimental method available for a direct measurement spatial field temperature.

10.3 Suggestions for Future Work

The MKMF1 RANS model is robust and can be effectively used to analyse advance gas flow and combustion strategies for HCCI, SI and DIESEL engine types. In addition, the mixing of fuel-air and other types of fuels can be analysed numerically, including the fuel wall film, break-up process and turbulence effects on droplets and combustion. Additional benefits can be utilised from the flow validation CFD model of the single cylinder engine for further applications of fuel injection and combustion engine models associated with the chemical kinetics reaction solver. This computational approach, which has been validated with real engine data could ultimately show a complete picture of the spatial effects which affect gas emissions and the creation of Particulate Matter (PM). The three dimensional model can also predict the effect of cycle-to-cycle variations during a cold engine start; with an additional catalyst model this could prove very useful for further spatial flow-reactive analyses, as well as combustion turbulence gas interactions.

The most advanced proposition lies in the area of numerical modelling and the LES concept of turbulent flow where an instantaneous flow field is obtained. Currently Birmingham University is capable of running a multigrid problem, such as parallel processes for an engine model based on 5-15 million computational cells. This approach is more realistic for any time dependent flow problem.

APPENDIX A

High Pressure Direct Injection System

The control box Figure 114 consists of six valve bodies; five of 3-way and two of 1-way types. Each valve is designed by Swagelock® to operate at a maximum pressure of 35 MPa. The main control panel and all the unions are connected to a high-pressure fuel rail and accumulator. The fuel purging 2-way valve is mounted on the engine cylinder head and is used during the fuel fill-up or removal phase. After finishing the test, the residual fuel from the accumulator or from the high-pressure rail is returned to the surge tank. All the maintained procedures of the high-pressure direct injection system are shown schematically in Figures 115 to 117.

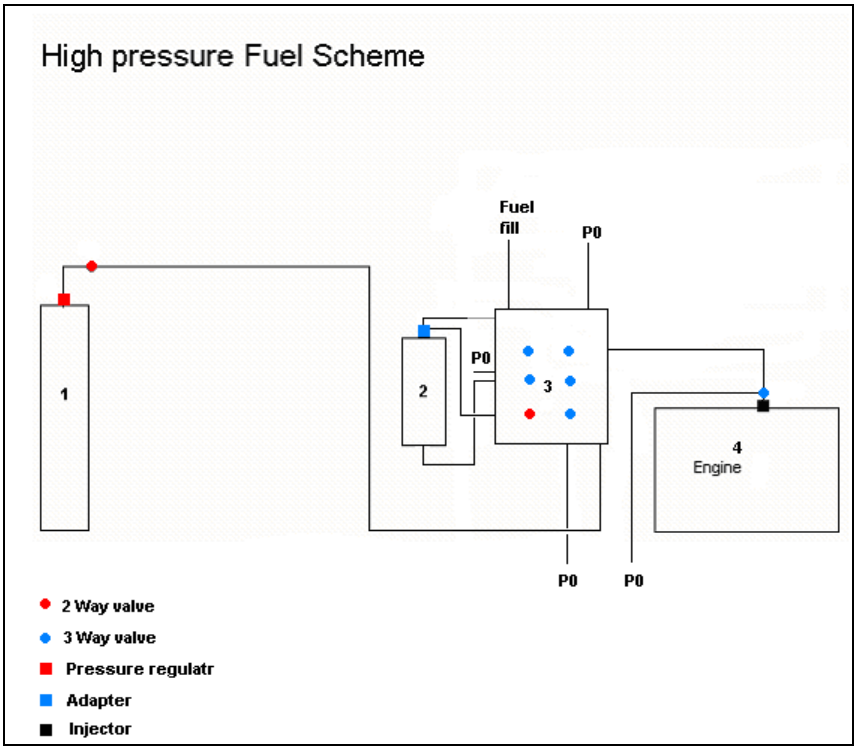

Figure 114: High Pressure Fuel Scheme

Legend:
1-N2 Bottle
2-Accumulator
3-Control Box
4-Engine

The direct injection system maintenance procedure is divided into three main stages:

1-SYSTEM PURGING

2-ACCUMULATOR FUEL FILL-UP

3-HIGH PRESSURE RUNNING

Stage 1-System Purging

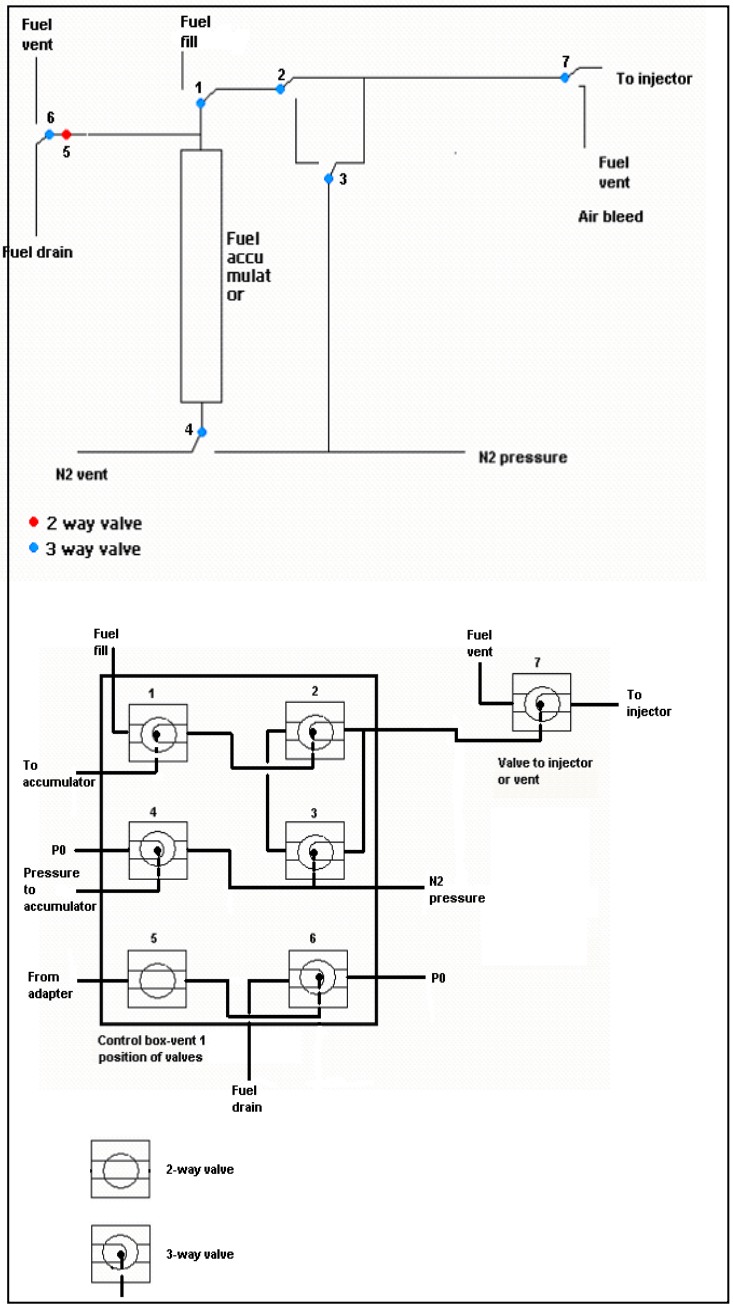

Figure 115: Schematic View of System Purging and Control Valves Box Set-Up

Stage 2- Fuel Accumulator Fill-up

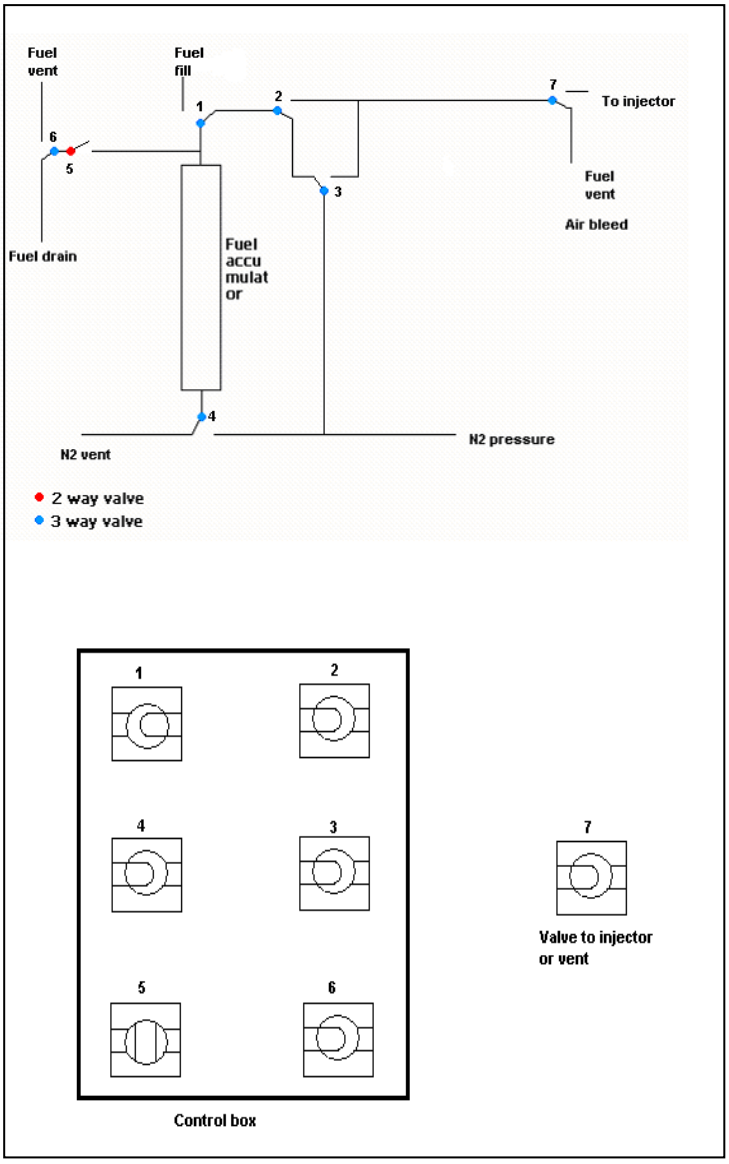

Figure 116: Schematic View of System Fuel Fill-Up and Control Valves Box Set-Up

Stage 3-High Pressure Running

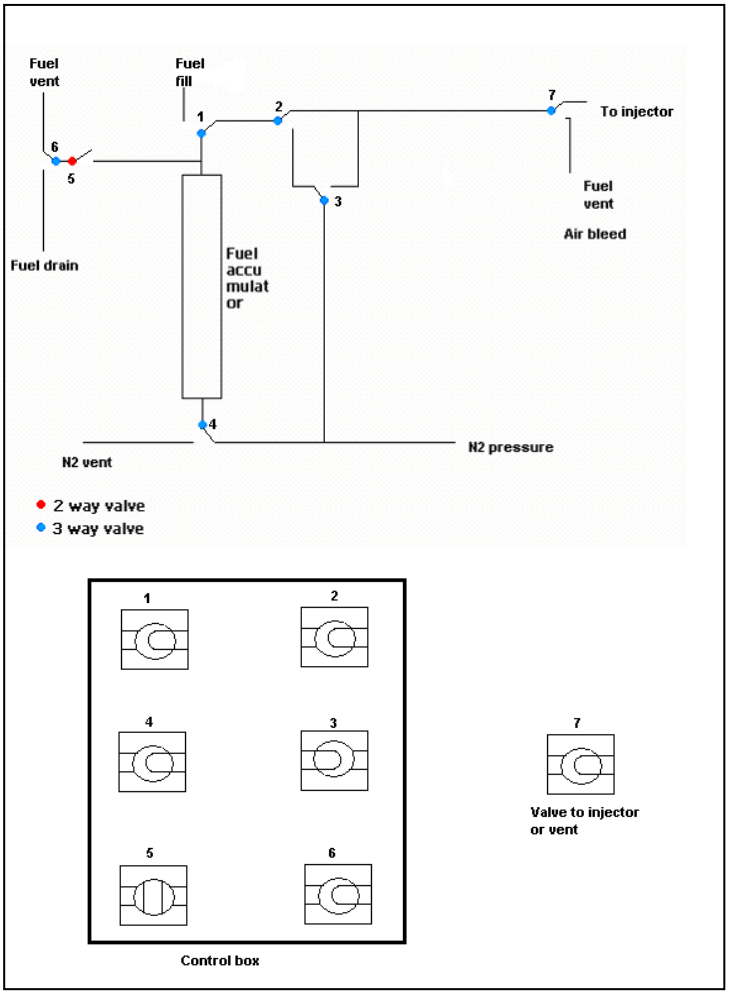

Figure 117: Schematic View of System High Pressure Operation and Control Valves Box Set-Up

For safety reasons, the emergency pressure damp valve is mounted at the high-pressure N2 rail side and is controlled by the pneumatic actuator. The pneumatic valve is opened in an emergency to suddenly release the Nitrogen pressure within the fuel accumulator. The described high-pressure direct injection system facility used for the optical engine is an integral part of the project and is used for the combustion and spray research.

References

1 J.L.Lumley,. 'Engines An Introduction'. 1999: Cambridge University Press, ISBN: 0521642779

2 J. Misztal, Phd 'Study of Homogeneous Charge Compressionignition (HCCI) Combustion and Emisson Characteristics in a Multi-Cylinder Engine'. University of Birmingham 2009.

3 S. Tanaka, et al.,'Two-stage Ignition in HCCI Combustion and HCCI Control by Fuels and Additives', Massachusetts Institute of Technology, Cambridge, MA, USA, Combustion and Flame, Volume 132, Issues 1-2, January 2003, Pages 219-239

4 M. Frackowiak, et al., 'The Effect of Exhaust Throttling on HCCI - Alternative Way to Control EGR and In-Cylinder Flow', University of Birmingham 2008, SAE Technical Paper Series, SAE 2008-01-1739, 2008.

5 Peng, Z.; Zhao, H.; Ladommatos, N., 'Effects of Air/Fuel Ratios and Egr Rates on HCCI Combustion of N-Heptane, a Diesel Type Fuel". SAE Technical Paper Series 2003, SAE 2003-01-0747.

6 O.Erlandsson, et al, 'Simulation of HCCI- Addressing Compression Ratio and Turbo Charging'. SAE Technical Paper Series 2002, SAE 2002-01-2862.

7 Z. Wang, et al., 'Study of the effect of spark ignition on gasoline HCCI Combustion' Proc. Inst Mech Engrs, Part D: Journal of Automobile Engineering 2006, 220, (6), 817-825.

8 J.L.Lumley,. 'Simulation and Modeling of Turbulent Flows. 1994: Oxford University Press, ISBN: 0195106431

9 H. Chen et al.,' The Effect of Temperature Inhomogeneity on Low-Temperature Autoignition of Fuel-Lean Premixed Hydrogen/air Mixtures' Combustion Research

Facility, Sandia National Laboratories, 3rd Joint Meeting US Sections of Combustion Institute, 2003

10 Lee, Dana W., 'A Study of Air Flow in An Engine Cylinder'. naca-report-653 1939

11 W.R.Hawthorne, Biographical memoir of H.R. Ricardo. In Biographical Memoirs of the Royal Society, volume 22, pages 359-380. Royal Society of London, London, UK, 1976

12 D.P. Hoult 'The Generation of Turbulence In an Internal-Combustion Engine' Massachusetts Institute of Technology, Cambridge, Plenum Press 1980, ISBN 0306404311

13 A.D. Gosman et al., 'Development of Prediction Methods for In-Cylinder Processes In Reciprocating Engines'. Plenum Press, pp 69-124, 1980.

14 B.E. Launder et al. 'The calculation of low-Reynolds-number phenomena with a two-equation model of turbulence'. Int. J. Heat Mass Transfer 16 (1973), pp. 1119–1130.

15 B.E. Launder and D.B. Spalding, Turbulence Models and their application to the prediction of Internal Flows,*Symposium on Internal Flows, Inst. of Mech. Engns* (1971)

16 P.O. Calendini et al., 'In-cylinder velocity measurements with stereoscopic particle image velocimetry in a si engine'. SAE Paper 2000-01-1798, 2000.

17 Y. Li et al., 'Tumbling Flow Analysis in a Four-Valve Spark Ignition Engine Using Particle Image Velocimetry'. International Journal of Engine Research, Volume 3, Number 3 / 2002, p 139-155,

18 Y. Li., 'An Investigation of In-cylinder Tumbling Motion in a Four Valve Spark Ignition Engine'. Proceedings of the Institution of Mechanical Engineers, Part D: Journal of Automobile Engineering, Volume 215, Number 2 / 2001,p 273-284

19 M. Christensen., 'The Effect of In-Cylinder Flow and Turbulence on HCCI Operation'. SAE Paper 2002-01-2864, 2002

20 H. Zhao et al., ‘Understanding the Effects of Recycled Burnt Gases on the Controlled Autoignition (CAI) Combustion in Four-Stroke Gasoline Engines’ SAE Paper 2001-01-3607, 2001

21 M. Sjoberg et al., ‘Comparing Enhanced Natural Thermal Stratification Against Retarded Combustion Phasing for Smoothing of HCCI Heat-Release Rates’. SAE Paper 2004-01-2994, 2004

22 W. C. Reynolds, "Modeling of fluid motion in engines—An introductory overview," in *Symposium on Combustion Modeling in Reciprocating Engines* (Plenum, New York, 1980).

23 A. P. Morse and J. H. Whitelaw Measurements of the In-Cylinder Flow of a Motored Four-Stroke Reciprocating Engine, *Proceedings of the Royal Society of London. Series A, Mathematical and Physical Sciences*, Vol. 377, No. 1770 (Jul. 8, 1981), pp. 309-329

24 C Chandrsuda, et al., ‘Turbulence Structure of a Reattaching Mixing Layer’. Journal of Fluid Mechanics Volume 110, September 1981, Pages 171-194

25 Clark et al., 1979R.A. Clark, J.H. Ferziger and W.C. Reynolds, ‘Evaluation of Subgrid-Scale Turbulence Models Using a Fully Simulated Turbulent Flow’, *J. Fluid Mech.* **91** (1979), pp. 1–16

26 H. Tennekes, J. L. Lumley, ‘A First Course in Turbulence’, 1972 ISBN: 9780262200196

27 A. D Gosman et al., ‘Computer Simulation of In-Cylinder Flow, Heat Transfer and combustion’ A Progress Report FS/78/38, Austria 1978.

28 M. Yao, Z. Zheng., ‘A Numerical Investigation on Effects of Charge Stratification on HCCI Combustion’. SAE Paper 2007-01-4132, 2007.

29 A. Leonard., ‘Energy Cascade In Large-Eddy Simulations of Turbulent Fluid Flows’. Department of Mechanical Engineering, Stanford University, Stanford 1974: Elsevier Science & Technology Books ISBN: 012018818X

30 Joel H. Ferziger et al., 'Computational Methods for Fluid Dynamics' Springer, ISBN**:** 3540653732, 1999

31 J. Laufer.,'The Structure Of Turbulence In Fully Developed Pipe Flow', Report 1174 National Bureau of Standards, 1954 - NASA

32 I. Shames, "Mechanics of Fluid', McGraw 1992, ISBN: 0071128158

33 S. Subramaniyam et al., 'Turbulent Flow Inside the Cylinder of a Diesel Engine - an Experimental Investigation Using Hot Wire Anemometer', Experiments in Fluids, Volume 9, Number 3 / May, 1990 ,pp 167-174, 2004

34 D.Choi et al., 'Evaluation of an Industrial CFD Code for LES Applications', Studying Turbulence Using Numerical Simulation Databases, 8. Proceedings of the 2000 Summer Program.pp 221-228,Nov. 01, 2000

35 C. Jimenez et al., 'Numerical Simulations of Combustion in a Lean Stratified Propane-Air Mixture', Studying Turbulence Using Numerical Simulation Databases, 8. Proceedings of the 2000 Summer Program.pp 215-221,Nov. 01, 2000

36 Stephen B. Pope 'Turbulent Flows', Cambridge University Press; 1 edition (January 15, 2000), ISBN-10: 0521598869

37 C. Meneveao, et al., 'Simple Multifractal Model for Fully Developed Turbulence',Physical Review Letters – 28 September 1987 (Volume 59, Issue 13), pp 1424 - 1427

38 Oertel Herbert (Ed.) 'Prandtl's Essentials of Fluid Mechanics', Springer, New York, 1952, ISBN: 978-0-387-40437-0

39 J.Anderson, 'Computational Fluid Dynamics', McGraw-Hill Science, ISBN: 0070016852, 1995

40 J. I. Ramos, 'Internal Combustion Engine Modelling', Taylor & Francis; 1 edition (June 1, 1989), ISBN: 0891161570

41 D.C.Wilcox, ‘Turbulence Modeling for Cfd’, DCW Industries; 2nd edition (December 2002), ISBN: 192872910X

42 P. Spalart., "Theoretical and numerical study of a three-dimensional turbulent boundary layer", *J. Fluid Mech.,* Vol. 205, pp. 319-359. (1989)

43 P. Spalart, P., and S. Allmaras, "A One-equation turbulence model for aerodynamic flows", Technical Report AIAA-92-0439 , American Institute of Aeronautics and Astronautics. (1992),

44 B.Launder and D.Spalding. ‘Lectures in Mathematical Models of Turbulence’. Academic Press, London England, 1972.

45 W. M. Henkes et all., ‘Natural Convection Flow in a Square Cavity Calculated with Low-Reynolds-Number Turbulence Models’ Int. J. Heat Mass Transfer*,* 34:1543-1557, 1990

46 Boussinesq, J. (1877), "Théorie de l’Écoulement Tourbillant", Mem. Présentés par Divers Savants Acad. Sci. Inst. Fr., Vol. 23, pp. 46-50

47 M. M. Gibson and B. E. Launder. ‘Ground Effects on Pressure Fluctuations in the Atmospheric Boundary Layer’. J. Fluid Mech., 86:491-511, 1978.

48 B. E. Launder. ‘Second-Moment Closure: Present... and Future?’, Inter. J. Heat Fluid Flow, 10(4):282-300, 1989

49 B. E. Launder, et al., ‘Progress in the Development of a Reynolds-Stress Turbulence Closure’. J. Fluid Mech.*,* 68(3):537-566, April 1975

50 M. Shur, et al., ‘Detached-Eddy Simulation of an Airfoil at High Angle of Attack’. In 4th Int. Symposium on Eng. Turb. Modeling and Experiments, Corsica, France, May 1999

51 F. Nicoud, et al., ‘Subgrid-Scale Stress Modelling Based on the Square of the Velocity Gradient Tensor’. J.Fluid Mech, Flow, Turbulence, and Combustion*,* 62(3):183-200, 1999

52 F. Nicoud. Et al,. ‘Subgrid-Scale Stress Modelling Based on the Square of the Velocity Gradient Tensor. J.Fluid Mech Flow, Turbulence, and Combustion’, 62(3):183-200, 1999.

53 S.-E. Kim, et al., 'Large eddy simulation using unstructured meshes and dynamic subgrid-scale turbulence models'. Technical Report AIAA-2004-2548, American Institute of Aeronautics and Astronautics, 34th Fluid Dynamics Conference and Exhibit, June 2004.

54 Fluent Inc. Centerra Resource Park 10 Cavendish Court Lebanon, USA, NH 03766-1442, tel: 603-643-2600

55 KIVA™ code, Energy Science and Technology Software Center (ESTSC) at (865) 576-2606. The mailing address for ESTSC is P.O. Box 1020, Oak Ridge, TN 37831-1020. The email address for ESTSC is estsc@osti.gov. KIVA code , Los Alamos National Laboratory, USA.

56 AVL-FIRE™, CFD-Department, Kleiststrasse 48 A-8020, Graz Austria, Tel.: +43 316 987-441

57 CONVERGE™, CFD code. Convergent Science, Inc.6405 Century Ave., Suite 102Middleton, WI 53562, USA, Phone: (608) 831-7940, Fax: (608) 831-1551, Email: contact@convergecfd.com

58 Davis, D.O., and Gessner, F.B., 'Experimental Investigation of Turbulent Flow Through a Circular-to-Rectangular Transition Duct', AIAA Journal, 30(2):367-375, 1992

59 T.Petrila, et al., 'Basics of Fluid Mechanics and Introduction to Computational Fluid Dynamics', Springer; 1 edition (December 15, 2004), ISBN: 0387238379

60 P.Wesseling, 'Principles of Computational Fluid Dynamics', Springer; 1 edition (November 27, 2000), ISBN: 3540678530

61 J.M. Cimbala, et al. 'Fluid Mechanics Fundamentals and Applications,1st Edition, McGraw- Hill, 2005. ISBN: 9780073301129

62 A. Chen, A. et al., 'Velocity Characteristics of Steady Flow Through a Straight Generic Inlet Port', International Journal for Numerical Methods in Fluids, 21:571-590, 1995.

63 O. G. Chkhetian, et al, 'The Inverse Energy Cascade and Self-organization in Homogeneous Turbulent Shear Flow', Springer Netherlands, Volume 51, Numbers 1-2 / June, 1993, pp 67-72, 1995

64 J. QIAO, et al. 'Fuel Reforming and Aftertreatment Technologies For Expanding the HCCI Engine Operating Boundary', JSAE Annual Congress, J. CODE: S0434A, VOL. NO.24-06, PAGE.29-32 (2006)

65 'Tempest Laser-Manual'-New Wave Research™

66 M. Raffel, et al., 'Particle Image Velocimetry: a Practical Guide', Springer; 2002, ISBN: 3540636838

67 'PIV Flow Master Manual: Davis 5'-LaVision™ 2000

68 H. Zhao, et al 'HCCI and CAI Engines for The Automotive Industry', Woodhead Publishing Limited, ISBN: 1845691288, 2009

69 A. McLandress (Daimler-Benz AG), et al., 'Intake and In-Cylinder Flow Modeling Characterization of Mixing and Comparison with Flow Bench Results', Paper SAE 960635

70 Herrmann Schlichting, Klaus Gersten, E. Krause, H. Jr. Oertel, C. Mayes "Boundary-Layer Theory" 8th edition Springer 2004 ISBN 3-540-66270-7

71 J.Lumely, 'Earlywork on Fluidmechanics in the Ic Engine', Annu. Rev. Fluid Mech. 2001. 33, pp:319–38

72 L. Cao, et al., 'Numerical Study of Effects of Fuel Injection Timings on CAI/HCCI Combustion in a Four-Stroke GDI Engine', SAE Paper: 2005-01-0144, 2005

73 S.V. Alekseenko, at el.,'Theory of Concentrated Vortices: An Introduction', Springer 2007, ISBN: 3540733752

74 J.B Heywood, 'Internal Combustion Engine Fundamentals',McGraw-Hill 1989, ISBN: 007028637X

75 I. Y. Ohm, et al.,'Mechanism of Axial Stratification and Its Effect in an SI Engine', SAE Paper: 2000-01-2843

76 H. Nakano, et al.,'An Investigation of the Effect of Thermal Stratification on HCCI Combustion by using Rapid Compression Machine', SAE Paper: JSAE 20077178

77 N. Dinler, et al.,'Numerical Simulation of Flow and Combustion in an Axisymmetric Internal Combustion Engine', Proceedings of World Academy of Science, Engineering and Technology Volume 22 JULY 2007 ISSN 1307-6884

78 T. Wilson, et al., 'Optical Study of Flow and Combustion in an HCCI Engine with Negative Valve Overlap', Journal of Physics: Conference Series 45 (2006), pp:94–103

79 CFD FLUENT™ Documentation

80 CFD FLUENT 6.3 documentation Remeshing Methods section 11.3.2

81 NASA-NPARC Alliance CFD Verification and Validation 'National Program for Aplications-Oriented Research in CFD'

82 H. Persson, et. al.,'The Effect of Swirl on Spark Assisted Compression Ignition (SACI)' SAE Paper: JSAE 20077167; SAE 2007-01-1856

83 C. M. GAO, et. al., 'Experimental Study on a Simple Ranque-Hilsch Vortex Tube', Department of Applied Physics, Eindhoven University of Technology, Publication: ISSN 0011-2275

84 A.C. Hoffmann, 'Gas Cyclones And Swirl Tubes: Principles, Design, And Operation', Springer Verlag 2007, ISBN: 3540746943

85 M.Achuth, et. al., 'Predictions of Tumble and Turbulence in Four-Valve Pentroof Spark Ignition Engines', International Journal of Engine Research, Volume 2, Number 3 / 2001, pp: 209-227

86 W. Roberts, et al., 'Turbulent Diffusion' Lectures, 790 Atlantic Drive Georgia Institute of Technology Atlanta, Georgia 30332-0355 USA